THE UNIVERSITY OF CHICAGO

DEVELOPING EMISSIVE PHOTOCHEMICAL REDUCTANTS FROM EARTH-ABUNDANT TRANSITION METALS

A DISSERTATION SUBMITTED TO THE

THE FACULTY OF THE DIVISION OF THE PHYSICAL SCIENCES

IN CANDIDACY FOR THE DEGREE OF

DOCTOR OF PHILOSOPHY

DEPARTMENT OF CHEMISTRY

BY

AYUSH GUPTA

CHICAGO, ILLINOIS

DECEMBER 2023

TABLE OF CONTENTS

Page

LIST OF FIGURES

LIST OF SCHEMES

LIST OF TABLES

LIST OF EQUATIONS

ACKNOWLEDGEMENTS

There are many people who I would like to acknowledge who have supported and mentored me on my way to completing this dissertation. I would like to first thank my advisor Professor Michael Hopkins. Throughout my years in his lab, he has always encouraged me to be inquisitive and to really delve into the problems I was working on. Whenever I was running into challenges with my research, he was always willing to hear me out and help me work through possible solutions. He has also helped me understand how to develop new chemical questions and understand how to develop them into new scientific research ideas some of which I was able to incorporate into this dissertation.

I would like to thank my high school science teachers Dr. Bill Lamb, Dr. Bevin Daglen, and Peter Langley who encouraged me to be more inquisitive about scientific research and were instrumental in beginning my interest in scientific research. Outside of high school, I would also like to thank Professor Carl Wamser at Portland State University. Through talking and working with him, I first got interested in doing renewable energy research and even got my first taste of working in a chemistry lab, starting me on my path as a chemist.

I would like to thank Professor James Blakemore and Professor Harry Gray at Caltech for starting me on my path to conducting high-level chemical research. Coming into Caltech, I was not sure what I wanted to study, leading me to pursue multiple possible interests. It wasn't until I had talked to Harry and started working in his lab that I decided that I wanted to pursue chemistry as my major.

I would like to thank both members of my committee Professor John Anderson and Professor Dmitri Talapin. Both have been really open for discussion during my time here at

UChicago and willing to talk science both about my project and projects going on in their labs. John has been very helpful in being a secondary person to sound out new research ideas with and discuss emerging scientific thought. Our discussions and disagreements have been really helpful in helping me understand chemistry and how to make sound chemical arguments while also providing new interesting areas of chemical research.

Working on the 4th floor with the other Wuttig, Anderson, and Jordan labs was a great experience. Being able to walk around and get help or just go to someone's desk and just talk made research a lot more manageable when things weren't working out. Occasional pub or other Hyde Park outings at the end of the day were also a great way to destress and relax. Even during COVID, it was always easy to find someone or something that you needed from another lab. Working with you all and even joining the Anderson lab group meetings for a couple of years greatly expanded my views on chemistry and provided a great environment to work in.

I would like to thank the members of the Hopkins lab for creating a collaborative work environment to pursue research. Starting out with Judith, Hunter, Mark, and Chris really accelerated me getting up to speed in all the new chemistry I was doing despite the large differences in the type of research we each were doing. Later on, after the lab had shrunk, doing day-to-day lab functions would not have been possible without working with Andrew who always managed to be a great help when anything in the lab needed to be done and without whom conducting research through COVID would not have been possible.

I would like to thank all of the friends I made throughout my time in Chicago both within the university and outside. Being able to explore Chicago, go to events, and try its food scene with Chris, Hannah, Jonathan, Harry, Malte or playing pool at the pub with Joe, Jeff, and others

was always great. Even casual conversations with other people around campus including Josh, Fauzia, Kim, Alex, Patrick, and Becca among others between seminars or at department events was a great way to break up doing science for the entire day and to relax a bit.

I would finally like to thank my family who have given me so much support over the years. I want to particularly thank my parents and my brother, for knowing when I needed a break and how to cheer me up after a rough day. Going on various backpacking or international trips was always a unique experience and provided a well-needed reprieve from working in lab. I wouldn't have been able to reach this point without you three.

ABSTRACT

Photoredox catalysis is a rapidly growing field in which energy gained from light absorption by a molecule is used to form and break chemical bonds to synthesize value-added products. The flexibility of photoredox catalysis has enabled design and realization of highly oxidizing and highly reducing chemical reactions with remarkable selectivity relevant for medicinal chemistry and renewable energy. Design of new chromophores is an important step in the general adoption of photoredox catalysis for large-scale applications where common chromophores such as $[Ru(bpy)_3]^{2+}$ and *fac*-$Ir(ppy)_3$ are unfeasible due to the high cost of the transition-metal center. This necessitates development of new strategies and new complexes that can drive these chemical reactions with cheaper, more abundant transition-metal centers in assembled architectures that are able to effectively harvest generated photocarriers. Bottom-up molecular design is a useful strategy for identifying new chromophore architectures and incorporating them into functional materials. This work describes the development of two different classes of chromophores and heterogenization of an optically active semiconductor with molecular catalysts.

The research described in Chapter 2 describes the synthesis and characterization of molecularly functionalized MoS_2 monolayers with transition-metal complexes. The resulting surface is studied using a variety of spectroscopic and physical characterization techniques to validate the presence of the added transition-metal species. The work in Chapter 3 describes the synthesis of some early transition-metal chromophores that are based on isoelectronic substitution of the W≡C core of emissive tungsten-alkylidyne complexes with a Mo≡C or Ta≡N core to understand the metal-ligand bonding and photophysics of these complexes. These complexes are further studied by protonation to form the corresponding cationic hydride

complex to differentiate the proton tautomerization of these hydride complexes in relation to the metal center and triply-bonded heteroatom. In Chapter 4, a computational study of a series of tungsten alkylidyne chromophores demonstrates how peripheral substitution affects excited-state properties of the triplet state. Trends in energies, bond lengths, and densities are studied in order to rationalize experimental photophysical data and suggest future improvements and studies for these complexes. The work described in Chapter 5 describes a second set of chromophores that are based on linear carbene-metal-amide copper complexes using deprotonated acridone as the amide. These complexes emit solely ligand-centered fluorescence. This copper complex is then compared to a potassium-cryptate salt and the parent protonated ligand to understand how deprotonation and coordination affects the ligand-centered photophysical processes.

CHAPTER 1

Introduction

1.1. Background.

Development of new sources of renewable energy is a pressing challenge facing the world going toward the middle of the 21st Century. Global energy usage has dramatically increased from an estimated 13.5 TW in 2001 to 16.2 TW in 2007 and 22.8 TW in 2019.[1-3] These numbers are projected to increase to 40 TW by the middle of the 21st century.[2] Meeting these energy demands requires development of multiple technologies that can work in concert to efficiently generate and store energy. Renewable sources of energy are particularly important to reduce the impact of climate change. Recent analyses by the Intergovernmental Panel on Climate Change have stressed that to avoid the worst consequences of climate change, global carbon emission must peak between 2020 to 2030 and become zero by 2050.[4] In order to achieve these goals, new technologies need to be developed not only to remove CO_2 from the atmosphere, but also to generate energy with net zero or negative CO_2 emission.

Multiple technologies have been developed to meet this energy need including wind, nuclear, geothermal, and solar. Of these, solar energy is a particularly attractive due to its high energy density and general availability in most habituated areas. Solar radiation under AM 1.5 illumination provides roughly 100 mW/cm^2.[5] Due to this high energy density, solar illumination can provide more energy in one hour to the earth's surface than is consumed in an entire year. Solar energy utilization is limited by its intermittency and its poor matching with regards to common peak usage hours which are in the morning and evening when solar flux is relatively small.[6] This necessitates solar energy capture to be paired with some form of energy storage.

While battery technology has dramatically improved with recent advances in lithium-oxygen batteries, redox-flow batteries, and high conductivity aqueous electrolytes, other technologies to improve solar energy harvesting and storage is still necessary.[7]

One possible form of storage is in the form of chemical bonds. When used as a source of energy these are called solar fuels, which commonly include simple fuel molecules such as methanol, hydrogen and ammonia. The energy density of these solar fuels greatly exceeds that of capacitors and batteries and can be made to be compatible with current energy infrastructure.[8] Photosynthesis in Nature is a convenient natural analogue of light-harvesting for energy storage. Here, the combination of light-absorbing and electron-transfer proteins are capable of generating and separating charge to drive chemical reactions and convert solar energy to a usable form by the organism. This involves a complex system involving multiple light absorption and charge transfer steps to achieve the overall reaction.[9] Drawing inspiration from photosynthesis, artificial photosynthesis aims to similarly convert sunlight into storable forms of energy. Many different artificial photosynthetic technologies have been developed and can generally be categorized as photocatalysis, photoelectrochemistry, and photovoltaic-driven electrolysis.[6] Mechanistically, these processes all rely on converting the initial energy delivered by photoactivation of a light harvesting center into a viable form of thermal or electrical energy to drive chemical reaction. Despite benefitting from commercially available components and high efficiency, photovoltaic electrochemical devices face challenges due to high costs, mass transport limitations, and poor scalability.[10-11] Photocatalytic devices, on the other hand, are comparatively simple and can be envisioned to be suitable for generation of solar fuels at a large scale despite current quantum efficiency limitations.[12] The generality of this reaction allows it to be highly flexible and has led

to developments in water splitting, CO_2 reduction, and even organic synthesis.[1-2, 6, 8, 12] Still, there are large scientific and technical challenges in making fuels like H_2 economical at scale.

Due to the importance of the initial light harvesting step in initiating the myriad of potential reaction sequences for artificial photosynthesis, chromophore design is a key initial step in reaction design for the synthesis of target product molecules. Some of the most important properties for designing chromophores are deliberate selection of its optical energy gap and ground-state energy levels. These provide energetic bounds for accessible reactions and are important for determining selectivity and photochemical accessibility of the desired reaction. Within the regime of visible light excitation, one can roughly access up to a 3 eV of additional driving force on top of the ground-state redox potential of the chromophore. This allows a huge range of potentials to be accessed by photoexcited electron-transfer which can be simply estimated using the Rehm-Weller Approximation.[13] For a photoreduction reaction, which could proceed following the general scheme shown in Figure 1.1, the excited-state oxidation potential is $E^{*/+} = E_{00} + E^{0/+}$. The simple additive nature of this approximation renders even conventional air-stable chromophores powerful photoreductants. For $[Ru(bpy)_3]^{2+}$ and *fac*-$Ir(ppy)_3$, this gives excited-state oxidation potentials of −1.25 V vs. $FeCp^{0/+}$ and −2.13 V vs. $FeCp^{0/+}$.[14] These values are close to that of strong ground-state reductants $CoCp_2$ and Na/Hg amalgam,[15] highlighting the tremendous electrochemical driving force accessible by typical chromophores. Furthermore, these potentials are nearly reducing enough to reduce CO_2 directly to its radical anion ($E^\circ = -2.5$ V vs. $FeCp^{0/+}$),[16] highlighting the utility of such reactions to drive even strongly uphill reactions for solar fuels production.

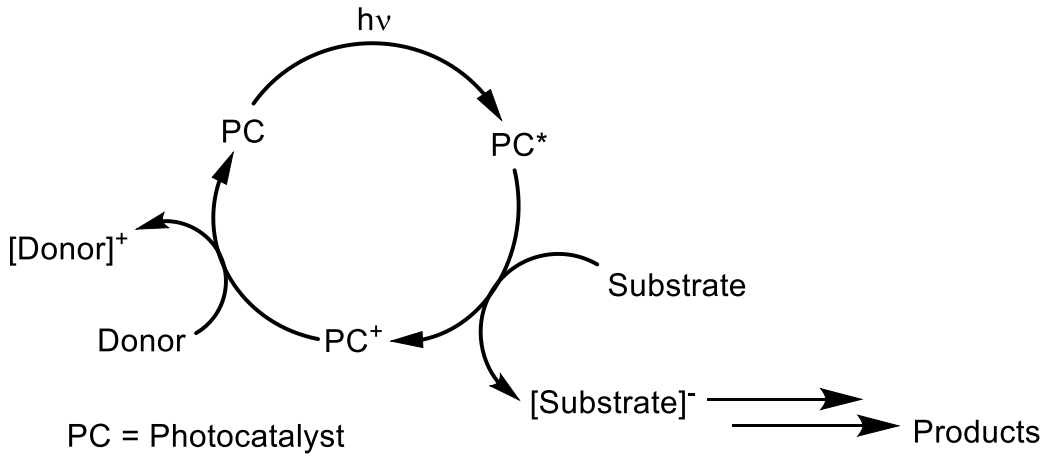

Figure 1.1 General photocatalytic cycle for reductive synthesis of solar fuels.

The research described in this thesis approaches chromophore design in the three distinct ways: the extension of prior studies of tungsten–alkylidyne photoredox chromophores to different metals, multiply bonded ligands, and computational models; the study of copper-carbene derivatives of an organic photoredox chromophore, as a model for modulating ligand-centered photophysical properties; and the functionalization of photoactive monolayer MoS_2 with transition-metal complexes, as a foundation for coupling the optical properties of transition-metal dichalcogenides with metal catalysts. The background and rationale for each of these topics is described below.

1.2. MoS_2 Surface Functionalization.

Understanding how to interface a light harvesting center with catalytic materials to drive production of photocatalytically generated products is an important step for the generation of solar fuels. Immobilization of catalysts on high aspect ratio photoactive materials is one route that is particularly attractive.[17-19] Here, the high aspect ratio enables high catalyst loading percentages and high activity due to the structurally open active sites. Common 2D materials

such as graphene and hexagonal boron nitride do not possess long-lived excited-states and are therefore not suitable for photogeneration of charge-carriers. Monolayer MoS_2 on the other hand is a direct band gap semiconductor with high charge carrier mobility suitable for a variety of electronic applications.[20-27] This suggests the possibility of using monolayer MoS_2 to generate photocarriers that can then be injected to a catalyst attached to the surface.

Surface-attachment of catalysts has been explored through covalent and noncovalent routes.[28-35] Noncovalent methods often utilize large aromatic π-faces or long chain alkanes to generate sufficient dispersion attraction to attach the catalyst to the surface. These methods frequently suffer from weak electronic coupling and limited stability. Alternatively, covalent approaches can provide much better stability and electronic coupling due to the formation of a direct bond between the surface and the catalyst.[36-44] Some studies have suggested that exfoliated MoS_2 may be suitable for covalent surface modification with transition-metal centers due to the presence of sulfur lone-pairs on the basal plane surface which could function akin to a ligand.[36, 44] This could enable facile interface between the optically active MoS_2 monolayer and the supported transition-metal catalyst. Due to limited literature precedent for this type of covalent modification with transition-metal centers, it is desirable to validate this type of surface functionalization with precise physical and spectroscopic techniques before study of any photocatalytic applications. We hypothesized that low-coordinate late transition metal complexes would be suitable for covalent modification due to the hard-soft acid base principle[45] and their ability to undergo associative ligand substitution with weak donor ligands.

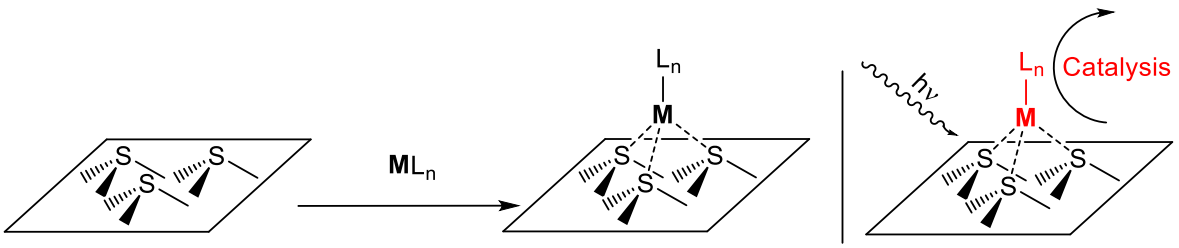

Figure 1.2. Strategy for functionalized MoS_2 derived photocatalytic materials.

In Chapter 2, we report an attempt to covalently functionalize the basal plane surface of MoS_2 using covalent functionalization with a transition-metal complex. Three different complexes were tested using a simple immersion-dose functionalization procedure. The presence of the surface-attached species was probed using a variety of spectroscopic and physical methods to establish surface-modification and perturbation of the attached species to the MoS_2 substrate.

1.3 Multiply Metal–Ligand Bonded Photoreductants.

Many common transition-metal chromophores use non-earth-abundant metals such as ruthenium and iridium. This presents an inherent challenge to general adoption of these photosynthetic schemes due to the limited availability and high cost of these elements.[46] Designing chromophores using cheaper and more abundant elements is therefore a necessary step in the adoption of these schemes in the global power grid. Transitioning from third and second row transition metals to first row metals is conceptually one simple method to reduce the cost of these materials while maintaining similar electronic structures and excited-states relative to their heavy-element congeners. Unfortunately, this seemingly trivial substitution does not always lead to stable and emissive chromophores suitable for light harvesting. This is largely attributed to the primogenic effect contracting the 3d orbitals compared to the larger 4d and 5d orbitals.[47] Consequently, this results in weaker metal-ligand bonds and reduces ligand-field

splitting, both of which contribute to the reduced stability and excited-state lifetimes of these chromophores hindering their use for energy applications at scale.

Pseudo-tetragonal complexes with metal-ligand multiple bonds are a well-studied class of luminescent transition metal complexes.[48-51] Complexes with d^2 configurations possess a doubly occupied nonbonding d_{xy} orbital with strongly destabilized π-antibonding d_{xz} and d_{yz} parentage unoccupied orbitals due to the strong π-bonding afforded by the multiply-bonded axial ligand.[52-54] The large energy gap between the d_{xy} HOMO and the d_{xz} and d_{yz} π-antibonding LUMO makes the electronic transition between them suitable for visible light excitation. Under C_{4v} symmetry, the electronic transition from HOMO to LUMO is dipole-allowed albeit weak due to its d-d parentage. Upon excitation, the excited singlet $^1[d_{xy} \rightarrow \pi^*]$ state undergoes ultrafast intersystem crossing to a phosphorescent triplet state, which is suitably long-lived to enable bimolecular reactivity.

Tungsten-alkylidyne complexes of the general form $W(CAr)L_4X$ (Ar = aryl, L = neutral sigma donor such as phosphine, X = anionic ligand such as halide) are a subset of this class of complexes whose photophysics and electronic structure are well understood (Figure 1.3).[52] Here, the strongly donating alkylidyne and d^2 tungsten center afford an electron rich metal-center that acts as a strong ground-state reductant. The π asymmetry of the phenyl ligand desymmetrizes the complex to C_{2v} symmetry and mixes the π* LUMO and π HOMO-1 orbitals to form the corresponding phenyl-conjugated bonding and antibonding orbitals respectively. Within this MO diagram, the nonbonding d_{xy} orbital with a_2 symmetry is orthogonal to the d_{yz} π bonding and antibonding orbitals with b_1 symmetry. Due to their orthogonal parentage, the a_2 orbital is sensitive to the choice of equatorial ligands while the b_1 orbitals are sensitive to the electronics of

the alkylidyne and trans axial ligand. This creates a large synthetic space in which the electronics and the photophysics of these complexes can be rationally tuned by the supporting ligands.[55-56]

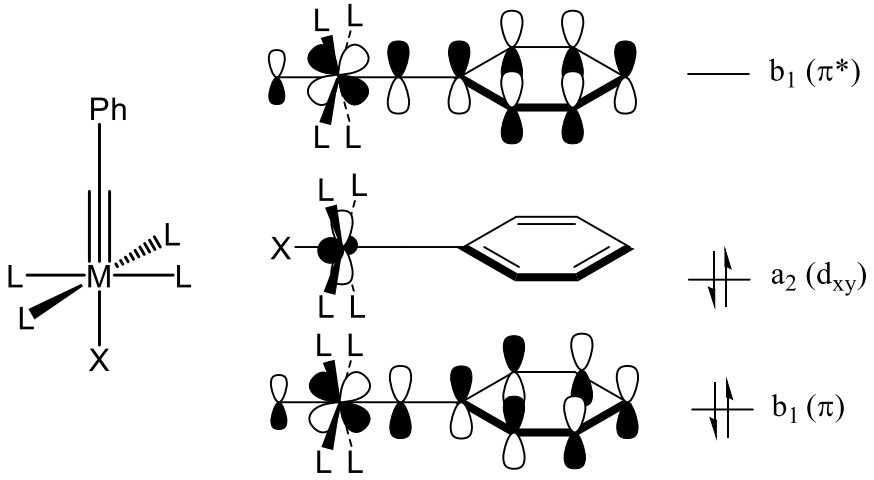

Figure 1.3 General electronic structure of d^2 tungsten benzylidyne studied here.

Translating the well-studied properties of tungsten-alkylidyne chromophores to related isoelectronic complexes with different metals and multiply bonded ligands is poorly developed. Such studies can be useful in identifying key electronic differences relevant to their photoredox catalytic activity. While substitution of the tungsten center with molybdenum might be envisioned to yield chromophores with similar excited state behavior and photophysical properties, the few prior studies of d^2 molybdenum alkylidyne complexes show poor photophysical properties such as photodecomposition and non-emissive excited-states,[57-62] and no room-temperature emissive molybdenum alkylidynes are known with a d-d excited-state. We hypothesized that synthesis of a molybdenum alkylidynes of form $Mo(CAr)L_4Cl$ with chelating L ligands may help to mitigate nonradiative processes and give rise to a long-lived emissive state. Further comparison with isoelectronic tungsten alkylidyne chromophores should allow direct comparison of how the metal center influences the bonding and reactivity at this unique metal-ligand triple bond.

Tantalum imido complexes are an interesting isoelectronic alternative to tungsten alkylidyne complexes. While luminescent d^0 tantalum imido complexes have been reported,[63-65] very few d^2 tantalum imido complexes have been reported with limited electronic characterization.[66-69] Since d^2 tantalum centers are more reducing than d^2 tungsten, $Ta(NAr)L_4X$ complexes may be able to produce even more reducing excited-states using visible light than their tungsten congeners as described by the Rehm-Weller Approximation. Additionally, the tantalum-nitrogen triple bond is expected to be more polarized than the tungsten-carbon triple bond due to the difference in their relative atomic orbital energies.[70] Comparison of $Mo(CAr)L_4X$ and $Ta(NAr)L_4X$ complexes to $W(CAr)L_4X$ complexes allows study of two disparate modifications to the core photoactive metal-center and how they impact the photophysics and electronic structure of this class of complexes.

In addition to their photophysical properties, tungsten alkylidyne complexes are known to activate H_2 to form d^0 alkylidyne hydride complexes.[71] Understanding the thermodynamics and kinetics of this reaction can help to further improve its utility. Related d^0 hydride complexes show interesting tautomerization processes in solution that are dependent on the transition-metal center and the triply bonded heteroatom.[72-75] This tautomerization is proposed to be mediated by protonation of the triply bonded heteroatom, which is rapid at room-temperature. Understanding hydride binding thermodynamics and tautomerization within a series of isoelectronic complexes can elucidate how the transition-metal center and triply-bonded heteroatom dictate hydride binding and further H_2 activation. This is important for usage of these complexes as renewable photoreductants since they would be able to directly convert electrons from dihydrogen into higher energy photoredox equivalents.

In Chapter 3, we report synthesis of a set of isoelectronic molybdenum benzylidyne and tantalum phenylimido complexes. These complexes were then analyzed using a suite of characterization methods to understand the effect of the transition-metal center and triply bonded heteroatom substituent on the electronic and photophysical properties of these molecules. Following syntheses of the d^2 congeners, d^0 hydride complexes were prepared and characterized as well. The electronic consequences of metal and heteroatom substitution are then investigated in the context of hydride bonding thermodynamics.

Computational models of these complexes have been developed that show good agreement with experimental findings and allow for facile interpretation of electronic properties.[55-56] Drawing from these models, ground- and excited-state properties can be predicted from the ground-state geometry and the corresponding HOMO and LUMO energy levels using simple correlation models. These correlations rely on the excited-state remaining $^3[d_{xy} \rightarrow \pi^*]$ for all compounds. They would not identify other emissive excited states generated by particular substitution patterns unless strong deviations from the correlations were found.

Experimental data for some tungsten alkylidyne compounds show unexpected spectroscopic features, such as vibronic structure, and much longer lifetimes than expected.[76] Computational modeling of excited triplet states can improve photophysical predictions for these complexes and provide insight on their excited-state dynamics. This can be achieved using DFT to directly calculate and optimize excited-state geometries and has been used in other systems to describe excited-state dynamics.[77] Use of analogous methods can help to further elucidate the excited-state relaxation of this class of chromophores to better predict the photophysical impact of peripheral substitution.

In Chapter 4, we report a computational study on a series of tungsten alkylidyne complexes and their excited-state structure and character in the relaxed T_1 state. A series of experimentally characterized complexes were studied computationally in the ground state to gain insight on the electronic effects of peripheral substitution. The relaxed T_1 state was then optimized using two different methods and compared to the ground-state geometry to understand electronic perturbations in the excited-state. These methods were finally compared against each other to validate the predicted geometry and gain insight on the computational validity of the predicted excited-state.

1.4 Ligand-Centered Copper Carbene Photoreductants.

In addition to molybdenum, tungsten, and tantalum chromophores, the low cost and high abundance of first-row transition-metal chromophores would also be economical for solar fuel production at scale. Copper is one of the few 1st row transition-metal elements that displays long-lived excited-states arising from ligand-centered charge-transfer states.[78-85] This is largely due to the d^{10} configuration of the Cu(I) ion, which avoids population of low-lying metal-centered excited-states that are commonly detrimental for other 1st row chromophores. Linear carbene-copper-amide complexes are interesting scaffolds for ligand-centered emission from a copper complex (Figure 1.4).[82-86] Here, the copper d_z2 is too low in energy to strongly participate in the lowest energy excited-states rendering absorption and emission to be largely dictated by the supporting ligands. These complexes are generally air-stable, electronically tunable, and display long-lived excited states with quantum yields up to unity arising from ligand-to-ligand charge transfer excited-states. Due to these desirable properties, recent work has focused on the application of these complexes in the emitting layer for OLED devices.[85, 87-88]

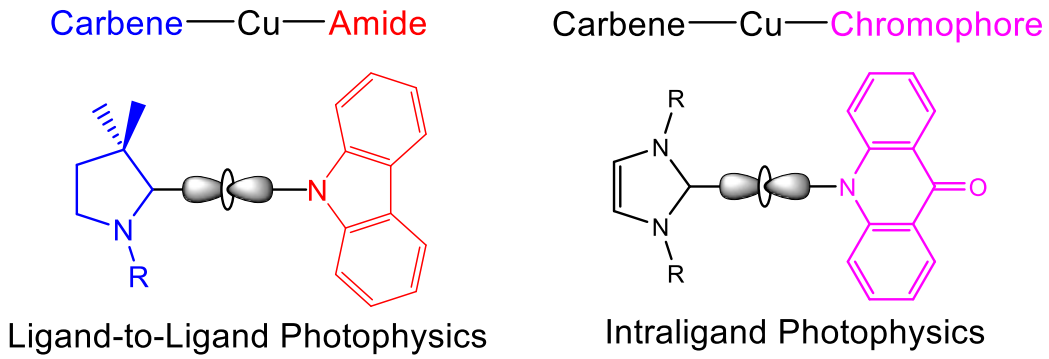

Figure 1.4. Linear copper chromophore design for intraligand-centered photophysics.

Anionic organic chromophores are an emerging design for generating strongly reducing photoreductants.[89-92] From the Rehm-Weller Approximation, these chromophores would also be expected to display strong photoreducing properties due to their low ground state oxidation potentials by nature of their anionic charge. Given the propensity for copper centers to stabilize and display long-lived ligand-centered photophysics, intraligand excited-states hosted by a copper center should also be accessible within the same ligand framework. This can be simply envisioned as a Lewis-acidic cationic copper carbene coordinated to an anionic chromophore ligand. From a photocatalytic perspective this is intriguing as this provides a route for stabilization and further tuning of the photophysical properties of the anionic chromophore which could be achieved by modification of the supporting carbene ligand.

In Chapter 5, we report synthesis of a linear NHC-copper-acridone complex and a free deprotonated acridone ligand anion. The electronic and photophysical properties of these complexes are studied and compared to that of the parent protonated acridone species. These properties are contextualized within the effect that deprotonation and coordination to the copper

center has on the acridone moiety and its relevance for harnessing anionic chromophores for photoredox applications.

1.5 References.

1. Kim, J. H.; Hansora, D.; Sharma, P.; Jang, J.-W.; Lee, J. S. *Chemical Society Reviews* **2019**, *48*, 1908-1971.

2. Lewis, N. S.; Nocera, D. G. *Proceedings of the National Academy of Sciences* **2006**, *103*, 15729-15735.

3. *Electricity Information: Overview*. International Energy Agency, 2021. https://www.iea.org/reports/electricity-information-overview.

4. Masson-Delmotte, V.; Zhai, P.; Pörtner, H.; Roberts, D.; Skea, J.; Shukla, P.; Pirani, A.; Moufouma-Okia, W.; Péan, C.; Pidcock, R. *Sustainable Development, and Efforts to Eradicate Poverty* **2018**.

5. Gueymard, C. A. *Solar Energy* **2004**, *76*, 423-453.

6. Wang, Q.; Pornrungroj, C.; Linley, S.; Reisner, E. *Nature Energy* **2022**, *7*, 13-24.

7. Eisenberg, R.; Gray, H. B.; Crabtree, G. W. *Proceedings of the National Academy of Sciences* **2020**, *117*, 12543-12549.

8. Romano, V.; D'Angelo, G.; Perathoner, S.; Centi, G. *Energy & Environmental Science* **2021**, *14*, 5760-5787.

9. Kärkäs, M. D.; Verho, O.; Johnston, E. V.; Åkermark, B. *Chemical Reviews* **2014**, *114*, 11863-12001.

10. McKone, J. R.; Lewis, N. S.; Gray, H. B. *Chemistry of Materials* **2014**, *26*, 407-414.

11. James, B. D.; Baum, G. N.; Perez, J.; Baum, K. N. *Technoeconomic Analysis of Photoelectrochemical (PEC) Hydrogen Production*; United States, 2009. https://www.osti.gov/biblio/1218403 DOI: 10.2172/1218403.

12. Pinaud, B. A.; Benck, J. D.; Seitz, L. C.; Forman, A. J.; Chen, Z.; Deutsch, T. G.; James, B. D.; Baum, K. N.; Baum, G. N.; Ardo, S.; et al. *Energy & Environmental Science* **2013**, *6*, 1983-2002.

13. Rehm, D.; Weller, A. *Israel Journal of Chemistry* **1970**, *8*, 259-271.

14. Prier, C. K.; Rankic, D. A.; MacMillan, D. W. C. *Chemical Reviews* **2013**, *113*, 5322-5363.

15. Connelly, N. G.; Geiger, W. E. *Chemical Reviews* **1996**, *96*, 877-910.

16. Hendy, C. M.; Smith, G. C.; Xu, Z.; Lian, T.; Jui, N. T. *Journal of the American Chemical Society* **2021**, *143*, 8987-8992.

17. Deng, D.; Novoselov, K. S.; Fu, Q.; Zheng, N.; Tian, Z.; Bao, X. *Nature Nanotechnology* **2016**, *11*, 218-230.

18. Wang, Y.; Mao, J.; Meng, X.; Yu, L.; Deng, D.; Bao, X. *Chemical Reviews* **2019**, *119*, 1806-1854.

19. Chia, X.; Pumera, M. *Nature Catalysis* **2018**, *1*, 909-921.

20. Splendiani, A.; Sun, L.; Zhang, Y.; Li, T.; Kim, J.; Chim, C.-Y.; Galli, G.; Wang, F. *Nano Letters* **2010**, *10*, 1271-1275.

21. Ponomarev, E.; Pásztor, Á.; Waelchli, A.; Scarfato, A.; Ubrig, N.; Renner, C.; Morpurgo, A. F. *ACS Nano* **2018**, *12*, 2669-2676.

22. Salehzadeh, O.; Djavid, M.; Tran, N. H.; Shih, I.; Mi, Z. *Nano Letters* **2015**, *15*, 5302-5306.

23. Eda, G.; Yamaguchi, H.; Voiry, D.; Fujita, T.; Chen, M.; Chhowalla, M. *Nano Letters* **2011**, *11*, 5111-5116.

24. Yin, Z.; Li, H.; Li, H.; Jiang, L.; Shi, Y.; Sun, Y.; Lu, G.; Zhang, Q.; Chen, X.; Zhang, H. *ACS Nano* **2012**, *6*, 74-80.

25. Radisavljevic, B.; Radenovic, A.; Brivio, J.; Giacometti, V.; Kis, A. *Nature Nanotechnology* **2011**, *6*, 147-150.

26. Zeng, Z.; Yin, Z.; Huang, X.; Li, H.; He, Q.; Lu, G.; Boey, F.; Zhang, H. *Angewandte Chemie International Edition* **2011**, *50*, 11093-11097.

27. Wu, F.; Tian, H.; Shen, Y.; Hou, Z.; Ren, J.; Gou, G.; Sun, Y.; Yang, Y.; Ren, T.-L. *Nature* **2022**, *603*, 259-264.

28. Park, J. H.; Sanne, A.; Guo, Y.; Amani, M.; Zhang, K.; Movva, H. C. P.; Robinson, J. A.; Javey, A.; Robertson, J.; Banerjee, S. K.; et al. *Science Advances* **2017**, *3*, e1701661.

29. Mutz, N.; Park, S.; Schultz, T.; Sadofev, S.; Dalgleish, S.; Reissig, L.; Koch, N.; List-Kratochvil, E. J. W.; Blumstengel, S. *The Journal of Physical Chemistry C* **2020**, *124*, 2837-2843.

30. Canton-Vitoria, R.; Gobeze, H. B.; Blas-Ferrando, V. M.; Ortiz, J.; Jang, Y.; Fernández-Lázaro, F.; Sastre-Santos, Á.; Nakanishi, Y.; Shinohara, H.; D'Souza, F.; et al. *Angewandte Chemie International Edition* **2019**, *58*, 5712-5717.

31. Padgaonkar, S.; Amsterdam, S. H.; Bergeron, H.; Su, K.; Marks, T. J.; Hersam, M. C.; Weiss, E. A. *The Journal of Physical Chemistry C* **2019**, *123*, 13337-13343.

32. Kwon, I. S.; Kwak, I. H.; Kim, J. Y.; Abbas, H. G.; Debela, T. T.; Seo, J.; Cho, M. K.; Ahn, J.-P.; Park, J.; Kang, H. S. *Nanoscale* **2019**, *11*, 14266-14275.

33. Davis, T. C.; Russell, S. R.; Claridge, S. A. *Chemical Communications* **2018**, *54*, 11709-11712.

34. Cincotti, S.; Rabe, J. P. *Applied Physics Letters* **1993**, *62*, 3531-3533.

35. Huang, Y.; Zhuge, F.; Hou, J.; Lv, L.; Luo, P.; Zhou, N.; Gan, L.; Zhai, T. *ACS Nano* **2018**, *12*, 4062-4073.

36. Liu, H.; Silva, W. C.; Santana Gonçalves de Souza, L.; Veiga, A. G.; Seixas, L.; Fujisawa, K.; Kahn, E.; Zhang, T.; Zhang, F.; Yu, Z.; et al. *Nanoscale* **2022**, *14*, 10801-10815.

37. Daukiya, L.; Teyssandier, J.; Eyley, S.; El Kazzi, S.; Rodríguez González, M. C.; Pradhan, B.; Thielemans, W.; Hofkens, J.; De Feyter, S. *Nanoscale* **2021**, *13*, 2972-2981.

38. Canton-Vitoria, R.; Sayed-Ahmad-Baraza, Y.; Pelaez-Fernandez, M.; Arenal, R.; Bittencourt, C.; Ewels, C. P.; Tagmatarchis, N. *npj 2D Materials and Applications* **2017**, *1*, 13.

39. Chen, X.; Berner, N. C.; Backes, C.; Duesberg, G. S.; McDonald, A. R. *Angewandte Chemie International Edition* **2016**, *55*, 5803-5808.

40. Vera-Hidalgo, M.; Giovanelli, E.; Navío, C.; Pérez, E. M. *Journal of the American Chemical Society* **2019**, *141*, 3767-3771.

41. García-Dalí, S.; Paredes, J. I.; Villar-Rodil, S.; Martínez-Jódar, A.; Martínez-Alonso, A.; Tascón, J. M. D. *ACS Applied Materials & Interfaces* **2021**, *13*, 33157-33171.

42. Li, D. O.; Chu, X. S.; Wang, Q. H. *Langmuir* **2019**, *35*, 5693-5701.

43. Karunakaran, S.; Pandit, S.; Basu, B.; De, M. *Journal of the American Chemical Society* **2018**, *140*, 12634-12644.

44. Liu, H.; Grasseschi, D.; Dodda, A.; Fujisawa, K.; Olson, D.; Kahn, E.; Zhang, F.; Zhang, T.; Lei, Y.; Branco, R. B. N.; et al. *Science Advances* **2020**, *6*, eabc9308.

45. Pearson, R. G. *Journal of the American Chemical Society* **1963**, *85*, 3533-3539.

46. Fleischer, M. *Journal of Chemical Education* **1954**, *31*, 446.

47. McCusker, J. K. *Science* **2019**, *363*, 484-488.

48. Bocarsly, A. B.; Cameron, R. E.; Rubin, H. D.; McDermott, G. A.; Wolff, C. R.; Mayr, A. *Inorganic Chemistry* **1985**, *24*, 3976-3978.

49. Da Re, R. E.; Hopkins, M. D. *Coordination Chemistry Reviews* **2005**, *249*, 1396-1409.

50. O'Hanlon, D. C.; Cohen, B. W.; Moravec, D. B.; Dallinger, R. F.; Hopkins, M. D. *Journal of the American Chemical Society* **2014**, *136*, 3127-3136.

51. Lovaasen, B. M.; Lockard, J. V.; Cohen, B. W.; Yang, S.; Zhang, X.; Simpson, C. K.; Chen, L. X.; Hopkins, M. D. *Inorganic Chemistry* **2012**, *51*, 5660-5670.

52. Manna, J.; Gilbert, T. M.; Dallinger, R. F.; Geib, S. J.; Hopkins, M. D. *Journal of the American Chemical Society* **1992**, *114*, 5870-5872.

53. Ballhausen, C. J.; Gray, H. B. *Inorganic Chemistry* **1962**, *1*, 111-122.

54. Da Re, R. E.; Hopkins, M. D. *Inorganic Chemistry* **2002**, *41*, 6973-6985.

55. Haines, D. E.; O'Hanlon, D. C.; Manna, J.; Jones, M. K.; Shaner, S. E.; Sun, J.; Hopkins, M. D. *Inorganic Chemistry* **2013**, *52*, 9650-9658.

56. Rudshteyn, B.; Vibbert, H. B.; May, R.; Wasserman, E.; Warnke, I.; Hopkins, M. D.; Batista, V. S. *ACS Catalysis* **2017**, *7*, 6134-6143.

57. Lee, F.-W.; Chi-Wang Chan, M.; Cheung, K.-K.; Che, C.-M. *Journal of Organometallic Chemistry* **1998**, *563*, 191-200.

58. Carter, J. D.; Kingsbury, K. B.; Wilde, A.; Schoch, T. K.; Leep, C. J.; Pham, E. K.; McElwee-White, L. *Journal of the American Chemical Society* **1991**, *113*, 2947-2954.

59. Cavalheiro, C. C. S.; Torraca, K. E.; Schanze, K. S.; McElwee-White, L. *Inorganic Chemistry* **1999**, *38*, 3254-3257.

60. Schoch, T. K.; Main, A. D.; Burton, R. D.; Lucia, L. A.; Robinson, E. A.; Schanze, K. S.; McElwee-White, L. *Inorganic Chemistry* **1996**, *35*, 7769-7775.

61. Sheridan, J. B.; Pourreau, D. B.; Geoffroy, G. L.; Rheingold, A. L. *Organometallics* **1988**, *7*, 289-294.

62. Kingsbury, K. B.; Carter, J. D.; Wilde, A.; Park, H.; McElwee-White, L.; Takusagawa, F. *Journal of the American Chemical Society* **1993**, *115*, 10056-10065.

63. Williams, D. S.; Korolev, A. V. *Inorganic Chemistry* **1998**, *37*, 3809-3819.

64. Heinselman, K. S.; Hopkins, M. D. *Journal of the American Chemical Society* **1995**, *117*, 12340-12341.

65. Wigley, D. E. Organoimido Complexes of the Transition Metals. In *Progress in Inorganic Chemistry*, Progress in Inorganic Chemistry, 1994; pp 239-482.

66. Rocklage, S. M.; Schrock, R. R. *Journal of the American Chemical Society* **1982**, *104*, 3077-3081.

67. Rocklage, S. M.; Schrock, R. R. *Journal of the American Chemical Society* **1980**, *102*, 7808-7809.

68. Gianetti, T. L.; Nocton, G.; Minasian, S. G.; Kaltsoyannis, N.; Kilcoyne, A. L. D.; Kozimor, S. A.; Shuh, D. K.; Tyliszczak, T.; Bergman, R. G.; Arnold, J. *Chemical Science* **2015**, *6*, 993-1003.

69. Korolev, A. V.; Rheingold, A. L.; Williams, D. S. *Inorganic Chemistry* **1997**, *36*, 2647-2655.

70. Kotochigova, S.; Levine, Z. H.; Shirley, E. L.; Stiles, M. D.; Clark, C. W. *Physical Review A* **1997**, *55*, 191-199.

71. Morales-Verdejo, C. A.; Newsom, M. I.; Cohen, B. W.; Vibbert, H. B.; Hopkins, M. D. *Chemical Communications* **2013**, *49*, 10566-10568.

72. Churchill, M. R.; Wasserman, H. J.; Turner, H. W.; Schrock, R. R. *Journal of the American Chemical Society* **1982**, *104*, 1710-1716.

73. Wengrovius, J. H.; Schrock, R. R.; Churchill, M. R.; Wasserman, H. J. *Journal of the American Chemical Society* **1982**, *104*, 1739-1740.

74. Holmes, S. J.; Clark, D. N.; Turner, H. W.; Schrock, R. R. *Journal of the American Chemical Society* **1982**, *104*, 6322-6329.

75. Holmes, S. J.; Schrock, R. R. *Journal of the American Chemical Society* **1981**, *103*, 4599-4600.

76. Vibbert, H. B. Group 6 Metal-Oxo and -Alkylidyne Complexes with High Reactivity Derived from π-Antibonding Orbitals. Ph.D., The University of Chicago, United States -- Illinois, 2018.

77. Wang, J.; Durbeej, B. *Journal of Computational Chemistry* **2020**, *41*, 1718-1729.

78. Harkins, S. B.; Peters, J. C. *Journal of the American Chemical Society* **2005**, *127*, 2030-2031.

79. Hashimoto, M.; Igawa, S.; Yashima, M.; Kawata, I.; Hoshino, M.; Osawa, M. *Journal of the American Chemical Society* **2011**, *133*, 10348-10351.

80. Blaskie, M. W.; McMillin, D. R. *Inorganic Chemistry* **1980**, *19*, 3519-3522.

81. McCusker, C. E.; Castellano, F. N. *Inorganic Chemistry* **2013**, *52*, 8114-8120.

82. Tzouras, N. V.; Martynova, E. A.; Ma, X.; Scattolin, T.; Hupp, B.; Busen, H.; Saab, M.; Zhang, Z.; Falivene, L.; Pisanò, G.; et al. *Chemistry – A European Journal* **2021**, *27*, 11904-11911.

83. Romanov, A. S.; Jones, S. T. E.; Gu, Q.; Conaghan, P. J.; Drummond, B. H.; Feng, J.; Chotard, F.; Buizza, L.; Foley, M.; Linnolahti, M.; et al. *Chemical Science* **2020**, *11*, 435-446.

84. Li, J.; Wang, L.; Zhao, Z.; Li, X.; Yu, X.; Huo, P.; Jin, Q.; Liu, Z.; Bian, Z.; Huang, C. *Angewandte Chemie International Edition* **2020**, *59*, 8210-8217.

85. Hamze, R.; Peltier, J. L.; Sylvinson, D.; Jung, M.; Cardenas, J.; Haiges, R.; Soleilhavoup, M.; Jazzar, R.; Djurovich, P. I.; Bertrand, G.; et al. *Science* **2019**, *363*, 601-606.

86. Ahn, J. M.; Ratani, T. S.; Hannoun, K. I.; Fu, G. C.; Peters, J. C. *Journal of the American Chemical Society* **2017**, *139*, 12716-12723.

87. Shi, S.; Jung, M. C.; Coburn, C.; Tadle, A.; Sylvinson M. R, D.; Djurovich, P. I.; Forrest, S. R.; Thompson, M. E. *Journal of the American Chemical Society* **2019**, *141*, 3576-3588.

88. Muniz, C. N.; Schaab, J.; Razgoniaev, A.; Djurovich, P. I.; Thompson, M. E. *Journal of the American Chemical Society* **2022**, *144*, 17916-17928.

89. Schmalzbauer, M.; Marcon, M.; König, B. *Angewandte Chemie International Edition* **2021**, *60*, 6270-6292.

90. Ghosh, I.; Ghosh, T.; Bardagi, J. I.; König, B. *Science* **2014**, *346*, 725-728.

91. Schmalzbauer, M.; Ghosh, I.; König, B. *Faraday Discussions* **2019**, *215*, 364-378.

92. Rieth, A. J.; Gonzalez, M. I.; Kudisch, B.; Nava, M.; Nocera, D. G. *Journal of the American Chemical Society* **2021**, *143*, 14352-14359.

CHAPTER 2

Modification of Monolayer MoS_2 with Molecular Transition-Metal Complexes

2.1. Introduction.

Since the first successful isolation of graphene and demonstration of its ambipolar field effect,[1] two-dimensional materials have received widespread interest as components for functional materials.[2-8] The ability to grow or cleanly scale down bulk materials to monolayer substances has shown great promise for developing functional nanomaterials with remarkable anisotropic physical and electronic properties. These properties arise from strong intraplanar covalent bonds that extend between atoms while interplane bonding is through weak van der Waals interactions.[9-10] Monolayer (1L) transition-metal dichalcogenides (TMDs) are a class of 2-D materials that have recently attracted tremendous attention as semiconducting materials for lightweight electronics and optoelectronics. TMDs are compositionally diverse with multiple stable structural phases giving rise to a variety of electronic structures, topologically non-trivial electronic states, and photonic properties.[2-8] Many of these unique properties arise from quantum confinement of the material to two dimensions and, as a result, are also layer dependent with TMD van der Waals heterostructures further diversifying the optical and electronic properties of these materials.[7, 11-13] Of the TMDs, MoS_2 has received the most attention due to its stability and processability. MoS_2 can exist in various structural phases of which the most common are the semiconducting trigonal prismatic 2H-MoS_2 and the metallic octahedral 1T-MoS_2. Theoretical calculations for 2H-MoS_2 predict a room-temperature electron mobility up to 1000 $cm^2 V^{-1} s^{-1}$,[14-15] comparable to polycrystalline silicon,[16] suggesting effective charge transport for MoS_2 based materials. MoS_2 has been studied for photonic applications in photodetectors,[17-20]

valleytronics,[21-23] and low-threshold lasing[24-26] in addition to electronic applications such as lithium-ion battery anodes[27] and as an atomically thin transistors.[28-31]

Due to their size-confined nature, light weight, high aspect ratio capable of hosting many active sites, and high processability, TMDs are inherently scalable for applications as high-specific-activity catalysts.[32-34] Two methods for surface doping can be categorized as noncovalent and covalent (Scheme 2.1). For MoS_2, noncovalent functionalization methods have been developed where the natural 2-D aspect ratio of the material and buried valence band facilitates van der Waals dispersion attraction with π-conjugated molecules, resulting in numerous reports of functionalization using aromatic macrocycles and long chain alkanes akin to studies on highly-oriented pyrolytic graphite.[35-41] While noncovalent approaches are reliable and well-characterized, they suffer from the low stability of the adsorbed complex and limited charge transfer kinetics, which limits its use for catalysis.

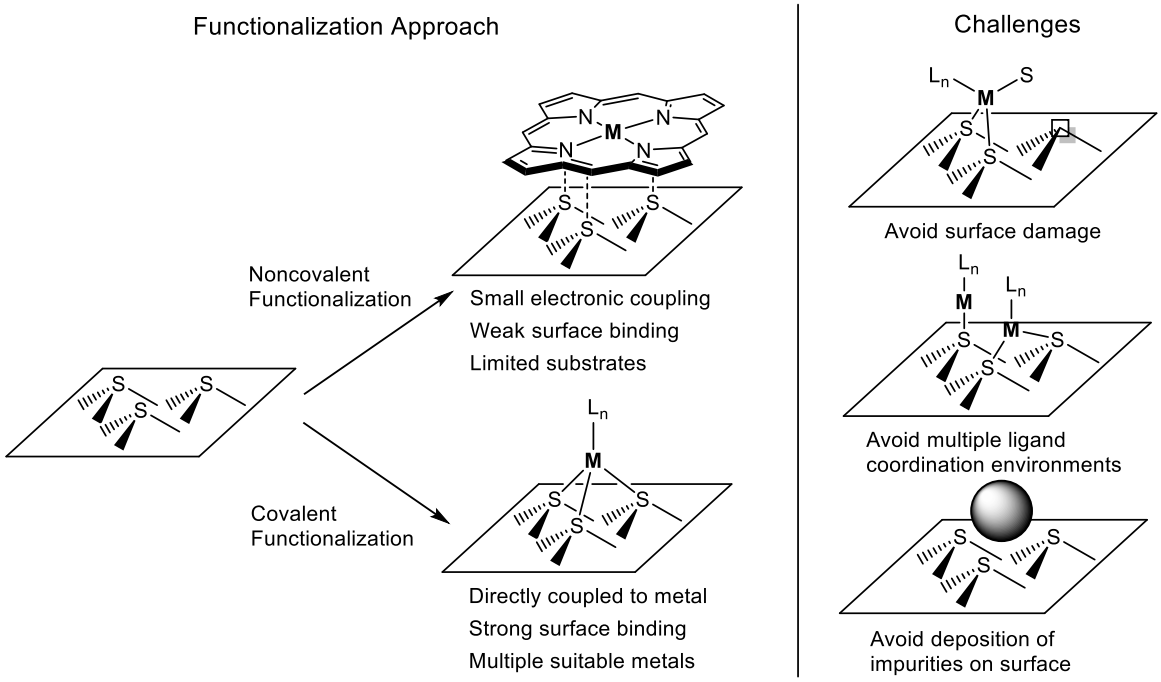

Scheme 2.1. Functionalization approaches for MoS_2 and associated challenges with covalent functionalization.

Covalent functionalization is an attractive complementary approach due to formation of a more robust chemical bond with the surface. Multiple methods have been developed for covalent functionalization of MoS_2, including thiol defect passivation, enhancing nucleophilicity via phase change to more nucleophilic MoS_2 phases, and electrochemical radical addition.[42-52] These methods have predominantly been used to attach organic moieties to the MoS_2 surface that can be used as a tether for further axial functionalization. We hypothesized that Lewis-acidic transition-metals may serve as interesting dopants using the surface chalcogen atoms as electron donors akin to a multidentate ligand. In principle, this provides a convenient and simple route for designing and producing lightweight materials where the transition-metal can be introduced through simple solution or vapor-phase deposition methods. Previous studies have established that exfoliated MoS_2 shows evidence of surface functionalization by various transition metal salts suggesting the viability of this method.[53-55] Tailoring of the transition-metal center and its TMD support could allow for incorporation of a wide variety of functionality to the surface including tunable optoelectronics, substrate supported catalysts, and low-dimensional magnetic materials.

Preparation of exfoliated 1L-MoS_2 for subsequent functionalization commonly uses harsh conditions including sonication-assisted liquid exfoliation, lithium intercalation, and solvothermal processing.[19, 28, 56-60] This can lead to defect formation, phase change, and eventual loss of some intrinsic properties of the material due to formation of trap states and local energy minima.[61-62] Furthermore, the presence of these defect sites also present multiple possible coordination environments for surface dopants. Developing a method to generate site-controlled, synthetically tunable active sites on highly crystalline surfaces would be of great use for further development of these materials. Use of an immersion-dose procedure on highly crystalline

grown monolayer TMDs could potentially avoid previous synthetic pitfalls arising from exfoliation and other mechanical processing and enable improved control over the surface-doped catalytic site. To attain better control of the surface chemistry and improve reproducibility, we sought to establish surface functionalization and characterization methods on highly crystalline 1L-MoS_2 grown on a silicon wafer support. This avoids complicating chemistry from defect sites, aggregation, and surface heterogeneity arising from mechanical or chemical exfoliation.

To narrow down the scope of potential transition metal centers capable of coordinating to the MoS_2 surface, certain design criteria were established to identify suitable precursors for surface functionalization. The inherent delicacy of the monolayer precludes methods that would generate mechanical stress at the surface such as sonication or solvent reflux, since the nucleation of gases at the surface may be sufficient to rupture the monolayer. In general, the transition-metal precursor is always added in great excess with respect to the available binding sites on the MoS_2 basal plane surface. This is inherent to the small amount of MoS_2 substrate used for each sample in this study. Using the crystal structure of MoS_2,[63] one can estimate the number of molybdenum atoms in a 1 cm^2 area to be approximately 10^{15} atoms, or roughly 2 nanomoles of molybdenum not including any defects or incomplete surface coverage. Use of excess of a transition-metal precursor sets a limit to the reactivity of the precursor since MoS_2 is the limiting reagent. This requires exclusive reaction of the precursor with the surface. Any side products that form must be soluble to prevent deposition of particles and other surface heterogeneities on the MoS_2 surface. The use of excess precursor introduces another potential complication in the form of aggregation and surface crystallization. These limitations led us to focus specifically on low-valent, low-coordinate, late transition metal complexes due to their associative substitution chemistry and generally high air stability.

Characterization of functionalized monolayer surfaces presents unique challenges. As most spectroscopic techniques probe a smaller subsection of the 1 cm^2 wafer, all spectroscopic and physical characterization methods must be sensitive to picomole amounts of material. As such, a general characterization route was developed to allow for facile screening of reaction conditions and precursors that gradually increases in preparative complexity. First, optical images and Raman spectra were collected using a confocal Raman microscope. This ensures that the phase and structure of the MoS_2 is preserved and may provide evidence of a new species on the surface by the presence of new vibrational bands. Optical images can confirm that no larger deposits of particles or crystallites are present on the surface. Subsequent X-ray photoelectron spectra (XPS) help to chemically identify the nature of the surface species and changes in MoS_2 in response to the surface dopant. High magnification AFM images are collected next. These aim to provide much greater detail on the topology of the functionalized surface and helps confirm the preservation of the MoS_2 monolayer, the molecularity of the surface modification, and the change in apparent height of the monolayer. Finally, high magnification scanning transmission electron microscope (HAADF-STEM) images are collected. These images provide atomic resolution of the surface dopant and can be used to help identify the binding mode of the dopant to the surface. Following this route and the design principles established above, we identified three suitable molecules for functionalization of the MoS_2 surface (Figure 2.1).

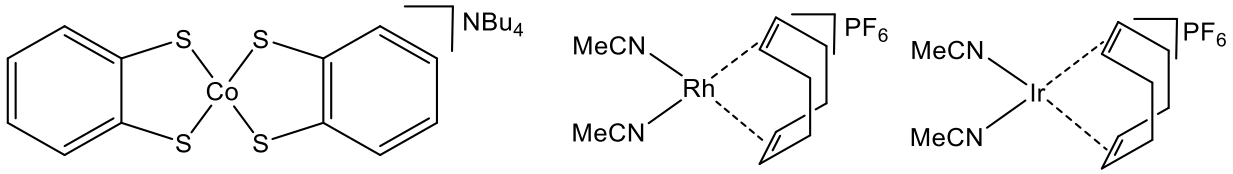

Co **Rh** **Ir**

Figure 2.1. Three complexes studied for surface functionalization of 1L-MoS_2.

The cobalt compound $[NBu^n_4][Co(bdt)_2]$ (**Co**; bdt = 1,2-bis(benzenedithiolate)) is an air-stable, square-planar complex that has been established as a catalyst for the hydrogen evolution reaction under photocatalytic and electrocatalytic conditions with high turnover.[64-65] Coordination polymers and heterogenized electrodes derived from these complexes have shown promise as architectures for incorporation into devices as a proton reduction catalyst.[66-68] Although certain cobalt dithiolene complexes can coordinate axial ligands, suggested the possibility of coordination of **Co** to the MoS_2 surface,[69-70] these interactions are expected to be weak at the van der Waals separation between molecular and TMD planes producing noncovalent functionalization. The anionic charge of $Co(bdt)_2^-$ might disfavor aggregation and favor formation of the desired monolayer functionalized surface. The presence of sulfur in the complex further allows fitting and integration of the S 2p XP spectra to get accurate estimates for the surface coverage. This presents a convenient and synthetically simple system in which to study the surface functionalize of MoS_2 without requiring formation of a covalent bond. The resulting **Co**-functionalized 1L-MoS_2 could have advantages defined by the following considerations. Edge-sites for MoS_2 are also well-known sites for the hydrogen evolution reaction with very low overpotential and fast rates.[71-73] Unfortunately, the inertness of the basal plane restricts the use of MoS_2 as an electrocatalyst since edge-sites are only a small fraction of the overall weight of the material. This precludes use of larger 2H-MoS_2 grains which display stable photoemission for high specific activity catalysis. Functionalization of the MoS_2 surface with **Co** could provide a compact coupled photosensitizer/catalyst material that can leverage the high aspect ratio of MoS_2 and its direct band-gap transition to photocatalytically drive the hydrogen evolution reaction at surface $[Co(bdt)_2]^-$ sites.

An approach to covalent functionalization using ligand substitution of low-coordinate, low-valent late transition metals was also tested. Late transition metals are generally more thiophilic due to the hard-soft acid base principle[74] while a low coordination number allows for associative ligand substitution that may facilitate surface functionalization under ambient conditions. Use of noble metals also helps with the stability of both the precursor and the functionalized surface. Simple 1,5-cyclooctadiene complexes $[Rh(COD)(MeCN)_2][PF_6]$ (**Rh**) and $[Ir(COD)(MeCN)_2][PF_6]$ (**Ir**)[75] were hypothesized to be suitable for mild functionalization of the MoS_2 surface. Both acetonitrile ligands are substitutionally labile and should favor substitution if the MoS_2 surface is an adequate ligand, while the cyclooctadiene ligand provides a convenient bidentate capping ligand for the surface-coordinated complex that should inhibit aggregation and may provide a suitable Raman spectroscopy handle. These precatalysts have been used in a myriad of reactions including alkenylation, hydroboration, and alkyne polymerization.[76-82] Single-site catalysts using isolated rhodium and iridium atoms have also been demonstrated for small molecule oxidation, hydroformylation, and oxygen reduction.[83-87] Facial coordination of the cyclic thioether ligand $[9]aneS_3$ to rhodium and iridium to form cationic $[M([9]aneS_3)(COD)]^+$ is known,[88] suggesting analogous coordination chemistry is possible on the MoS_2 surface. Mild synthetic methods capable of introducing these catalytic sites on the MoS_2 could allow for greater synthetic control of the active site and its ligation allowing for increased selectivity for the desired reaction.

2.2. Results and Discussion

2.2.1. Noncovalent 1L-MoS_2 functionalization with Co

The compound **Co** can be deposited onto the surface of 1L-MoS_2, forming a functionalized material denoted Co-MoS_2, by soaking a SiO_2-supported 1L-MoS_2 wafer in a solution of **Co** in acetonitrile, and then rinsing and drying the sample (Scheme 2.2; see Section 2.4 for full details). To get detailed information of the picomole amounts of material being introduced to the surface, we formulated a gradually focusing approach relying on highly surface-specific spectroscopic and physical characterization methods to characterize the functionalized surface. First, confocal Raman spectroscopy was used to investigate whether a compound was present and if its adsorption affected the vibrational spectrum of **Co** and MoS_2. Next, X-ray photoelectron spectroscopy (XPS) was used to deduce the presence of new elements on the surface, their relative elemental ratios, and any perturbation to orbital energy levels. Finally, high quality atomic-force microscopy (AFM) and scanning transmission electron microscopy (STEM) were used to investigate the molecularity of the adsorbed species.

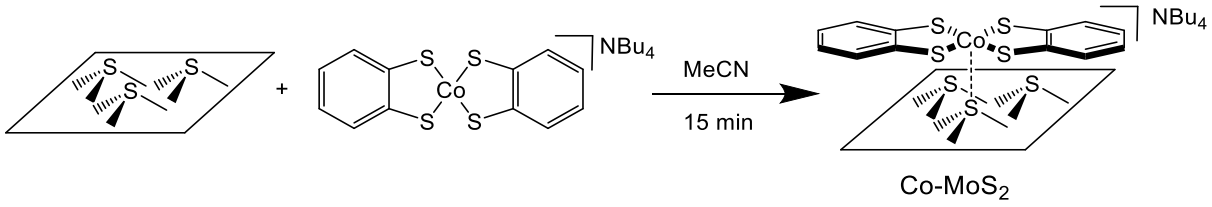

Scheme 2.2. Synthesis of Co-MoS_2.

Comparison of the confocal Raman spectra of 1L-MoS_2, Co-MoS_2, and **Co** shows that $Co(bdt)_2^-$ is present on the surface in a noncrystalline form. The confocal Raman spectrum of untreated 1L-MoS_2 on SiO_2 (Figure 2.2) shows two intense bands at 380 cm^{-1} and 406 cm^{-1} assigned to the E_g and A_{1g} modes, respectively, of 2H-MoS_2, lower intensity features assigned to

phonon modes,[89] and an intense band at 520 cm^{-1} and broad phonon band at 1000 cm^{-1} that arise from the SiO_2 substrate. Upon functionalization with **Co**, the confocal Raman spectra show multiple new bands attributed to $Co(bdt)_2^-$, in addition to those present from MoS_2.[90] Four low frequency bands are found at 196 cm^{-1}, 472 cm^{-1}, 495 cm^{-1}, and 503 cm^{-1} with multiple new high energy bands observed at 1123 cm^{-1}, 1432 cm^{-1} and 1556 cm^{-1} (Figure 2.3). The intensities of the $Co(bdt)_2^-$ Raman bands are presumably resonantly enhanced due to the presence of an intense LMCT band of 14,000 $M^{-1}cm^{-1}$ at 595 nm,[90] which is near the Raman excitation wavelength (532 nm). Notably, the $Co(bdt)_2^-$ bands all are shifted to higher frequency compared with those observed for a microcrystalline sample of **Co** (Figure 2.4). These bands have been previously assigned as carbon ring C–C and C–S stretching modes, while the band at 196 cm^{-1} is due to a Co–S bending mode. The fact that the frequencies differ between adsorbed $Co(bdt)_2^-$ and crystalline **Co** indicates that the compound is not present on the surface as crystallites. The A_{1g} and E_g frequencies of 1L-MoS_2 are not shifted by the presence of **Co** but a slight damping of the A_{1g} mode is observed (Figure 2.5). This damping has been proposed to be indicative of n-type doping of MoS_2.[91] As-synthesized 1L-MoS_2 has been found to be n-doped from either atmosphere or surface charge accumulation.[92-93] It is unclear whether the damping is attributable to the presence of **Co** or exposure to solvent during **Co** deposition.

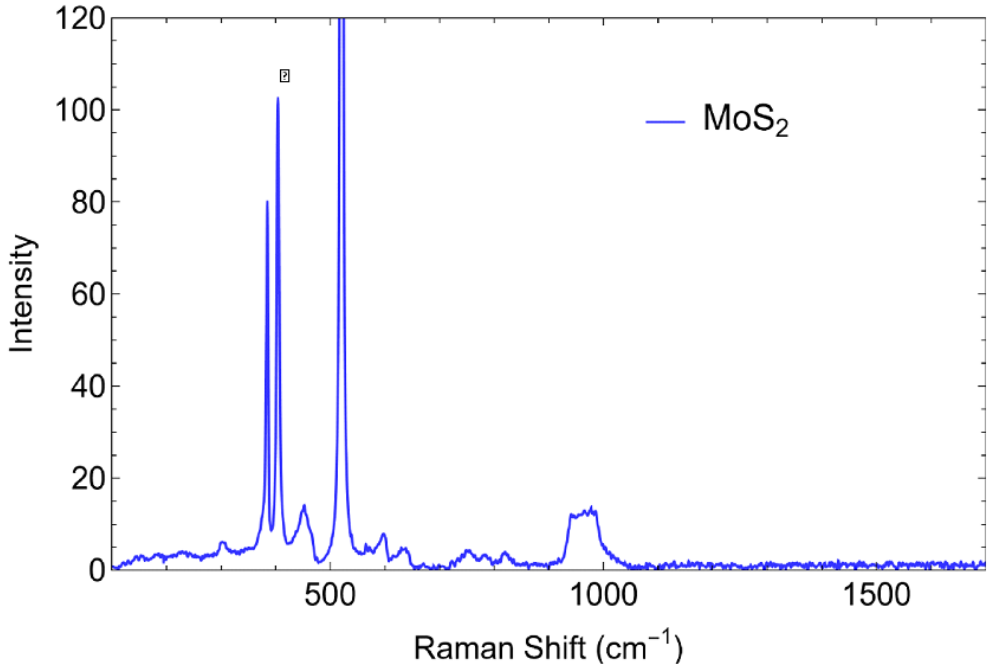

Figure 2.2. Confocal Raman spectrum (λ_{ex} = 532 nm) of untreated 1L-MoS_2 on a SiO_2 support.

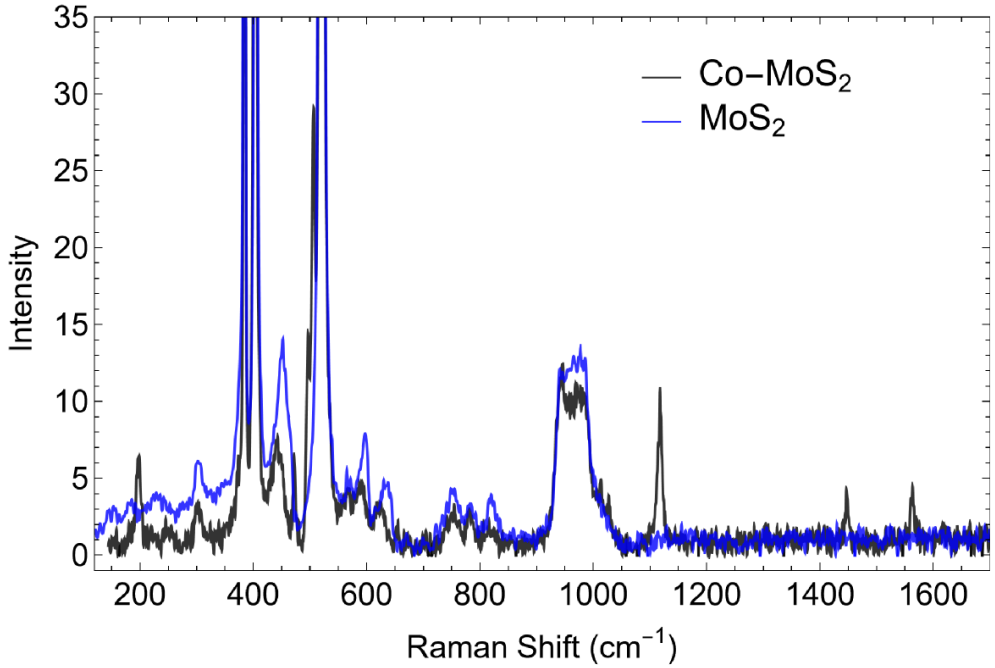

Figure 2.3. Confocal Raman spectra (λ_{ex} = 532 nm) of 1L-MoS_2 (blue) and Co-MoS_2 (black).

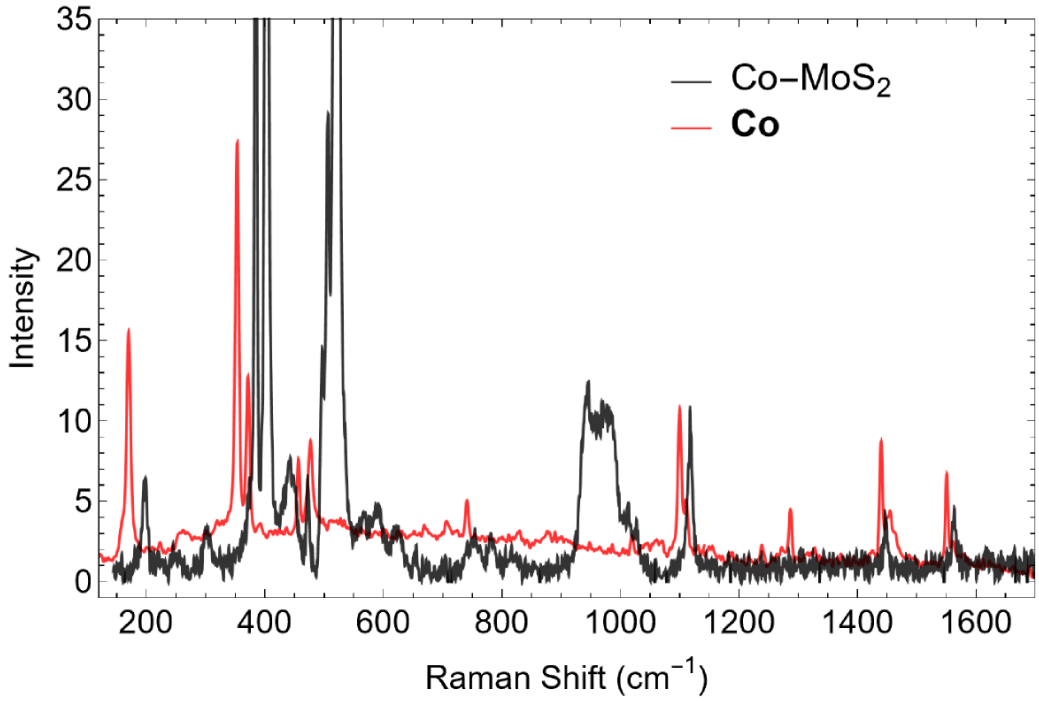

Figure 2.4. Confocal Raman spectra (λ_{ex} = 532 nm) of Co-MoS_2 (black) and microcrystalline **Co** (red)**.**

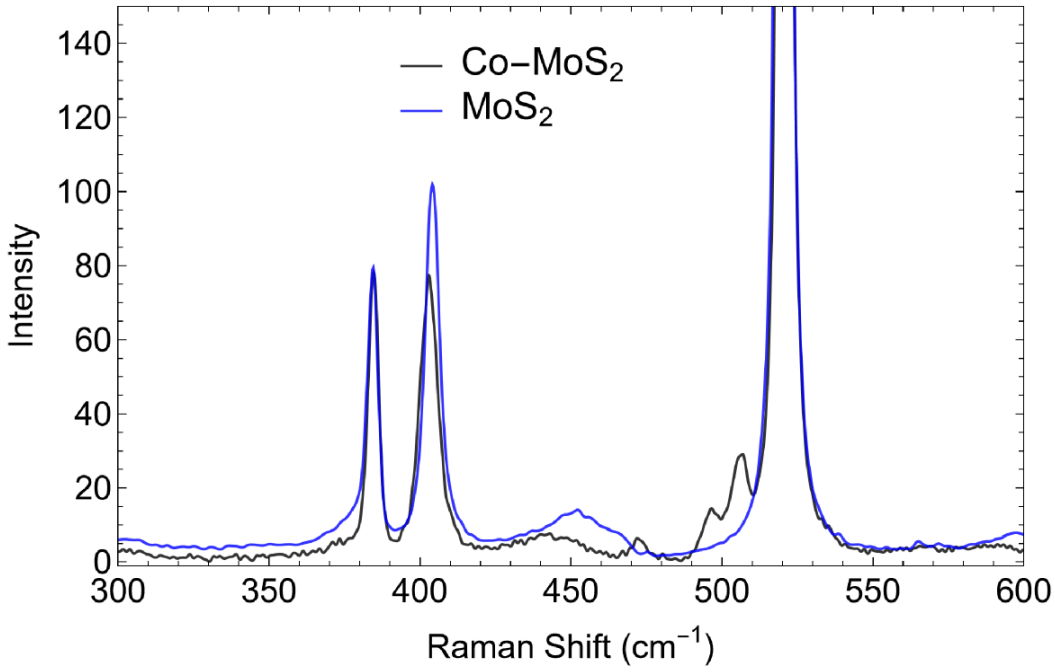

Figure 2.5. Confocal Raman spectra (λ_{ex} = 532 nm) of Co-MoS_2 (black) and untreated 1L-MoS_2 (blue) in the region of the E_g (380 cm^{-1}) and A_{1g} (406 cm^{-1}) bands, showing A_{1g} intensity damping for Co-MoS_2.

X-ray photoelectron spectra of Co-MoS_2 confirm the presence of $Co(bdt)_2^-$ on the surface and establish the surface coverage. Survey spectra of untreated 1L-MoS_2 on SiO_2 show peaks arising from C, O, Si, Mo, and S (Figure 2.6).[94] These arise from SiO_2, MoS_2, and adventitious carbon, the latter of which is known to form on surfaces upon exposure to atmosphere.[95-97] The spectrum of Co-MoS_2 (Figure 2.7) shows new peaks arising from Co and, in some samples but not others, Na; the latter is interpreted as originating from the NaCl used to dry the furnace used for MoS_2 growth, although corresponding Cl features are not observed.[98] Signals due to N from the $[NBu_4]^+$ ion of **Co** were not observed. A N 1s peak (expected at 399 eV) would be obscured by overlap with the Mo 3p peaks (393 eV), preventing its observation, but no N KLL Auger peak is observed at 1011.6 eV, which is uncongested by other signals. This suggests that the $[NBu_4]^+$ counterion from **Co** is present at substoichiometric levels. This observation, together with the absence of Cl signals deriving from the NaCl source, suggests that the sodium is providing charge compensation for $[Co(bdt)_2]^-$ in this spectrum. This varies from sample to sample. Integration of the Co 2p and Mo 3p regions, after correcting for residual sensitivity factors, gives an approximate 1:3 Co:Mo ratio (6.96%:21.59% = 32.2%, Table 2.1). There is error in this ratio due to the limited collection interval of survey spectra and large separation between the Co 2p region and Mo 3p region, so the high-resolution S 2p spectra is preferred for surface coverage analysis (see below).

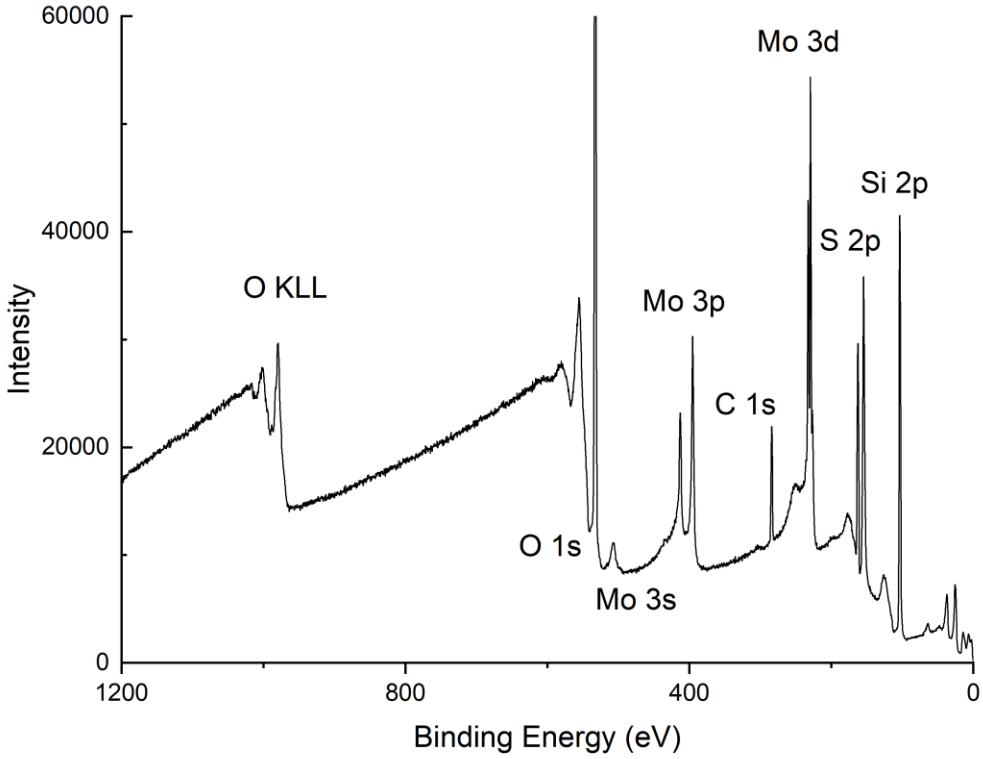

Figure 2.6. Survey XP spectrum of untreated 1L-MoS_2 on SiO_2.

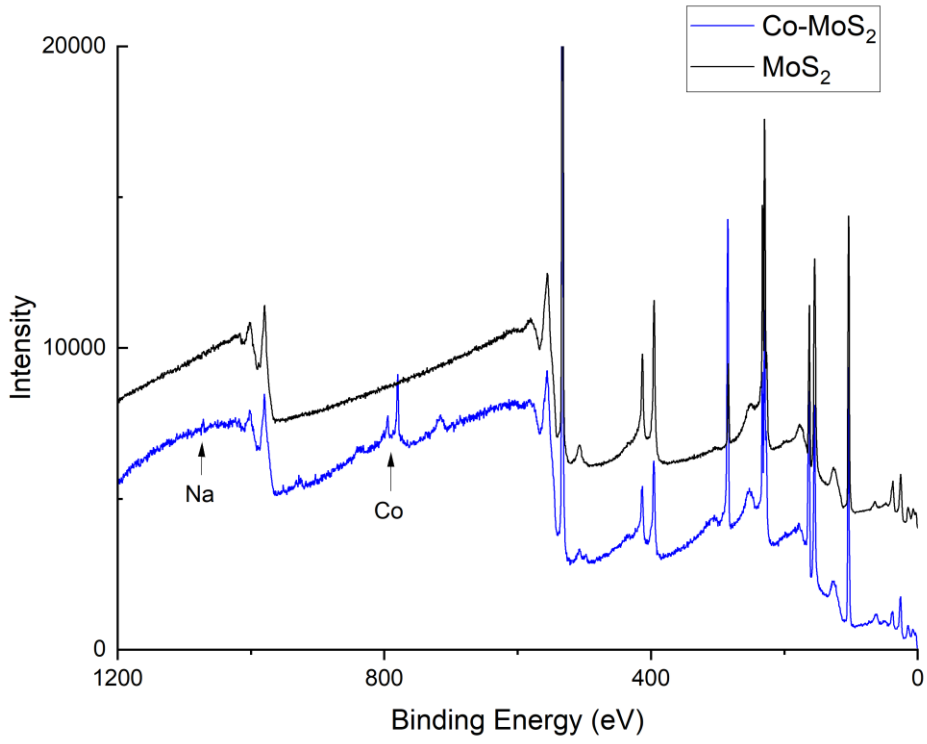

Figure 2.7. Survey XP spectra of Co-MoS_2 (blue) and untreated 1L-MoS_2 (black).

Table 2.1. Survey XPS fitting data for Co-MoS_2.

Co-MoS_2			
Region	Position (eV)[a]	Integrated Area	Atomic %
Co 2p	779.91	4568	6.96
Mo 3p	395.41	6407	21.59
S 2p	162.91	4105	71.45

[a] Denotes center of integrated region in survey spectrum.

High resolution XPS data were collected of untreated 1L-MoS_2 and Co-MoS_2 to get greater detail for the latter about the coverage and chemical effects of adsorption. The photoelectron spectra for untreated 1L-MoS_2 on SiO_2 exhibit a doublet assigned to S 2p (Figure 2.8), a single band assigned to S 2s (Figure 2.9), two bands arising from Mo 3d (Figure 2.9), and a band assigned to Mo 4s (Figure 2.10). The Mo 3d region shows an additional high-binding-energy doublet that matches MoO_x oxide species[94] originating from trace aerobic oxidation of MoS_2. Spectra of Co-MoS_2 samples show these bands and new features arising from the $[Co(bdt)_2]^-$ ion. The spectra in the cobalt $2p_{3/2}$ and $2p_{1/2}$ region show a doublet of asymmetric peaks (Figure 2.11). The $2p_{3/2}$ peak energy of 779.22 eV is close to that of Co^{II}(salen) at 779.9 eV and less than that of $Co^{III}(NH_3)_3Cl_3$ at 781.2 eV.[94] The oxidation state of $[Co(bdt)_2]^-$ is Co(III) if one counts the bdt ligand as a dianion, but there is some ambiguity in the literature about the cobalt oxidation state and the observed 2p energy is suggestive of Co(II).[64, 99] No other Co 2p peaks are observed, indicating that $[Co(bdt)_2]^-$ is the only cobalt-containing species on the MoS_2 surface. The $S = 1$ spin state of **Co** gives rise to satellite features on the higher-binding energy tail, giving the peak an asymmetric shape.[100] High-resolution spectra of the S 2p region show a pair of doublets (Figure 2.12). The larger intensity doublet matches that of untreated 1L-MoS_2 (Figure 2.8), while the weaker doublet is assigned to the dithiolene ligands of **Co**. Spectral deconvolution of this lineshape to a pair of doublets allows accurate estimation of the surface Co:Mo ratio by the relative integrated area of the two sets of peaks divided by the cobalt to

dithiolene sulfur stoichiometry (Figure 2.12). From this, the Co:Mo ratio is estimated to be ~1:5 (0.5(13.4%:36.6% = 18.5%); Table 2.2). A similar estimate can be made from the S 2s region collected with the Mo 3d region (Figure 2.13 and Table 2.3). The S 2s feature is broader and more intense than that for 1L-MoS2, indicating a second S 2s contribution from **Co**. Spectral deconvolution of this region also gives a Co:Mo ratio of ~1:5 (0.5(17.58:41.89) = 21.0%; Table 2.3). To estimate maximal coverage of a **Co** monolayer on 2H-MoS_2, the area templated of adjacent coplanar **Co** units from a (100) slice in the single crystal unit cell[64] were taken and divided by that of the 2H-MoS_2 unit cell to give an estimated ~1:10 (9.54%) Co:Mo ratio (Figure 2.38). Based on an average 1:5 Co:Mo ratio from the S 2p and S 2s fits, this indicates that the **Co** coverage is approximately that of a bilayer if coplanar with the surface or adsorbed edge on.

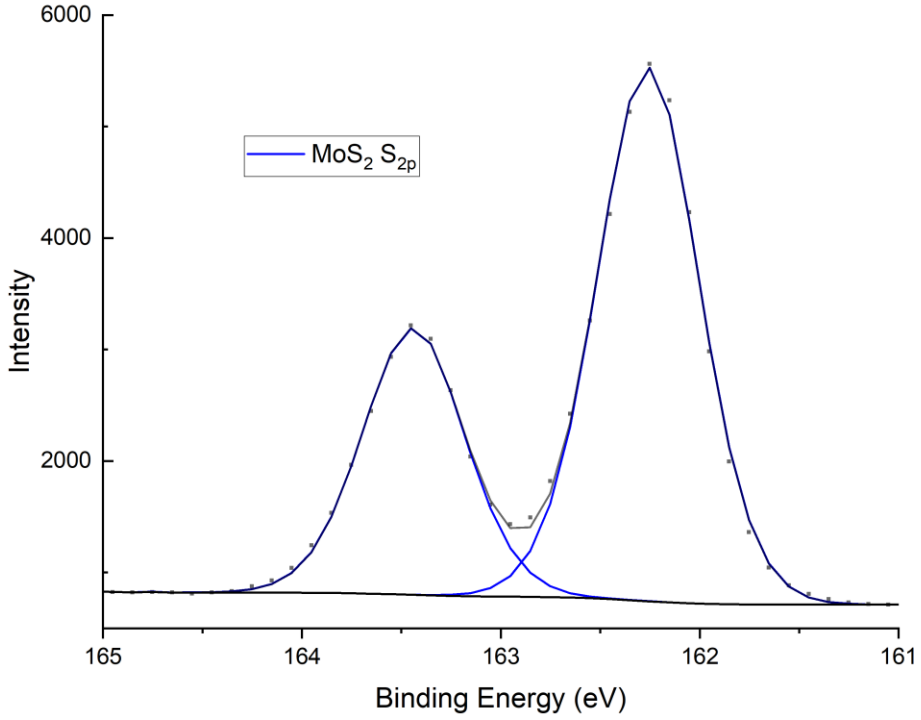

Figure 2.8. High resolution XP spectra of untreated 1L-MoS_2 in the S 2p region.

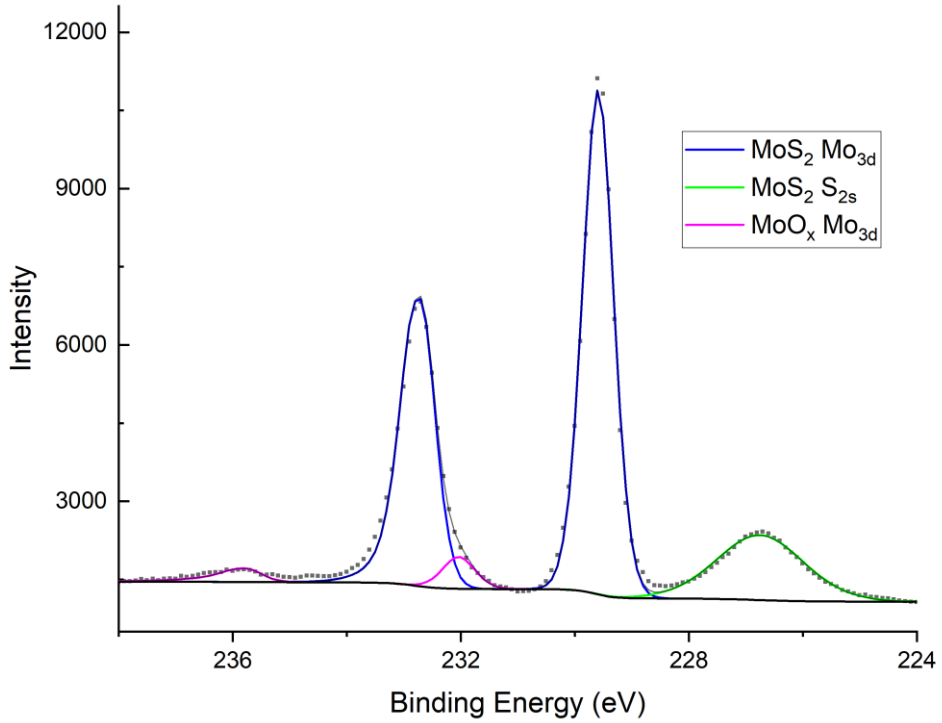

Figure 2.9. High resolution XP spectra of untreated 1L-MoS_2 in the S 2s and Mo 3d region.

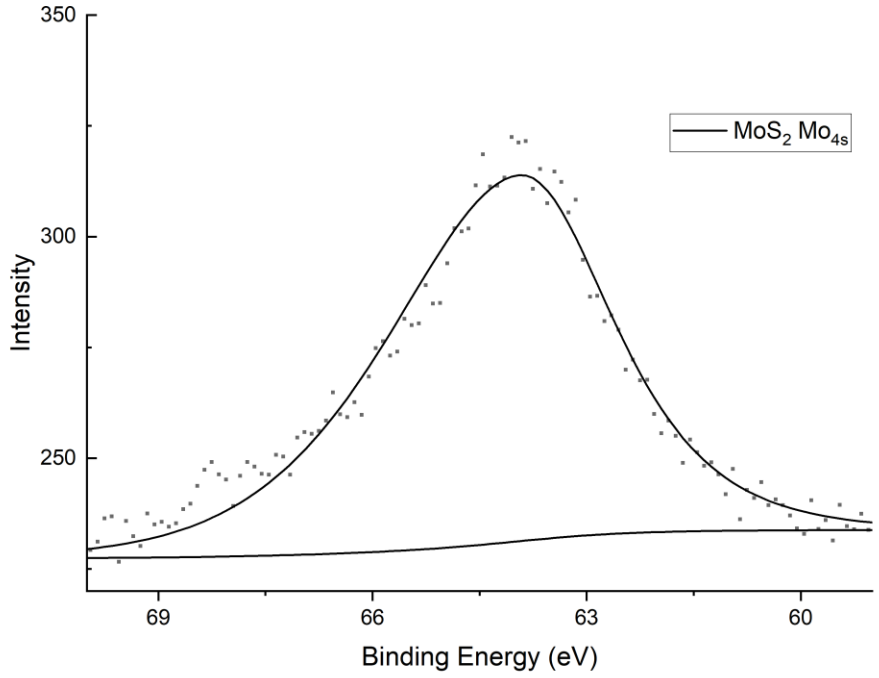

Figure 2.10. High resolution XP spectra of untreated 1L-MoS_2 in the Mo 4s region.

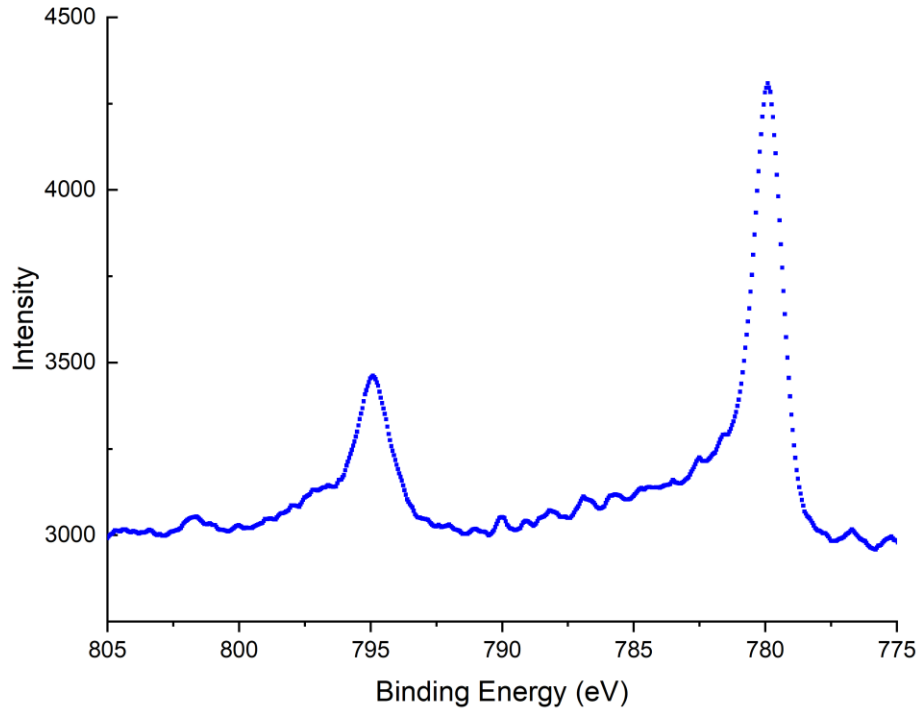

Figure 2.11. High resolution XP spectra of Co-MoS_2 in the Co 2p region.

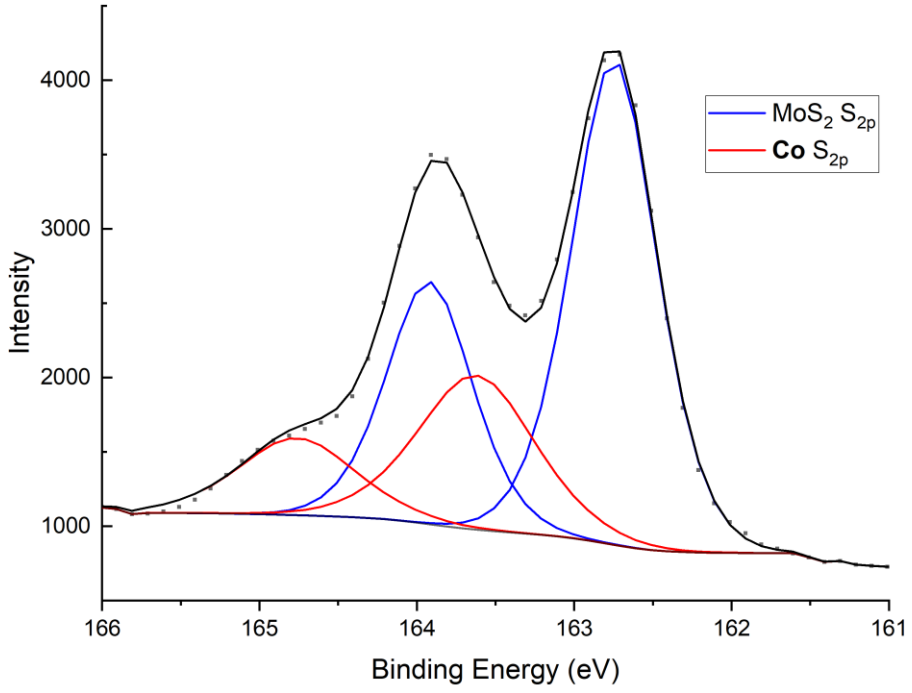

Figure 2.12. High resolution XP spectra of Co-MoS_2 in the S 2p region.

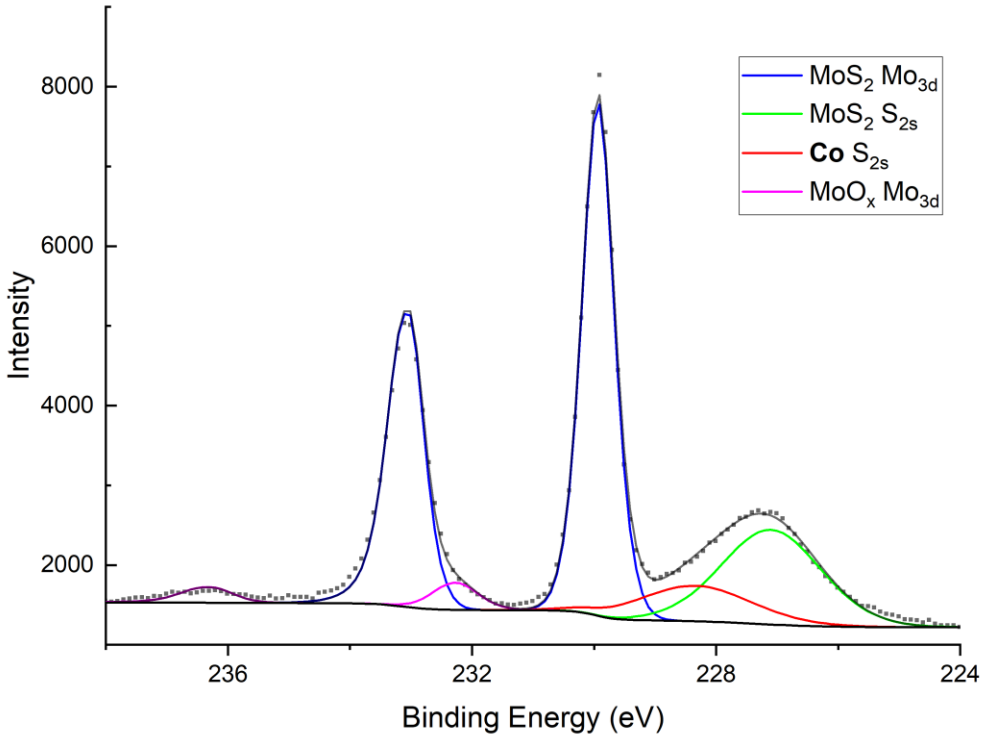

Figure 2.13. High resolution XP spectra of Co-MoS_2 in the S 2s and Mo 3d region.

Table 2.2. High resolution XP spectra S 2p region fits.

MoS_2					
Peak	Position (eV)	FWHM (eV)	Line Shape[a]	Area	Atomic %
MoS_2 S $2p_{3/2}$	162.26	0.60	GL(30)	3132	50.00
MoS_2 S $2p_{1/2}$	163.44	0.60	GL(30)	1566	50.00
Co-MoS_2					
Peak	Position (eV)	FWHM (eV)	Line Shape[a]	Area	Atomic %
MoS_2 S $2p_{3/2}$	162.38	0.66	GL(50)	2585	36.60
MoS_2 S $2p_{1/2}$	163.58	0.66	GL(50)	1321	36.60
Co S $2p_{3/2}$	163.41	0.86	GL(50)	957	13.54
Co S $2p_{1/2}$	164.59	0.86	GL(50)	478	13.25

[a] GL lineshapes are Gaussian/Lorentzian product functions implemented in CasaXPS with the number in parenthesis indicating the Lorentzian contribution percentage.

Table 2.3. High resolution XP spectra Mo 3d region fits.

MoS_2					
Peak	Position (eV)	FWHM (eV)	Line Shape[a]	Area	Atomic %
MoS_2 Mo $3d_{5/2}$	229.45	0.63	GL(50)	7534	28.73
MoS_2 Mo $3d_{3/2}$	232.57	0.63	GL(50)T(2)[b]	5022	27.74
MoS_2 S2s	226.63	1.79	GL(30)	2658	39.84
MoO_x $Mo3d_{5/2}$	231.91	0.66	GL(30)	495	1.89
MoO_x $Mo3d_{3/2}$	235.61	0.66	GL(30)T(2) [b]	330	1.82
Co-MoS_2					
Peak	Position (eV)	FWHM (eV)	Line Shape[a]	Area	Atomic %
MoS_2 Mo $3d_{5/2}$	229.93	0.62	GL(50)	4451	19.22
MoS_2 Mo $3d_{3/2}$	233.04	0.62	GL(50)T(2) [b]	2967	18.56
MoS_2 S 2s	227.10	1.92	GL(30)	2468	41.89
Co S 2s	228.34	2.15	GL(30)	1036	17.58
MoO_x Mo $3d_{5/2}$	232.28	0.88	GL(30)	326	1.41
MoO_x Mo $3d_{3/2}$	236.29	0.88	GL(30)T(2) [b]	217	1.36

[a] GL lineshapes are Gaussian/Lorentzian product functions implemented in CasaXPS with the number in parenthesis indicating the Lorentzian contribution percentage.

[b] Asymmetry in the $Mo3d_{3/2}$ peaks were fit using an additional asymmetric blend function convolution implemented in CasaXPS.

Inspection of the binding energies of the functionalized surface can also provide insight into the electronic effects of **Co** binding (Tables 2.2 and 2,3). In the S 2p region of MoS_2, the binding energies for Co-MoS_2 are increased by 0.12 eV compared to untreated 1L-MoS_2. This energy difference is probably within experimental error and therefore not specifically attributable to **Co** binding. High resolution spectra of the Mo 3d region shows much larger increases in binding energy compared to S 2p region. Here, the Mo $3d_{5/2}$ and S 2s peaks shift 0.5 eV higher in energy in the **Co** functionalized surface. This is indicative of a larger perturbation of the electronic structure of MoS_2 from **Co**, possibly from coupling of the frontier orbitals.[101]

AFM images of the Co-MoS_2 obtained were obtained to explore whether structural information could be obtained about the functionalized surface (Figure 2.14). Images were

collected in the attractive mode to mitigate surface damage by the AFM tip while still allowing measurement of the surface topology. This comes at the cost of reducing the accuracy of the observed height. Images collected on a partial monolayer of MoS_2 on SiO_2 allow step-edge height profiles of individual 1L-MoS_2 crystallites to be measured and compared to analogous acetonitrile washed 1L-MoS_2. This allows direct analysis of the added height due to **Co** functionalization and avoids convolution with solvent adsorption or other effects. Images of washed MoS_2 samples show flat islands of 1L-MoS_2 on top of a similarly flat SiO_2 surface (Figure 2.14). Measurement of the MoS_2 monolayer step-edge height gives a value of 1 nm, which is not experimentally distinguishable from the crystallographically determined lattice spacing of 1.232 nm.

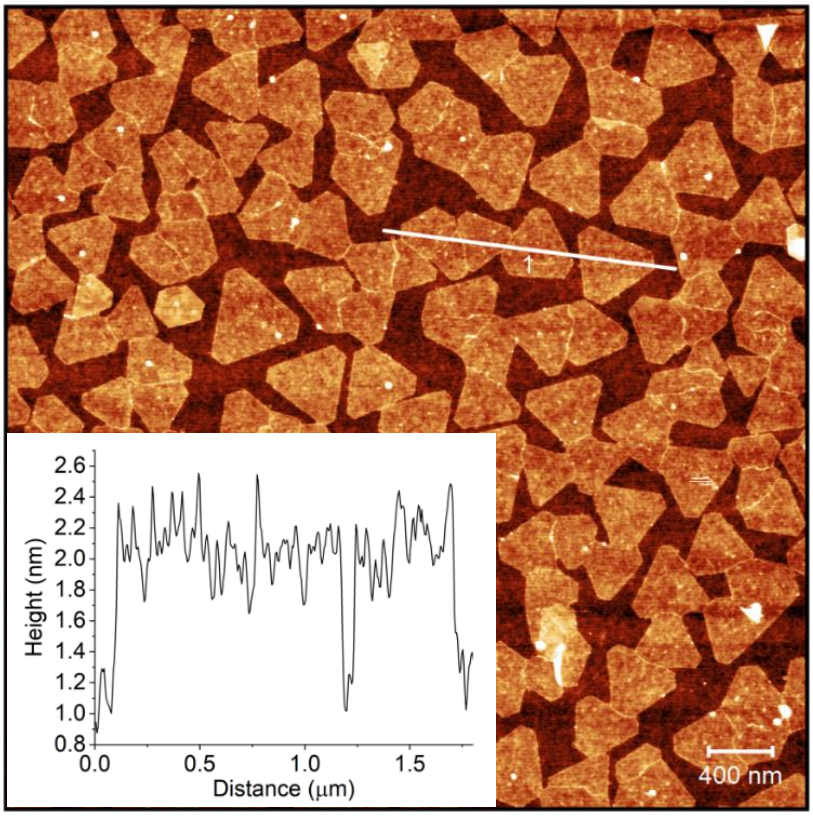

Figure 2.14. AFM image of MeCN washed 1L-MoS_2. Inset shows height profile along path labeled 1.

Upon functionalization with **Co**, AFM images of Co-MoS_2 show an increased roughening of the MoS_2 basal plane surface with height varying up to ~1 nm (Figure 2.15). The lack of any large features on the surface suggests that the molecular functionalization is not simple deposition of large **Co** aggregates or crystallites, consistent with the confocal Raman spectroscopic results. The measured step-edge height also increases to 1.5 nm. This difference is indicative of another chemical species on the surface. Due to measurement in attractive mode, this difference in height cannot be directly assigned to the height of the surface species as apparent height will be sensitive to the tip-substrate interaction. Aggregates observed at the edge of the MoS_2 islands are attributed to MoO_x species, which are found to be sample dependent.

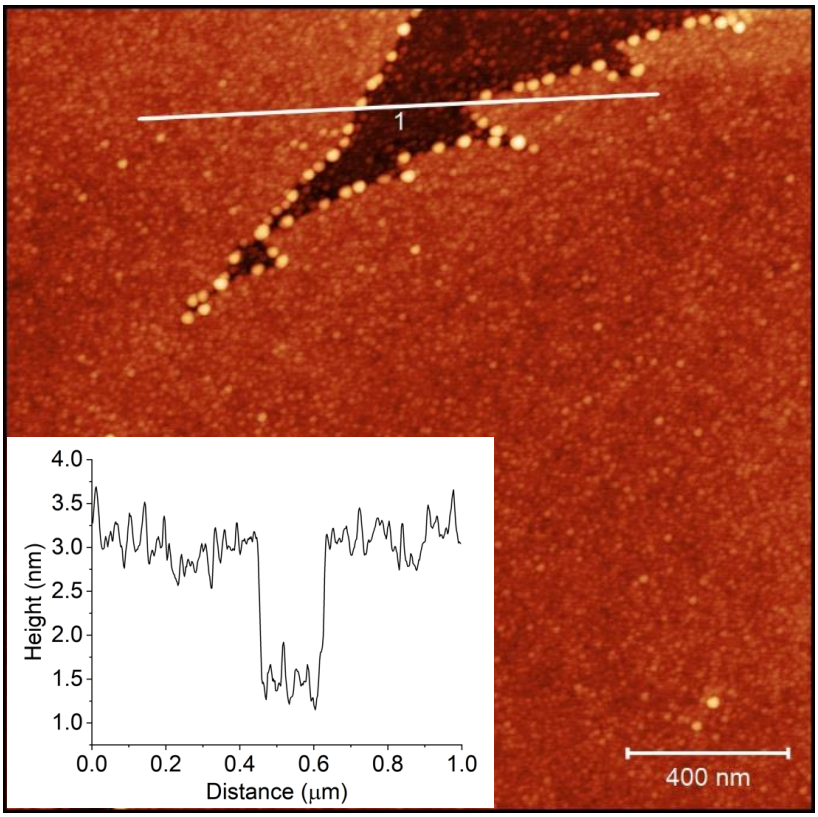

Figure 2.15. AFM image of Co-MoS_2. Inset shows height profile along path labeled 1.

Collectively, the Raman, XPS, and AFM data suggest molecular functionalization of MoS_2 by **Co** with an average coverage of bilayer (if adsorbed face on) or monolayer (if side on) over the basal plane surface. Raman vibrational spectra confirm the presence of **Co** on the surface and shifts in $Co(bdt)_2^-$ frequencies indicate a difference in structure from crystalline **Co** due to adsorption. The XPS data allow quantification of the amount of **Co** on the surface and provide the estimates of coverage. Finally, AFM images show relatively uniform coverage of the MoS_2 surface with no large aggregates or crystallites. The π-conjugated nature of **Co** inherently presents a large face for van der Waals attraction, which is assumed to be the mode for adsorption. Other van der Waals bilayers of MoS_2 and other aromatic molecules such as porphyrins and phthalocyanines are known and can be formed through simple solution methods as well.[35] The next logical step in these studies would have been to investigate the electrochemical properties of Co-MoS_2. Unfortunately, our attempts at these measurements did not yield useful results, so the project was discontinued at this point.

2.2.2. Covalent Functionalization of 1L-MoS_2 with Rh.

Preparation of **Rh**-MoS_2 functionalized surfaces was accomplished by soaking 1L-MoS_2 on SiO_2 samples with a dilute solution of **Rh** in acetonitrile (Scheme 2.3; see Section 2.4 for full details). This was followed by rinsing with acetonitrile to remove excess **Rh** and drying under high vacuum. Confocal Raman spectra of the modified surface showed only bands due to 1L-MoS_2 (Figure 2.16) and no new peaks corresponding to **Rh** (Figure 2.17). This is likely due to the absence of any strong electronic-absorption bands of rhodium bis-olefin complexes[102] near the 532 nm Raman excitation line, precluding resonance enhancement. Slight damping of the A_{1g} MoS_2 stretch is observed (Figure 2.17), although the significance of this observation is inconclusive as described above.

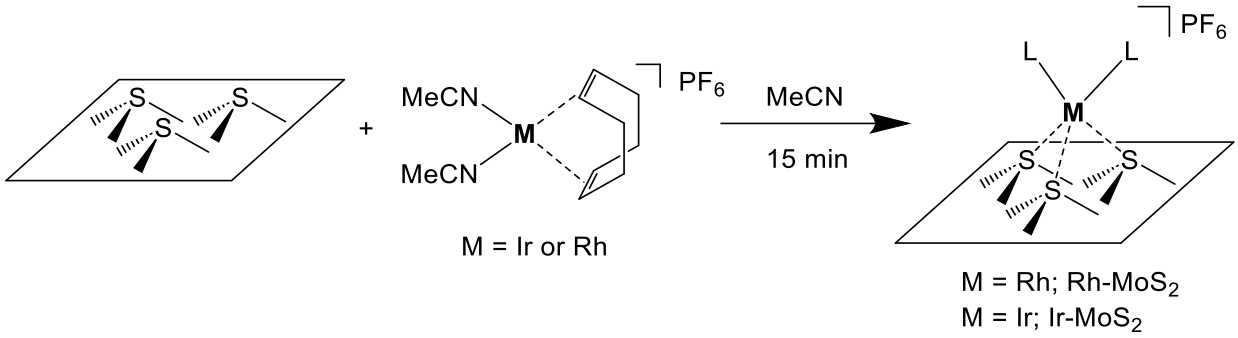

Scheme 2.3. Synthesis of Rh-MoS_2 and Ir-MoS_2.

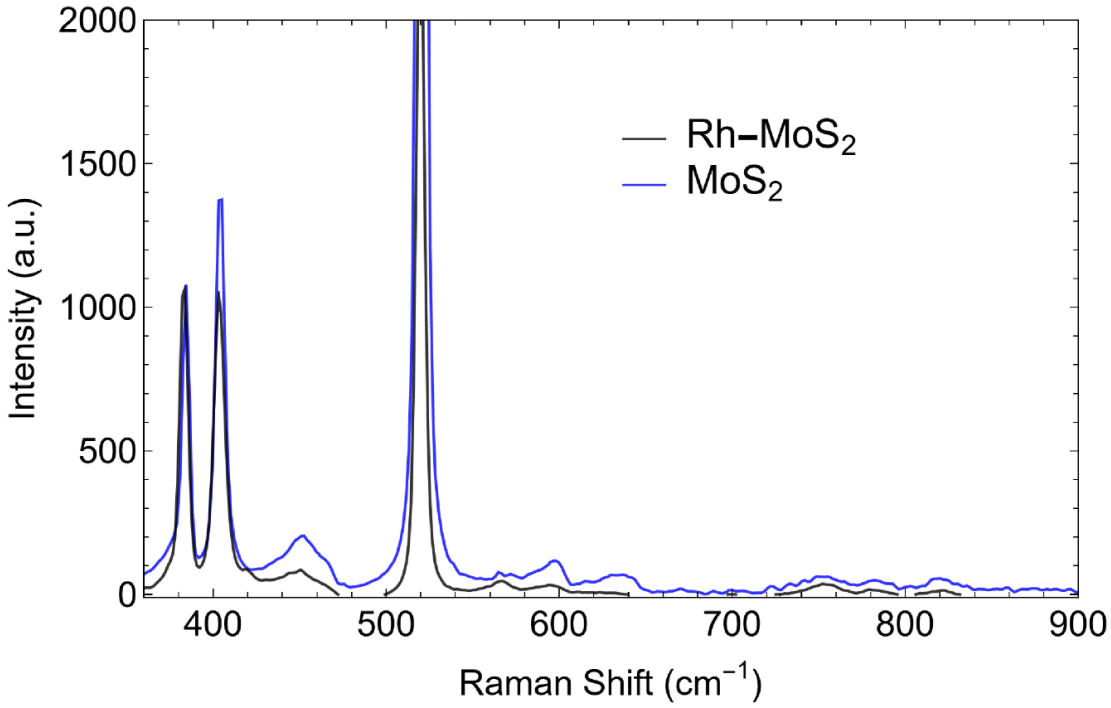

Figure 2.16. Confocal Raman spectra (λ_{ex} = 532 nm) of Rh-MoS_2 (black) compared to untreated 1L-MoS_2 (blue).

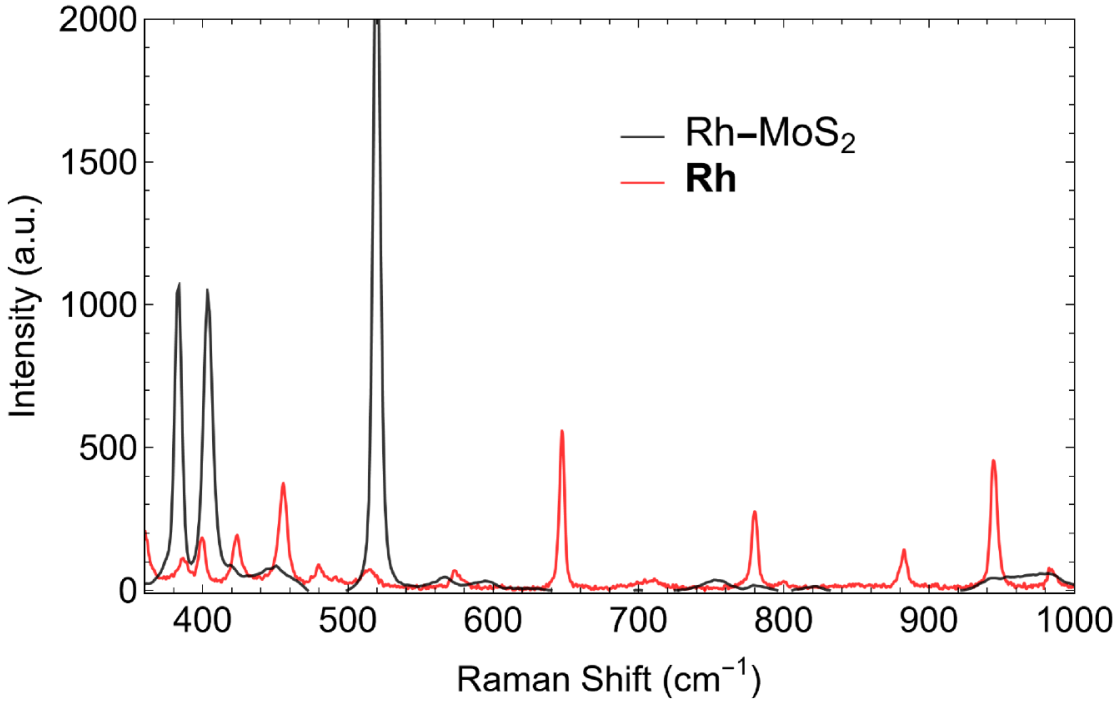

Figure 2.17. Confocal Raman spectra (λ_{ex} = 532 nm) of Rh-MoS_2 (black) compared to microcrystalline **Rh** (red).

XP spectra were collected for the **Rh** treated MoS_2 surfaces to determine whether a Rh-containing species is present and its chemical identity. Survey spectra show new peaks corresponding to rhodium and fluorine (Figure 2.18), indicating the presence of both a rhodium compound and PF_6 on the surface. Since PF_6 is not expected to adsorb to or be incorporated into 1L-MoS_2, the presence of the F suggests that the PF_6 counterion is still paired to a positively charged Rh-containing species. This also suggests that **Rh** is not binding to surface defects that can carry negative charge.[103] Signals for phosphorus are not observed, which is due to the weak residual sensitivity factor of the phosphorus 2p peak and overlap with much stronger signals from sulfur. Integration of the Rh 3d and Mo 3d regions following correction for residual sensitivity factors gives a Rh:Mo ratio of ~1:20 (1.57:33.17 = 4.7%; Table 2.4). This is much

smaller than the rough estimate of the Rh:Mo ratio of ~1:6 (16.6%) using the method described before from the crystal structure of [Rh([9]aneS$_3$)(cod)][BF$_4$] (Figure 2.39).[88]

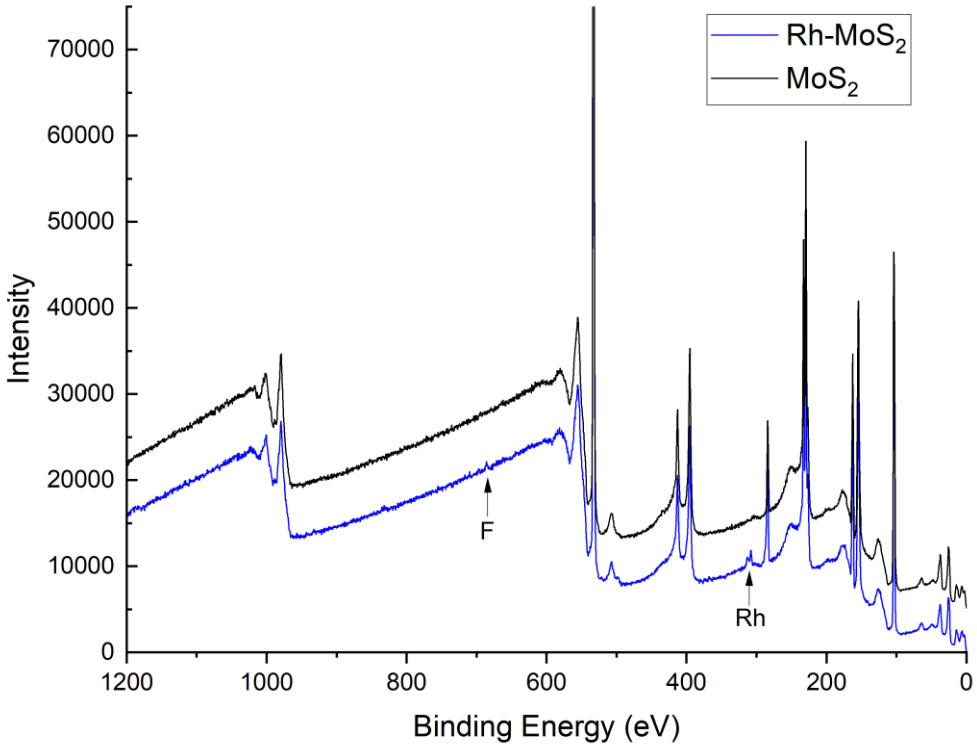

Figure 2.18. Survey XP spectra of Rh-MoS$_2$ (blue) and untreated 1L-MoS$_2$ (black).

Table 2.4. Survey XPS fitting data for Rh-MoS$_2$.

Rh-MoS$_2$			
Region	Position[a]	Integrated Area	Atomic %
Rh 3d	307.73	588	1.57
Mo 3p	395.73	7602	33.17
S 2p	162.93	2895	65.26

[a] Denotes center of integrated region in survey spectrum.

High resolution spectra of the Rh 3d region show an asymmetric doublet (Figure 2.19). The Rh 3d$_{5/2}$ peak is centered at 308.05 eV (Table 2.5). This confirms that the rhodium is not metallic, but conclusive assignment of the rhodium oxidation state is difficult. This binding

energy lies between $Rh(PPh_3)_3Br$ at 307.8 eV and $Rh(PPh_3)_3Cl$ at 309 eV.[94] Rh(III) species are mostly found above 309 eV suggesting more Rh(I)-like character. Binding energies are dependent on the supporting ligands, which are not rigorously defined in this system. As oxidative addition of a Rh^I species with the surface seems unlikely and the binding energy is more in line with other square-planar Rh(I) complexes, the Rh(I) oxidation state is proposed. The Mo 3d/S 2s and S 2p regions (Figures 2.20 and 2.21, respectively) are essentially unchanged from those in spectra in untreated MoS_2 (Figures 2.8 and 2.9). Both the S $2p_{3/2}$ and Mo $3d_{5/2}$ peaks for MoS_2 are only shifted higher by 0.1 eV, which is within reasonable experimental error for XPS (Tables 2.6 and 2.7). Considering the cationic charge of **Rh**, this is slightly unusual, since a larger shift to higher binding energy may be expected due to the electron-deficient and cationic charge of **Rh**. It is possible that the low valent nature, sparse coverage, and charge pairing with the PF_6^- anion are enough to limit strong p-doping of the surface.

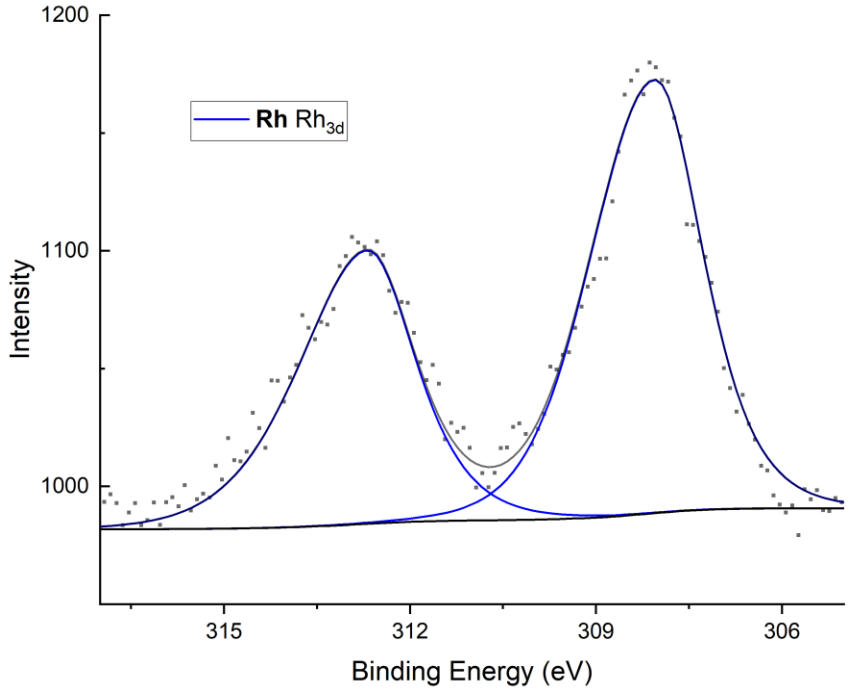

Figure 2.19. High resolution XP spectra of Rh-MoS_2 in the Rh 3d region.

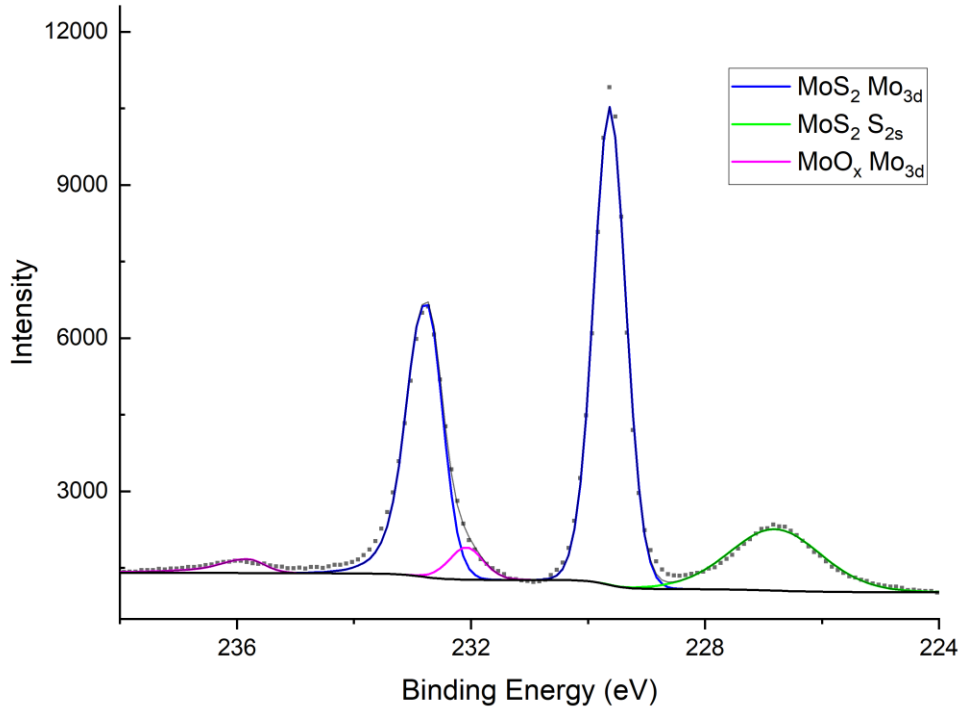

Figure 2.20. High resolution XP spectra of Rh-MoS_2 in the S 2s and Mo 3d region.

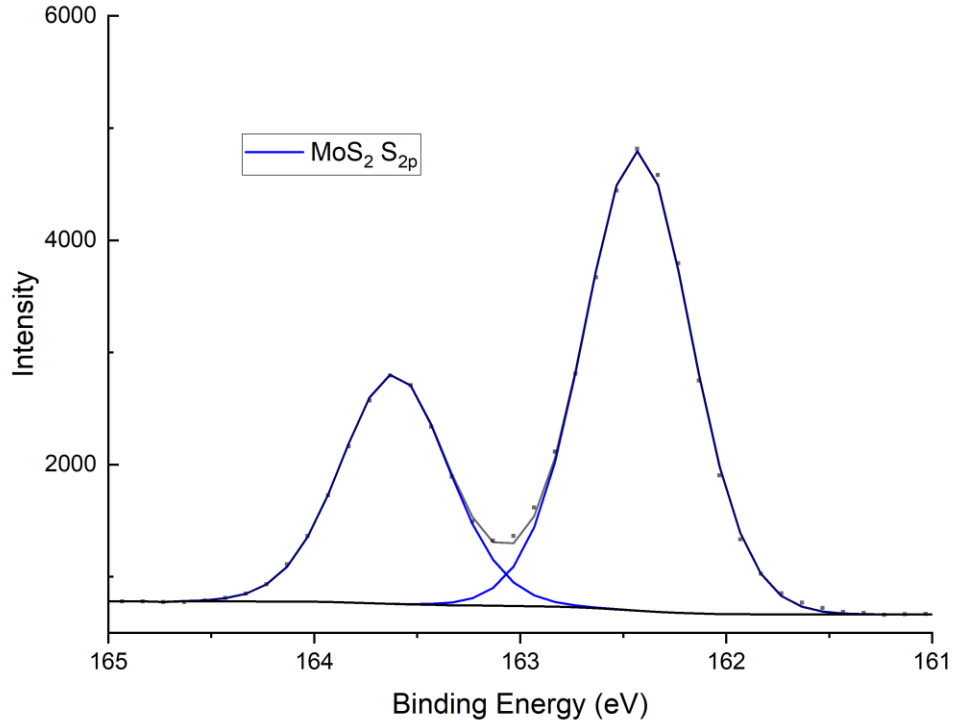

Figure 2.21. High resolution XP spectra of Rh-MoS_2 in the S 2p region.

Table 2.5. High resolution XP spectra Rh 3d region fits of Rh-MoS_2.

Rh-MoS_2					
Peak	Position (eV)	FWHM (eV)	Line Shape[a]	Area	%Area
Rh $3d_{5/2}$	308.05	1.87	LF(1,2,2,0)	447	50.90
Rh $3d_{3/2}$	312.70	1.87	LF(1,2,2,0)	298	49.10

[a] GL lineshapes are Gaussian/Lorentzian product functions implemented in CasaXPS with the number in parenthesis indicating the Lorentzian contribution percentage.

Table 2.6. High resolution XP spectra Mo 3d region fits of Rh-MoS_2.

Rh-MoS_2					
Peak	Position (eV)	FWHM (eV)	Line Shape[a]	Area	Atomic %
MoS_2 Mo $3d_{5/2}$	229.59	0.64	GL(50)	6712	28.46
MoS_2 Mo $3d_{3/2}$	232.72	0.64	GL(50)T(2) [b]	4474	27.47
MoS_2 S 2s	226.75	1.79	GL(30)	2424	40.39
MoO_x Mo $3d_{5/2}$	232.04	0.67	GL(30)	442	1.87
MoO_x Mo $3d_{3/2}$	235.78	0.67	GL(30)T(2) [b]	295	1.81

[a] GL lineshapes are Gaussian/Lorentzian product functions implemented in CasaXPS with the number in parenthesis indicating the Lorentzian contribution percentage.

[b] Asymmetry in the $Mo3d_{3/2}$ peaks were fit using an additional asymmetric blend function convolution implemented in CasaXPS.

Table 2.7. High resolution XP spectra S 2p region fits of Rh-MoS_2.

Rh-MoS_2					
Peak	Position (eV)	FWHM (eV)	Line Shape[a]	Area	Atomic %
MoS_2 S $2p_{3/2}$	162.39	0.61	GL(30)	2789	50.00
MoS_2 S $2p_{1/2}$	163.57	0.61	GL(30)	1394	50.00

[a] GL lineshapes are Gaussian/Lorentzian product functions implemented in CasaXPS with the number in parenthesis indicating the Lorentzian contribution percentage.

AFM images of the **Rh** modified surface were also collected in the attractive mode (Figure 2.22). Here, increased roughening of the MoS_2 basal plane surface with variance up to ~1 nm is observed. This is slightly greater than that found for acetonitrile washed 1L-MoS_2 (Figure 2.14) which displays variance up to 0.8 nm although this is close to experimental error. The

increased roughening is suggestive of molecular adsorption to the surface and suggests that some additional reaction beyond solvent adsorption has occurred at the surface in the presence of **Rh**. No crystallites were observed. The step-edge height of the MoS_2 grains also increased from ~1 nm for the acetonitrile washed MoS_2 to 1.7 nm for Rh-MoS_2. Given the low coverage measured from XPS, this large change in step-edge height may be more indicative of a perturbation in the tip-surface interaction. Collectively, the AFM data indicate the presence of a new molecular surface species adsorbed to the surface of the MoS_2 derived from **Rh**.

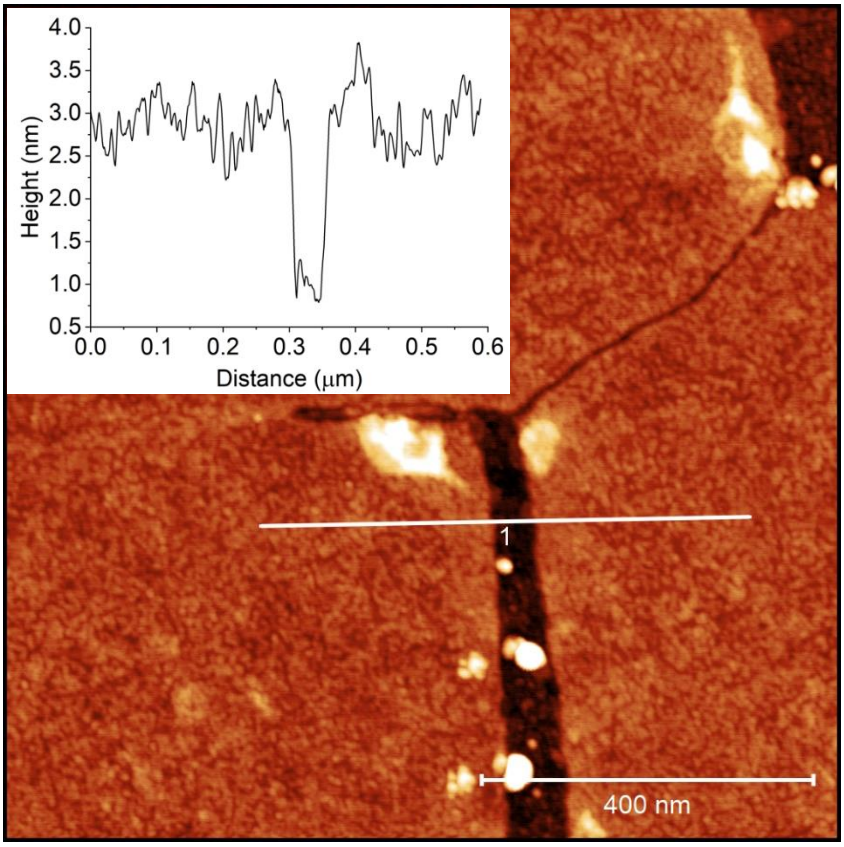

Figure 2.22. AFM image of Rh-MoS_2. Inset shows height profile along path labeled 1.

High-angle annular dark field scanning transmission electron microscopy (HAADF-STEM) was conducted to image the atomic geometry of the rhodium centers atop the MoS_2 surface. These samples were prepared by delamination of the 1L-MoS_2 from the SiO_2 wafer

using water to give a free-standing monolayer.[98] This monolayer was then transferred to the TEM grid and dried under vacuum. This method ensures that no solvent contacts the functionalized MoS_2 surface and reduces surface contamination. Images were collected using 80 kV accelerating voltages to minimize damage to the MoS_2 lattice by the electron beam and improve resolution. These images show the presence of bright features overlaying the MoS_2 surface assigned to mononuclear rhodium sites lying on top of the hexagonal MoS_2 lattice, as well as clusters of rhodium atoms of varying size evidenced by bright, cloudy patches in the image (Figure 2.23). The atomic contrast in these images is not particularly good due to the small difference in atomic weight between rhodium and molybdenum and the Z-sensitive contrast for HAADF-STEM. This results in relatively poor resolution of individual rhodium atoms, which is further complicated by loss of contrast from clustering of rhodium atoms and observed migration of isolated rhodium atoms across the surface under the influence of the electron beam. Imaging of this migration was not possible for rhodium but was possible for iridium as shown below.

To confirm the identity of these atoms, *in situ* EELS spectra were collected. Unfortunately, due to the fragility of the monolayer and flux necessary to get sufficient resolution, collection inevitably resulted in destruction of material within that region. Despite these limitations, higher magnification images (Figure 2.23) show that isolated rhodium atoms appear to preferentially sit atop molybdenum sites. This would suggest threefold coordination by the surface sulfur atoms. Considering the 1:20 Rh:Mo ratio found by XPS, the observed coverage of rhodium on the surface is much less than maximal. This can potentially be accounted for by the clustering of rhodium also observed on the surface (Figure 2.23) as the aforementioned interspersed bright patches on the MoS_2 surface. The image quality of the **Rh** functionalized MoS_2 is generally poor, precluding in-depth studies and analysis of the modified surface. To

improve the resolution of the HAADF-STEM images and potentially improve stability, functionalization using the analogous iridium complex was attempted to improve image quality while maintaining similar chemistry to **Rh**.

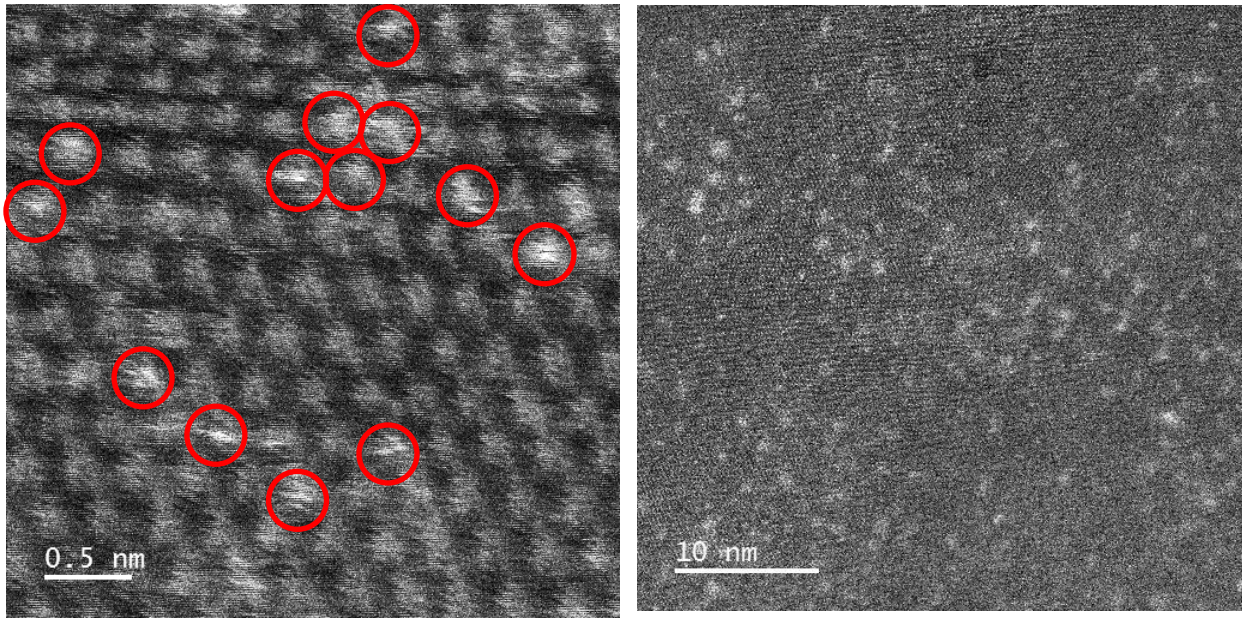

Figure 2.23. HAADF-STEM images of Rh-MoS_2. Circled bright spots in left image are individual rhodium atoms.

2.2.3. Covalent Functionalization of 1L-MoS_2 with Ir.

As with Rh, functionalization of the MoS_2 surface by **Ir** to provide Ir-MoS_2 was conducted by soaking the SiO_2 supported 1L-MoS_2 in a dilute acetonitrile solution of **Ir** followed by rinsing with acetonitrile and drying under vacuum (Scheme 2.3; see Section 2.4 for details). Like with Rh-MoS_2, confocal Raman spectra of the modified surface are essentially identical to untreated monolayer MoS_2 except for slight damping of the A_{1g} mode (Figure 2.24).[91] No Raman bands due to **Ir** are observed (Figure 2.25). AFM images collected of Ir-MoS_2 show similar roughening as observed for Rh-MoS_2 beyond solvent adsorption, indicating the presence of an adsorbed species (Figure 2.26).

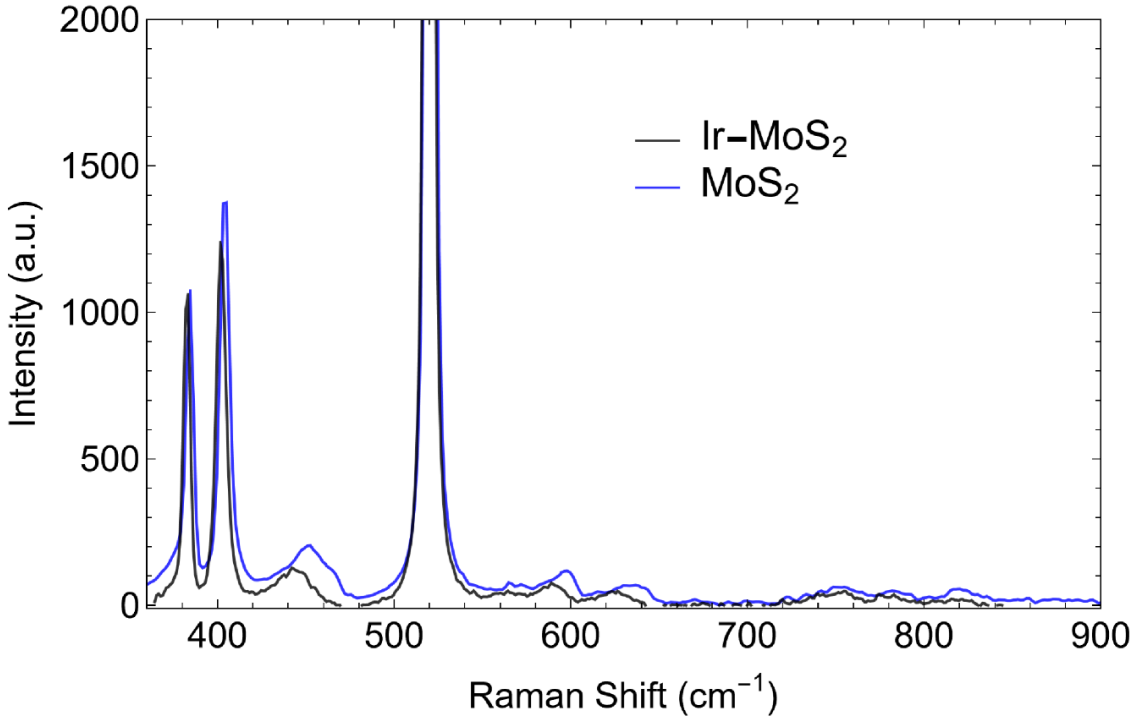

Figure 2.24. Confocal Raman spectra of (λ_{ex} = 532 nm) Ir-MoS_2 (black) and untreated MoS_2 (blue).

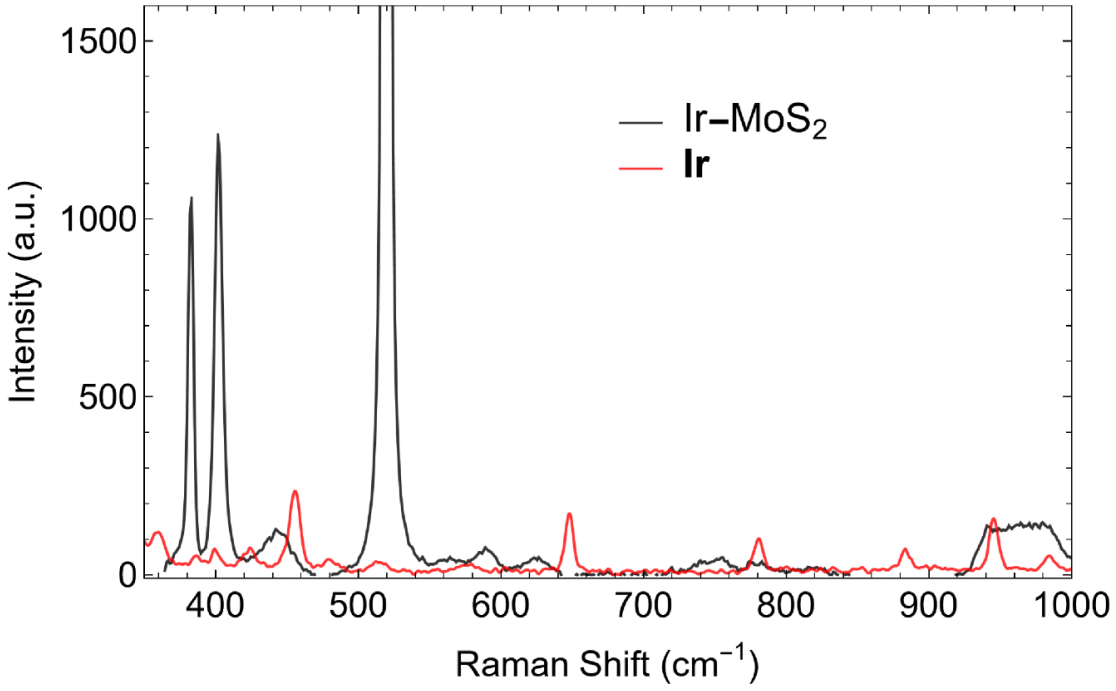

Figure 2.25. Confocal Raman spectra (λ_{ex} = 532 nm) of Ir-MoS_2 (black) and microcrystalline **Ir** (red).

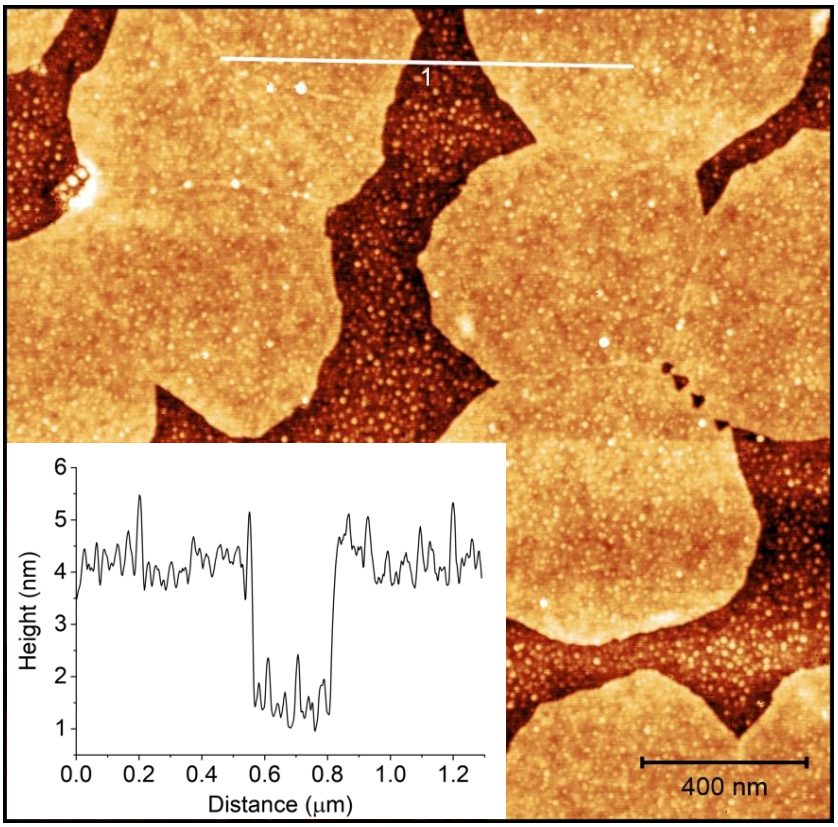

Figure 2.26. AFM image of Ir-MoS_2. Inset shows height profile along path labeled 1.

XPS spectra were collected of Ir-MoS_2 to look for signatures of the deposited complex. Survey spectra show signals attributable to fluorine and iridium, in addition to those for 1L-MoS_2 (Figure 2.27).[94] Integration of the survey spectra gives a ~1:16 (6.3%) Ir:Mo ratio, which is similar to the 1:20 Rh:Mo ratio observed for Rh-MoS_2 (Table 2.8). The iridium $4f_{7/2}$ and $4f_{5/2}$ doublet overlaps with the molybdenum 4s peak (Figure 2.28). To deconvolute the two peaks, the Mo 4s region was collected for untreated MoS_2 (Figure 2.10). The overall line shape was then deconvoluted by introducing a static Mo 4s peak and fitting the Ir 4f doublet to the residual lineshape. Assignment of the oxidation state of this complex is difficult. The Ir $4f_{7/2}$ peak is centered at 62.05 eV (Table 2.9).[94] This lies between $Ir(PPh_3)Cl(CO)_2$ at 61.7 eV and $IrCl_3$ at 62.8 eV. The much narrower range for iridium 4f binding energies potentially allows for

assignment as the +1 or +3 oxidation state depending on the supporting ligands. Following the previous arguments for **Rh** of coordination environment and charge pairing, the oxidation state is assigned to the +1 state, consistent with **Ir** functionalization of the surface. As with **Rh**, small shifts of ~0.15 eV from untreated MoS_2 are observed for the S 2p, Mo 3d, and S 2s peaks which is near experimental error for XPS peak energies (Tables 2.10 and 2.11 and Figures 2.29 and 2.30).

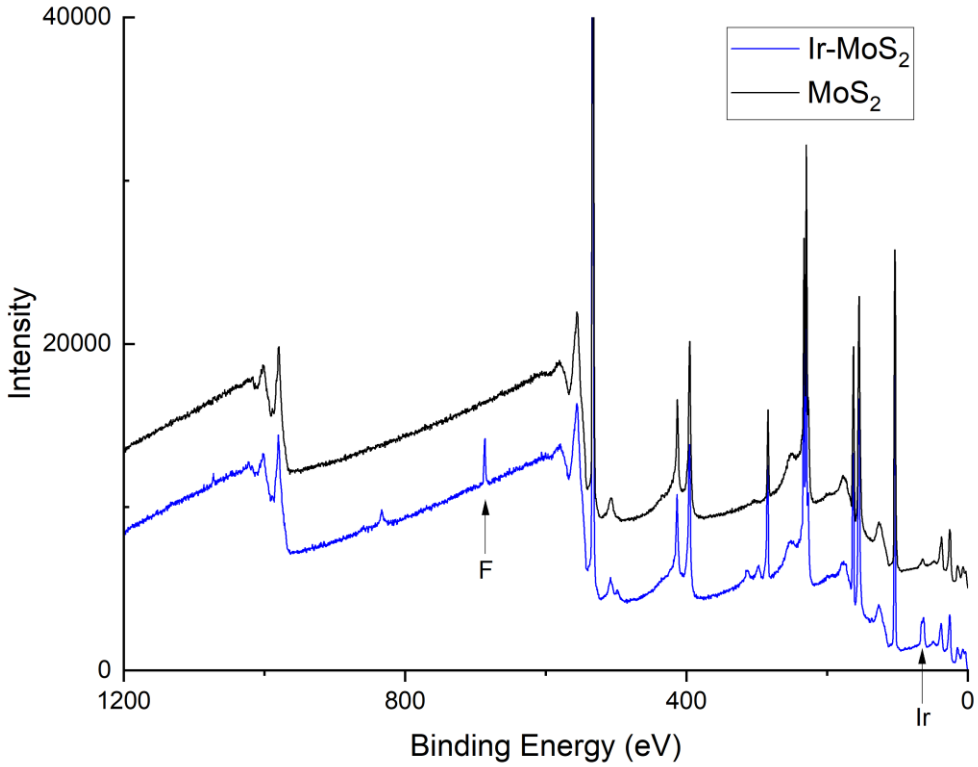

Figure 2.27. Survey XP spectra of Ir-MoS_2 (blue) and untreated MoS_2 (black).

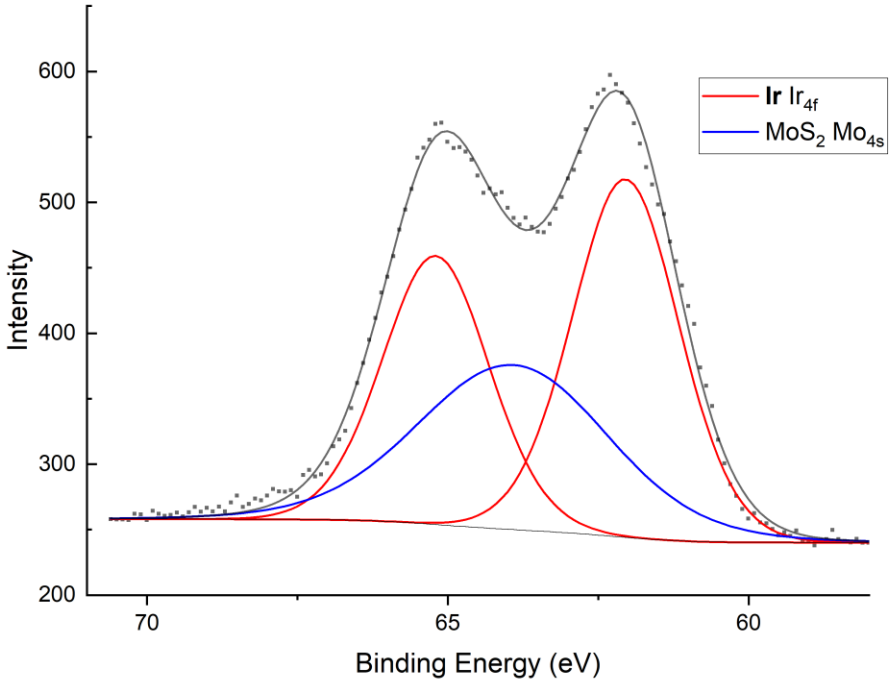

Figure 2.28. High resolution XP spectra of **Ir** functionalized MoS_2 in the Ir 4f region.

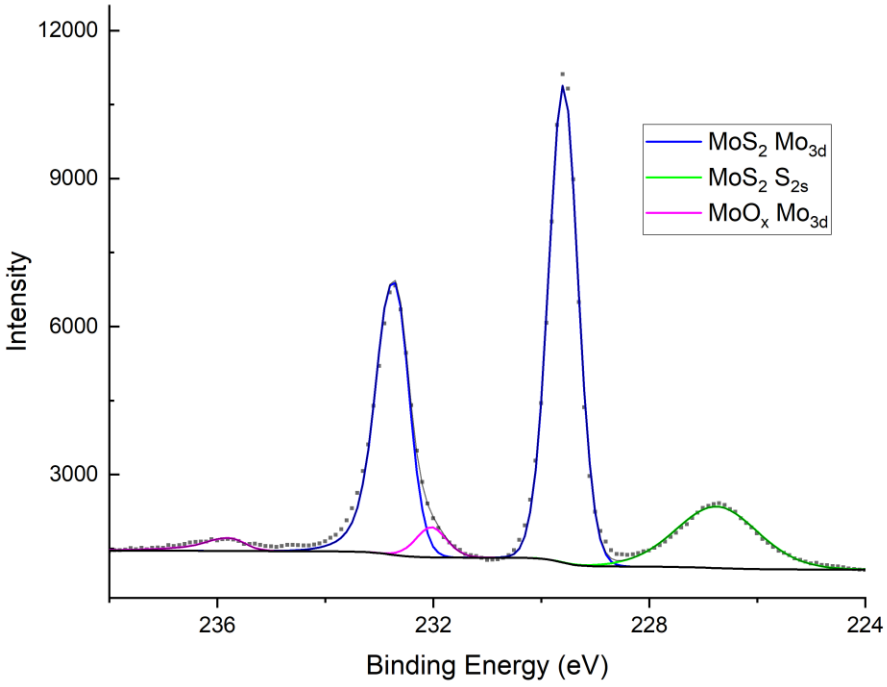

Figure 2.29. High resolution XP spectra of Ir-MoS_2 in the S 2s and Mo 3d region.

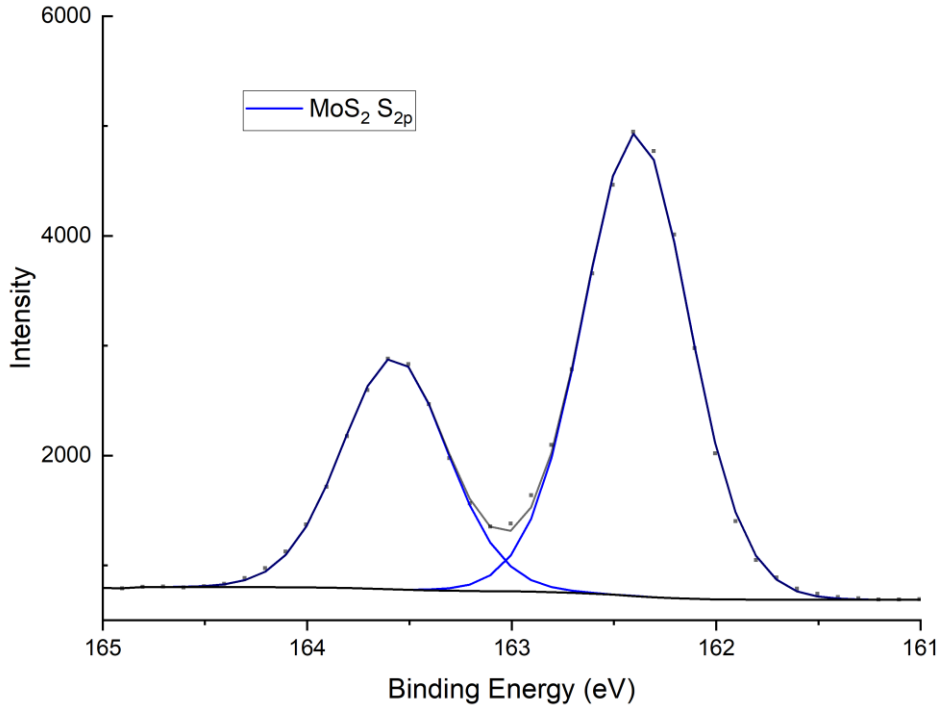

Figure 2.30. High resolution XP spectra of Ir-MoS_2 in the S 2p region.

Table 2.8. Survey XPS fitting data for Ir-MoS_2.

Ir-MoS_2			
Region	Position (eV)[a]	Integrated Area	Atomic %
Ir 4d	296.97	966	2.08
Mo 3p	395.31	4661	32.91
S 2p	162.55	2747	65.01

[a] Denotes center of integrated region in survey spectrum.

Table 2.9. High resolution XP spectra Ir 4f region fits for Ir-MoS_2.

Ir-MoS_2					
Peak	Position (eV)	FWHM (eV)	Line Shape[a]	Area	%Area
Ir $4f_{7/2}$	62.05	2.09	GL(30)	620	6.00
Ir $4f_{5/2}$	65.20	2.09	GL(30)	465	5.73
MoS_2 Mo 4s	63.91	3.73	LF(1,1,2,0)[b]	515	88.26

[a] GL lineshapes are Gaussian/Lorentzian product functions implemented in CasaXPS with the number in parenthesis indicating the Lorentzian contribution percentage.

[b] LF lineshape is a four parameter asymmetric Gaussian/Lorentzian product function implemented in CasaXPS.

Table 2.10. High resolution XP spectra Mo 3d region fits for Ir-MoS_2.

Ir-MoS_2					
Peak	Position (eV)	FWHM (eV)	Line Shape[a]	Area	Atomic %
MoS_2 Mo $3d_{5/2}$	229.63	0.65	GL(50)	6571	28.34
MoS_2 Mo $3d_{3/2}$	232.75	0.65	GL(50)T(2) [b]	4380	27.37
MoS_2 S 2s	226.80	1.85	GL(30)	2416	40.96
MoO_x Mo $3d_{5/2}$	232.08	0.68	GL(30)	466	2.01
MoO_x Mo $3d_{3/2}$	235.82	0.68	GL(30)T(2) [b]	311	1.34

[a] GL lineshapes are Gaussian/Lorentzian product functions implemented in CasaXPS with the number in parenthesis indicating the Lorentzian contribution percentage.

[b] Asymmetry in the $Mo3d_{3/2}$ peaks were fit using an additional asymmetric blend function convolution implemented in CasaXPS.

Table 2.11. High resolution XP spectra S 2p region fits for Ir-MoS_2.

Ir-MoS_2					
Peak	Position (eV)	FWHM (eV)	Line Shape[a]	Area	Atomic %
MoS_2 S $2p_{3/2}$	162.43	0.61	GL(30)	2722	50.00
MoS_2 S $2p_{1/2}$	163.61	0.61	GL(30)	1361	50.00

[a] GL lineshapes are Gaussian/Lorentzian product functions implemented in CasaXPS with the number in parenthesis indicating the Lorentzian contribution percentage.

To confirm molecular functionalization of the surface, HAADF-STEM images were collected of the modified surface (Figure 2.31). As expected, use of the heavier iridium complex instead of rhodium gives dramatically better contrast compared to the background MoS_2 lattice. Iridium atoms are found occupying sites above molybdenum atoms of the MoS_2 lattice, which would be consistent with threefold coordination to the sulfur atoms as observed for Rh-MoS_2. Iridium atoms appear as both isolated sites on top of the MoS_2 lattice as well as in few-atom clusters. These iridium atoms are mobile on the MoS_2 surface during STEM imaging. After collection of an image, some iridium atoms migrate to other suitable binding sites (Figure 2.31). This is attributed to the electron beam pushing around the iridium atoms on the surface.[53]

Upon closer inspection of the images, it appears that all iridium atoms are found in clouded areas marked by reduced background contrast. This is an odd phenomenon and warranted further analysis. These cloudy areas are inconsistently spread across the entirety of the MoS_2 surface and are indicative of a chemical species adsorbed to the surface which we attribute to amorphous carbon. Amorphous carbon is a material that forms on surfaces exposed to ambient conditions.[95, 98] In the absence of a highly controlled atmosphere, an amorphous carbon layer is capable of forming upon contact with organic material.[96-97, 104-107] Trace amorphous carbon can be clearly observed in HAADF-STEM images of untreated MoS_2 as well (Figure 2.34). Use of a lower energy 80 kV accelerating voltage allows visualization of the amorphous carbon despite its low atomic weight due to increased contrast from the reduced accelerating voltage, whereas conventional 200 kV accelerating voltages will tunnel directly through the carbon. The fact that iridium is observed only in regions where amorphous carbon is observed suggests that there is some chemical feature connecting these two species. Areas with larger amounts of amorphous carbon, indicated by reduced background contrast, seem to show greater clustering of iridium atoms while areas with thinner layers of carbon show isolated iridium atoms. This explains why larger coverage percentages of rhodium or iridium are observed by XPS but seem to show a mix of sparse and clumped atomic coverage by HAADF-STEM.

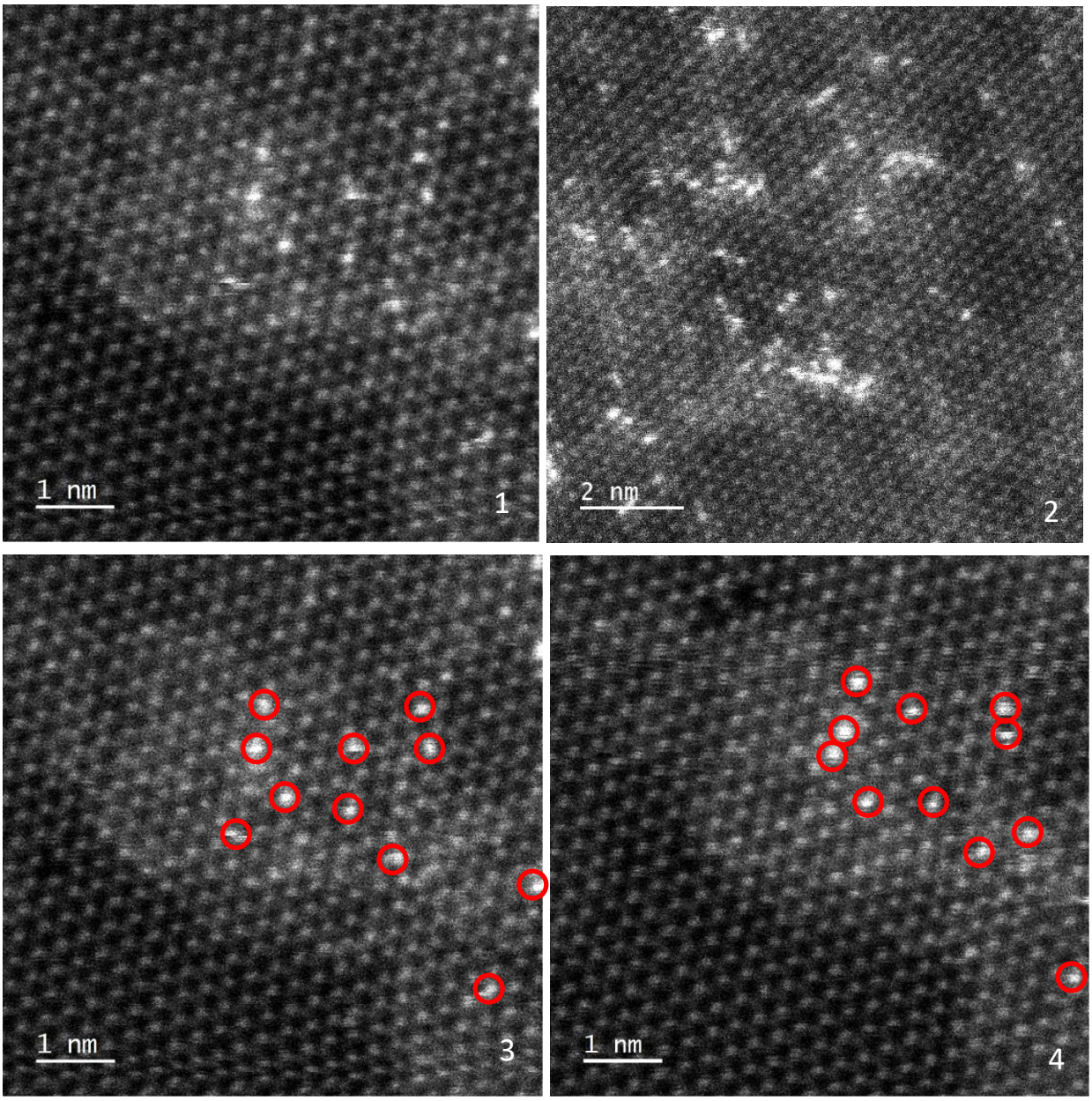

Figure 2.31. HAADF-STEM images of Ir-MoS_2. 1) High magnification showing individual iridium atoms. 2) other region showing increased amorphous carbon. 3,4) High magnification image showing migration of iridium atoms on surface with iridium atoms circled in red.

To probe whether amorphous carbon on the surface was driving surface functionalization, two additional controls were performed. First, untreated 1L-MoS_2 was subjected to identical workup with acetonitrile as the functionalized surfaces without **Ir** or **Rh**. This would help

confirm that exposure to organic solvents is contributing to formation of amorphous carbon on the MoS_2 surface. Second, cleaning of amorphous carbon after **Ir** functionalization was attempted by vacuum pyrolysis at 200 °C. This would help determine whether amorphous carbon was binding to the surface and the iridium was binding to the carbon or if iridium was binding to the surface and then templating adsorption of amorphous carbon on top. If the amorphous carbon is on top of the iridium sites, then we would expect to observe some isolated iridium atoms in regions where no amorphous carbon is observed after pyrolysis since the iridium is bound to the MoS_2 substrate and it should not be volatile under the mild vacuum pyrolysis conditions. If the iridium is situated on top of the amorphous carbon, then pyrolysis should remove some amorphous carbon and any overlying iridium atoms along with it. This would result in the continued observation of colocalized iridium and amorphous carbon.

HAADF-STEM images of the acetonitrile treated MoS_2 show similar amounts of amorphous carbon as the **Rh** and **Ir** functionalized surfaces confirming that exposure to acetonitrile does lead to deposition of amorphous carbon on the MoS_2 monolayer (Figure 2.32). This also suggests that part of the surface roughening observed by AFM can be attributed to deposition of amorphous carbon. Next, images of the pyrolyzed Ir-MoS_2 surfaces were studied. Amorphous carbon is still observed on the surface but appears reduced in intensity, suggestive of removal by the vacuum pyrolysis procedure. Higher magnification images still show clustering of iridium atoms and localization only in areas that have amorphous carbon (Figure 2.33). Multiple images were collected to determine if isolated iridium atoms could be observed away from any amorphous carbon, but no clear evidence of such a site could be found. This confirms that the observed functionalization of the MoS_2 surface by **Ir** and **Rh** are due to binding to amorphous carbon deposited on the surface and not coordination to the surface sulfur atoms of

MoS_2. This agrees with theoretical studies which predict low interaction energies for 2H-MoS_2.[108]

Other reports of basal plane functionalization of MoS_2 by transition metals have been limited. In general, these utilize defect-rich, exfoliated MoS_2 monolayers as a substrate and do not rigorously confirm basal plane binding of the transition-metal species using site-selective spectroscopic or physical characterization. In one example, deposited $AuCl_x$ species on the basal plane MoS_2 was observed with atomic resolution HAADF-STEM.[53] These sites are reported to be axially ligated by only one sulfur atom. Close inspection of these images shows amorphous carbon colocalized with the $AuCl_x$ sites here as well. Additionally, MoS_2 is being used as a reductant for the Au(III) precursor to form the proposed Au(I) species binding the surface. This presumably has a strong influence on the electrostatic attraction of the Au species to the surface and strongly differentiates this method from our desired mild synthetic protocol. Overall, the lack of reactivity of basal plane MoS_2 with transition metal reactants is exemplary of its stability and utility as a 2D material. Unfortunately, this also hinders it ability as a substrate to build chemically assembled architectures for catalysis.

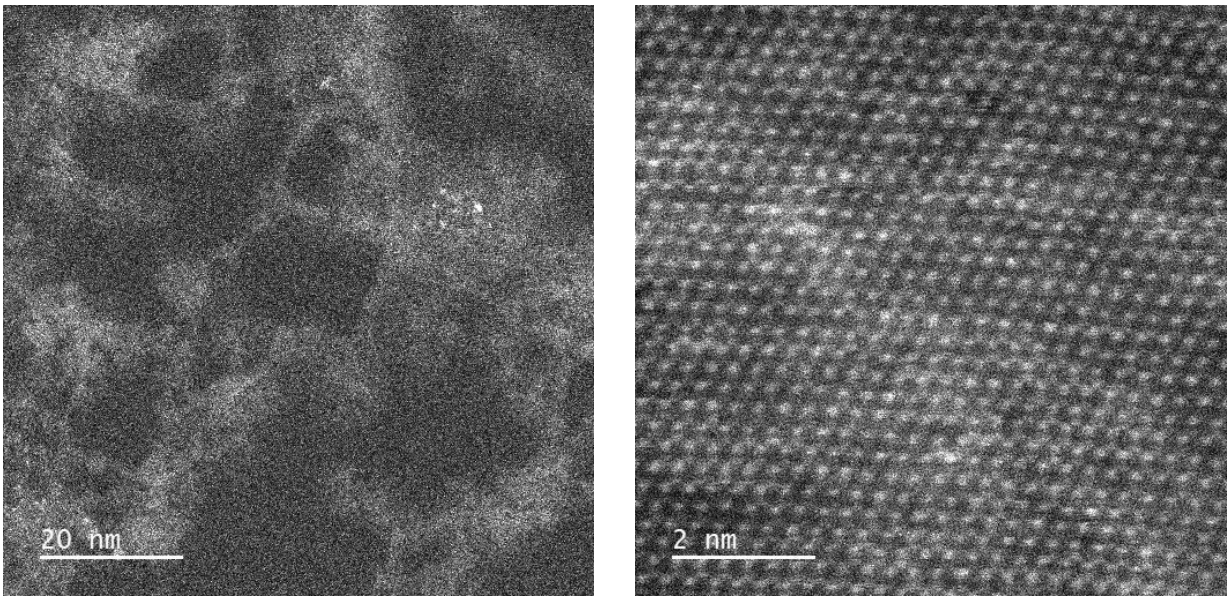

Figure 2.32. HAADF-STEM image of MeCN treated 1L-MoS_2 showing patches of amorphous carbon.

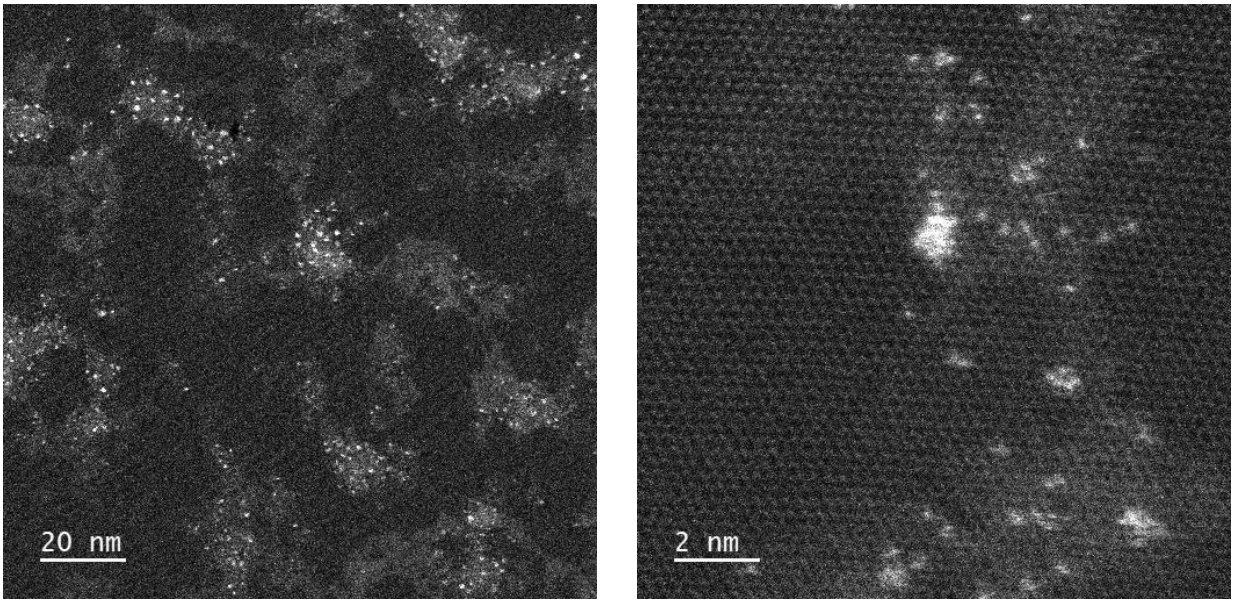

Figure 2.33. HAADF-STEM image of vacuum pyrolyzed Ir-MoS_2 sample showing iridium atoms and amorphous carbon.

2.3. Conclusions.

In this chapter, design principles and characterization protocols for synthesis of transition-metal functionalized MoS_2 monolayers were developed. These involved careful control of synthetic procedures to minimize damage to the surface while maintaining the intrinsic properties of 2H-MoS_2. Simple immersion-dose procedures of **Co** show evidence of noncovalent **Co** adsorption to the surface by Raman, XPS, and AFM Analogous functionalization procedures using **Rh** and **Ir** show low coverage on the surface with limited Raman evidence of functionalization. XPS establishes the presence of monovalent transition metal species on the surface consistent with the precursor oxidation state. High magnification HAADF-STEM images show both isolated atoms and few atom clusters on the MoS_2 surface occupying trigonal coordination sites above the molybdenum sites. Closer inspection of the HAADF-STEM images shows increased amounts of amorphous carbon colocalized with the doped transition-metal species. Control studies done to study the impact of amorphous carbon on binding of **Ir** to the surface confirm that iridium atoms only appear in regions with amorphous carbon and that iridium does not appear to be binding to the bare MoS_2 surface. This highlights the difficulty in developing general methods for surface functionalization of highly crystalline 2H-MoS_2.

2.4. Experimental Section

2.4.1. General Procedures

Solvents used for synthesis were HPLC grade and purified by passing through an anaerobic, stainless-steel system consisting of either two 4.5 in × 24 in (1 gal) columns of activated A2 alumina. Wafers of monolayer MoS_2 on SiO_2 supports were generously provided by Prof. Jiwoong Park's research group at the University of Chicago, which they prepared according

to their published procedure.[98] In our laboratory, these wafers were cut into multiple samples measuring 1 cm × 1 cm for use. All MoS_2 samples were stored under vacuum and shielded from light to limit degradation. The compounds **Co**,[64] **Rh**,[109] and **Ir**,[110] were synthesized according to published procedures.

2.4.2. Preparation of Functionalized Surfaces

Monolayer MoS_2 samples were functionalized with Co, Rh, and Ir by the following general procedure (Schemes 2.2 and 2.3). To a 20 mL scintillation vial was added 5 mL of a syringe-filtered (0.45 micron) 1 mM solution of the transition-metal complex. The SiO_2 supported 1L-MoS_2 was then gently placed in the solution along with a small stir bar and shielded from light. This solution was stirred for 15 min before removal of the SiO_2 wafer. The wafer was then rinsed with fresh acetonitrile (3 × 5 mL) and dried under high vacuum. Samples were stored under vacuum when not in use.

2.4.3. X-ray Photoelectron Spectroscopy

XPS data were collected using a Kratos Axis Nova X-ray Photoelectron Spectrometer. The sample chamber was kept at $<5 \times 10^{-9}$ torr and ejected electrons were collected at an angle of 90° from the surface normal. The XPS data were analyzed using the program Computer Aided Surface Analysis for X-ray Photoelectron Spectroscopy (CasaXPS).[111] All XPS signals reported here are binding energies and are reported in eV and corrected to the SiO_2 peak at 104.5 eV.[94] Backgrounds were fit with standard Shirley backgrounds. Element peaks were fit with a standard variable proportion Gaussian-Lorentzian line shape. Calculated atomic percentages were corrected using standard residual sensitivity factors.[94] Fits were constrained only based on

FWHM for spin-orbit split peaks. This resulted in reasonable agreement with expected peak area ratios and peak-to-peak separation.

2.4.4. Scanning Transmission Electron Microscopy

STEM images were collected using a JEOL JEM-ARM200CF Aberration Corrected Cold Field Emission Scanning Transmission Electron Microscope using an accelerating voltage of 80kV. Samples were prepared by delamination of the MoS_2 from the SiO_2 support by slowly dipping into water with the MoS_2 plane aligned nearly parallel to the water surface, according to standard procedures.[98] The freestanding MoS_2 monolayer on the water surface was then transferred to a Lacey Carbon grid and dried under vacuum for 24 hrs.

2.4.5. Atomic Force Microscopy

AFM images were collected using an Asylum Research Cypher ES AFM. An Arrow UHF tip was used to facilitate rapid image sampling. Samples were prepared by affixing the SiO_2 supported MoS_2 monolayer wafer to a magnetic 15 mm AFM metal specimen disc using a 12mm PELCO carbon conductive tab.

2.4.6. Confocal Raman Spectroscopy

Confocal Raman spectra were collected using a HORIBA LabRAM HR Evolution confocal Raman microscope using a 532 nm laser source and a 100X objective lens. Raman spectra were externally referenced to the Si(111) Raman vibrational mode at 520 cm^{-1}.

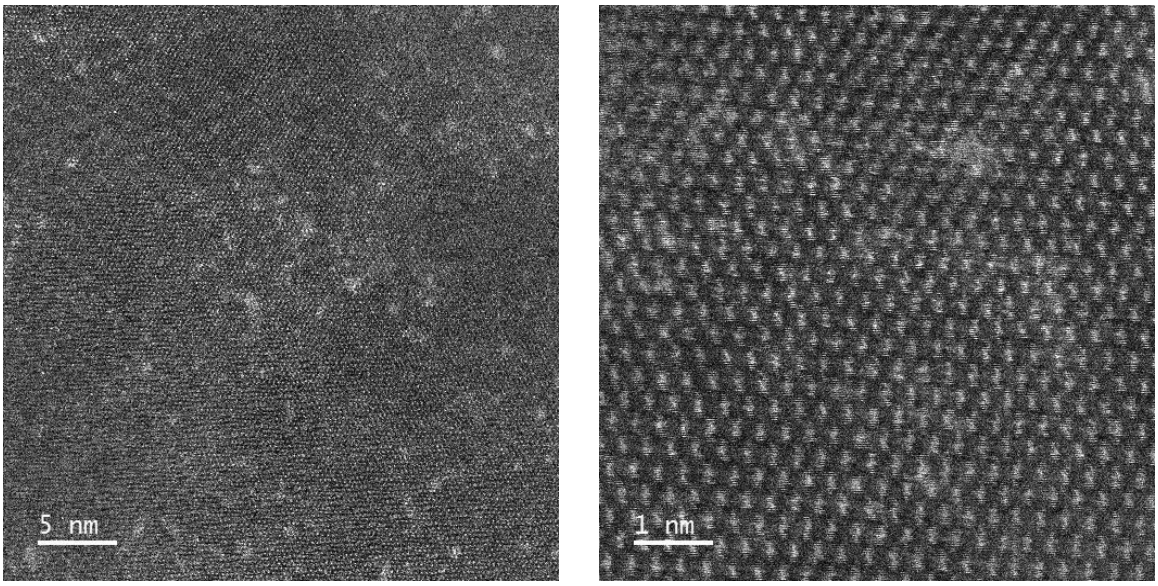

Figure 2.34. HAADF-STEM images of untreated MoS_2.

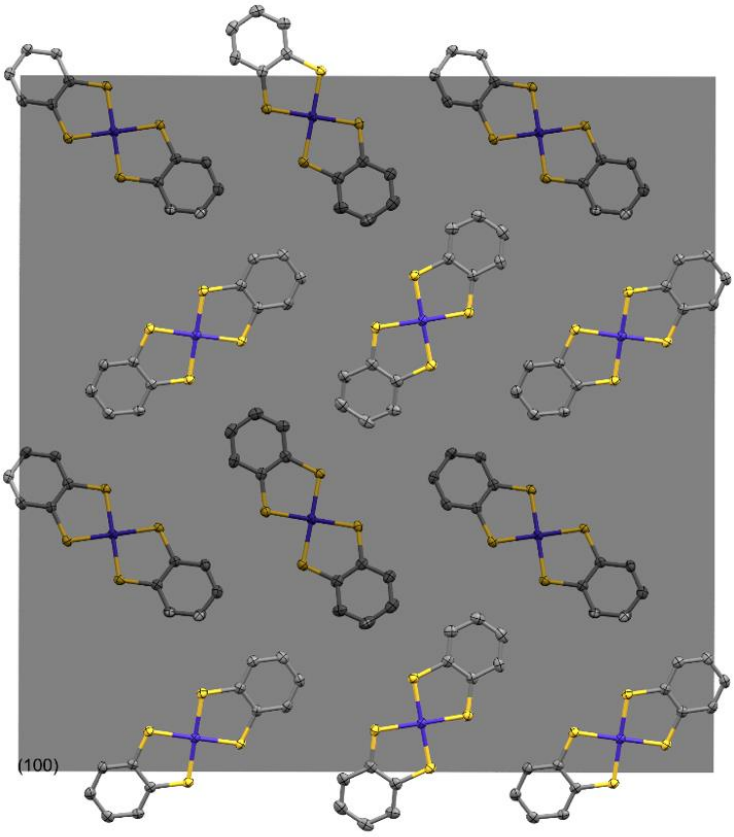

Figure 2.35. (100) slice of **Co** crystal with slice side length 32 Å in gray.

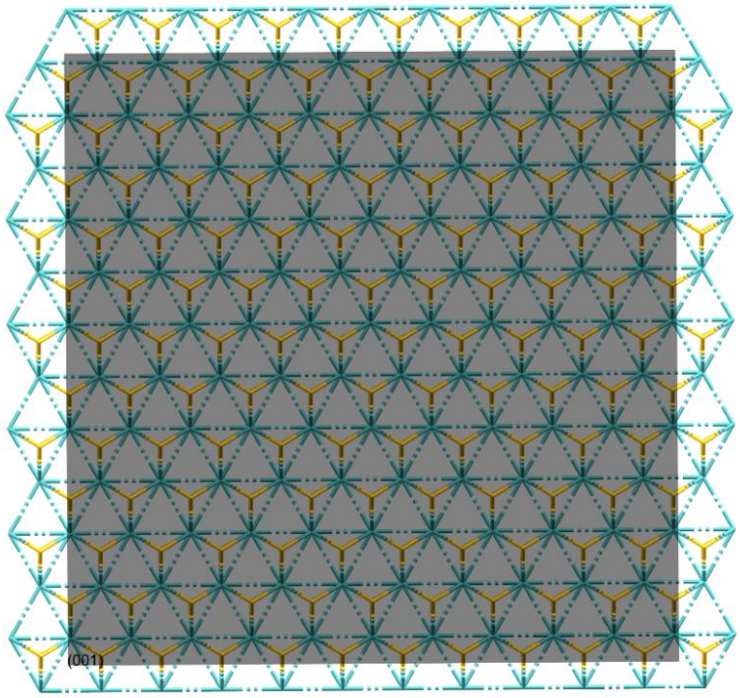

Figure 2.36. (001) slice of MoS_2 crystal with slice side length 32 Å in gray.

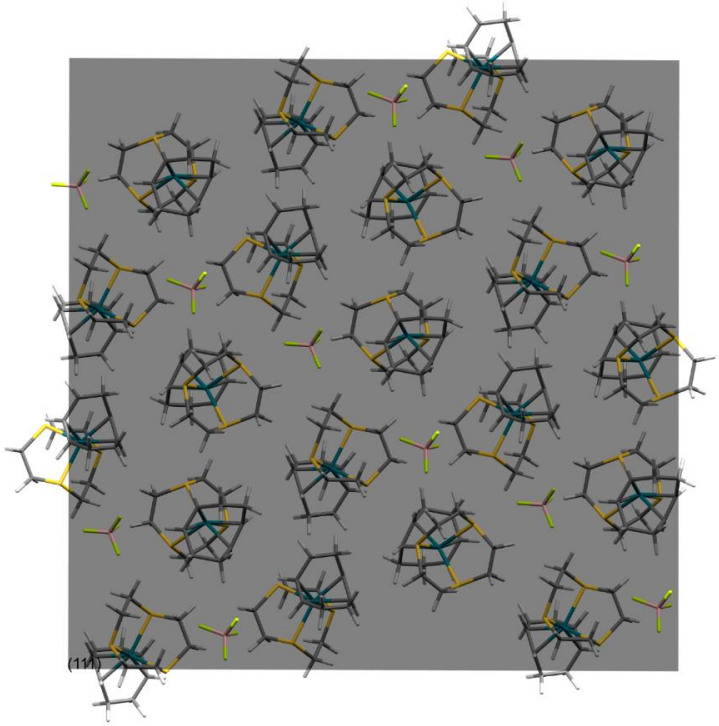

Figure 2.37. (111) slice of [Rh([9]aneS_3)(cod)][BF_4] crystal with slice side length 32 Å.

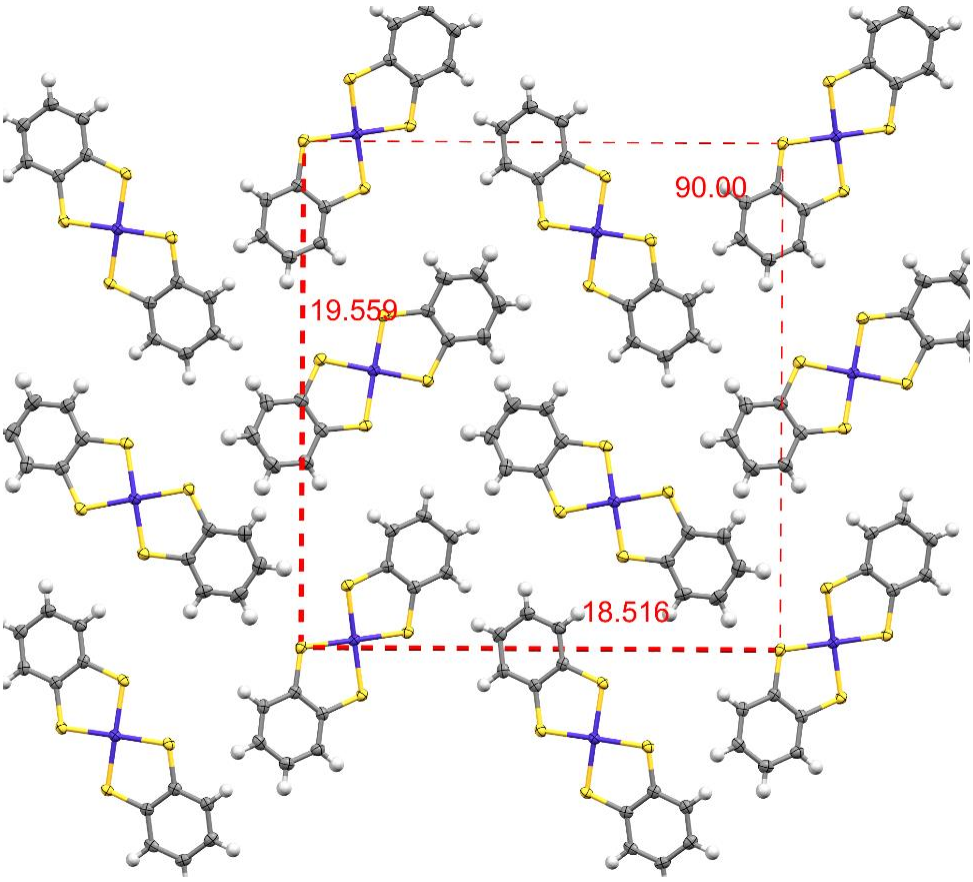

Figure 2.38. (100) slice of **Co** crystal showing unit cell packing used for estimated monolayer coverage.

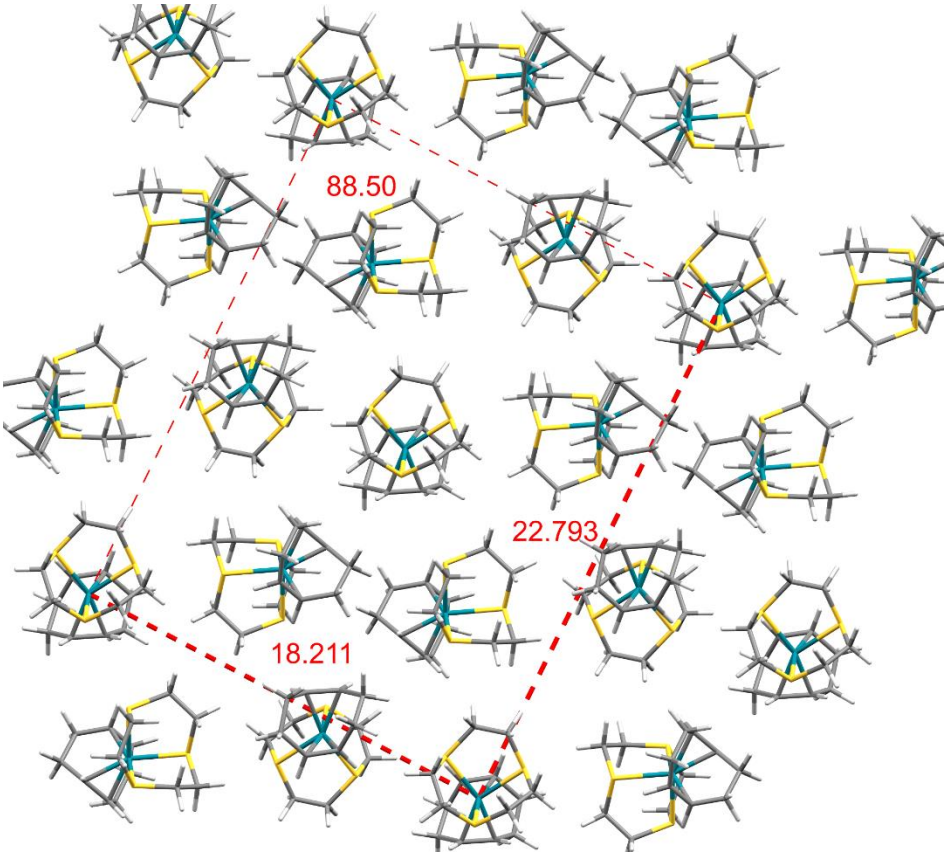

Figure 2.39. (111) slice of [Rh([9]aneS_3)(cod)][BF_4] crystal showing unit cell packing used for estimated monolayer coverage.

2.5 References.

1. Novoselov, K. S.; Geim, A. K.; Morozov, S. V.; Jiang, D.; Zhang, Y.; Dubonos, S. V.; Grigorieva, I. V.; Firsov, A. A. *Science* **2004**, *306*, 666-669.

2. Koppens, F. H. L.; Mueller, T.; Avouris, P.; Ferrari, A. C.; Vitiello, M. S.; Polini, M. *Nature Nanotechnology* **2014**, *9*, 780-793.

3. Xu, X.; Yao, W.; Xiao, D.; Heinz, T. F. *Nature Physics* **2014**, *10*, 343-350.

4. Mak, K. F.; Shan, J. *Nature Photonics* **2016**, *10*, 216-226.

5. Manzeli, S.; Ovchinnikov, D.; Pasquier, D.; Yazyev, O. V.; Kis, A. *Nature Reviews Materials* **2017**, *2*, 17033.

6. Chowdhury, T.; Sadler, E. C.; Kempa, T. J. *Chemical Reviews* **2020**, *120*, 12563-12591.

7. Novoselov, K. S.; Mishchenko, A.; Carvalho, A.; Castro Neto, A. H. *Science* **2016**, *353*.

8. Gibertini, M.; Koperski, M.; Morpurgo, A. F.; Novoselov, K. S. *Nature Nanotechnology* **2019**, *14*, 408-419.

9. Dickinson, R. G.; Pauling, L. *Journal of the American Chemical Society* **1923**, *45*, 1466-1471.

10. Wilson, J. A.; Yoffe, A. D. *Advances in Physics* **1969**, *18*, 193-335.

11. Liu, Y.; Weiss, N. O.; Duan, X.; Cheng, H.-C.; Huang, Y.; Duan, X. *Nature Reviews Materials* **2016**, *1*, 16042.

12. Duong, D. L.; Yun, S. J.; Lee, Y. H. *ACS Nano* **2017**, *11*, 11803-11830.

13. Geim, A. K.; Grigorieva, I. V. *Nature* **2013**, *499*, 419-425.

14. Kaasbjerg, K.; Thygesen, K. S.; Jacobsen, K. W. *Physical Review B* **2012**, *85*, 115317.

15. Li, X.; Mullen, J. T.; Jin, Z.; Borysenko, K. M.; Buongiorno Nardelli, M.; Kim, K. W. *Physical Review B* **2013**, *87*, 115418.

16. Kamins, T. I. *Journal of Applied Physics* **1971**, *42*, 4357-4365.

17. Zhang, W.; Chuu, C.-P.; Huang, J.-K.; Chen, C.-H.; Tsai, M.-L.; Chang, Y.-H.; Liang, C.-T.; Chen, Y.-Z.; Chueh, Y.-L.; He, J.-H.; et al. *Scientific Reports* **2014**, *4*, 3826.

18. Roy, K.; Padmanabhan, M.; Goswami, S.; Sai, T. P.; Ramalingam, G.; Raghavan, S.; Ghosh, A. *Nature Nanotechnology* **2013**, *8*, 826-830.

19. Yin, Z.; Li, H.; Li, H.; Jiang, L.; Shi, Y.; Sun, Y.; Lu, G.; Zhang, Q.; Chen, X.; Zhang, H. *ACS Nano* **2012**, *6*, 74-80.

20. Lopez-Sanchez, O.; Lembke, D.; Kayci, M.; Radenovic, A.; Kis, A. *Nature Nanotechnology* **2013**, *8*, 497-501.

21. Mak, K. F.; McGill, K. L.; Park, J.; McEuen, P. L. *Science* **2014**, *344*, 1489-1492.

22. Mai, C.; Barrette, A.; Yu, Y.; Semenov, Y. G.; Kim, K. W.; Cao, L.; Gundogdu, K. *Nano Letters* **2014**, *14*, 202-206.

23. Wu, S.; Ross, J. S.; Liu, G.-B.; Aivazian, G.; Jones, A.; Fei, Z.; Zhu, W.; Xiao, D.; Yao, W.; Cobden, D.; et al. *Nature Physics* **2013**, *9*, 149-153.

24. Salehzadeh, O.; Djavid, M.; Tran, N. H.; Shih, I.; Mi, Z. *Nano Letters* **2015**, *15*, 5302-5306.

25. Ye, Y.; Wong, Z. J.; Lu, X.; Ni, X.; Zhu, H.; Chen, X.; Wang, Y.; Zhang, X. *Nature Photonics* **2015**, *9*, 733-737.

26. Wu, S.; Buckley, S.; Schaibley, J. R.; Feng, L.; Yan, J.; Mandrus, D. G.; Hatami, F.; Yao, W.; Vučković, J.; Majumdar, A.; et al. *Nature* **2015**, *520*, 69-72.

27. Stephenson, T.; Li, Z.; Olsen, B.; Mitlin, D. *Energy & Environmental Science* **2014**, *7*, 209-231.

28. Radisavljevic, B.; Radenovic, A.; Brivio, J.; Giacometti, V.; Kis, A. *Nature Nanotechnology* **2011**, *6*, 147-150.

29. Wu, F.; Tian, H.; Shen, Y.; Hou, Z.; Ren, J.; Gou, G.; Sun, Y.; Yang, Y.; Ren, T.-L. *Nature* **2022**, *603*, 259-264.

30. Lembke, D.; Kis, A. *ACS Nano* **2012**, *6*, 10070-10075.

31. Desai, S. B.; Madhvapathy, S. R.; Sachid, A. B.; Llinas, J. P.; Wang, Q.; Ahn, G. H.; Pitner, G.; Kim, M. J.; Bokor, J.; Hu, C.; et al. *Science* **2016**, *354*, 99-102.

32. Deng, D.; Novoselov, K. S.; Fu, Q.; Zheng, N.; Tian, Z.; Bao, X. *Nature Nanotechnology* **2016**, *11*, 218-230.

33. Wang, Y.; Mao, J.; Meng, X.; Yu, L.; Deng, D.; Bao, X. *Chemical Reviews* **2019**, *119*, 1806-1854.

34. Chia, X.; Pumera, M. *Nature Catalysis* **2018**, *1*, 909-921.

35. Padgaonkar, S.; Amsterdam, S. H.; Bergeron, H.; Su, K.; Marks, T. J.; Hersam, M. C.; Weiss, E. A. *The Journal of Physical Chemistry C* **2019**, *123*, 13337-13343.

36. Mutz, N.; Park, S.; Schultz, T.; Sadofev, S.; Dalgleish, S.; Reissig, L.; Koch, N.; List-Kratochvil, E. J. W.; Blumstengel, S. *The Journal of Physical Chemistry C* **2020**, *124*, 2837-2843.

37. Kwon, I. S.; Kwak, I. H.; Kim, J. Y.; Abbas, H. G.; Debela, T. T.; Seo, J.; Cho, M. K.; Ahn, J.-P.; Park, J.; Kang, H. S. *Nanoscale* **2019**, *11*, 14266-14275.

38. Park, J. H.; Sanne, A.; Guo, Y.; Amani, M.; Zhang, K.; Movva, H. C. P.; Robinson, J. A.; Javey, A.; Robertson, J.; Banerjee, S. K.; et al. *Science Advances* **2017**, *3*, e1701661.

39. Huang, Y.; Zhuge, F.; Hou, J.; Lv, L.; Luo, P.; Zhou, N.; Gan, L.; Zhai, T. *ACS Nano* **2018**, *12*, 4062-4073.

40. Cincotti, S.; Rabe, J. P. *Applied Physics Letters* **1993**, *62*, 3531-3533.

41. Davis, T. C.; Russell, S. R.; Claridge, S. A. *Chemical Communications* **2018**, *54*, 11709-11712.

42. Bertolazzi, S.; Gobbi, M.; Zhao, Y.; Backes, C.; Samorì, P. *Chemical Society Reviews* **2018**, *47*, 6845-6888.

43. García-Dalí, S.; Paredes, J. I.; Villar-Rodil, S.; Martínez-Jódar, A.; Martínez-Alonso, A.; Tascón, J. M. D. *ACS Applied Materials & Interfaces* **2021**, *13*, 33157-33171.

44. Ippolito, S.; Ciesielski, A.; Samorì, P. *Chemical Communications* **2019**, *55*, 8900-8914.

45. Canton-Vitoria, R.; Gobeze, H. B.; Blas-Ferrando, V. M.; Ortiz, J.; Jang, Y.; Fernández-Lázaro, F.; Sastre-Santos, Á.; Nakanishi, Y.; Shinohara, H.; D'Souza, F.; et al. *Angewandte Chemie International Edition* **2019**, *58*, 5712-5717.

46. Li, D. O.; Chu, X. S.; Wang, Q. H. *Langmuir* **2019**, *35*, 5693-5701.

47. Daukiya, L.; Teyssandier, J.; Eyley, S.; El Kazzi, S.; Rodríguez González, M. C.; Pradhan, B.; Thielemans, W.; Hofkens, J.; De Feyter, S. *Nanoscale* **2021**, *13*, 2972-2981.

48. Chen, X.; Bartlam, C.; Lloret, V.; Moses Badlyan, N.; Wolff, S.; Gillen, R.; Stimpel-Lindner, T.; Maultzsch, J.; Duesberg, G. S.; Knirsch, K. C.; et al. *Angewandte Chemie International Edition* **2021**, *60*, 13484-13492.

49. Vera-Hidalgo, M.; Giovanelli, E.; Navío, C.; Pérez, E. M. *Journal of the American Chemical Society* **2019**, *141*, 3767-3771.

50. Chen, X.; Berner, N. C.; Backes, C.; Duesberg, G. S.; McDonald, A. R. *Angewandte Chemie International Edition* **2016**, *55*, 5803-5808.

51. Karunakaran, S.; Pandit, S.; Basu, B.; De, M. *Journal of the American Chemical Society* **2018**, *140*, 12634-12644.

52. Canton-Vitoria, R.; Sayed-Ahmad-Baraza, Y.; Pelaez-Fernandez, M.; Arenal, R.; Bittencourt, C.; Ewels, C. P.; Tagmatarchis, N. *npj 2D Materials and Applications* **2017**, *1*, 13.

53. Liu, H.; Grasseschi, D.; Dodda, A.; Fujisawa, K.; Olson, D.; Kahn, E.; Zhang, F.; Zhang, T.; Lei, Y.; Branco, R. B. N.; et al. *Science Advances* **2020**, *6*, eabc9308.

54. Backes, C.; Berner, N. C.; Chen, X.; Lafargue, P.; LaPlace, P.; Freeley, M.; Duesberg, G. S.; Coleman, J. N.; McDonald, A. R. *Angewandte Chemie International Edition* **2015**, *54*, 2638-2642.

55. Liu, H.; Silva, W. C.; Santana Gonçalves de Souza, L.; Veiga, A. G.; Seixas, L.; Fujisawa, K.; Kahn, E.; Zhang, T.; Zhang, F.; Yu, Z.; et al. *Nanoscale* **2022**, *14*, 10801-10815.

56. Li, H.; Wu, J.; Yin, Z.; Zhang, H. *Accounts of Chemical Research* **2014**, *47*, 1067-1075.

57. Chhowalla, M.; Shin, H. S.; Eda, G.; Li, L.-J.; Loh, K. P.; Zhang, H. *Nature Chemistry* **2013**, *5*, 263-275.

58. Eda, G.; Yamaguchi, H.; Voiry, D.; Fujita, T.; Chen, M.; Chhowalla, M. *Nano Letters* **2011**, *11*, 5111-5116.

59. Zeng, Z.; Yin, Z.; Huang, X.; Li, H.; He, Q.; Lu, G.; Boey, F.; Zhang, H. *Angewandte Chemie International Edition* **2011**, *50*, 11093-11097.

60. Coleman, J. N.; Lotya, M.; O'Neill, A.; Bergin, S. D.; King, P. J.; Khan, U.; Young, K.; Gaucher, A.; De, S.; Smith, R. J.; et al. *Science* **2011**, *331*, 568-571.

61. Fan, X.; Xu, P.; Li, Y. C.; Zhou, D.; Sun, Y.; Nguyen, M. A. T.; Terrones, M.; Mallouk, T. E. *Journal of the American Chemical Society* **2016**, *138*, 5143-5149.

62. Ponomarev, E.; Pásztor, Á.; Waelchli, A.; Scarfato, A.; Ubrig, N.; Renner, C.; Morpurgo, A. F. *ACS Nano* **2018**, *12*, 2669-2676.

63. *MoS_2 Crystal Structure: Datasheet*; Springer-Verlag Berlin Heidelberg & Material Phases Data System (MPDS), Switzerland & National Institute for Materials Science (NIMS), Japan: https://materials.springer.com/isp/crystallographic/docs/sd_0453841.

64. McNamara, W. R.; Han, Z.; Alperin, P. J.; Brennessel, W. W.; Holland, P. L.; Eisenberg, R. *Journal of the American Chemical Society* **2011**, *133*, 15368-15371.

65. McNamara, W. R.; Han, Z.; Yin, C.-J.; Brennessel, W. W.; Holland, P. L.; Eisenberg, R. *Proceedings of the National Academy of Sciences* **2012**, *109*, 15594-15599.

66. Eady, S. C.; MacInnes, M. M.; Lehnert, N. *Inorganic Chemistry* **2017**, *56*, 11654-11667.

67. Clough, A. J.; Yoo, J. W.; Mecklenburg, M. H.; Marinescu, S. C. *Journal of the American Chemical Society* **2015**, *137*, 118-121.

68. Downes, C. A.; Marinescu, S. C. *Journal of the American Chemical Society* **2015**, *137*, 13740-13743.

69. Dance, I. G.; Miller, T. R. *Inorganic Chemistry* **1974**, *13*, 525-535.

70. Balch, A. L.; Dance, I. G.; Holm, R. H. *Journal of the American Chemical Society* **1968**, *90*, 1139-1145.

71. Hinnemann, B.; Moses, P. G.; Bonde, J.; Jørgensen, K. P.; Nielsen, J. H.; Horch, S.; Chorkendorff, I.; Nørskov, J. K. *Journal of the American Chemical Society* **2005**, *127*, 5308-5309.

72. Kibsgaard, J.; Chen, Z.; Reinecke, B. N.; Jaramillo, T. F. *Nature Materials* **2012**, *11*, 963-969.

73. Li, Y.; Wang, H.; Xie, L.; Liang, Y.; Hong, G.; Dai, H. *Journal of the American Chemical Society* **2011**, *133*, 7296-7299.

74. Pearson, R. G. *Journal of the American Chemical Society* **1963**, *85*, 3533-3539.

75. Green, M.; Kuc, T. A.; Taylor, S. H. *Journal of the Chemical Society D: Chemical Communications* **1970**, 1553-1554.

76. Ikeda, S.; Hanamura, Y.; Tada, H.; Shintani, R. *Journal of the American Chemical Society* **2021**, *143*, 19559-19566.

77. Lichosyt, D.; Zhang, Y.; Hurej, K.; Dydio, P. *Nature Catalysis* **2019**, *2*, 114-122.

78. Nambo, M.; Noyori, R.; Itami, K. *Journal of the American Chemical Society* **2007**, *129*, 8080-8081.

79. Burrows, A. D.; Green, M.; Jeffery, J. C.; Lynam, J. M.; Mahon, M. F. *Angewandte Chemie International Edition* **1999**, *38*, 3043-3045.

80. Duursma, A.; Boiteau, J.-G.; Lefort, L.; Boogers, J. A. F.; de Vries, A. H. M.; de Vries, J. G.; Minnaard, A. J.; Feringa, B. L. *The Journal of Organic Chemistry* **2004**, *69*, 8045-8052.

81. Li, Z.; Chen, Y.; Ji, S.; Tang, Y.; Chen, W.; Li, A.; Zhao, J.; Xiong, Y.; Wu, Y.; Gong, Y.; et al. *Nature Chemistry* **2020**, *12*, 764-772.

82. Zhao, J.; Ji, S.; Guo, C.; Li, H.; Dong, J.; Guo, P.; Wang, D.; Li, Y.; Toste, F. D. *Nature Catalysis* **2021**, *4*, 523-531.

83. Hülsey, M. J.; Zhang, B.; Ma, Z.; Asakura, H.; Do, D. A.; Chen, W.; Tanaka, T.; Zhang, P.; Wu, Z.; Yan, N. *Nature Communications* **2019**, *10*, 1330.

84. Lang, R.; Li, T.; Matsumura, D.; Miao, S.; Ren, Y.; Cui, Y.-T.; Tan, Y.; Qiao, B.; Li, L.; Wang, A.; et al. *Angewandte Chemie International Edition* **2016**, *55*, 16054-16058.

85. Kwon, Y.; Kim, T. Y.; Kwon, G.; Yi, J.; Lee, H. *Journal of the American Chemical Society* **2017**, *139*, 17694-17699.

86. Lei, Z.; Cai, W.; Rao, Y.; Wang, K.; Jiang, Y.; Liu, Y.; Jin, X.; Li, J.; Lv, Z.; Jiao, S.; et al. *Nature Communications* **2022**, *13*, 24.

87. Xiao, M.; Zhu, J.; Li, G.; Li, N.; Li, S.; Cano, Z. P.; Ma, L.; Cui, P.; Xu, P.; Jiang, G.; et al. *Angewandte Chemie International Edition* **2019**, *58*, 9640-9645.

88. Blake, A. J.; Halcrow, M. A.; Schröder, M. *Journal of the Chemical Society, Chemical Communications* **1991**, 253-256.

89. Lee, C.; Yan, H.; Brus, L. E.; Heinz, T. F.; Hone, J.; Ryu, S. *ACS Nano* **2010**, *4*, 2695-2700.

90. Petrenko, T.; Ray, K.; Wieghardt, K. E.; Neese, F. *Journal of the American Chemical Society* **2006**, *128*, 4422-4436.

91. Chakraborty, B.; Bera, A.; Muthu, D. V. S.; Bhowmick, S.; Waghmare, U. V.; Sood, A. K. *Physical Review B* **2012**, *85*, 161403.

92. Qi, L.; Wang, Y.; Shen, L.; Wu, Y. *Applied Physics Letters* **2016**, *108*, 063103.

93. Siao, M. D.; Shen, W. C.; Chen, R. S.; Chang, Z. W.; Shih, M. C.; Chiu, Y. P.; Cheng, C. M. *Nature Communications* **2018**, *9*, 1442.

94. Briggs, D. C. D. W., W. M. Riggs, L. E. Davis, J. F. Moulder and G. E.Muilenberg. *Surface and Interface Analysis* **1981**, *3*.

95. Li, Z.; Wang, Y.; Kozbial, A.; Shenoy, G.; Zhou, F.; McGinley, R.; Ireland, P.; Morganstein, B.; Kunkel, A.; Surwade, S. P.; et al. *Nature Materials* **2013**, *12*, 925-931.

96. Li, Z.; Kozbial, A.; Nioradze, N.; Parobek, D.; Shenoy, G. J.; Salim, M.; Amemiya, S.; Li, L.; Liu, H. *ACS Nano* **2016**, *10*, 349-359.

97. Kurokawa, A.; Odaka, K.; Azuma, Y.; Fujimoto, T.; Kojima, I. *Journal of Surface Analysis* **2009**, *15*, 337-340.

98. Kang, K.; Xie, S.; Huang, L.; Han, Y.; Huang, P. Y.; Mak, K. F.; Kim, C.-J.; Muller, D.; Park, J. *Nature* **2015**, *520*, 656-660.

99. Ray, K.; DeBeer George, S.; Solomon, E. I.; Wieghardt, K.; Neese, F. *Chemistry – A European Journal* **2007**, *13*, 2783-2797.

100. Borod'ko, Y. G.; Vetchinkin, S. I.; Zimont, S. L.; Ivleva, I. N.; Shul'ga, Y. M. *Chemical Physics Letters* **1976**, *42*, 264-267.

101. Amsterdam, S. H.; Stanev, T. K.; Zhou, Q.; Lou, A. J. T.; Bergeron, H.; Darancet, P.; Hersam, M. C.; Stern, N. P.; Marks, T. J. *ACS Nano* **2019**, *13*, 4183-4190.

102. Meißner, A.; König, A.; Drexler, H.-J.; Thede, R.; Baumann, W.; Heller, D. *Chemistry – A European Journal* **2014**, *20*, 14721-14728.

103. Addou, R.; Colombo, L.; Wallace, R. M. *ACS Applied Materials & Interfaces* **2015**, *7*, 11921-11929.

104. Bernett, M. K.; Zisman, W. A. *The Journal of Physical Chemistry* **1970**, *74*, 2309-2312.

105. Zubkov, T.; Stahl, D.; Thompson, T. L.; Panayotov, D.; Diwald, O.; Yates, J. T. *The Journal of Physical Chemistry B* **2005**, *109*, 15454-15462.

106. Choi, K.; Eom, T.-J.; Lee, C. *Thin Solid Films* **2003**, *435*, 227-231.

107. Boinovich, L. B.; Emelyanenko, A. M.; Pashinin, A. S.; Lee, C. H.; Drelich, J.; Yap, Y. K. *Langmuir* **2012**, *28*, 1206-1216.

108. Tang, Q.; Jiang, D.-e. *Chemistry of Materials* **2015**, *27*, 3743-3748.

109. Rodman, G. S.; Mann, K. R. *Inorganic Chemistry* **1988**, *27*, 3338-3346.

110. Day, V. W.; Klemperer, W. G.; Main, D. J. *Inorganic Chemistry* **1990**, *29*, 2345-2355.

111. Fairley, N.; Fernandez, V.; Richard-Plouet, M.; Guillot-Deudon, C.; Walton, J.; Smith, E.; Flahaut, D.; Greiner, M.; Biesinger, M.; Tougaard, S.; et al. *Applied Surface Science Advances* **2021**, *5*, 100112.

CHAPTER 3

Metal– and Multiply Bonded Ligand–Dependent Properties of Isoelectronic Photochemical Super-Reductants

3.1. Introduction

Photoredox catalysis has undergone a resurgence over the past 15 years because it has shown great promise in accessing difficult chemical transformations relevant for organic synthesis and renewable chemistry.[1-4] These reactions utilize a chromophore that absorbs light to form an excited-state sufficiently long lived to engage in a subsequent electron-transfer reaction with a substrate or sacrificial redox partner, allowing direct utilization of the energy of a photon to drive chemical reactions. Within the visible light range of excitation, chromophores can convert up to roughly 3 eV (69 kcal/mol) of driving force from photoexcitation, allowing reactions that are strongly uphill in the ground state to be accessible. This has allowed a variety of chemical reactions to be developed stemming from the initial activation of the substrate by the photocatalyst. The ability to access these reactions with light is particularly attractive since light sources are relatively cheap and abundant for most practical applications, allowing widespread use without specialized equipment.

Many commonly used visible-light photocatalysts are transition-metal complexes.[1] This is due to their long excited-state lifetimes, strong absorption in the visible region, and reversible one-electron redox chemistry.[5] The long excited-state lifetimes are especially important for facilitating excited-state single-electron transfer and arise from the large spin-orbit coupling of the transition-metal center. This facilitates rapid intersystem-crossing from the singlet to the triplet manifold, which then requires spin-forbidden relaxation from the excited triplet state to

the singlet ground state leading to long excited-state lifetimes. While many complexes are not strongly reducing or oxidizing in the ground-state, upon photoexcitation they can become potent single-electron-transfer reagents in which the increase in driving force is directly related to the energy of the excited-state (Figure 3.1). For a photoreductant, this is encapsulated by the Rehm-Weller Approximation: $E^{*/+} = E^{0/+} - E_{00}$ for excited-state reductants and $E^{*/-} = E^{0/-} + E_{00}$ for excited-state oxidants.[6] From this relationship, it becomes clear that to attain a more reducing photoreductant, one must increase E_{00} and/or decrease $E^{0/+}$. For highly reducing visible light photocatalysts (> −3.0 V), simply raising E_{00} will reach a limit using blue light excitation (~3 eV) at which point the excited-state potential will be limited by the ground-state oxidation potential. Visible-light excitation is preferred over UV light excitation because competitive UV absorption by the substrate can result in nonselective photocatalysis and detrimental side products leading to lower yields.[7-8] The alternative would be to use photocatalysts with a more reducing ground state such that efficient photoexcitation can be achieved with lower energy green or red light.

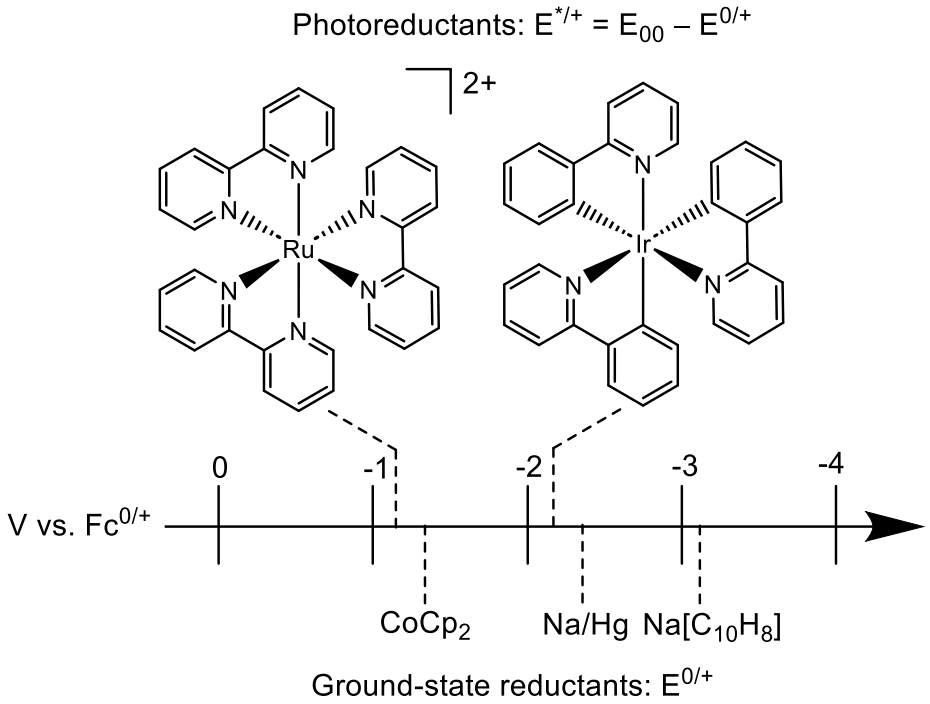

Figure 3.1. Potentials accessible from common ground-state and excited-state reductants.

Highly reducing photocatalysts are desirable due to their ability to activate a variety of foundational precursor molecules such as aryl halides.[9-12] Upon reduction of the latter, loss of halide forms an aryl radical that can react to form a variety of aryl functionalized products.[13-14] The challenge associated with most aryl halides is their highly negative one-electron reduction potentials. The most easily reduced simple aryl halide is iodobenzene, which is reduced at −2.69 V vs. $FeCp_2^{0/+}$.[14] Putting this in context with the redox potentials of the extensively used photoreducing *fac*-$Ir(ppy)_3$ chromophore, the $PhI^{0/-}$ couple is 0.46 V negative of the excited-state oxidation potential of *fac*-$Ir(ppy)_3$ (−2.23 V vs. $FeCp_2^{0/+)}$ and equal to the ground-state oxidation potential of *fac*-$Ir(ppy)_3^-$ (−2.69 V vs. $FeCp_2^{0/+}$), which is produced in situ upon excitation in the presence of a sacrificial reductant.[1] For the cheaper and more desirable substrate chlorobenzene, the reduction potential is −3.25 V vs. $FeCp_2^{0/+}$.[14] This presents a high barrier for activation for even the strongest of photoreductants. Therefore, understanding and designing strongly reducing

photocatalysts that can be accessed using visible light is highly desirable for economical use of photoredox catalysis.

Our group has recently developed tungsten benzylidyne complexes of the general form $W(CAr)L_4X$ (Ar = aryl, L = neutral ligand such as phosphine, X = halide or other anionic ligand) as a class of highly reducing photoredox catalysts.[15] These complexes possess a d^2 tungsten center axially supported by a triply bonded benzylidyne trans to a halide or pseudohalide and equatorially supported by four phosphine ligands (Figure 3.2). The benzylidyne ligand provides a strong axial ligand field that separates the d_{xy} HOMO from the rest of the d orbital manifold.[16-17] The interaction between the d_{xz} and d_{yz} orbitals and alkylidyne carbon p orbitals produces π(WC) and π*(WC) orbitals that are further split by the π-orbital plane of the phenyl group to give a set of phenyl-conjugated π(WCPh) HOMO–1 π*(WCPh) and LUMO orbitals that are well separated from the d_{xy} HOMO. This orbital splitting results in symmetry-orthogonal HOMO and LUMO orbitals of a_1 and b_1 symmetry, respectively (Figure 3.2). The lowest-lying electronic transition is a dipole-allowed HOMO and LUMO transition. The initially produced $^1[d_{xy} \rightarrow \pi^*]$ excited state undergoes fast intersystem crossing due to the influence of the large spin–orbit coupling of tungsten to produce a long-lived luminescent $^3[d_{xy} \rightarrow \pi^*]$ state. The orthogonal symmetry and parentage of the HOMO and LUMO orbitals allow independent energetic tuning of each orbital by peripheral substitution. This, in combination with the highly reducing nature of the d^2 tungsten center, presents a highly modular system in which to study and design highly reducing photoredox catalysts.[18-21] Judicious choice of equatorial phosphine ligand and para-substitution of the benzylidyne have given photoredox catalysts with $E^{*/+}$ as negative as −3.26 V vs. $FeCp_2^{0/+}$ with a λ_{max} of 455 nm.[15]

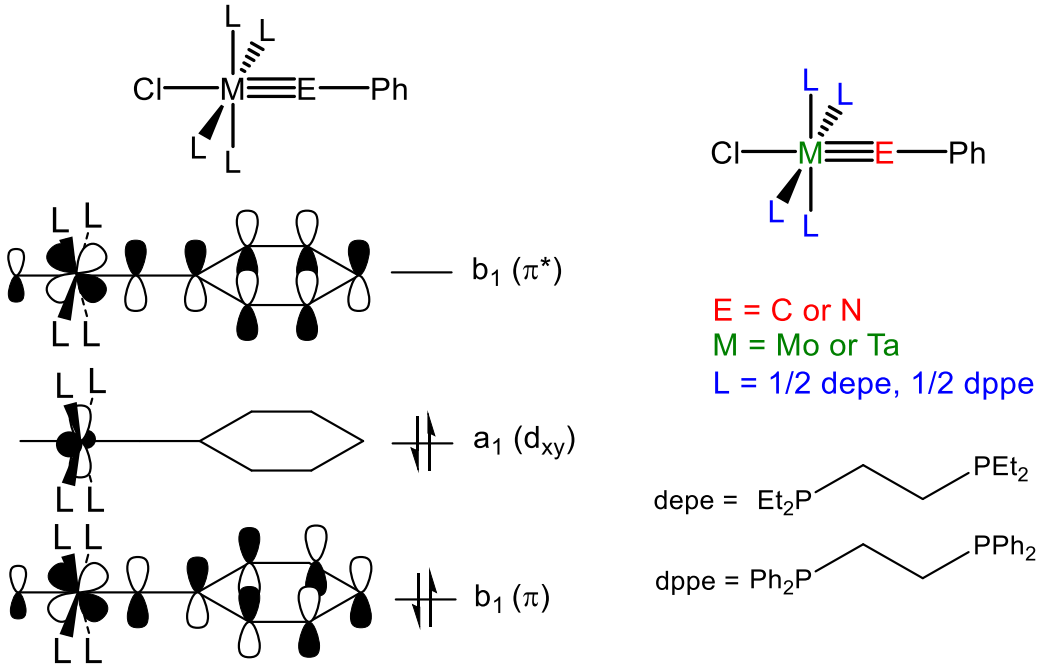

Figure 3.2. General molecular orbital diagram and structures for d^2 complexes studied here.

The purpose of the present study was to study the effect of perturbing the core of the metal–ligand triple bond on the properties of these chromophores. This has not been previously explored in any depth. Substitution of tungsten with the lighter group 6 element molybdenum should introduce electronic and photophysical differences arising solely from the metal center. The molybdenum 4d orbitals lie lower in energy than tungsten 5d orbitals, which one might expect to affect ground-state redox potentials and electronic transition energies. Further, the smaller spin–orbit coupling of Mo relative to W could affect intersystem crossing rates and other photophysical properties. While periodic trends among second and third row transition-metal chromophores are generally well understood,[5, 22] there are comparatively few experimental studies for how these trends influence emissive d-d transitions. [23-24] Many designs for third row transition-metal chromophores have been developed across the span of the transition metal series due to their generally better photophysical properties, but extending these designs to their second

row analogues can be challenging.[25-29] This has generally hampered development for these elements for which some advantages can include lower cost and increased availability. Some recent studies in the development of second row chromophores have highlighted the use of multidentate ligands to stabilize the excited-state leading to longer lifetimes and stable luminescence.[30-33] Similar benefits could be observed for molybdenum benzylidyne chromophores allowing study of this unique d-d transition. To this end, two molybdenum–alkylidyne complexes were prepared and studied (Figure 3.2): Mo(CPh)(dppe)$_2$Cl (**Mo1**; dppe = 1,2-bis(diphenylphosphino)ethane) and Mo(CPh)(depe)$_2$Cl (**Mo2**; depe = 1,2-bis(diethylphosphino)ethane)). These were compared with well-studied tungsten analogues W(CPh)(dppe)$_2$Cl (**W1**) and W(CPh)(depe)$_2$Cl (**W2**).[15, 19]

A second isoelectronic perturbation to the tungsten–carbon triply bonded core of these chromophores that was explored in this study involves moving laterally across the periodic table to a tantalum–nitrogen core. This is expected to dramatically perturb relative orbital energies both by going from tungsten to tantalum (raising energies) and from carbon to nitrogen (lowering energies). Tantalum-based photoredox chromophores are interesting due to tantalum's lower ionization potential compared to tungsten.[34] This should result in a more reducing ground state and therefore could allow access to even more reducing photocatalysts at a given excited-state energy. Nitrogen, on the other hand, has a higher electronegativity than carbon, indicating the possibility of a lower energy LUMO. The combination of the two should result in a more polarized metal-ligand triple bond that provides an interesting electronic comparison to the tungsten–alkylidyne. Very few mononuclear d^2 tantalum imido complexes have been isolated and their photophysics and electronic structure are similarly little studied.[35-36] This lies in contrast with d^0 tantalum–imido complexes whose electronic structures have been studied by multiple

groups[37-40] and have been shown to luminesce from a $^3[\pi \rightarrow d_{xy}]$ LMCT-like state that is orbitally related to the $^3[d_{xy} \rightarrow \pi^*]$ MLCT-like state from which the d^2 complexes emit. From this, a d^2 tantalum imido complexes may also exhibit luminescence at room temperature and may be able to access even higher excited-state reduction potentials beyond tungsten alkylidynes while providing a unique comparison of isoelectronic transition-metal multiple bonding across different periodic groups. For this purpose, two compounds of form similar to **Mo1** and **Mo2** were prepared: $Ta(NPh)(dppe)_2Cl$ (**Ta1**) and $Ta(NPh)(depe)_2Cl$ (**Ta2**).

In addition to study of the electronic structure and photophysics of these complexes, protonation of these complexes to form seven-coordinate d^0 hydride species of type $[M(EPh)(H)L_4Cl]^+$ was also of interest. This was motivated by the fact that formation of d^0 hydrides of this type have been implicated in photocatalytic reactions using tungsten–benzylidyne chromophores,[15] and because it has been found that d^1 tungsten alkylidynes react with dihydrogen to form the d^0 alkylidyne hydride complex, potentially providing a direct route to activate renewable reducing equivalents for photocatalysis.[41] These seven-coordinate d^0 alkylidyne hydride compounds are fluxional in solution. Tautomerization has been found where the basicity of the alkylidyne is sufficient to compete with metal-bound hydride species (Scheme 3.1),[41-45] resulting in an equilibrium between an alkylidene-like structure and the alkylidyne hydride. This equilibrium is delicate and can be influenced by simple perturbations such as steric bulk and choice of X ligand trans to the triple-bond, indicative of its sensitivity towards changes in electronic structure. A parallel study of the synthesis and structures of d^0 hydride species was conducted prepared from the molybdenum alkylidyne and tantalum imido species, allowing insight in the role of the metal and heteroatom on the thermodynamics of protonation and its potential role in the photoreactivity of these chromophores.

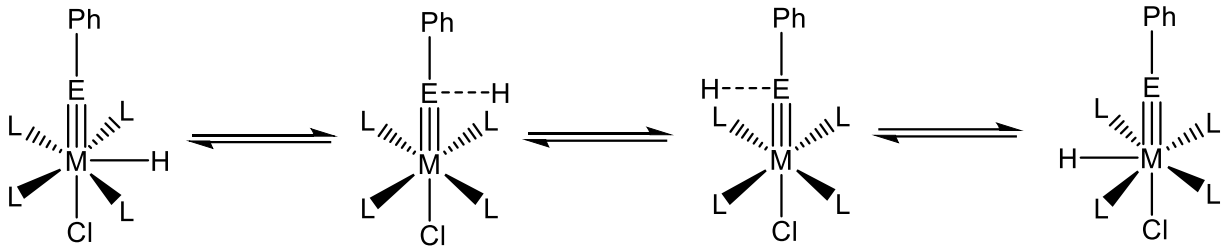

Scheme 3.1. Proposed tautomerization mechanism for d^0 hydride complexes.

3.2. Results and Discussion

3.2.1. Synthesis and Characterization of Mo(CPh)(P–P)$_2$Cl Complexes

The d^2 complexes **Mo1** and **Mo2** were synthesized via ligand substitution reactions from the labile precursor Mo(CPh){P(OMe)$_3$}$_4$Cl first reported by Mayr (Scheme 3.2).[46] Following that procedure, the complex Mo(CPh)(CO){P(OMe)$_3$}$_3$Cl was synthesized from the reaction between Mo{C(O)Ph}(CO)$_5$ and oxalyl chloride, which provides *in-situ* thermally unstable Mo(CPh)(CO)$_4$Cl, followed by addition of P(OMe)$_3$.[47] Rather than isolating this compound as per the published procedure, it was converted in a one-pot reaction to Mo(CPh){P(OMe)$_3$}$_4$Cl using a separate procedure described in that paper. The route used in our study combines the reported syntheses of the tris and tetrakis-phosphite complex into one route without isolation of the intermediate tris-phosphite compound. The final yield of Mo(CPh){P(OMe)$_3$}$_4$Cl is 34%, which is lower than the reported combined yield of the two-step synthesis (56%) but faster overall and can be conducted at multigram scales. This allows for convenient synthesis of the coordinatively labile Mo(CPh){P(OMe)$_3$}$_4$Cl in two simple steps from Mo(CO)$_6$.

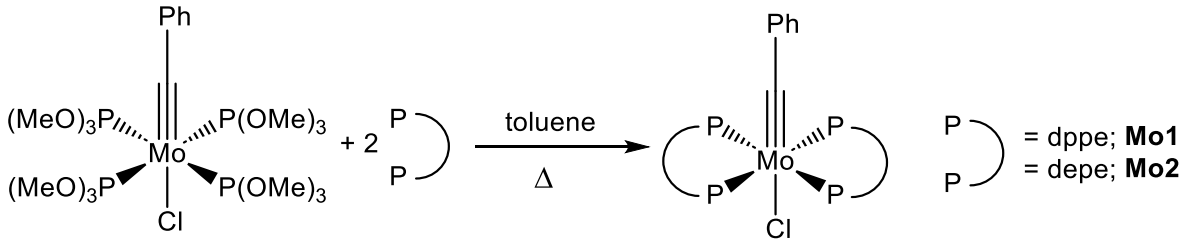

Scheme 3.2. Synthesis of **Mo1** and **Mo2.**

The chromophores **Mo1** and **Mo2** can be synthesized by simply refluxing Mo(CPh){P(OMe)$_3$}$_4$Cl with 2.1 equivalents of the corresponding bidentate phosphine in toluene. An immediate color change is visible upon addition of the phosphine, indicating facile substitution of phosphite ligands, but heating of the reaction mixture is necessary for full conversion to the desired complex. Isolation by filtration and recrystallization gives the final products in high yields as microcrystals. These complexes are stable at elevated temperatures and display only moderate air-sensitivity in solution with full decomposition occurring on the order of hours for **Mo2** and days for **Mo1**. **Mo2** is soluble in common organic solvents including pentane. **Mo1**, on the other hand, shows good solubility in THF and DCM, limited solubility in toluene, and is insoluble in acetonitrile, Et_2O and pentane.

Standard NMR and HRMS spectroscopic characterization were used to confirm the identity of the products. The ^{31}P, ^{1}H, and ^{13}C{^{1}H} NMR spectra of **Mo1** and **Mo2** show the expected resonances corresponding to their formulations. The chemical shifts and multiplet splitting are also close to their previously reported tungsten congeners and allows for facile assignment.[20, 48] The alkylidyne ^{13}C-NMR resonance for **Mo2** is found at 258.1 ppm as a quintet due to splitting by four equivalent phosphorus nuclei. The low solubility of **Mo1** prevented observation of the alkylidyne ^{13}C resonance even with saturated solutions and collection over

multiple hours. HRMS provided molecular weights for these complexes that matched their expected formulation and confirms the identity of these complexes.

3.2.2. Synthesis and Characterization of Ta(NPh)(P–P)$_2$Cl Complexes.

The new tantalum complexes **Ta1** and **Ta2** were synthesized following the general method for Ta(NPh)L$_4$Cl compounds reported by Schrock (Scheme 3.3).[35-36] Briefly, Ta(NPh)(dme)Cl$_3$ is stirred with 2.1 equivalents of the appropriate bidentate phosphine in THF at room temperature for one hour. This forms a cloudy yellow precipitate that is presumed to be a cationic tantalum imido phosphine complex. The final yield of product is improved by stirring this solution before addition of the reductant, with 1–2 hours found to be optimal depending on the phosphine steric bulk. This is similar to observations for the reduction of tungsten d^0 alkylidynes to d^2 complexes.[44] The rate of this initial complexation appears to be dependent on the donor strength and/or steric bulk of the phosphine. For depe, nearly immediate formation of the precipitate is observed upon addition of the phosphine, whereas for dppe precipitate only begins to visibly form 15 minutes after addition. Cooling this suspension to −30 ˚C before addition of 0.4 wt% Na/Hg was also found to be critical for good yield. Upon addition, the suspension gradually dissolves to form the product, which can then be isolated in pure form upon filtration and crystallization.

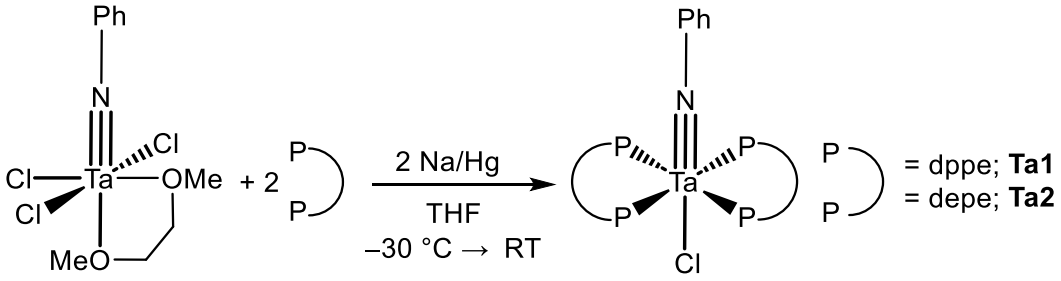

Scheme 3.3. Synthesis of **Ta1** and **Ta2.**

Both complexes are very air sensitive and rapidly decompose upon exposure to air or moisture. Complex **Ta2** is not stable at room temperature and decomposes slowly even in the solid state at −30 ˚C to form free depe and an uncharacterized grey powder over the course of a month. Decomposition occurs more readily in polar solvents such as THF, which necessitated workup and crystallization in Et_2O and pentane. Complex **Ta1** is relatively more stable and was observed to undergo slow decomposition at room temperature over the course of two months. For comparison, the dmpe complex reported by Schrock and coworkers was also synthesized and found to decompose in the solid-state at an even faster rate than that of the depe complex.[35] While the mechanism of decomposition for these complexes is unclear, increased steric bulk of the phosphine does seem to increase the stability of these complexes, with stability decreasing from dppe>depe>dmpe. It is likely that the instability of these complexes is due to the highly nucleophilic and reducing nature of the Ta(III) center. Attempts to synthesize $Ta(NPh)\{P(OMe)_3\}_4Cl$ via this route were unsuccessful with only intractable mixtures being formed following reduction. Complex **Ta2** was found to very soluble in common organic solvents, but rapid decomposition was observed in DCM. Complex **Ta1** is soluble and stable in common solvents such as THF, DCM, and toluene, but was oddly completely insoluble in acetonitrile and slightly soluble in Et_2O.

3.2.3. Molecular Structures of the Mo and Ta Chromophores.

The molecular structures of **Mo1**, **Mo2**, **Ta1**, and **Ta2** were determined using single-crystal X-ray diffraction studies. Both molybdenum complexes exhibit pseudo-tetragonal geometries with the phenyl plane of the benzylidyne oriented such that the plane splits the phosphine backbone to minimize steric clash with the other substituents on the phosphine (Figure 3.3). No strong intermolecular interactions are found for either structure. The crystal

structure for **Mo2** displays four unique molecules within the asymmetric unit. Short Mo≡C bond lengths of 1.8093(12) Å and 1.8036[19] Å are found for both **Mo1** and **Mo2,** respectively, consistent with a triple bond (Table 3.1).[49] Due to the large trans-influence of the alkylidyne, correspondingly long Mo−Cl bond lengths of 2.5526(3) Å and 2.5937[5] Å, respectively, are found for **Mo1** and **Mo2** as well. Both complexes display similar bond metrics to Mo(CPh){P(OMe)$_3$}$_4$Cl, which displays a short Mo≡C bond length of 1.793(8) Å and a long Mo−Cl bond length of 2.585(3) Å.[46] The Mo−P$_{avr.}$ bond length for **Mo1** (2.5014[3] Å) is longer than that for **Mo2** (2.4689[5] Å) and is attributed to the increased steric bulk of the dppe ligand leading to larger steric clash around the metal center. A similar Mo–P distance of 2.514[3] Å is observed in Mo(CSiMe$_3$)(dppe)$_2$Br.[50]

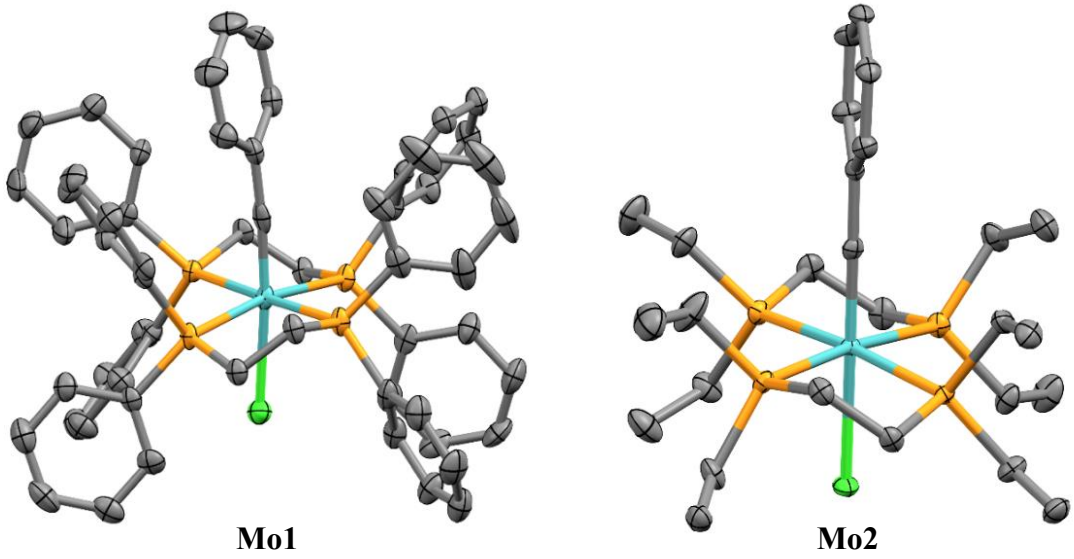

Figure 3.3. Thermal-ellipsoid representation of the structure of **Mo1** and **Mo2** (50% probability ellipsoids). Hydrogen atoms and interstitial solvent have been omitted for clarity.

Table 3.1. Crystallographically Determined Bond Lengths (Å) and Angles (˚) for d^2 Complexes.

	M≡E	M–Cl	M–P_{avr}	E–C(2)	E–M–Cl	E–M–P_{avr}
W1[a]	1.833(5)	2.5373(14)	2.4881[14]	1.441(8)	177.05(17)	92.74[16]
W2[b]	1.817(4)	2.577(1)	2.456[1]	1.448(7)	178.3(3)	93.33[1]
Mo1	1.8093(12)	2.5526(3)	2.5014[3]	1.4534(16)	176.12(4)	92.69[4]
Mo2	1.8036[19]	2.5937[5]	2.4689[5]	1.447[3]	177.38[6]	93.25[6]
Ta1	1.844(3)	2.5031(11)	2.5736[9]	1.368(5)	179.64(11)	93.63[10]
Ta2	1.826[3]	2.5368[10]	2.5439[10]	1.378[5]	178.29[10]	94.11[10]

[a] Ref 19. [b] Ref 15.

Inspection of the CSD database indicates that **Ta1** and **Ta2** are the first examples of crystallographically characterized d^2 tantalum imido complexes with phosphine ligands. The molecular structures of **Ta1** and **Ta2** are qualitatively similar to each other and to **Mo1** and **Mo2** (Figure 3.4 and Table 3.1). The phenylimido ligand is oriented such that the phenyl plane splits the phosphine backbone to minimize steric clash with the larger substituents on the phosphine. Complexes **Ta1** and **Ta2** possess short Ta≡N bond lengths of 1.844(3) Å and 1.826[3] Å, respectively, consistent with a tantalum-nitrogen triple bond.[51] These bond lengths are slightly longer than that for Ta(NAr*)Cl_3(dme) (1.771(6) Å; Ar* = 2,6-diisopropylphenyl),[40] due to the larger radius of the Ta(III) center compared to a Ta(V) center . The Ta−Cl bond length for both complexes is influenced by the strong trans influence of the imido ligand, leading to a slightly longer Ta−Cl bond of 2.5368[10] Å for **Ta2** than 2.5031(11) Å for **Ta1** due to the former's shorter Ta≡N bond. The geometry at the metal center is pseudo-tetragonal with N−Ta−Cl being close to linear for both complexes (**Ta1** 179.64(11), **Ta2** 178.29[10]) and the equatorial phosphine plane being near perpendicular to the vertical axis (Cl–Ta−P_{avr}: **Ta1** 93.63[10], **Ta2** 94.11[10]). The Ta−P_{avr} bond lengths of 2.5736[9] Å and 2.5439[10] Å for **Ta1** and **Ta2**, respectively, are consistent with other d^2 tantalum complexes.[52-55]

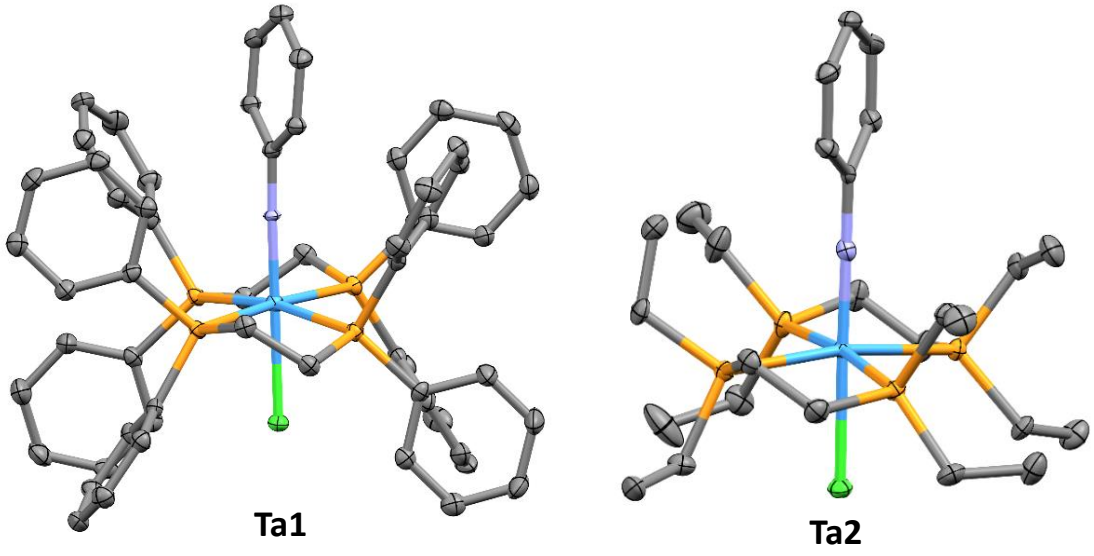

Figure 3.4. Thermal-ellipsoid representation of the structure of **Ta1** and **Ta2** (50% probability ellipsoids). Hydrogens and interstitial solvent have been omitted for clarity.

Compared to the structures of the closely related tungsten complexes **W1** and **W2**, both sets of complexes show similar bond distances and angles about the metal center (Table 3.1). Differences in the M≡C and M−Cl bond lengths between the between molybdenum and tungsten centers are less than 0.02 Å for **Mo1**[19] and within a 3σ error range for **Mo2**,[15] while the C−M−Cl, C(2)−C−M, C−M−$P_{avr.}$ bond angles are all within error of each other for both complexes.[19] The W≡C and Ta≡N bond lengths are within 3σ of each other despite the differences among the atomic radii. This is attributed to the contracted nitrogen p orbitals relative to carbon p orbitals offsetting the increase in radius of the more diffuse tantalum d orbitals. The reduced trans influence of the imido ligand can also be seen from the contracted Ta−Cl bond length by over 0.3 Å compared to the alkylidyne ligand. This can be demonstrated more clearly for the depe complexes, where phosphine sterics should not be a factor. The increase in Ta−P bond lengths can be attributed to the increase in tantalum d orbital size relative to tungsten,

resulting in longer Ta−P bond lengths by nearly 0.1 Å. Aside from these differences about the metal center, the geometries for these isoelectronic complexes are very close and allow for in-depth comparisons between the electronic structures of the W≡C and Ta≡N core.

DFT calculations were performed to get better insight on the electronic structure of these complexes and to further analyze their bonding (Table 3.2). The calculated and experimentally determined geometries show very close agreement. Slight differences in the Mo≡C bond length are observed with the calculated bond length within 0.02 Å error for **Mo1** and **Mo2**. While the metal-carbon bond length is critical to the overall electronic structure of the complex, this error is small enough such that the optimized structure is suitable for doing further computational analysis. This leads to slight difference in the Mo−Cl bond lengths as well, which are slightly overestimated due to the increased trans effect from the shorter calculated Mo≡C bond length. Good agreement was found between the calculated and experimental geometries with Ta≡N and Ta–P_{avr} bond lengths within 0.01 Å. The sole exception appears to be the Ta−Cl bond length which is slightly overestimated here as well.

Table 3.2. DFT Calculated Bond Lengths (Å) and Angles (˚) for Reported d^2 Complexes.

		M≡E	M–Cl	M–P_{avr}	E–C(2)	E–M–Cl	Cl–M–P_{avr}
Mo1	Expt.	1.8093(12)	2.5526(3)	2.5014[3]	1.4534(16)	176.12(4)	92.69[4]
	Calc.	1.796	2.585	2.504	1.448	177.3	95.2
Mo2	Expt.	1.8036[19]	2.5937[5]	2.4689[5]	1.447[3]	177.38[6]	93.25[6]
	Calc.	1.789	2.609	2.477	1.446	178.59	94.32
Ta1	Expt.	1.844(3)	2.5031(11)	2.5736[9]	1.368(5)	179.64(11)	93.63[10]
	Calc.	1.842	2.523	2.577	1.366	176.48	96.41
Ta2	Expt.	1.826[3]	2.5368[10]	2.5439[10]	1.378[5]	178.29[10]	94.11[10]
	Calc.	1.836	2.559	2.557	1.361	178.37	96.09

3.2.4. Electrochemical Characterization.

Cyclic voltammetry of both sets of complexes was conducted in THF using 0.1 M $[N^nBu_4][PF_6]$ as a supporting electrolyte (Table 3.3). Both molybdenum complexes show reversible one-electron oxidations at −0.53 V vs. $Fc^{0/+}$ for **Mo1** (Figure 3.5) and −0.81 V vs. $Fc^{0/+}$ for **Mo2** (Figure 3.6). As discussed elsewhere,[20] the oxidation potential for $M(CPh)L_4Cl$ complexes increases with the π-acidity of the phosphine ligand. To examine the reversibility of the processes, Randles-Sevcik analyses were conducted. Both anodic and cathodic currents display the expected square-root dependence of current on scan-rate indicating free diffusion of the analyte in solution (Figures 3.7 and 3.8). Near identical slopes for both cathodic and anodic scan-rate dependencies indicate reversibility of the redox couple. As a comparison, the previously reported compound $Mo(CPh)\{P(OMe)_3\}_4Cl$ was studied by cyclic voltammetry (Figure 3.9).[46] This complex displays an irreversible oxidation wave at −0.26 V vs. $Fc^{0/+}$. The electrochemical irreversibility of $Mo(CPh)\{P(OMe)_3\}_4Cl$ also highlights one of the design principles for designing stable second row photoreductants. One-electron oxidation of these types of complexes leads to weaker backbonding to the phosphine ligand and bond elongation, as observed in d^1 tungsten derivatives.[17, 19] Use of a bidentate chelating phosphine mitigates this issue by inhibiting ligand dissociation and helping to deliver a complex with a fully reversible redox couple suitable for photoredox applications.

Table 3.3. Experimental Oxidation Potentials (THF, 0.1 M $[N^nBu_4][PF_6]$).

	$E_{1/2}^{0/+}$ (V)[c]	$E_{pa}^{+/2+}$ (V)[c,d]
W1[a]	-0.58	0.63
W2[b]	-0.84	0.19
Mo1	-0.54	N.D.
Mo2	-0.81	N.D.
Ta1	-1.19	0.04
Ta2	-1.36	0.08

[a]Ref 20 [b]Ref 15 [c]Potentials referenced vs. $FeCp_2^{0/+}$ [d]irreversible

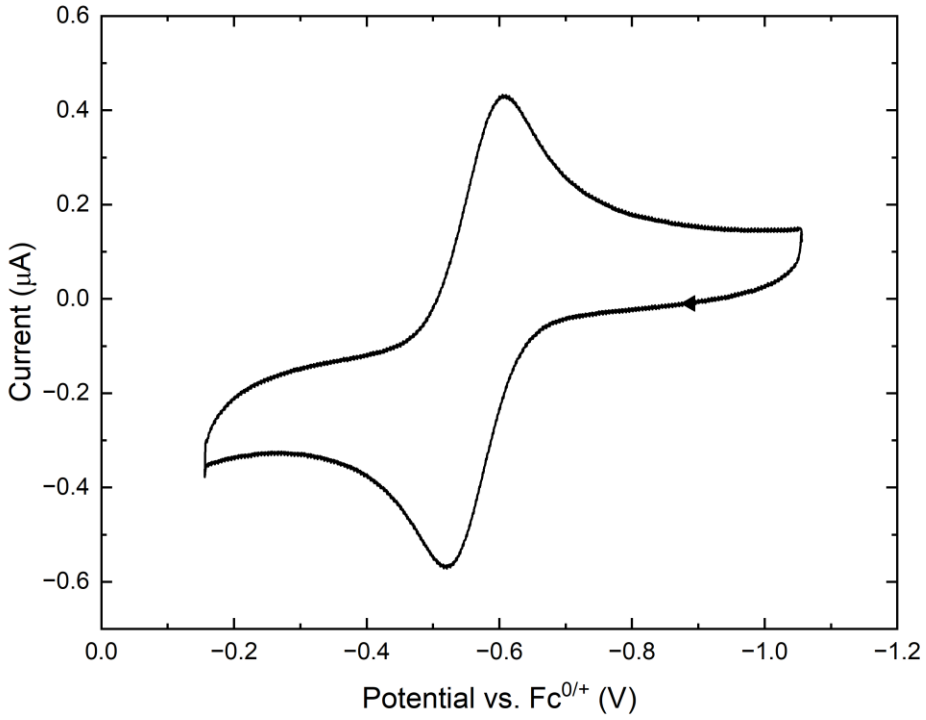

Figure 3.5. Cyclic voltammogram of **Mo1** (0.001 M) in THF containing 0.1M $[N^nBu_4][PF_6]$ (ν = 100 mVs^{-1}).

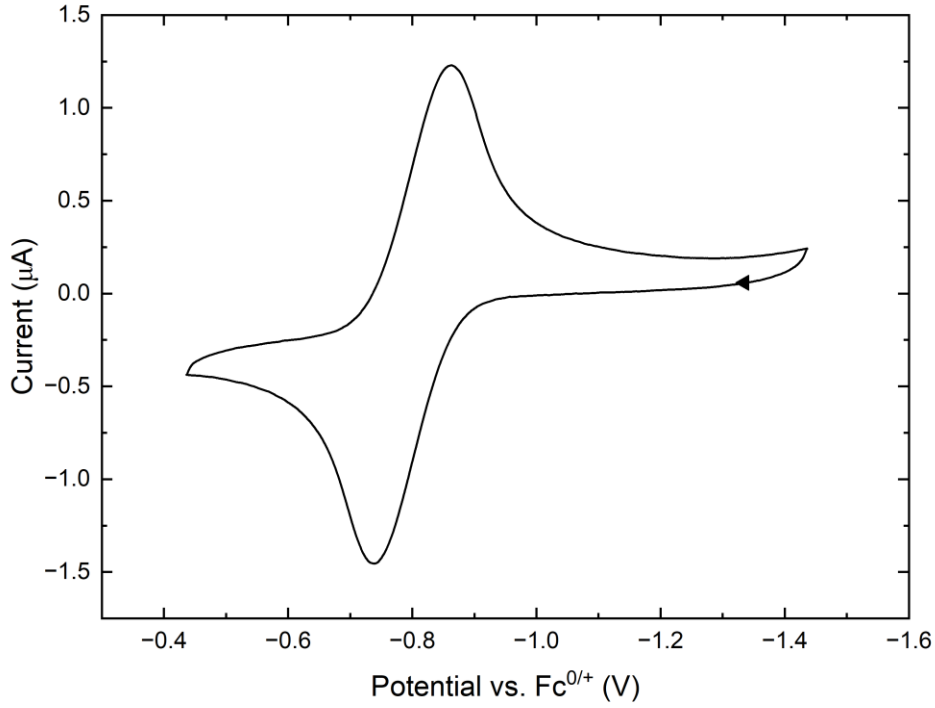

Figure 3.6. Cyclic voltammogram of **Mo2** (0.001 M) in THF containing 0.1M $[N^nBu_4][PF_6]$ (ν = 100 mVs^{-1}).

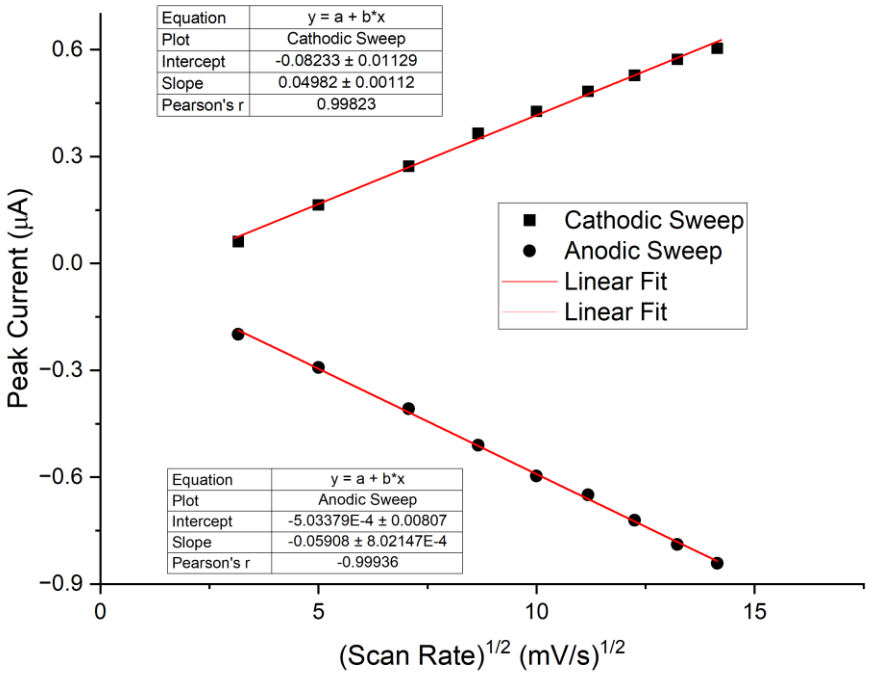

Figure 3.7. Randles-Sevcik plot of **Mo1** in THF containing 0.1M $[N^nBu_4][PF_6]$.

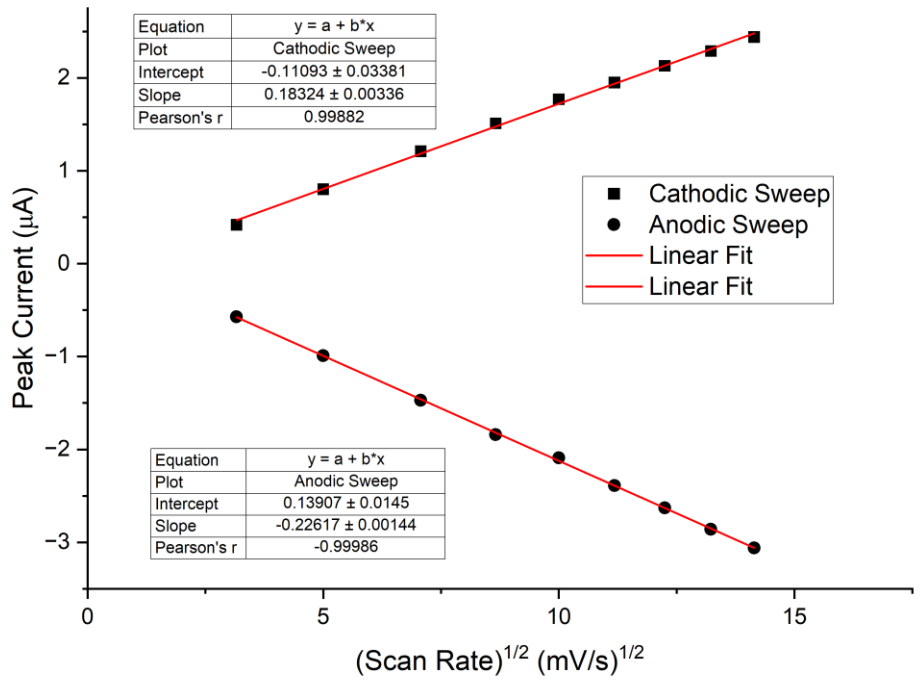

Figure 3.8. Randles-Sevcik plot of **Mo2** in THF containing 0.1M $[N^nBu_4][PF_6]$.

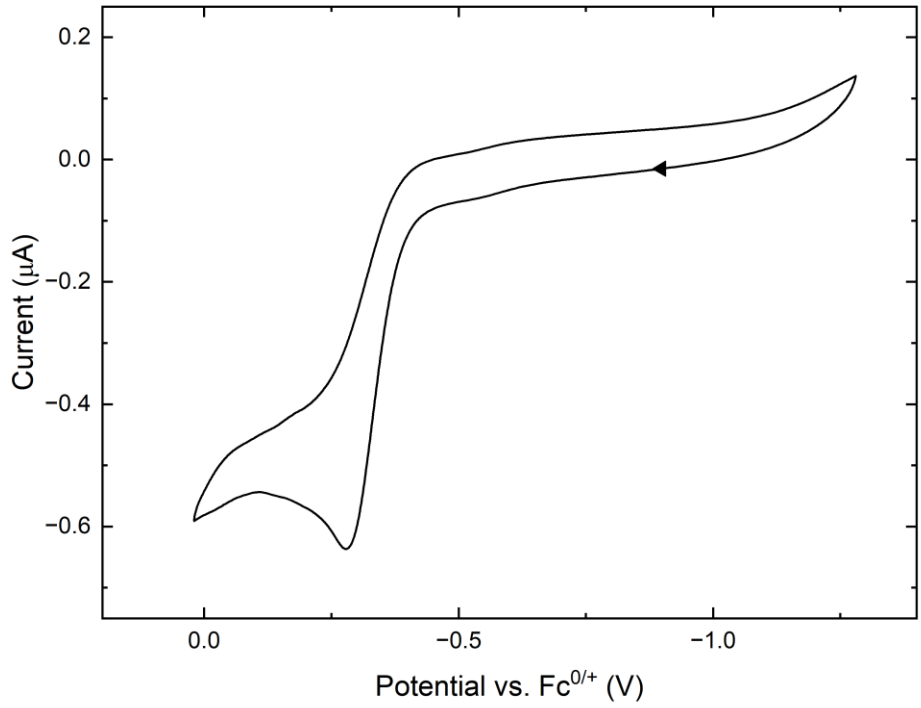

Figure 3.9. Cyclic voltammogram of $Mo(CPh)\{P(OMe)_3\}_4Cl$ (0.001 M) in THF containing 0.1M $[N^nBu_4][PF_6]$ (ν = 100 mVs^{-1}).

The oxidation potentials for the molybdenum complexes are very close to those observed for their tungsten analogues (**Mo1** = –0.53 V, **W1** = −0.58 V vs. $Fc^{0/+}$; **Mo2** = –0.81 V, **W2** = −0.84 V vs. $Fc^{0/+}$).[15, 20] The slightly less reducing nature of the molybdenum analogues is attributed to the standard periodic trend of their lower energy d orbitals. Cyclic voltammetry of W(CPh){P(OMe)$_3$}$_4$Cl displays irreversible oxidation at E_{pa}= –0.24 V vs. $Fc^{0/+}$,[21] similar to that found here for Mo(CPh){P(OMe)$_3$}$_4$Cl (E_{pa}= –0.26 V vs. $Fc^{0/+}$). The tungsten compound shows a small return wave at room-temperature with an additional return wave at E_{pc} = −0.7 V vs. $Fc^{0/+}$ likely arising from an oxidative decomposition product. The absence of a return wave for Mo(CPh){P(OMe)$_3$}$_4$Cl under identical measurement conditions suggests that the oxidative decomposition of the molybdenum complex is kinetically faster than the tungsten complex.

Tantalum complexes **Ta1** and **Ta2** display one electron oxidation waves at $E_{1/2}^{0/+}$ = −1.19 V vs. $Fc^{0/+}$ for **Ta1** and $E_{1/2}^{0/+}$ = −1.36 V vs. $Fc^{0/+}$ for **Ta2** (Figures 3.10 and 3.11). A second irreversible redox wave assigned to oxidation of the d^1 metal center is observed at E_{pa} = 0.05 V vs. $Fc^{0/+}$ for **Ta1** and E_{pa} = −0.13 V vs. $Fc^{0/+}$ for **Ta2**. The first oxidation potentials are similar to that found for the d^2 niobium imido complex {[Nb(BDI)N^{t}Bu]$_2$(μ-C_6H_6)} (BDI = *N*,*N*′-diisopropylbenzene-β-diketiminate) (−0.48 V vs. $Ag^{0/+}$).[56] The higher oxidation potential of **Ta1** relative to **Ta2** is consistent with the greater π-acidity of the aryl-phosphine ligand, as noted for the molybdenum compounds. The difference between the first and second oxidation potentials are nearly identical for both complexes (ΔE: **Ta1** = 1.24 V, **Ta2** = 1.23 V), suggesting the second oxidations have similar orbital origins. For **Ta2**, this second oxidation leads to complete decomposition of the complex, with subsequent anodic scans showing complete loss of the redox active species (Figure 3.12), whereas for **Ta1** a reverse wave for the first oxidation event is still preserved (Figure 3.10).

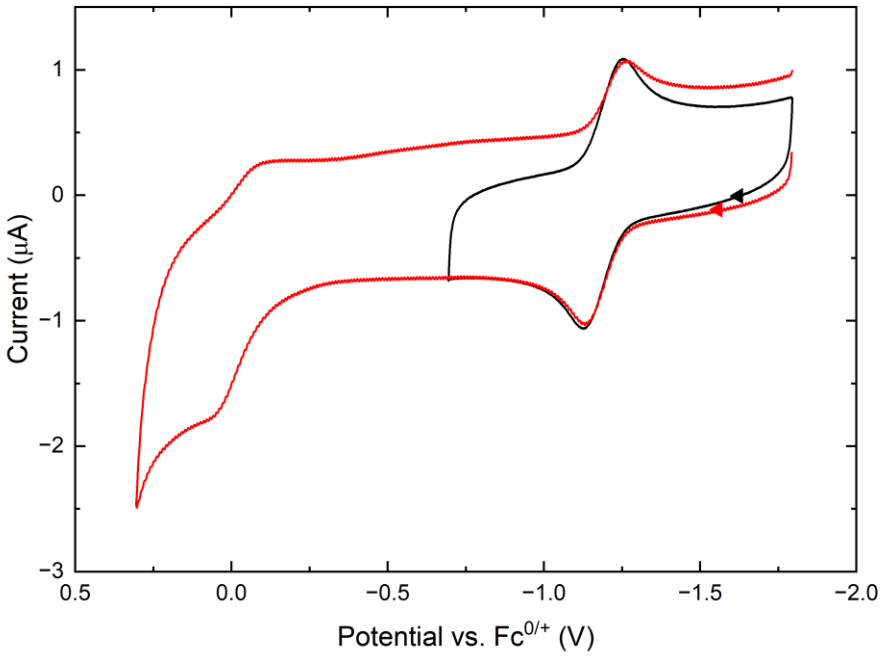

Figure 3.10. Cyclic voltammogram of **Ta1** (0.001 M) in THF containing 0.1M $[N^nBu_4][PF_6]$ (ν = 100 mVs^{-1}) using two different sweep windows.

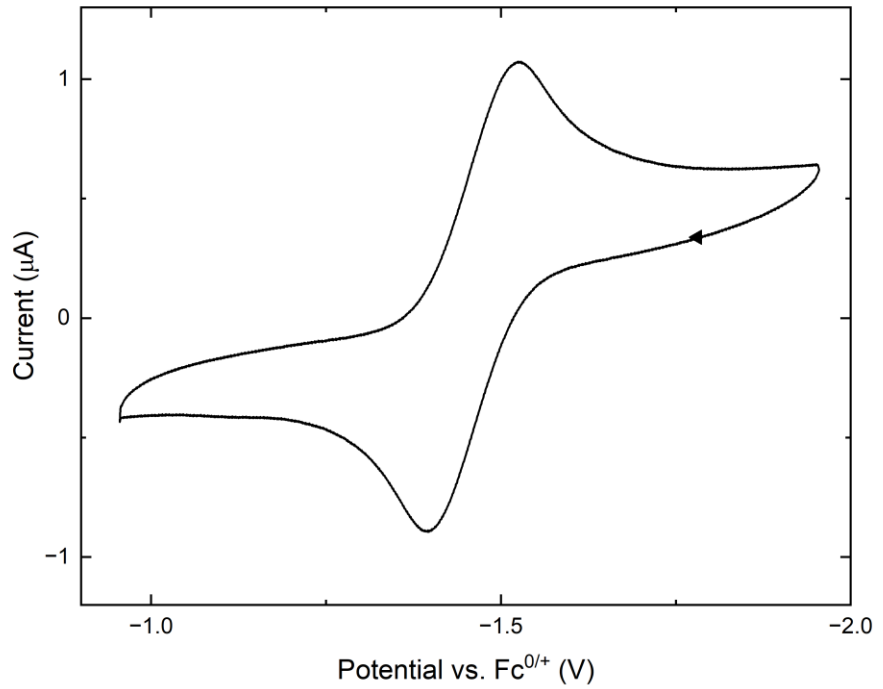

Figure 3.11. Cyclic voltammogram of **Ta2** (0.001 M) in THF containing 0.1M $[N^nBu_4][PF_6]$ (ν = 100 mVs^{-1}).

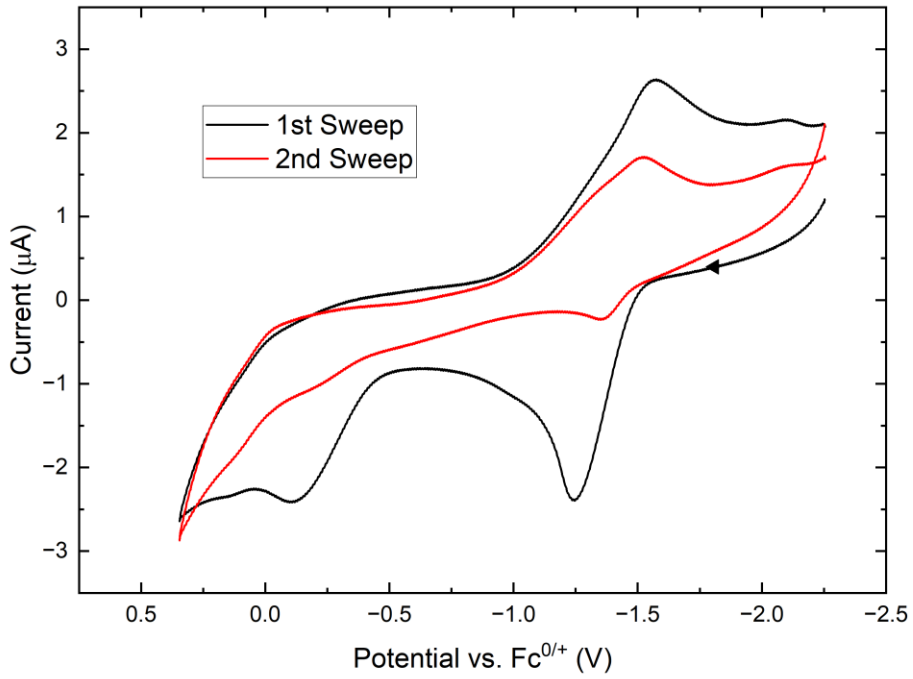

Figure 3.12. Cyclic voltammogram of **Ta2** (0.001 M) in THF containing 0.1M $[N^nBu_4][PF_6]$ (ν = 100 mVs^{-1}) showing decomposition after 1st voltametric sweep.

Scan-rate dependence of the peak anodic and cathodic current for **Ta1** were plotted and fit using the Randles-Sevcik equation. A square-root dependence of peak current on scan rate was found confirming the diffusional nature of the redox-active species (Figure 3.13). Despite seemingly reversible behavior from experiments at fast scan rates, deviations from linearity across the measured scan rates and incommensurate slopes for the cathodic and anodic peaks lead us to assign the redox event as quasi-reversible (formally irreversible). Such analysis was not possible for **Ta2** due to its instability in solution, so the first redox wave was assigned as quasi-reversible by analogy to **Ta1**. Periodic redox cycling of just the first oxidation event for **Ta2** during a Randles-Sevcik analysis showed gradual decrease in current over the course of five minutes in addition to bleaching of the solution in the absence of any applied potential. This is

attributed to the instability of **Ta2**, which is gradually decomposing under the measured electrochemical conditions.

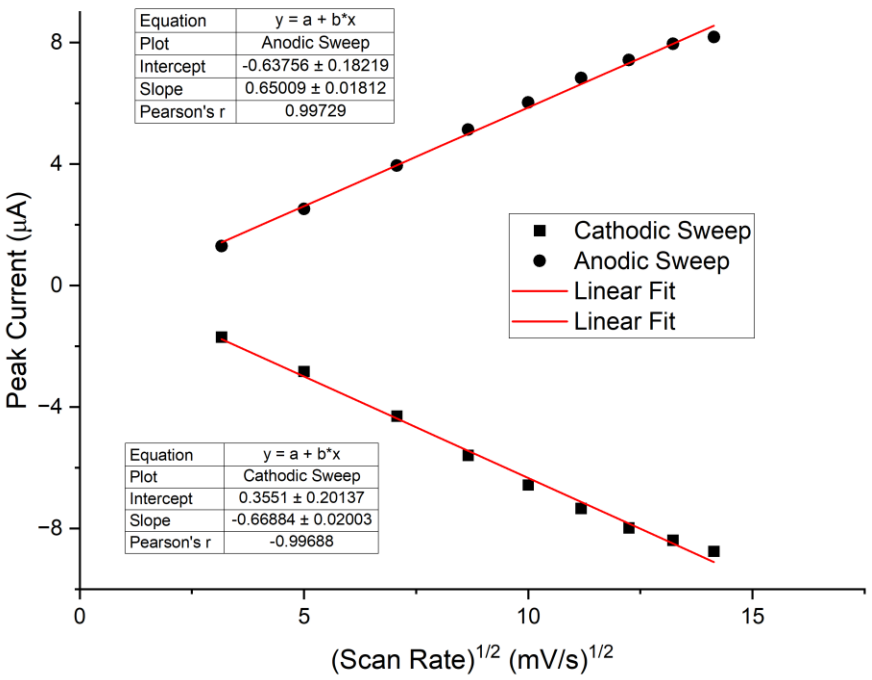

Figure 3.13. Randles-Sevcik plot of **Ta1** in THF containing 0.1M $[N^nBu_4][PF_6]$.

The tantalum complexes are dramatically more reducing than their tungsten counterparts, with the one-electron oxidation potentials of **Ta2** and **Ta1** being 0.52 V and 0.61 V lower, respectively (Table 3.3).[20] The lower oxidation potential is consistent with the Ta center's lower ionization energy.[34] While the alkylidyne is more donating than the corresponding imido, this effect is of secondary importance because the oxidation potential here is associated with the metal-centered d_{xy} orbital, which is orthogonal by symmetry to MEPh orbitals. Unlike the tungsten complexes, both tantalum complexes also display a formally irreversible first oxidation. The reduced stability of the electrochemically generated d^1 species is consistent with the observation that both tantalum complexes were found to be thermally unstable and extremely air

sensitive, whereas both tungsten complexes are indefinitely stable under an inert atmosphere and only display slow decomposition under ambient conditions.

3.2.5. Electronic Absorption Spectra.

Complexes **Mo1**, **Mo2**, **Ta1**, and **Ta2** were characterized by UV-Vis spectroscopy (Table 3.4). The molybdenum complexes **Mo1** (Figure 3.14) and **Mo2** (Figure 3.15) display strong absorptions in the UV region at 345 nm and 340 nm, respectively, assigned to the $^1[\pi \rightarrow \pi^*]$ transition, with a lower intensity shoulder found for **Mo2** at 352 nm. The $^1[d_{xy} \rightarrow \pi^*]$ band for **Mo2** is found at 555 nm and has an extinction coefficient of 103 M^{-1} cm^{-1}, consistent with a transition with formal d-d parentage (Figure 3.16). For **Mo1**, the $^1[d_{xy} \rightarrow \pi^*]$ band appears at 536 nm, where it overlaps with a rising absorption feature beginning at ca. 500 nm that maximizes at 420 nm. This latter band is assigned to a d_{xy} to phosphine charge transfer and is only observed in **Mo1** due to the low-lying unoccupied orbitals on the aryl phosphine ligands. This matches a similar band observed for the analogous tungsten complex (λ = 430 nm).[15] The unoccupied orbitals for an alkyl phosphine are much higher in energy so a corresponding transition is not observed in the visible region for **Mo2**. The $d_{xy} \rightarrow \pi^*$ bands are analogous to those well-established for other pseudo-tetragonal transition-metal complexes with metal ligand multiple bonds.[16, 19, 57-58]

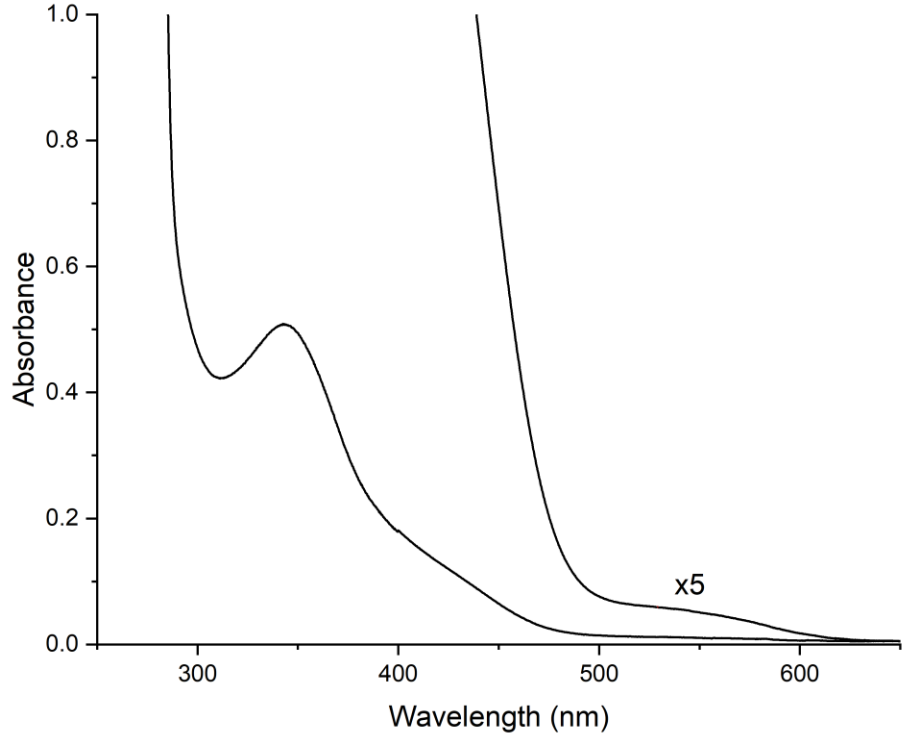

Figure 3.14. Electronic absorption spectrum of **Mo1** in toluene.

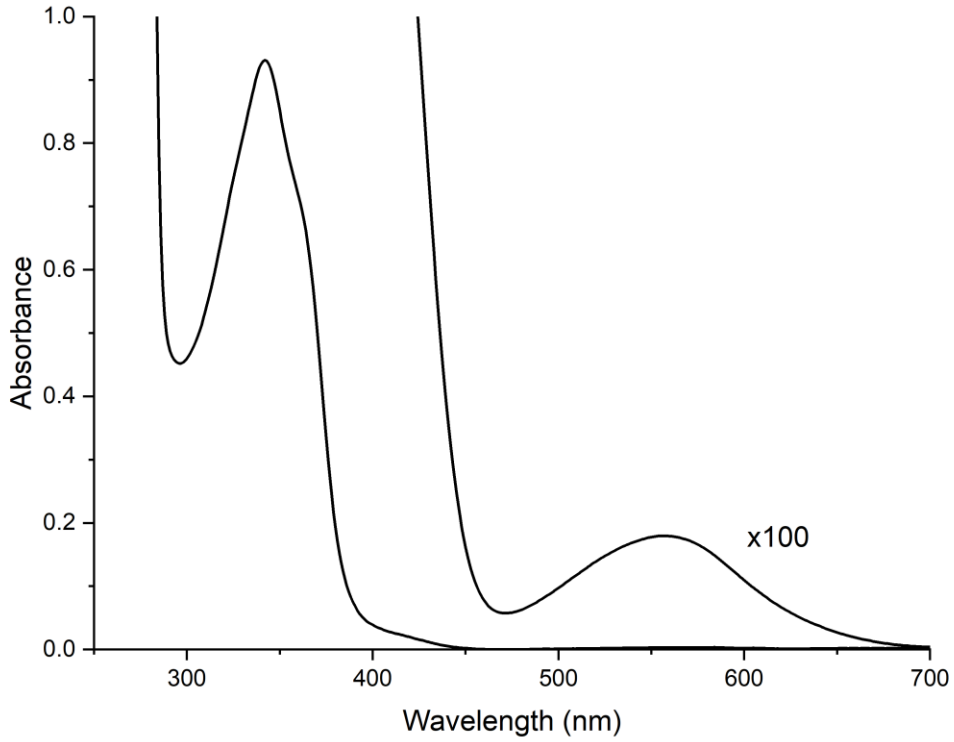

Figure 3.15. Electronic absorption spectrum of **Mo2** in toluene.

Table 3.4. Electronic Absorption Band Maxima (toluene).

	$^1[\pi\rightarrow\pi^*]$ (nm)	$^1[d_{xy}\rightarrow\pi^*]$ (nm)
W1[a]	338	532
W2[b]	339	546
Mo1	345	536
Mo2	340	555
Ta1	310	700
Ta2	320	728

[a] Ref 20 [b] Ref 15

The band maxima for the molybdenum complexes are close to those of their tungsten analogues, with the $^1[d_{xy}\rightarrow\pi^*]$ transition energies for molybdenum being slightly lower than that of the tungsten congeners.[16] This can be clearly resolved for **Mo2** where the $^1[d_{xy}\rightarrow\pi^*]$ is only slightly lower energy at 555 nm than the corresponding tungsten complex at 546 nm (by 0.04 eV). The $^1[\pi\rightarrow\pi^*]$ band maxima are also essentially identical at 339 nm. The extinction coefficient for the $^1[d_{xy}\rightarrow\pi^*]$ band of **Mo2** (103 M^{-1} cm^{-1}) is also notably smaller than that of its tungsten analogue (533 M^{-1} cm^{-1}) by roughly a factor of five (Figure 3.16). This is attributed to an increase in formally forbidden d-d character for the molybdenum complex.

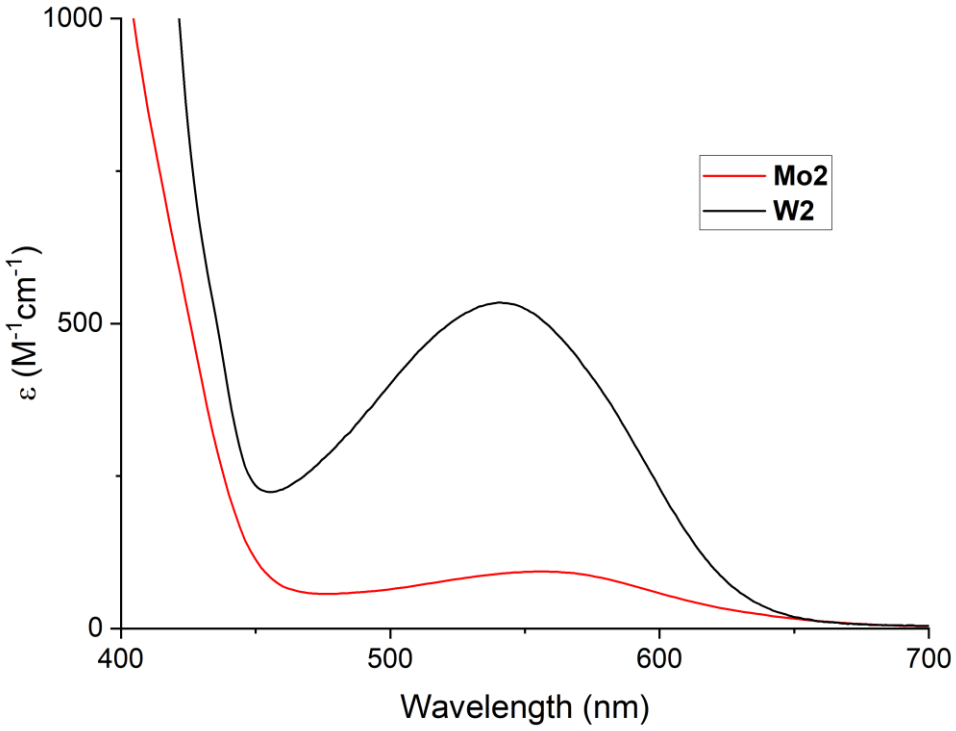

Figure 3.16. Electronic absorption spectra of **Mo2** compared to **W2** in toluene.

The electronic spectra of tantalum complexes **Ta1** (Figure 3.17) and **Ta2** (Figure 3.18) exhibit similarities but also strong differences from those of the molybdenum and tungsten complexes. The spectra display strong absorptions in the UV region at 310 nm and 320 nm for **Ta1** and **Ta2**, respectively, assignable to the $^1[\pi\rightarrow\pi^*]$ transition; this band is found from 338-345 nm for the Mo and W derivatives.[36-37] Complex **Ta1** displays an additional intense band 480 nm that tails into a weak absorption centered at 700 nm. The 480 nm transition is assigned to a d_{xy} to phosphine charge transfer transition by analogy to the previously described bands of the **Mo1** and **W1** analogues.[19] For **Ta1**, a low energy band at 700 is assigned to a $^1[d_{xy}\rightarrow\pi^*]$ transition by analogy to **Mo1** and **W1**. However, the absorption spectrum of **Ta2** shows much more structure than **Ta1**. Three low intensity absorption bands can be found in the visible region centered at 533 nm, 641 nm, and 720 nm. Conclusive assignments for these bands cannot be offered on the basis

of the available data. One possible explanation is that the two lower energy bands arise from two $^1[d_{xy} \rightarrow \pi^*]$ transitions corresponding to the non-phenyl conjugated and phenyl-conjugated π bonds. Their similar intensity and small energy difference would require that the phenyl ring only minorly contributes to this transition and is instead dominated by its d-d character. This is consistent with the finding from DFT for the phenyl-conjugated π* orbital where the N character is only 3%. Similarly, the non-phenyl-conjugated π* orbital possesses 9.98% and 8.10% N character for **Ta1** and **Ta2** respectively. The third absorption band at 533 nm is also challenging to assign. We tentatively assign this to a d_{xy} to phosphine charge transfer transitions due to its similar intensity to analogous transitions found for **W2** and **Mo2** and due to its energetic overlap with a d_{xy} to phosphine charge transfer transitions in **Ta1**.

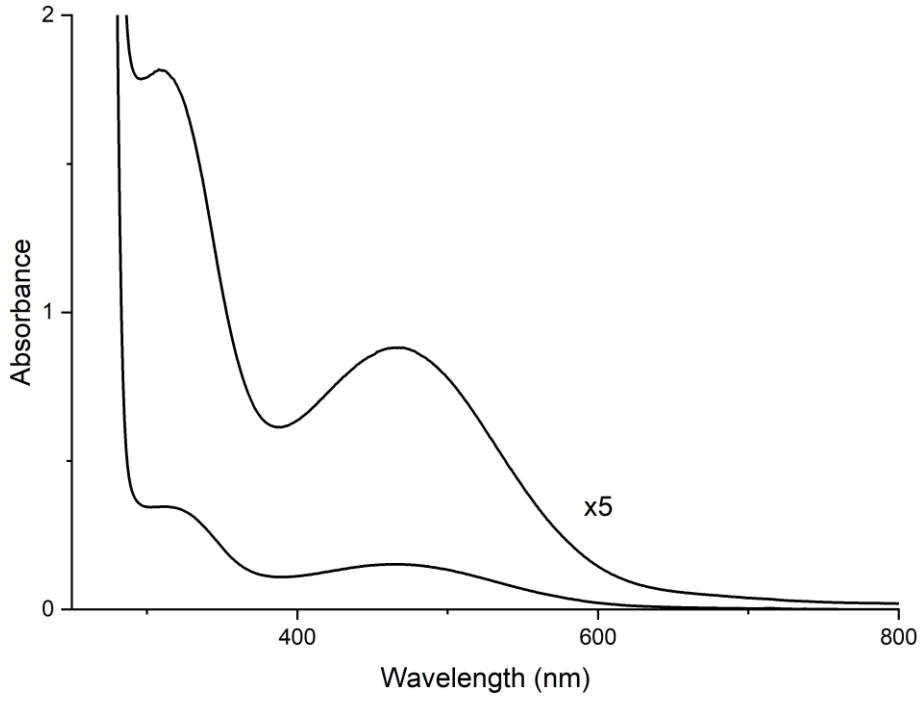

Figure 3.17. Electronic absorption spectrum of **Ta1** in toluene.

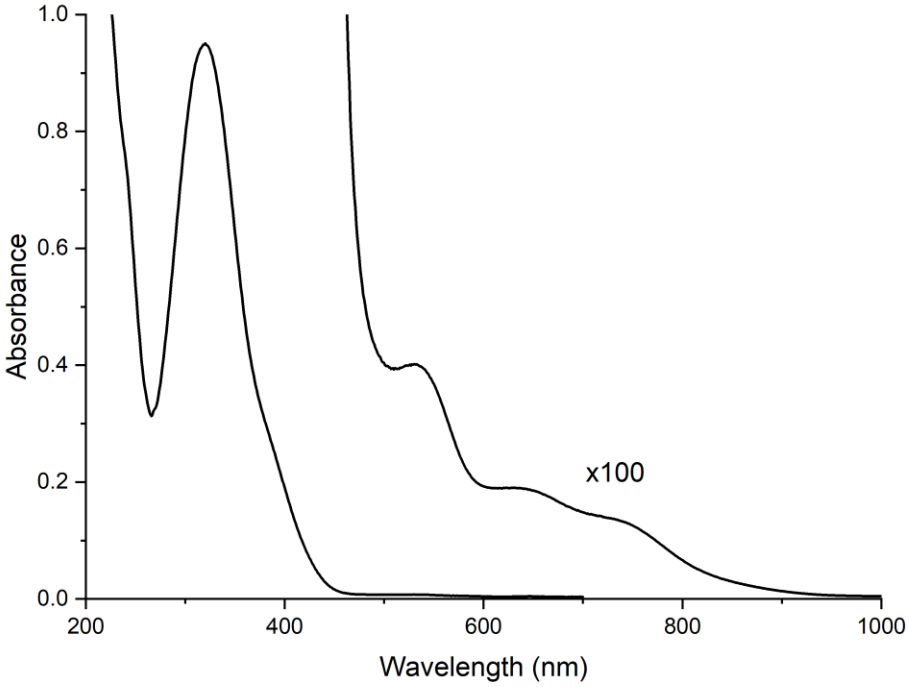

Figure 3.18. Electronic absorption spectrum of **Ta2** in pentane.

The measured redox potentials and UV-Vis transition energies can be used to construct an experimental MO orbital energy diagram for the frontier π and d_{xy} orbitals (Figure 3.19 and Table 3.5). From this, it becomes clear that the origin of the lower energy of the tantalum $^1[d_{xy} \rightarrow \pi^*]$ transitions is due to the higher energy d_{xy} orbital. This diagram also allows comparison of the π* orbital energies which are key for determining the photoreducing power of the chromophore. Despite the more reducing tantalum center in the ground state, the π* orbital energy is minimally perturbed for the tantalum imido compared to the tungsten alkylidyne and suggests that both complexes should in fact display similar excited-state oxidation potentials. Moreover, the high energy of the d_{xy} orbital for the tantalum complexes might be detrimental to photocatalysis due to the resulting redshift of the $^1[d_{xy} \rightarrow \pi^*]$ transition, which is expected to lead to faster nonradiative decay through the Energy-Gap Law and shorter excited-state lifetimes.

Table 3.5. Experimental Oxidation Potentials and Electronic Transition Energies.

	$^1[\pi\rightarrow\pi^*]$ (eV)	$^1[d_{xy}\rightarrow\pi^*]$ (eV)	$E_{1/2}^{0/+}$ (V)[c]	$E_{pa}^{+/2+}$ (V)[c,d]
Wl[a]	3.66	2.33	-0.58	0.63
W2[b]	3.65	2.27	-0.84	0.19
Mo1	3.59	2.31	-0.54	N.D.
Mo2	3.64	2.23	-0.81	N.D.
Ta1	3.99	1.77	-1.19	0.04
Ta2	3.87	1.68	-1.36	0.08

[a]Ref 20 [b]Ref 15 [c]Potentials referenced vs. $FeCp_2^{0/+}$ [d]irreversible

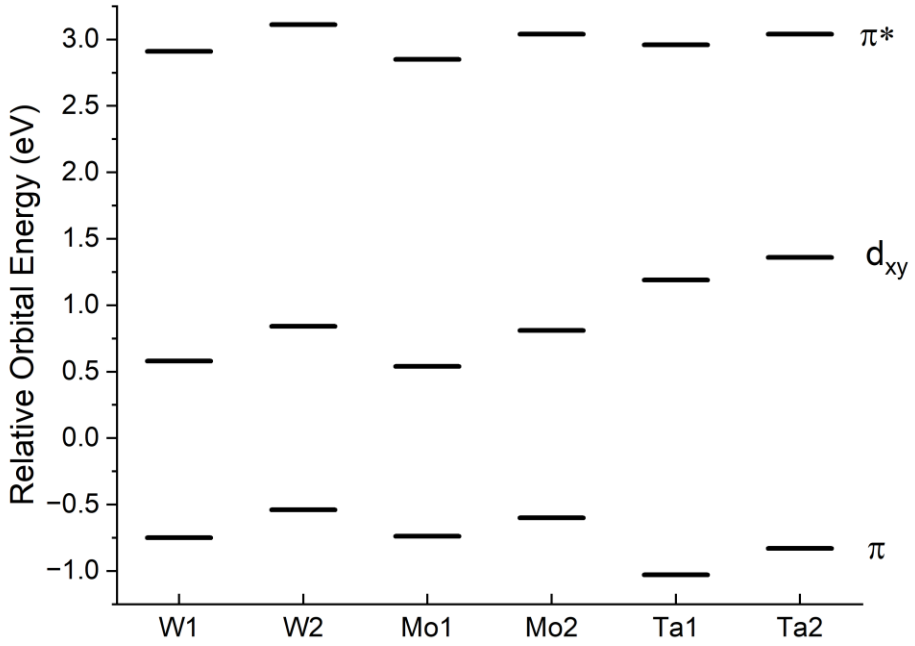

Figure 3.19. Relative orbital energy diagram derived from experimental data (Table 3.5).

To shed light on the nature of the low-lying absorption bands of **Ta1** and **Ta2**, simulation of the spectra was attempted using TDDFT.[59-61] The computational methods were benchmarked for **Mo1** and **Mo2**, whose spectroscopic assignments are clear. The calculated transition energies

and intensities show reasonable agreement with their observed values (Figures 3.20 and 3.21). The calculated transition energies are slightly higher than observed but within error to allow for confirmation of their character. The lowest energy transition is confirmed to be the weak $^1[d_{xy} \rightarrow \pi^*]$ transition and the intense transition in the UV region is the $^1[\pi \rightarrow \pi^*]$ transition. The shoulder at 400 nm in the spectra for **Mo2** can also be identified as a d_{xy} to phosphine charge transfer. General spectroscopic broadening observed in the UV region for **Mo1** can also be assigned to multiple overlapping weaker a d_{xy} to phosphine charge transfer transitions overlapping with the more intense $^1[\pi \rightarrow \pi^*]$ transition.

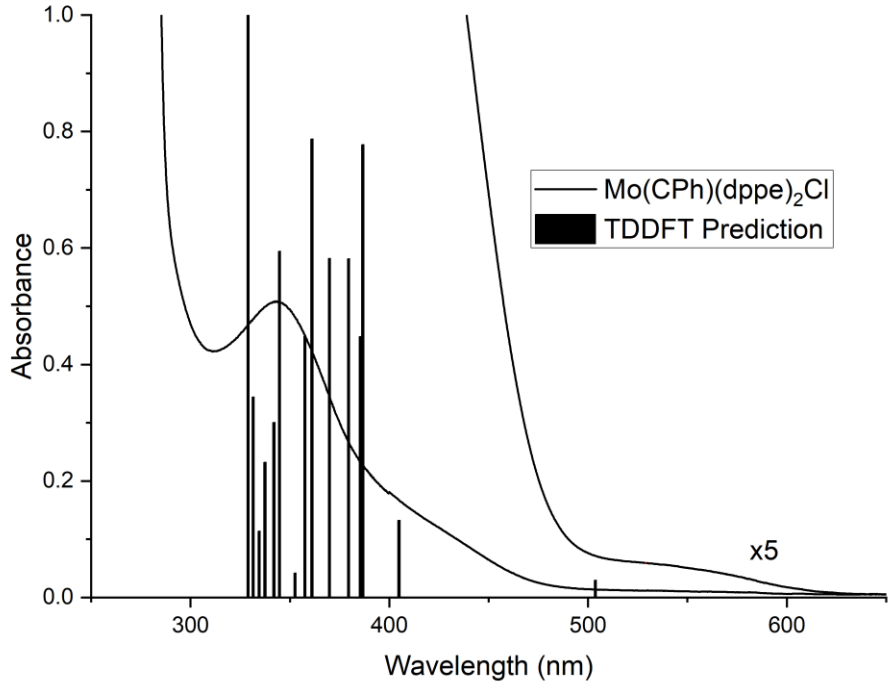

Figure 3.20. Electronic absorption spectra of **Mo1** in toluene overlaid with predicted TDDFT transitions.

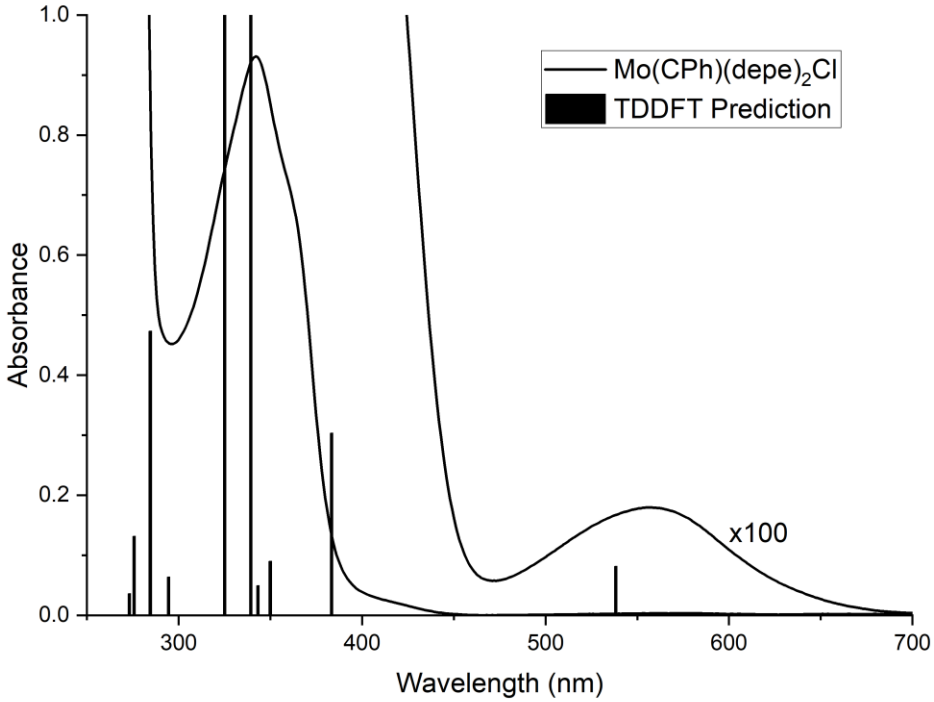

Figure 3.21. Electronic absorption spectra of **Mo2** in toluene overlaid with predicted TDDFT transitions.

In contrast to the molybdenum complexes, attempts to simulate and assign the UV-Vis spectra of **Ta1** and **Ta2** using TDDFT were determined to be unsuccessful (Figures 3.22 and 3.23). For **Ta1**, multiple overlapping absorptions are predicted between 350-550 nm assigned to d_{xy} to phosphine charge transfer transitions. One isolated $^1[d_{xy} \rightarrow \pi^*]$ is predicted at 632 nm. These predicted transitions show reasonable agreement with the overall absorption band shape of **Ta1.** Clear experimental deviations from predictions can be seen for **Ta2** where the calculated spectrum is unable to simulate any low energy bands aside from the HOMO-LUMO $^1[d_{xy} \rightarrow \pi^*]$ transition, which it also overestimates in energy. Attempts to simulate the absorption spectra by multireference methods like CASSCF/NEVPT2 were similarly unable to give good agreement with the measured spectra.

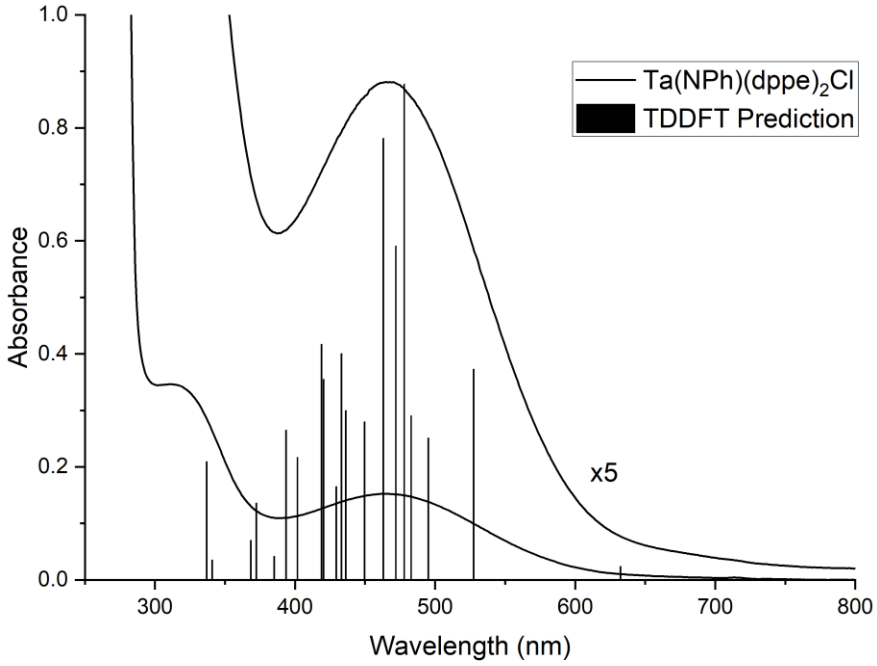

Figure 3.22. Electronic absorption spectrum of **Ta1** in toluene overlaid with predicted TDDFT transitions.

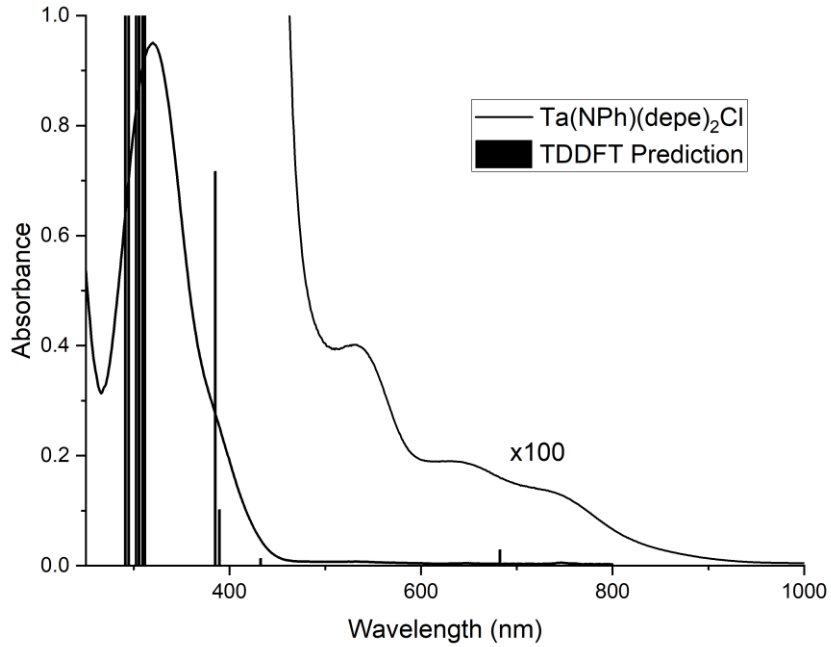

Figure 3.23. Electronic absorption spectrum of **Ta2** in pentane overlaid with predicted TDDFT transitions.

3.2.6. DFT Analysis of Electrochemical and Spectroscopic Data.

The electrochemical and UV-Vis results for **Mo1**, **Mo2**, **Ta1**, and **Ta2** were further explored using DFT calculations. The atomic parentage of the Kohn-Sham orbitals was also determined. With a few exceptions, the frontier orbitals of the tantalum-imido compounds are markedly different from each other and from the Mo and W alkylidyne complexes. For the Mo and W alkylidyne complexes, the calculated frontier Kohn-Sham orbitals for all complexes agree with expectation for this general class of compounds, with a π(MEPh) bonding orbital for HOMO-1, a well-separated d_{xy} non-bonding HOMO, and a π*(MEPh) LUMO (Table 3.6).[17] The d_{xy} HOMO of all complexes shows a roughly constant minor contribution from the phosphine ligands, as expected for a nominally nonbonding orbital. Comparing **Mo1**/**W1** and **Mo2**/**W2**, the π HOMO–1 and π* LUMO of the former pair gain aryl phosphine character due to the π-acidity of the phosphines. For the tantalum compounds, the d_{xy} HOMO has comparable atomic parentage to those for the Mo and W complexes. For **Ta2**, the HOMO–1 and LUMO may be assigned as π(MEPh) and π*(MEPh), similarly to the Mo and W alkylidynes, albeit with substantially more metal character in the LUMO and less metal character in the HOMO-1. This is generally consistent with the higher lying 5d orbitals of Ta relative to W (and more so relative to Mo). The HOMO–1 of **Ta1** is similarly π(MEPh), but, in contrast, the LUMO is essentially phosphine localized with the π*(MEPh) orbital mixed with multiple phosphine localized orbitals.

Table 3.6. DFT Calculated Frontier Orbitals and their Corresponding Atomic Parentage.

				Atomic Parentage (%)				
	Orbital	Energy (eV)		M	E	PR_n	Cl	Ph
W1	LUMO	-0.854	π*	18.5	7.38	28.13	1.42	44.57
	HOMO	-4.54	d_{xy}	73.65	0.12	26.03	0.11	0.09
	HOMO-1	-5.27	π	33.6	23.64	7.5	9.1	26.16
W2	LUMO	-0.67	π*	21.62	7.8	8.87	1.32	60.39
	HOMO	-4.21	d_{xy}	75.53	0	24.43	0.04	0
	HOMO-1	-5.10	π	35.46	23.27	9.72	8.64	22.91
Mo1	LUMO	-0.93	π*	21.75	1.27	22.39	3.9	50.69
	HOMO	-4.64	d_{xy}	76.7	0.09	22.17	0.17	0.07
	HOMO-1	-5.36	π	33.28	26.74	11.87	3.33	24.78
Mo2	LUMO	-0.68	π*	25.39	7.37	4.3	1.04	61.9
	HOMO	-4.36	d_{xy}	77.33	0.1	22.48	0.03	0.06
	HOMO-1	-5.11	π	33.43	24.52	8.24	9.32	24.49
Ta1	LUMO	-0.70	PR_n	3.35	0.61	93.55	0.28	2.21
	HOMO	-3.86	d_{xy}	71.32	0.02	28.56	0.06	0.04
	HOMO-1	-5.41	π	14.86	23.4	4.5	4.19	53.05
Ta2	LUMO	-0.47	π*	35.39	3.74	16.87	2.46	41.54
	HOMO	-3.58	d_{xy}	71.73	0	28.19	0.04	0.04
	HOMO-1	-5.97	π	16.42	24.1	4.01	3.91	51.56

The calculated energy levels of the Kohn-Sham orbitals can be used to gain insight into the electrochemical and electronic-absorption spectroscopic properties of the compounds. The calculated d_{xy} HOMO is substantially separated in energy from the HOMO-1 confirming assignment of the oxidation event to removal of an electron from the d_{xy} orbital. The HOMO energy for **Mo1** (−4.64 eV) is slightly lower than that for **Mo2** (−4.36 eV). This matches the relative ordering determined from cyclic voltammetry and is close to the observed difference in the one-electron oxidation potentials for these two complexes (calc, 0.28 eV; CV, 0.27 V). Comparison of the energy levels and orbital contributions of the molybdenum and tungsten complexes confirm that the tungsten complexes are slightly more reducing in the ground state

(**W1**$_{HOMO}$ = −4.54 eV, **Mo1**$_{HOMO}$ = −4.64 eV and **W2**$_{HOMO}$ = −4.21 eV, **Mo2**$_{HOMO}$ = −4.36 eV). Calculated HOMO Kohn-Sham orbital energies for **Ta1** and **Ta2** are found at dramatically higher energies at −3.86 eV and −3.58 eV, respectively. This is consistent with the dramatically lower oxidation potentials for both tantalum complexes. Compared to **W1** and **W2**, **Ta1** and **Ta2** possess 0.61 V and 0.52 V lower one-electron oxidation potentials compared to the 0.68 eV and 0.63 eV difference in HOMO energy, respectively. The electronic absorption band energies of the Mo and W compounds are similarly well rationalized by LUMO energy levels with corresponding HOMO−1, HOMO, and LUMO orbitals for the tungsten complexes approximately 0.1 eV higher than that for the molybdenum complexes. This renders the HOMO-LUMO energy gaps effectively identical for both sets of complexes resulting in the observed similarity in their UV-Vis transitions. However, the DFT calculations do not resolve the ambiguities about the electronic spectra of the tantalum compounds. Here, the non-phenyl conjugated π* orbital is strongly mixed with a phosphine accepting orbital as the LUMO+2 and is 1.27 eV higher in energy that the π*(MEPh) LUMO for **Ta2** compared to the 0.21 eV difference observed by UV-Vis (Table 3.7). The corresponding phosphine accepting orbital is found at 0.86 eV. This suggests that the d_{xy} to phosphine charge transfer transition should be close to the non-phenyl conjugated $^1[d_{xy} \rightarrow \pi^*]$ transition but does not rationalize why this transition is so low in energy.

Table 3.7. Orbital Energy and Parentage for Non-Phenyl-Conjugated π-Orbitals.

	Orbital		Atomic Parentage				
	Energy	Symmetry	M	E	P	Cl	Ph
W1	0.59	π*	26.94	30.99	32.99	2.25	6.83
	-5.63	π	37.74	28.44	12.53	16.77	4.52
W2	1.05	π*	32.19	21.44	40.81	1.69	3.87
	-5.25	π	41.61	34.79	7.71	9.58	6.31
Mo1	0.49	π*	28.41	36.54	27.38	1.84	5.83
	-5.76	π	33.59	26.34	14.29	22.66	3.12
Mo2	0.57	π*	33.23	33.72	25.3	2.07	5.68
	-5.51	π	35.95	25.99	12.34	20.26	5.46
Ta1	0.29	π*	30.24	9.98	54.09	1.82	3.87
	-6.23	π	14.55	27.50	37.36	15.24	5.35
Ta2	0.80	π*	35.58	8.10	50.81	2.27	3.24
	-5.97	π	15.84	31.67	30.63	15.74	6.12

3.2.7. Photoluminescence of Mo2.

Photoluminescence studies were conducted on **Mo1**, **Mo2**, Mo(CPh){P(OMe)$_3$}$_4$Cl, **Ta1**, and **Ta2** to explore their relationship to the long-lived emission generally observed for tungsten alkylidyne compounds. Only **Mo2** was found to exhibit photoluminescence in solution at room temperature. The lack of emission from **Mo1** and Mo(CPh){P(OMe)$_3$}$_4$Cl was surprising in view of the strong luminescence found for their tungsten analogues. There are no comparison data for the tantalum complexes, which were also found to be nonemissive in the solid state at 77 K. Emissive compound **Mo2** displays a broad band at room-temperature with λ_{max} = 755 nm in toluene that tails into the NIR-II region (Figure 3.24). The emission profile matches that of other reported d^2 alkylidyne complexes and is consistent with emission from a triplet $^3[d_{xy} \rightarrow \pi^*]$ excited-state.[16, 18-19, 62] The time-resolved emission decay of **Mo2** could be fit with a monoexponential function to give a 595 ns excited-state lifetime across multiple half-lives

(Figure 3.25). Using **W1** as an external reference, the luminescence quantum yield of **Mo2** was determined to be 0.89%.

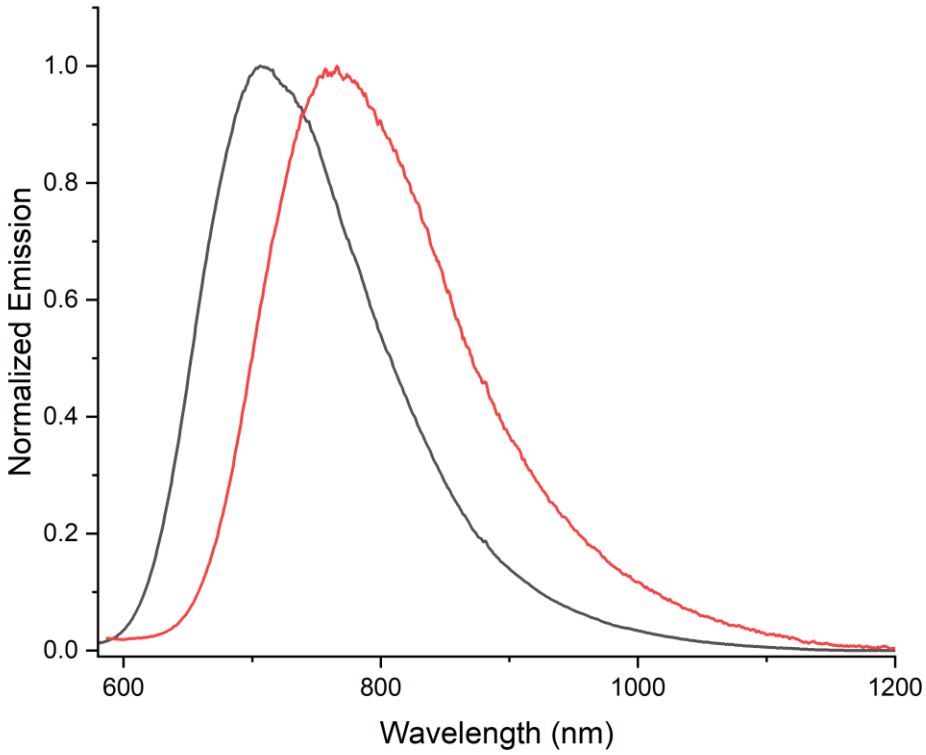

Figure 3.24. Normalized emission spectra of **W2** (black) and **Mo2** (red) in toluene.

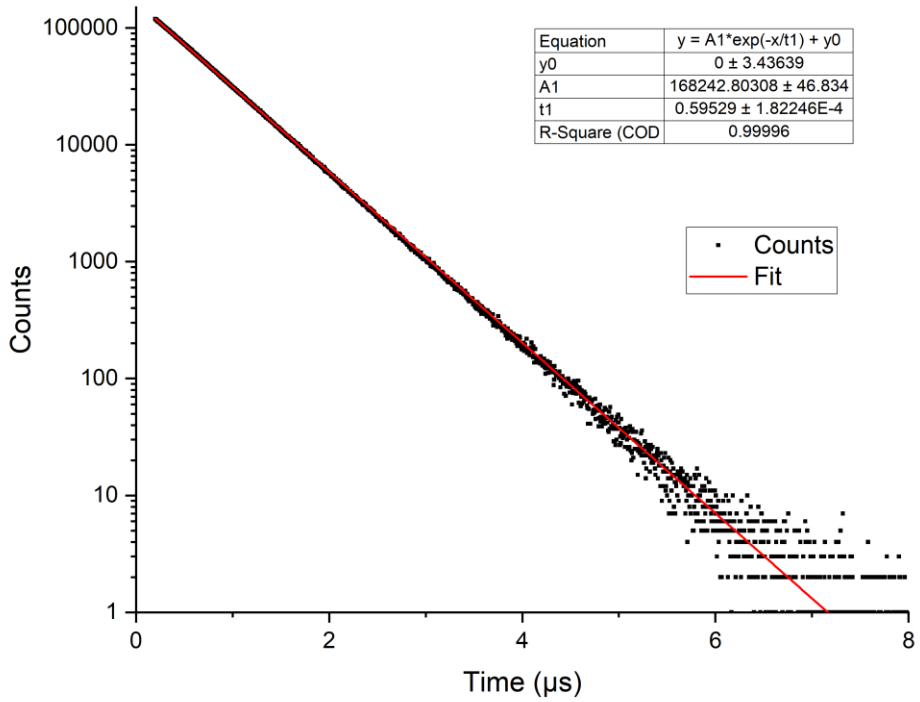

Figure 3.25. TCSPC trace of **Mo2** in toluene using 405 nm excitation and collected using a 680 nm bandpass filter with a 50 nm FWHM.

Compared to its tungsten analogue **W2**, the nonradiative decay rate of **Mo2** is slightly smaller and the radiative decay rate is nearly an order of magnitude smaller (Table 3.8).[15] The reduced radiative decay rate can be partially explained using a Strickler-Berg relationship from the roughly fivefold smaller extinction coefficient of **Mo2,** which, paired with reduced spin-orbit coupling of the second-row transition metal, would lead to smaller radiative decay rates. By itself, the difference in nonradiative decay rate is likely too small for any meaningful conclusions, but slower nonradiative decay rate from a complex with longer emission wavelength emission is contrary to the Energy-Gap Law if these complexes couple similarly to nonradiative decay processes. Plotting this complex on a standard energy-gap law plot compared to similar tungsten alkylidyne chromophores shows **Mo2** well below the trendline (Figure 3.26).

Instead, increased d-d character and the contracted 4d orbitals of **Mo2** help to decouple the excited-state from other active nonradiative decay pathways to increase the excited-state lifetime.

Table 3.8. Photophysical Data for **Mo2** Compared to its Tungsten Analogue.

	λ_{max} (nm)	τ (ns)	Φ_{em}	k_r (s^{-1})	k_{nr} (s^{-1})	$E^{*/ox}$ (V)[b]
Mo2	765	595	0.0089	1.49×10^4	1.67×10^6	-2.6
W2[a]	700	340	0.04	1.1×10^5	2.8×10^6	-2.8

[a] Ref [15] [b] Estimated from sum of $E^{0/+}$ and intersection of normalized absorption and emission profile (Figure 3.27).

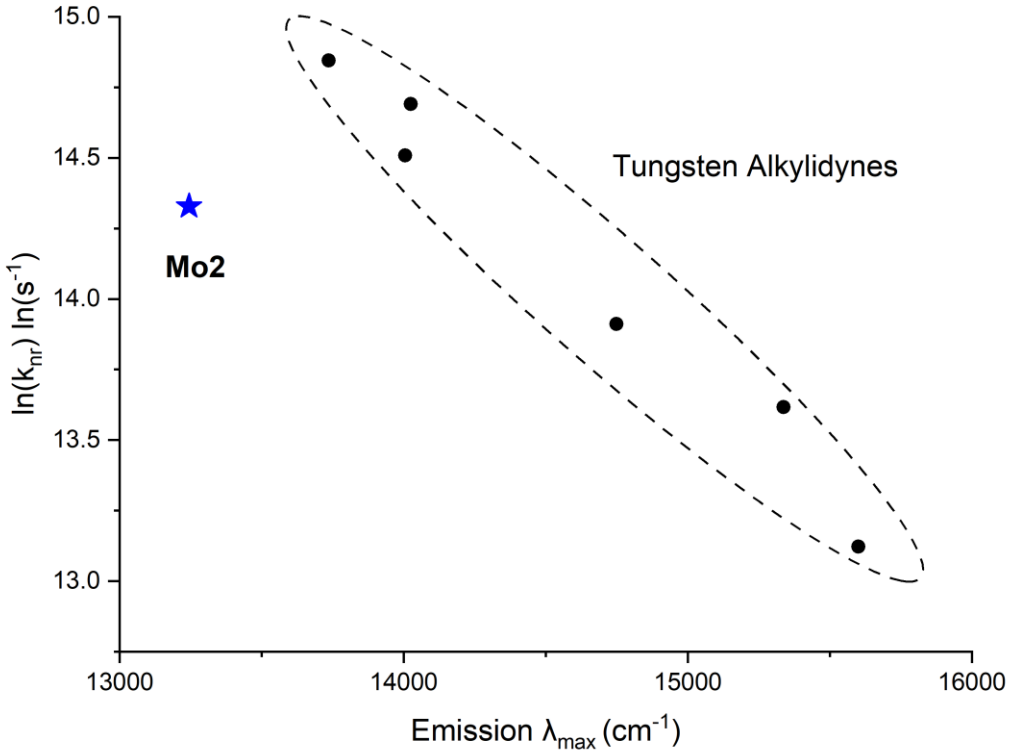

Figure 3.26. Energy gap law plot of **Mo2** compared to other W(CPh-4-R)$(PP)_2$X tungsten alkylidynes.[15]

The emissive $^3[d_{xy} \rightarrow \pi^*]$ excited state was further elaborated using DFT (Table 3.9). To estimate the geometry of the triplet state, an unrestricted open-shell triplet geometry optimization calculation was run for **Mo2**. Inspection of the geometric distortions is consistent with the

population of a $^3[d_{xy} \rightarrow \pi^*]$ state (Table 3.9). Depopulation of the d_{xy} orbital and population of the π^* orbital results in subtle changes in bond lengths about the molybdenum center, including elongation of the calculated Mo≡C bond length by 0.058 Å and elongation of the Mo−$P_{avr.}$ bond length by 0.037 Å. These are both fully consistent with bonding changes from reduced backbonding to the phosphines and formal reduction of the Mo≡C bond order by 0.5.[19] An E_{00} of 14590 cm^{-1} can be estimated by taking the difference in single point energies between the two optimized geometries. This is very close to the experimentally estimated E_{00} of 15200 cm^{-1} by taking the intersection of the intensity normalized emission and absorption bands (Figure 3.27). From previous tungsten benzylidyne work,[15] E_{00} can be estimated using the energy at 10% intensity on the blue flank of the emission band. This gives E_{00} = 15197 cm^{-1}, in good agreement with other values. This supports our calculated geometry being close to the relaxed triplet excited-state. Similar bond changes were observed in a combined experimental and theoretical study on a structurally similar tungsten alkylidyne with supporting dppe ligand by X-ray transient absorption spectroscopy and DFT.[19]

Table 3.9. Comparison of S_0 and T_1 Geometry Bond Lengths (Å) and Angles (˚) for **Mo2**.

	Mo≡C(1)	Mo–Cl	Mo–$P_{avg.}$	C(1)–C(2)	C–Mo–Cl	C(2)–C(1)–Mo	C(1)–Mo–P_{avg}
S_0	1.789	2.609	2.477	1.446	178.59	179.15	94.32
T_1	1.847	2.615	2.504	1.393	177.9	179.7	91.35

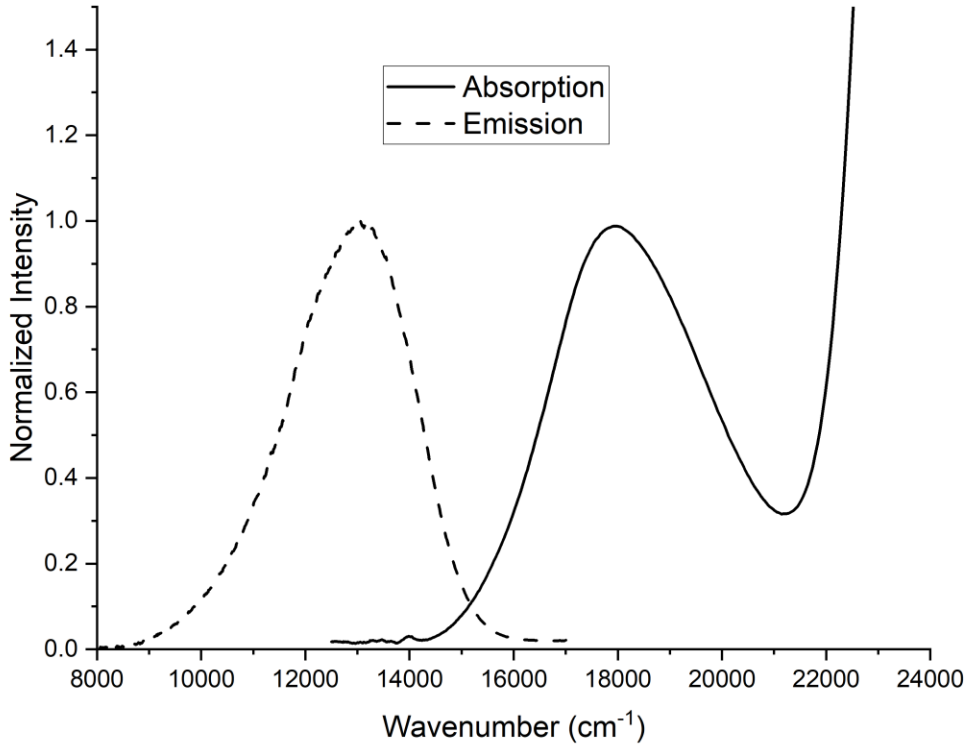

Figure 3.27. Normalized absorption and emission spectra of **Mo2** in toluene.

This is the first example of a molybdenum alkylidyne complex with a room-temperature emissive $^3[d_{xy} \rightarrow \pi^*]$ state. Only one other example of a $^3[d_{xy} \rightarrow \pi^*]$ emissive molybdenum alkylidyne has been reported before (Mo(CPh)(Cp)(CO){$P(OMe)_3$}).[28] The excited-state of this complex was found to be emissive only under cryogenic conditions with an emission lifetime of 8.3 μs at 77 K and did not display detectable emission above the glass-transition temperature of the solvent. From transient-absorption data, it was found to have a 49 ns lifetime at room temperature that was capable of photoreducing $CHCl_3$.[63] The distinct difference in excited-state properties is likely due to several factors. First, the presence of a carbon monoxide ligand has been found to greatly reduce the benzylidyne π* character in the LUMO, leading to increased Mo to CO charge transfer character in the excited state.[64] Consequently, studies of tungsten and

molybdenum alkylidynes with supporting carbonyl ligands have been found to undergo CO photodissociation or insertion to form a ketene as competitive nonradiative decay process.[65-68] The cyclopentadienyl ligand similarly can lead to nonradiative decay pathways due to facile rotation of the ring leading to nonradiative energy loss. Full substitution of the equatorial plane with chelating phosphines removes these limitations and provides improved steric protection of the molybdenum center. While **Mo1** also fits this description, no emission was observed from this complex at room temperature. One possibility is that this results from thermal population of a higher lying triplet d to phosphine charge transfer state from the $^3[d_{xy} \rightarrow \pi^*]$ state that can then nonradiatively relax back to the ground state. Faster nonradiative decay has also been observed in the related **W1** complex[15] compared with **W2**, although it is luminescent.

3.2.8. Synthesis and Characterization of a Seven-Coordinate Molybdenum Hydride.

Given the similarity between **Mo1** and **Mo2** and their isoelectronic tungsten analogues, a d^0 hydride complex analogous to known tungsten and tantalum compounds of form $M(CR)(H)L_4X$ was prepared (Scheme 3.4).[41-45] This was achieved by protonation of **Mo2** by reaction with $HCl \cdot Et_2O$ in THF. Immediately upon addition of acid, a white solid precipitates that is presumed to be the chloride salt $[Mo(CPh)(H)(dppe)_2Cl]Cl$. Salt metathesis with KPF_6 in acetonitrile improves solubility and allows for recrystallization of the final product as a microcrystalline product $[Mo(CPh)(H)(dppe)_2Cl][PF_6]$ (**Mo2H**). Complex **Mo2H** is soluble in polar solvents such as THF, acetonitrile, and 1,3-difluorobenzene. Attempts to prepare the analogous hydride complex from **Mo1** led to formation of an insoluble yellow powder. Attempts at salt metathesis at elevated temperatures with various counterions and solvents did not provide a soluble product suitable for characterization and crystallization.

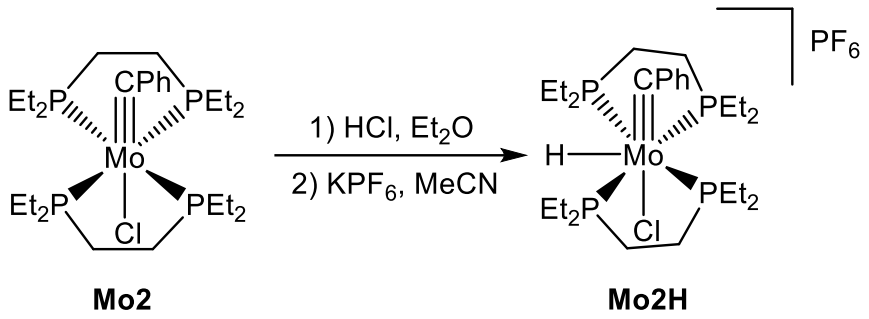

Mo2 **Mo2H**

Scheme 3.4. Synthetic route for **Mo2H**.

Compound **Mo2H** was characterized by NMR spectroscopy and X-ray crystallography. The ^{1}H NMR spectrum of **Mo2H** displays a quintet at −0.05 ppm corresponding to the hydride ligand split by four equivalent phosphorus nuclei (Figure 3.28). This indicates rapid tautomerization across the alkylidyne on the NMR timescale as proposed by Schrock and observed in related tungsten and tantalum hydride complexes.[42-45] A similar quintet was observed for $[W(CPh)(H)(dppe)_2Cl]^+$.[41] The ^{31}P{^{1}H} NMR displays a single broad resonance at 57.7 ppm, similar to that seen in related tungsten compounds and consistent with dynamic behavior and fast tautomerization on the NMR timescale. The alkylidyne α carbon resonance was not observed by standard ^{13}C{^{1}H} NMR spectroscopy, probably because of the effect of the ^{31}P broadening on the lineshape of the expected quintet, so a double ^{1}H and ^{31}P decoupling scheme was used to allow resolution of the alkylidyne resonance at 274.0 ppm. This resonance is shifted downfield from the alkylidyne resonance in **Mo2** by 15.9 ppm and is consistent with an alkylidyne species. The other ^{13}C resonances show relatively little shift from **Mo2** by comparison, indicating relatively little electronic perturbation outside of the Mo−C fragment.

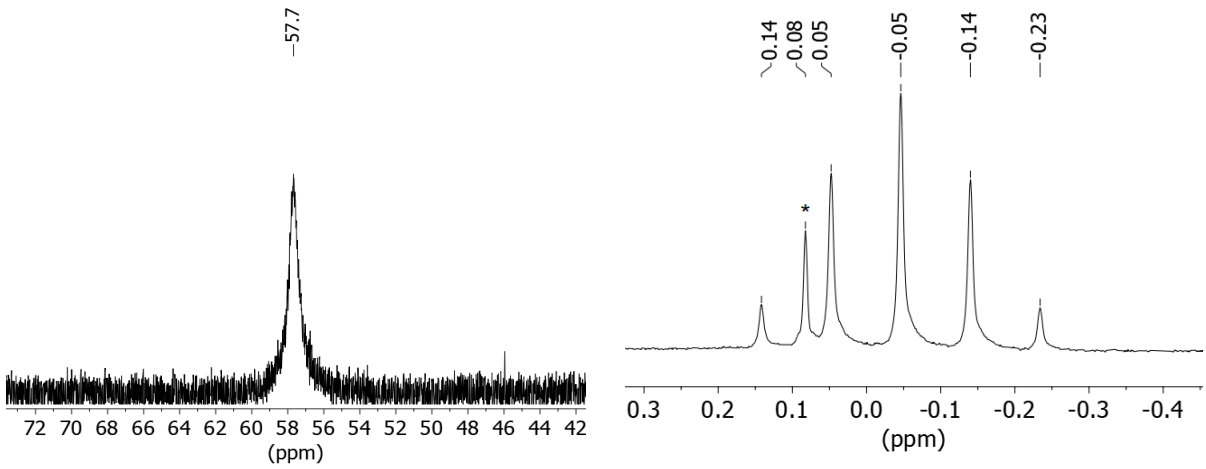

Figure 3.28. NMR spectra of **Mo2H**. Left: $^{31}P\{^{1}H\}$ NMR (202 MHz, CD_2Cl_2) of phosphine region. Right: ^{1}H NMR (400 MHz, CD_2Cl_2) of hydride region. *denotes silicone grease impurity.

The molecular structure of **Mo2H** was determined by single crystal X-ray diffraction (Figure 3.29 and Table 3.10). The metal bound hydride was clearly resolved in the difference Fourier map and was able to be independently refined without any constraints. The hydride is found to occupy the equatorial plane of the complex between the two chelating phosphines to form a pentagonal bipyramidal geometry. The measured Mo−H bond of 1.67(3) Å is consistent with a molybdenum hydride. The presence of the hydride in the equatorial plane leads to an opening in the cleft between the two phosphines leading to desymmetrization and elongation of the proximal and distal metal-phosphorus bonds to Mo−$P_{avr.}$ 2.5585[6] Å and 2.4809[6] Å respectively. The Mo≡C bond length of 1.793(2) Å is within error of that observed for **Mo2** with slight contraction of the Mo−Cl bond from 2.5937[5] Å to 2.5638(6) Å. The expansion of the equatorial ligands, elongation of the Mo−P bonds, and lack of a change in the metal-alkylidyne bond length all suggest that the metal d_{xy} orbital participates in the Mo–H bond and matches with the refined location of the hydride. Axial bond angles along the alkylidyne are only slightly perturbed and further highlight the equatorial coordination of the hydride in **Mo2H**.

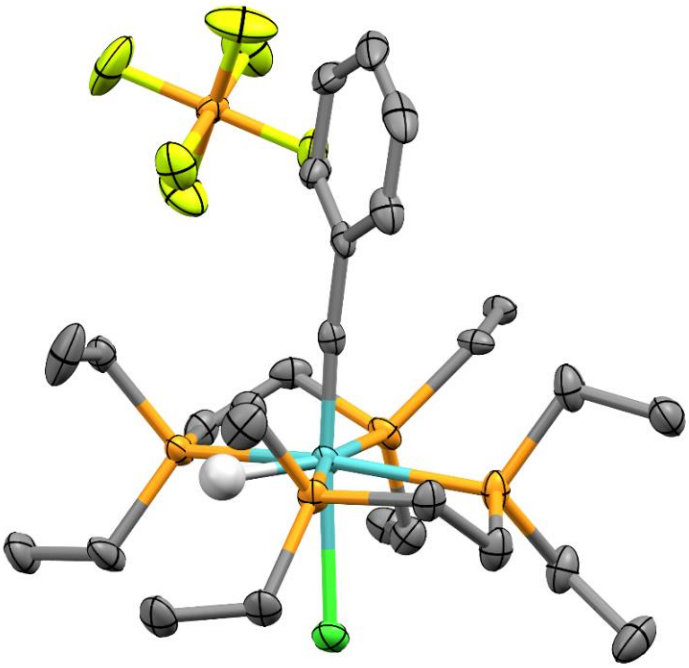

Figure 3.29. Thermal-ellipsoid representation of the structure of **Mo2H** (50% probability ellipsoids). Hydrogens except for hydride and interstitial solvent have been omitted for clarity.

Table 3.10. Crystallographic Bond Lengths (Å) and Angles (˚) for **Mo2** and **Mo2H**.

	Mo≡C(1)	Mo–Cl	Mo–P_{avr}		C(1)–C(2)	C(1)–Mo–Cl	C(2)–C(1)–Mo
Mo2	1.8036[19]	2.5937[5]	2.4689[5]		1.447[3]	177.38[6]	177.90[15]
Mo2H	1.793(2)	2.5638(6)	2.4809[6]	2.5584[6]	1.449(3)	175.03(6)	175.73(15)

With confirmation of the structure **Mo2H** established, understanding the bonding of the hydride to the molybdenum center and how it compares to related third row seven-coordinate hydrides was studied. The pK_a of **Mo2H** was estimated using pK_a bracketing experiments. As both the base (**Mo2**) and conjugate acid (**Mo2H**) have been isolated, NMR equilibration studies for protonation and deprotonation of the alkylidyne were performed by addition of the appropriate acid or base respectively. These measurements were conducted in THF-H_8 spiked with C_6D_6 for NMR lock and analyzed using $^{31}P\{^1H\}$ NMR spectroscopy (Figure 3.64). From

this, the pK_a of **Mo2H** was found to lie between collidine and dimethylamino-pyridine (DMAP) bracketing the pK_a between 13.6 and 10.4.[69] This is notably less basic than that determined for a related of $[W(H)(CPh)(dmpe)_2Cl][B(C_6F_5)_4]$ complex at 16.8.[41] To further compare the binding strength of the hydride, the BDFE of the two complexes in THF were calculated using standard free energy relationships for PCET (Equation 3.1),[70] which was determined to be 63.8 kcal/mol for $[W(H)(CPh)(dmpe)_2Cl][B(C_6F_5)_4]$, and 59.7<BDFE<55.4 8 kcal/mol for **Mo2H**. In general, isoelectronic second and third row transition metals have comparable BDFE values.[71] The comparison between these two complexes is complicated by the difference in steric demand of the two phosphines and the difference in counterion. Bond differences about the metal center between the two complexes are marginal and both counterions are expected to be sufficiently noncoordinating to limit any significant electronic effect. A similar trend in BDFE was found for a set of structurally related $M(H)(CO)_2(PP)_2$ hydrides.[72] While no discussion of this difference was made, the observation of this BDFE difference in a structurally related seven-coordinate metal hydride suggests that this property may arise from the inherent ability of these metals to adopt a seven-coordinate geometry.

Equation 3.1 $BDFE_{sol}(X-H) = 1.37pK_a + 23.06E^{\circ} + C_{G,sol}$

3.2.9. Synthesis and Characterization of a Seven-Coordinate Tantalum Hydride.

A seven coordinate d^0 tantalum hydride was hypothesized to also be accessible using the same synthetic protocol. Due to the instability of **Ta2**, **Ta1** was used as the synthon for the hydride. Initial protonation attempts using $HCl{\cdot}Et_2O$ showed evidence of forming the desired product by ^{31}P NMR but attempts at purification and recrystallization of the product invariably led to decomposition. Upon salt metathesis with KPF_6, one decomposition product was isolated

and identified as [H·dppe][PF_6], suggesting ligand dissociation and decomposition of the tantalum complex. Protonation with dilute ethereal solutions of HBF_4, TfOH, and HPF_6 at low temperature were all unable to deliver the final product in stable form. Protonation was also attempted using weaker organic acids such as [H·Py][PF_6], but despite the expected higher basicity of the tantalum center, no reaction was observed even at elevated temperatures. Moving to even larger counterions, protonation was attempted using [$HBArF_{20}$][Et_2O]$_2$ as an acid (Scheme 3.5).[73] This product showed better stability than other derivatives, but still decomposed to the corresponding phosphonium salt and an uncharacterized grey powder even at low temperatures. The solubility of the [$BArF_{20}$]$^-$ counterion also inhibited recrystallization the product as the product was soluble in all solvents except for pentane. This prevented separation of the phosphonium salt and the [$HBArF_{20}$][Et_2O]$_2$ reagent from the desired hydride due to the similar solubility of these complexes. This product always formed as an oil in all solvents except when cooled in pentane solutions, which would deposit the product as a sticky solid and prevented further separation of products.

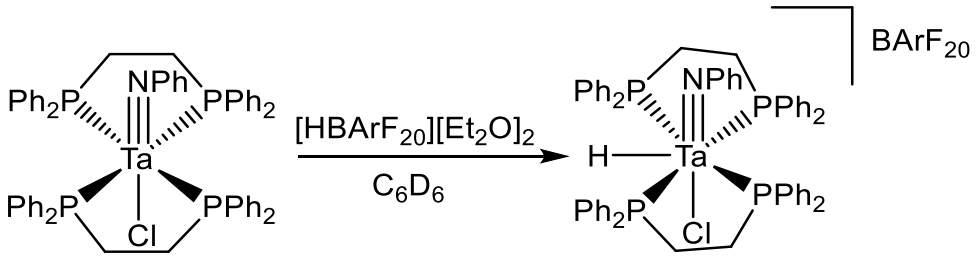

Scheme 3.5. Synthetic route for **Ta1H**.

Compound **Ta1H** was characterized in situ by measuring its NMR spectrum immediately upon addition of [$HBArF_{20}$][Et_2O]$_2$ to **Ta1** in a J. Young tube in C_6D_6 (Scheme 3.5). Rapid color change from dark brown to colorless is observed upon addition of acid. The ^{1}H NMR spectrum of the reaction displays a diagnostic hydride resonance as a triplet of triplets at 11.32 ppm with

J_{HP} = 89.2 and 12.5 Hz corresponding to ^{31}P splitting by the proximal and distal phosphines in the pentagonal plane (Figure 3.30). The chemical shift and coupling constants are fully consistent with a tantalum-centered hydride and match splitting patterns for $Ta(H)(CCMe_3)(dmpe)_2(ClAlMe_3)$ and, at low temperature, for $[W(H)(CPh)(dppe)_2][PF_6]$.[41-42] Despite the presence of decomposition products, unique aryl and aliphatic proton resonances of the hydride complex were identified from the phosphine and from the imido that integrated correctly with respect to the hydride consistent with the formulation as protonated **Ta1H**. Similarly, $^{31}P\{^1H\}$ NMR showed two complex multiplets at δ = 53.3 ppm and δ = 27.5 ppm at room temperature indicating desymmetrization of the four phosphorus nuclei into two separate pairs matching observed splitting patterns for the complexes described above.

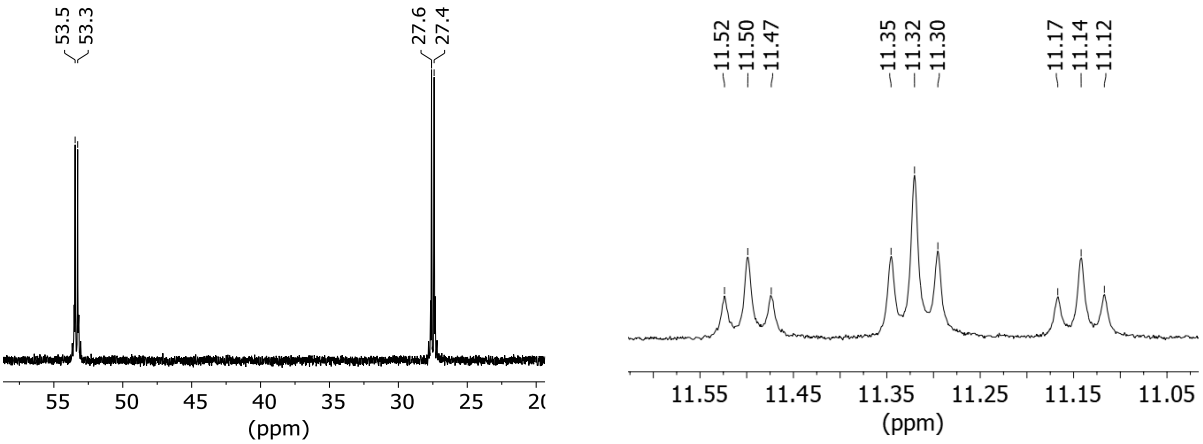

Figure 3.30. NMR spectra of *in-situ* generated **Ta1H**. Left: $^{31}P\{^1H\}$ NMR (202 MHz, C_6D_6) of phosphine region. Right: ^1H NMR (500 MHz, C_6D_6) of hydride region.

3.2.10. DFT Calculations of the Hydride Complexes.

The experimental analysis of **Mo2H** was supplemented with DFT calculations using a simplified geometry by omitting the PF_6 counterion (Figure 3.31 and Table 3.11). The optimized geometry shows good agreement with the experimental geometry with general bond length

deviations under 0.05 Å. In addition to the optimized metal hydride global minimum, an "alkylidene" (protonated alkylidyne α-carbon atom) local minimum was optimized as well. For the alkylidyne protonated minimum, the geometry about Mo returns more closely to the unprotonated d^2 structure with some symmetrization of the equatorial phosphines and the proton binding side-on to the alkylidyne in the same plane as the phenyl ring. This leads to slight deviation of the C−Mo−Cl bond angle from linearity to 166.1 degrees. The proton is most closely bound to the alkylidyne with a C−H bond length of 1.186 Å, but also exhibits close contact with the molybdenum center with a Mo−H bond length of 1.820 Å. A short Mo≡C bond length of 1.846 Å is observed indicating that the molybdenum-carbon bond should still be described as a benzylidyne and not a benzylidene. This suggests that the alkylidyne protonated minimum may be better described as a protonation of a Mo≡C π bonding orbital. Energetically, alkylidyne protonation is found to be only 2.95 kcal/mol above metal-centered protonation consistent with facile proton equilibration observed by NMR spectroscopy. Similar calculations for analogous tungsten complex $[W(H)(CPh)(dmpe)_2Cl]^+$ showed metal-centered protonation favored by 5.84 kcal/mol. This is close to the experimental BDFE difference determined experimentally between **Mo2** and $[W(H)(CPh)(dmpe)_2Cl][B(C_6F_5)_4]$.

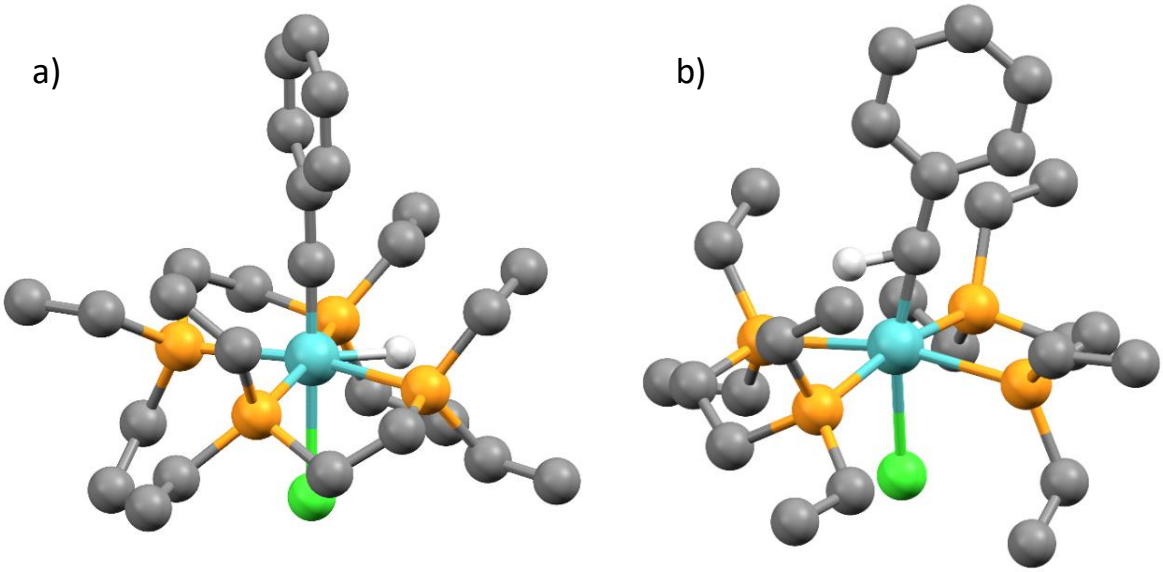

Figure 3.31. DFT optimized geometries of **Mo2H** with a) metal protonation and b) alkylidyne protonation.

Table 3.11. Comparison of DFT Calculated Bond Lengths (Å) and Angles (˚) at Different Protonation Sites.

	Mo2H		$[Ta(H)(NPh)(dmpe)_2Cl]^+$	
Geometry	Mo−H	Alkylidyne-H	Ta−H	Imido−H
M≡E	1.778	1.846	1.820	1.978
M–Cl	2.589	2.506	2.512	2.454
$M–P_{avr}$	2.512 2.592	2.5313	2.581 2.662	2.576
E–C(2)	1.444	1.446	1.366	1.41
M-H	1.70	1.82	1.820	2.366
E–M–Cl	178.3	166.1	174.9	177.6
C(2)–E–M	179.4	177.4	176.4	151.6
P(1)-M-P(2)	86.17	97.5	85.3	102.2
P(3)-M-P(4)	117.7	98.5	122.6	99.6

Complex **Ta1H** was studied by DFT using a simplified model substituting phosphine phenyl groups with methyl groups to reduce computational cost (Figure 3.32). This will slightly increase the basicity of the metal center but otherwise reproduce the electronic structure of the compound. Calculated geometric distortions about the metal center upon metal-centered protonation are like those observed for the molybdenum alkylidyne hydride, including desymmetrization of the Ta−P bond lengths, opening of the phosphine cleft, and contraction of the Ta−Cl bond length. The calculated short Ta−H bond length of 1.820 Å is consistent with a tantalum hydride. The predicted Ta−H bond length is close to that of $Ta(H)(CCMe_3)(dmpe)_2(ClAlMe_3)$ (1.796(49) Å) determined by single crystal X-ray diffraction.[42] The imido-protonated ("amide") geometry was also optimized to gain insight into the structural rearrangement during tautomerization. Here, the Ta≡N bond length is elongated by 0.158 Å with a corresponding contraction of the trans Ta−Cl bond by 0.056 Å. The C−N−Ta angle is distorted away from linearity with a long Ta−H distance of 2.366 Å. These structural features indicate protonation of the imido to form a N−H bond. As the predicted C(2)–N–Ta bond angle is 151.6˚ and not quite 120˚, we suggest that this complex still possesses some imido character.

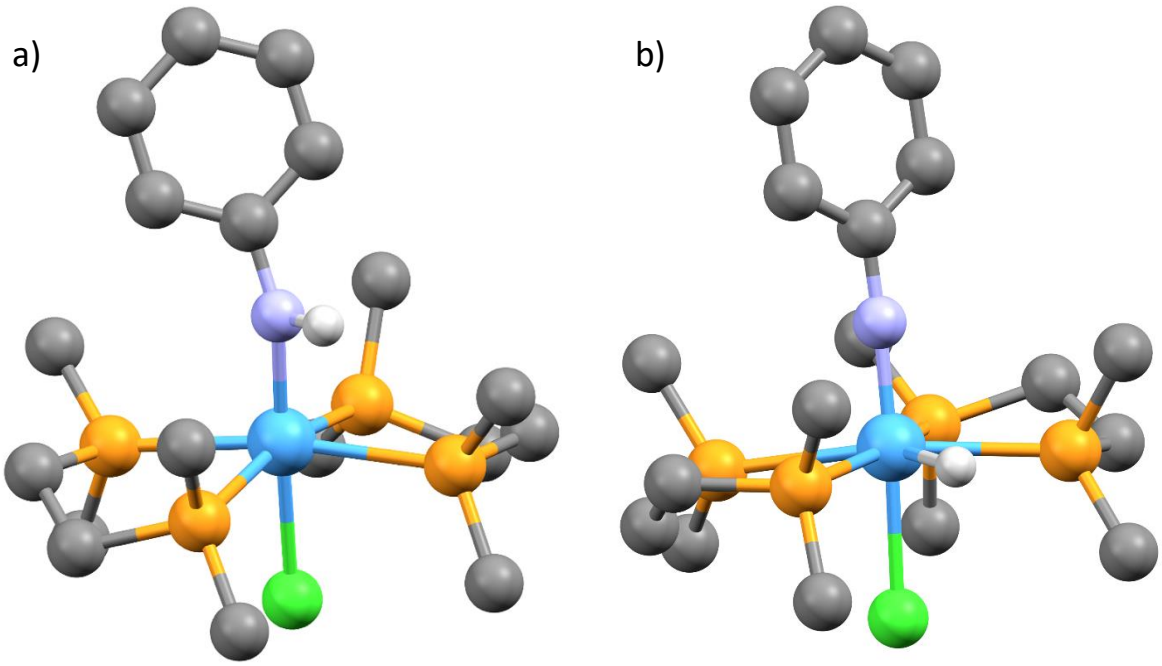

Figure 3.32. DFT optimized geometries of $[Ta(H)(NPh)(dmpe)_2Cl]^+$ with a) metal protonation and b) imido protonation.

The structural perturbations for **Ta1H** strongly differ from the alkylidyne-protonated geometry calculated for **Mo2H**. The large Ta−H bond length indicates that the proposed π-bond interaction observed in the molybdenum alkylidyne is not present. Energetically, the imido protonated tautomer is found to be 22.7 kcal/mol higher in energy by DFT than the metal-protonated imido. This large energy barrier is consistent with the absence of tautomerization observed at room temperature by NMR spectroscopy. Assuming the BDFE for $[W(H)(CPh)(dmpe)_2Cl][B(C_6F_5)_4]$ and **Ta1H** are close due to their isoelectronic description, the increase in pK_a of the metal center can be estimated from the decrease in the one-electron oxidation potential of **Ta2** from Equation 3.1. This is found to be 9.3 kcal/mol, which is much smaller than the differences in the calculated tautomerization barrier between this complex and both **Mo2H** and $[W(H)(CPh)(dmpe)_2Cl]^+$ (Ta: 22.7 kcal/mol, W: 5.84 kcal/mol, Mo: 2.95

kcal/mol). This indicates that other factors contribute to the large tautomerization barrier. The DFT calculated geometry shows dramatic structural deformation upon imido protonation which can contribute to this energetic barrier. Additionally, the basicity of the imido can be compared to the carbyne by analysis of the relative HOMO-1 π-bonding orbital energies. For **Ta2**, this orbital is 0.86 eV lower than the corresponding orbital for **Mo2** suggesting that the imido should be less basic than the carbyne. These three effects contribute to the high barrier for imido protonation leading to the observed splitting pattern for the hydride. The steric profile of the dppe ligand should not play a major role in hindering tautomerization since the isoelectronic $[W(H)(CPh)(dppe)_2][PF_6]$ displayed rapid tautomerization on the NMR timescale at room temperature.[41] Tautomer freezing could allow for interesting studies on the relative kinetics of heteroatom-centered protonation and metal-centered protonation and their influence on H_2 splitting and hydrogen atom transfer reactions.[15, 41] Unfortunately, this complex was unable to be isolated in stable form which prevented further study. Given that the tantalum alkylidyne hydride $Ta(H)(CCMe_3)(dmpe)_2(ClAlMe_3)$ is reportedly stable,[42] another question that arises is whether metal-centered protonation facilitates decomposition through ligand dissociation.

3.3. Conclusions.

The successful synthesis of the isoelectronic tantalum imido and molybdenum alkylidyne complexes presented here in addition to previously reported tungsten alkylidyne complexes allow for a unique comparison of complexes with metal-ligand multiple bonds and how their electronic structure and reactivity change with this perturbation. Structurally, these complexes possess very similar geometries around the metal center with exception of the elongation of the $Ta{-}P_{avr}$ bond length due to the increased size of the Ta d_{xy} orbital. Electronically, the Ta d_{xy} orbital is dramatically destabilized compared to the group 6 complexes and results in contracted

HOMO-LUMO energy gaps experimentally manifested as a redshift in the $^1[d_{xy} \rightarrow \pi^*]$ absorption energy. For the molybdenum complexes, the d_{xy} orbital is slightly less reducing due to the reduced energy of the 4d compared to 5d orbitals but effectively no change in $^1[d_{xy} \rightarrow \pi^*]$ absorption energy is found due to concomitant lowering of the LUMO energy. This results in **Mo2** possessing suitable electronic properties to serve as a photocatalyst akin to tungsten alkylidyne complexes. Complex **Mo2** was found to luminesce with a lengthened excited-state lifetime and lower quantum yield than **W2**. The higher energy of the tantalum d_{xy} orbital on the other hand leads to nonradiative quenching of the excited state due to the contracted HOMO-LUMO energy gap. Finally, protonation of the molybdenum and tantalum complexes to the corresponding hydride was successfully studied by NMR. The molybdenum hydride bears close resemblance to the previously reported tungsten complexes and displays rapid tautomerization across the alkylidyne. The tantalum hydride was found to be unstable and was unable to be isolated. Characterization of the NMR of this complex *in-situ* shows freezing of the hydride within a phosphine cleft attributed both to increased basicity of the tantalum center, reduced basicity of the imido nitrogen, and increased reorganization energy.

3.4. Experimental Section

3.4.1. General Procedures

All manipulations were performed under a nitrogen atmosphere using standard Schlenk and glovebox techniques, unless otherwise noted. Solvents used for synthesis and electrochemistry were HPLC grade and purified by passing through an anaerobic, stainless steel system consisting of either two 4.5 in × 24 in (1 gal) columns of activated A2 alumina (CH_3CN, Et_2O, CH_2Cl_2 (DCM), THF) or one column of activated A2 alumina and one column of activated

BASF R3-11 catalyst (toluene, pentane)[74] and stored over activated 4A molecular sieves. Solvents used for NMR spectroscopy were degassed using three freeze-pump-thaw cycles and stored under N_2 over 4A molecular sieves. $[Mo\{C(O)Ph\}(CO)_5][NMe_4]$,[47] $Ta(NPh)(dme)Cl_3$ (dme = 1,2-dimethoxyethane),[75] $W(CPh)(depe)_2Cl$,[15] $W(CPh)(dppe)_2Cl$,[15] $[HColl][PF_6]$,[76] and $[HBArF_{20}][Et_2O]_2$[73] were prepared according to literature methods. $[NBu_4][PF_6]$ was recrystallized twice from absolute ethanol and then dried under vacuum at 100 °C for 12 h. Ferrocene was recrystallized from absolute ethanol and then sublimed under vacuum. All other reagents were procured from commercial sources and used as received. ^1H, $^{13}C\{^1H\}$, and $^{31}P\{^1H\}$-NMR spectra were collected using a 500 MHz Bruker Avance-II+ spectrometer equipped with a $^1H\{^{19}F, ^{13}C, ^{31}P\}$ QNP probe, using Topspin 2.1. Chemical shifts were referenced against known solvent resonances.[77]

3.4.2. Electronic Spectroscopic and Photophysical Measurements.

Solution samples for electronic spectroscopy were prepared in the glovebox in sealable cuvettes with 1 cm path lengths. Electronic-absorption spectra were collected using a Cary 300 UV-visible spectrophotometer. Emission spectra were recorded with a wavelength-calibrated Photon Technology International (PTI) Quantmaster fluorimeter equipped with Peltier-cooled R928 photomultiplier tube (PMT) and InGaAs array detectors. The emission monochromator was wavelength-calibrated using the emission lines of an Ar lamp with wavelength accuracy < 0.5 nm over the entire detection range. The excitation monochromator was wavelength-calibrated using the calibrated emission monochromator. Emission spectra were collected using both detectors, individually corrected for instrument response, intensity-normalized in the overlapping wavelength region (700–800 nm) and merged into a single spectrum. Relative emission quantum yields were measured using optically dilute samples (absorbance < 0.1) against an absorbance-

matched sample of $W(CPh)(dppe)_2Cl$ in toluene.[15] Time-domain lifetimes were measured on a ChronosBH fluorometer (ISS, Inc.) using time-correlated single photon counting (TCSPC) methods. The fluorometer contained Becker-Hickl SPC-130 detection electronics and an HPM-100-40 Hybrid PMT detector. Excitation was provided by a 405 nm picosecond pulsed laser source (Hamamatsu PLP-10). Emission was collected using a red-sensitive amplified PMT H7422-50 detector. The instrument response function (IRF) was measured to be approximately 0.1 ns using a 1% concentration scattering solution of Ludox LS colloidal silica in deionized water. Luminescence decay lifetimes were fit via using Origin software. Analysis of residual plots indicate all samples exhibit single exponential decay with additional decay components not significantly improving the overall goodness of fit.

3.4.3. Electrochemistry

Cyclic voltammetry experiments were conducted at room temperature under a nitrogen atmosphere in a glovebox with a Bioanalytical Systems 100 B/W Electrochemical Workstation. A three-electrode configuration was utilized with a Pt-disk working electrode (area ~ 0.2 cm^2), a Pt-disk counter electrode, and a Ag-wire quasi-reference electrode. Ferrocene was added at the conclusion of each experiment as an internal redox-potential reference. Measurements were performed on THF solutions containing roughly 0.001 M analyte and 0.1 M $[NBu_4][PF_6]$ as supporting electrolyte.

3.4.4. Density Functional Theory (DFT) Calculations

DFT calculations were performed using ORCA software package version 4.2.1.[78-79] Geometry optimizations were carried out using the PBE0 hybrid functional.[80-81] For Mo compounds, the Def2-SVP basis set was used for all atoms.[82] For Ta and W compounds, the

SARC-ZORA-SVP basis set[83] was used for Ta and W with custom Grid IntAcc set to 10 and the ZORA-Def2-SVP basis set was used for all other atoms with the ZORA hamiltonian.[84] No symmetry constraints were applied. The RIJCOSX algorithm[85-86] was used with DEF2/J auxiliary basis sets[87-88] to accelerate the calculation with GRID5 and GRIDX5 integration grids (Mo compounds) or GRID6 and GRIDX6 integration grids (Ta/W compounds) for all atoms. The lack of imaginary frequencies confirmed that the calculated geometries were local minima on the calculated potential energy surface. Kohn-Sham orbitals were visualized using Avogadro 1.2.0.[89]

3.4.5. Single-Crystal X-Ray Diffraction Measurements

Diffraction data were measured at 100 K on a Bruker D8 VENTURE diffractometer equipped with a microfocus Mo-target X-ray tube (λ = 0.71073 Å) and PHOTON 100 CMOS detector. Data were collected using ω scans to survey a sphere of reciprocal space. Data reduction and integration were performed with the Bruker APEX3 software package (Bruker AXS, version 2017.3-0, 2018). Data were scaled and corrected for absorption effects using the multi-scan procedure as implemented in SADABS (Bruker AXS, version 2014/5).[90] The structure was solved by SHELXT (Version 2018/2)[91] and refined by a full-matrix least-squares procedure using OLEX2[92] (XL refinement program version 2018/3)[91]. All atoms were refined with anisotropic thermal parameters. Hydrogen atoms were included in idealized positions for structure factor calculations.

3.4.6. Synthesis and Characterization of Compounds

3.4.6.1. Mo(CPh){P(OMe)$_3$}$_4$Cl. Synthesis of this complex was adapted from a method reported by Mayr and coworkers.[46] A stirred solution of [Mo{C(O)Ph}(CO)$_5$][NMe$_4$] (2.41 g, 5.77 mmol) in DCM (30 mL) was cooled to −78 ˚C using a dry-ice/isopropanol bath. To this,

oxalyl chloride (3 mL, 2M in DCM) was slowly added via syringe, causing the reaction mixture to rapidly turn black. The solution was stirred for 1 h before slowly warming to −30 ˚C by switching the dry-ice/isopropanol bath to a $CaCl_2$/ice bath. Over the course of 15 minutes, the solution slowly lightened to a light orange color. After 15 minutes, $P(OMe)_3$ (5 mL, 42.3 mmol) was added, and the solution was allowed to warm to room temperature. The reaction mixture was then heated to 55 ˚C for 5 h, during which it slowly turned brownish-orange. The solution was then allowed to cool, filtered through Celite, and washed with additional DCM (3 × 15 mL). The filtrate and volatile components removed under vacuum to leave an orange-brown solid. This solid was suspended in neat trimethyl phosphite (30 mL) and heated for 16 h at 70 ˚C, during which the solution gradually turned dark orange. Volatile components were removed once again under vacuum, leaving a dark orange solid. This solid was extracted into Et_2O (15 mL), filtered through Celite, and washed with additional Et_2O (3 × 10 mL) until the filtrate was colorless. The filtrate was then concentrated in vacuo to 10 mL and cooled to −30 ˚C overnight to yield a large crystalline mass, which was collected by filtration and dried under vacuum (1.41g, 34% yield). The ^1H and ^{31}P NMR spectra match literature values for this compound.[46]

3.4.6.2. Mo(CPh)(dppe)$_2$Cl (Mo1). To a stirred solution of $Mo(CPh)\{P(OMe)_3\}_4Cl$ (0.200 g, 0.278 mmol) in toluene (30 mL) at room temperature was added 1,2-bis(diphenylphosphino)ethane (0.232 g, 0.584 mmol). The solution was then heated to 110 ˚C for 16 h, during which the color changed from orange to blood red to finally red-orange. The reaction mixture was then cooled to room temperature and reduced in volume to 15 mL under vacuum. Diethyl ether (50 mL) was added, which induced precipitation of an orange powder that was collected by filtration. The crude product was recrystallized by dissolving it in a minimum amount of dichloromethane (20 mL), adding diethyl ether (100 mL), and cooling the resulting

suspension to –30 ˚C. The resulting orange microcrystalline powder was isolated by filtration and dried under vacuum (0.210 g, 74% yield). Crystals suitable for single-crystal X-ray diffraction experiments were grown by slow vapor diffusion of diethyl ether into a THF solution of the compound at –30 ˚C. ^{1}H NMR (500 MHz, C_6D_6, Figures 3.33 and 3.34): δ 7.63 (br, 8H, o-PPh_2), 7.54 (br, 8H, o-PPh_2), 7.01 (m, 4H, p-PPh_2), 6.95 (m, 12H m, p-PPh_2), 6.84 (t, 8H, m-PPh_2), 6.76 (t, 1H, p-CPh), 6.54 (m, 2H, m-CPh), 5.75 (d, 2H, o-CPh), 2.74 (br m, 4H, $PC\underline{H}_2C\underline{H}_2P$), 2.47 (br m, 4H, $PC\underline{H}_2C\underline{H}_2P$). ^{13}C{^{1}H} NMR (126 MHz, CD_2Cl_2, Figures 3.35 and 3.36): δ 146.57 (ipso-C_6H_4), 140.35 (mC_6H_4), 138.88 (C_6H_4), 134.29 (PPh_2), 133.69 (PPh_2), 130.67 (C_6H_4), 128.92 (PPh_2), 128.75 (PPh_2), 127.91 (PPh_2), 127.54 (PPh_2), 126.18 (PPh_2), 124.07 (PPh_2), 29.72 (q, PCH_2CH_2P); MoC not observed. ^{31}P{^{1}H} NMR (202 MHz, CD_2Cl_2, Figure 3.37): δ 57.7 (s). HR-MS (THF, 0V, *m/z*): 1012.1903 (Calc. 1012.1854).

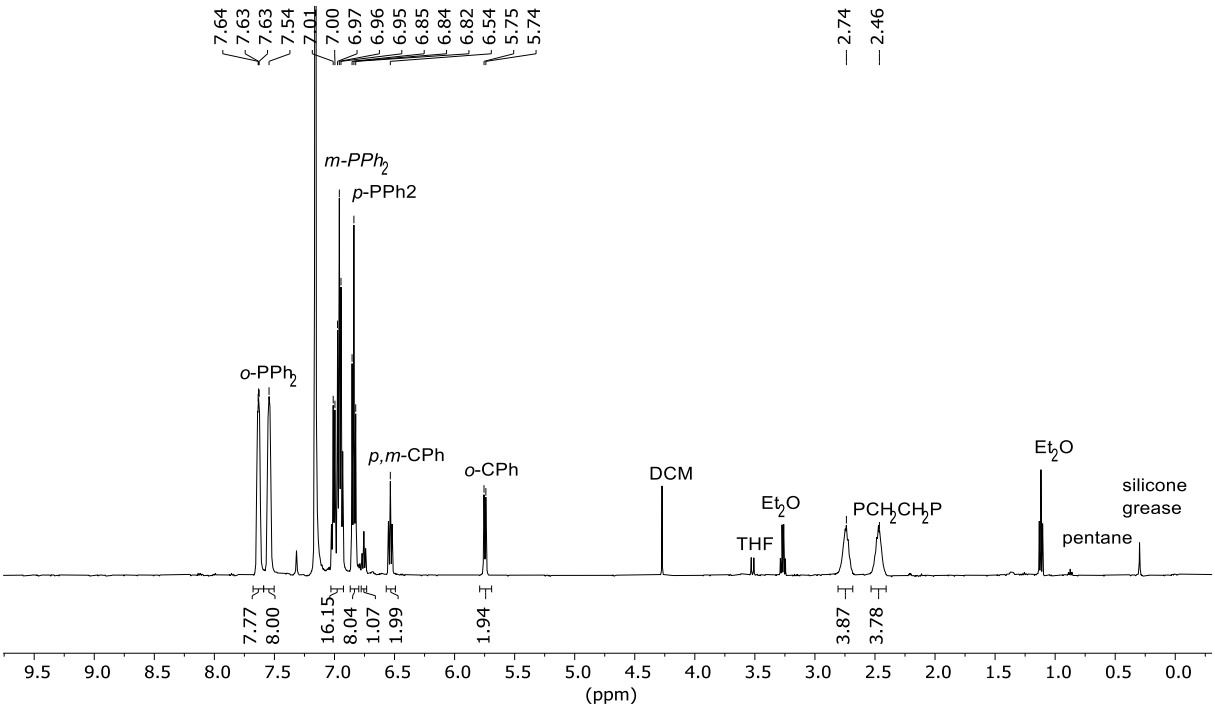

Figure 3.33. ^{1}H NMR spectrum (500 MHz) of **Mo1** in C_6D_6 (7.16 ppm).

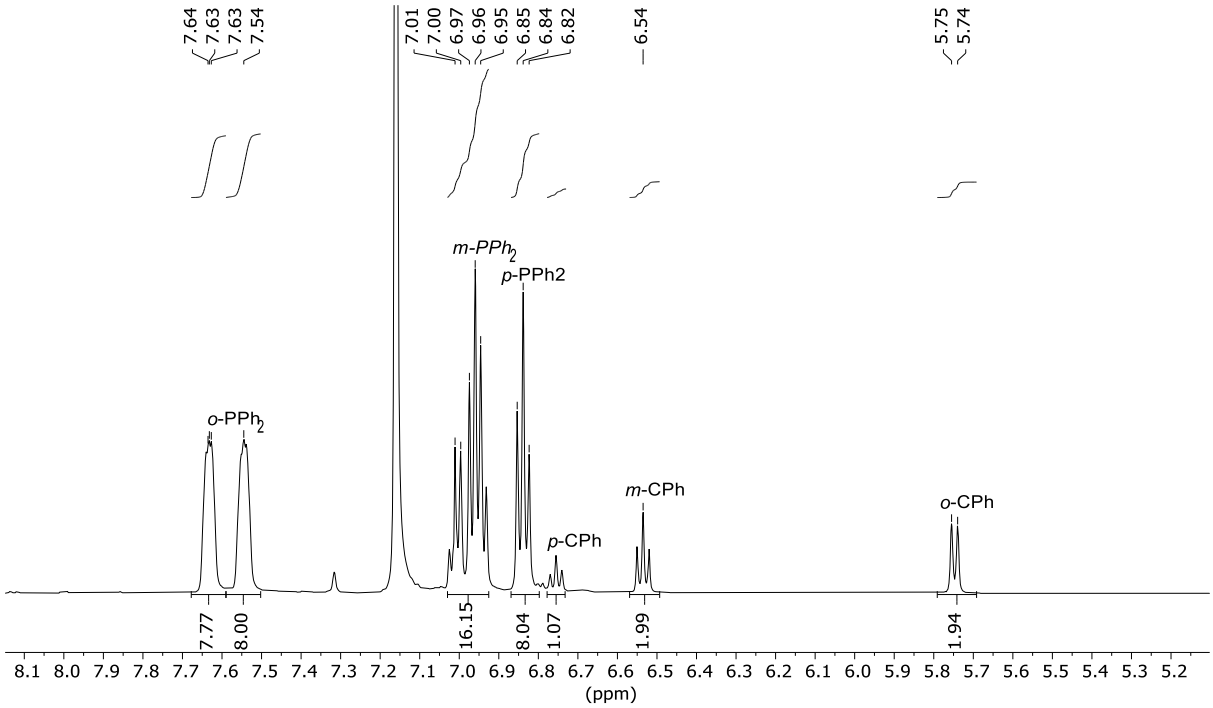

Figure 3.34. ^{1}H NMR spectrum (500 MHz) of **Mo1** in C_6D_6 (7.16 ppm) showing aromatic region.

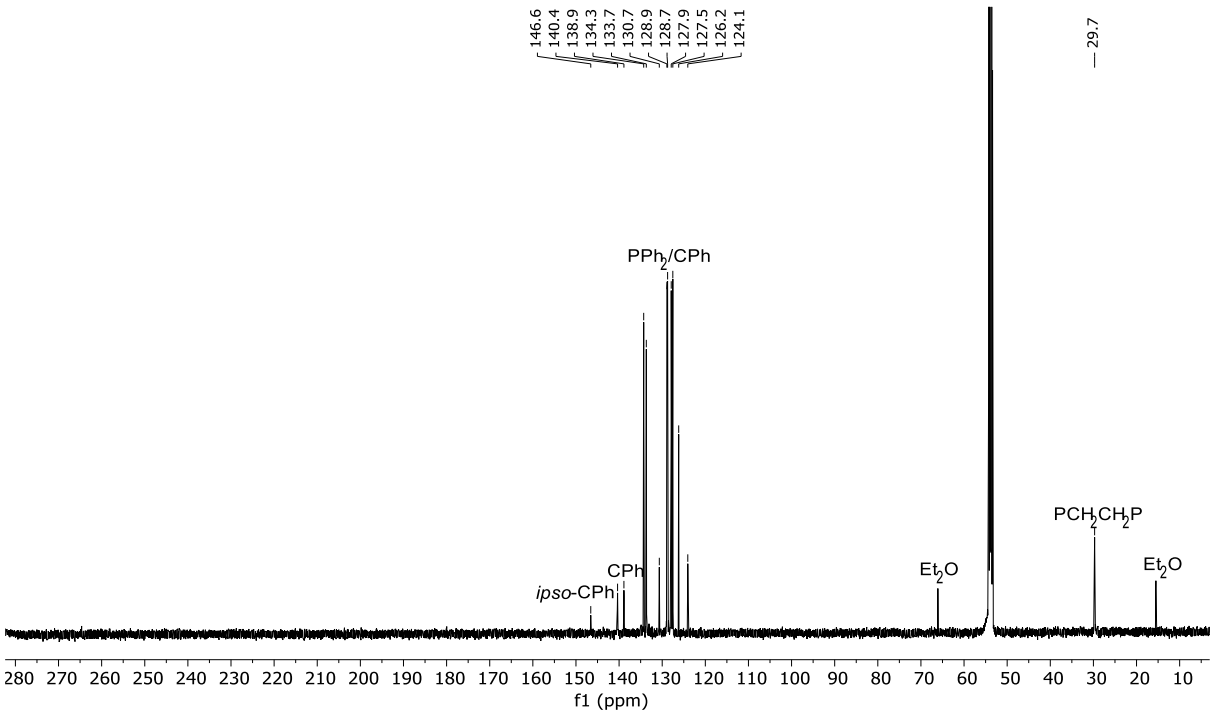

Figure 3.35. ^{13}C{^{1}H} NMR spectrum (126 MHz) of **Mo1** in CD_2Cl_2 (53.84 ppm).

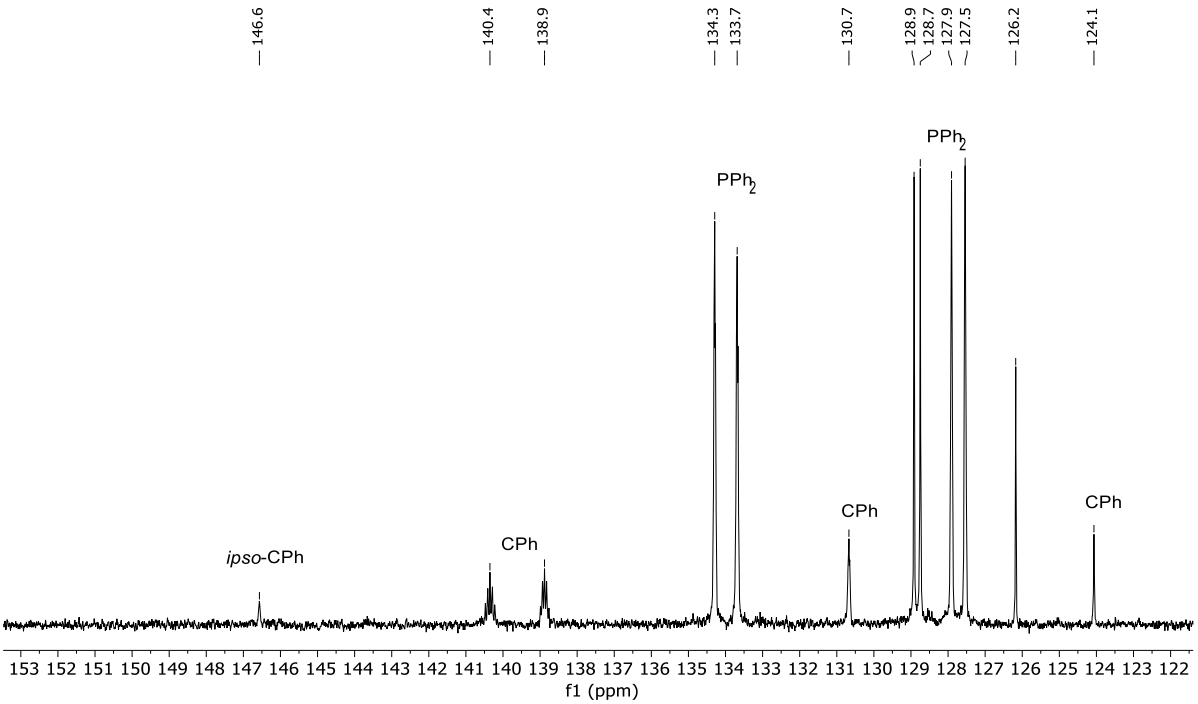

Figure 3.36. $^{13}C\{^{1}H\}$ NMR spectrum (126 MHz) of **Mo1** in CD_2Cl_2 showing aromatic region.

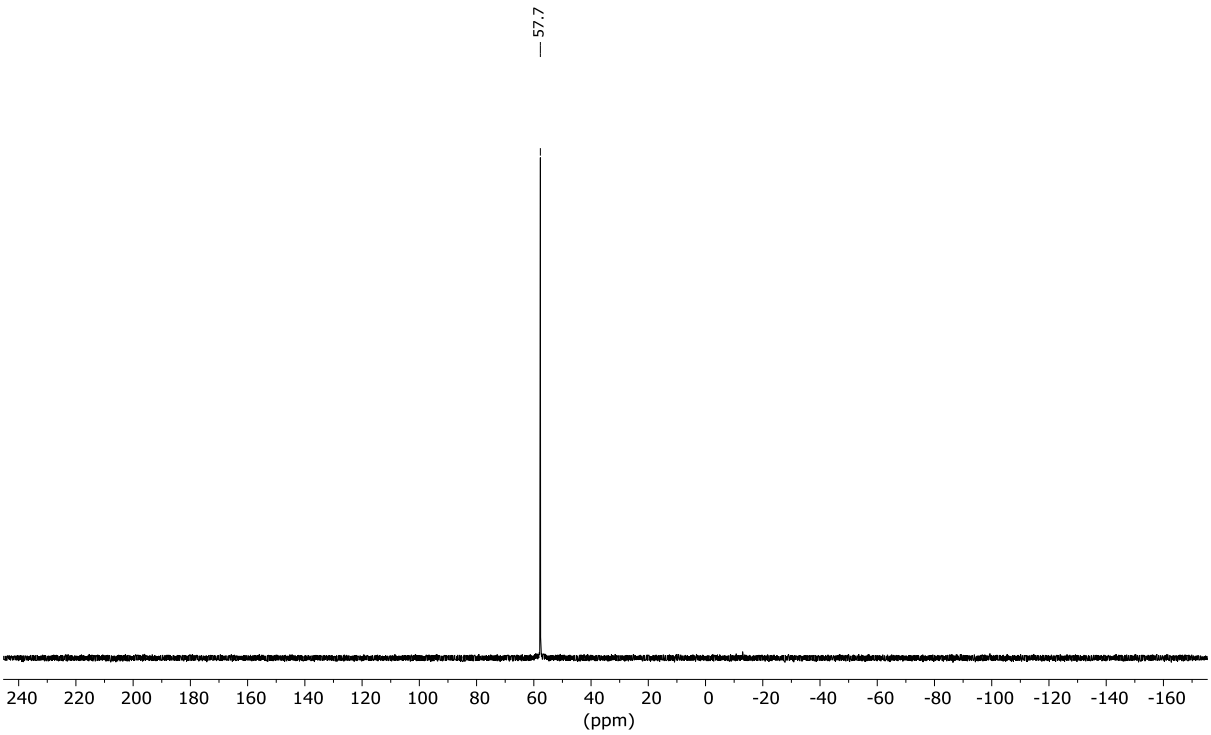

Figure 3.37. $^{31}P\{^{1}H\}$ NMR spectrum (202 MHz) of **Mo1** in CD_2Cl_2.

3.4.6.3. Mo(CPh)(depe)$_2$Cl (Mo2). To a stirred solution of Mo(CPh){P(OMe)$_3$}$_4$Cl (0.200 g, 0.278 mmol) in toluene (30 mL) at room-temperature was added 1,2-bis(diethylphosphino)ethane (0.120 g, 0.584 mmol), resulting in an immediate color change from orange to red-orange. The reaction mixture was then heated to 100 ˚C for 16 h, during which time the color changed to a deep purple. The reaction mixture was cooled to room temperature and the volatile components removed under vacuum. The remaining sticky residue was extracted into diethyl ether (30 mL) and filtered through Celite, which was then washed with diethyl ether (3 × 5 mL). The volatile components were removed from the filtrate under vacuum and the remaining solid then suspended in pentane (5 mL) and cooled to –30 ˚C. After 16 h, this resulted in the formation of deep purple needles that were collected by filtration and dried under vacuum (0.160 g, 91% yield). Crystals suitable for single-crystal X-ray diffraction experiments were grown by slow solvent evaporation from a pentane solution of the compound at –10 ˚C. ^{1}H NMR (500 MHz, C_6D_6; Figure 3.38): δ 6.93 (m, 2H, m-CPh), 6.88 (m, 2H, o-CPh), 6.83 (t, 1H, p-CPh), 2.29 (m, 4H, PC$\underline{H}_2$CH$_3$), 1.88 (m, 12H, PC$\underline{H}_2$CH$_3$), 1.72 (m, 4H, PC$\underline{H}_2$C$\underline{H}_2$P), 1.49 (br, 4H, PC$\underline{H}_2$C$\underline{H}_2$P), 1.10 (m, 12H, PCH$_2$C$\underline{H}_3$), 1.04 (m, 12H, PCH$_2$C$\underline{H}_3$). ^{13}C{^{1}H} NMR (126 MHz, C_6D_6, Figures 3.39–3.41): δ 258.10 (q, MoC), 148.54 (ipso-C_6H_5), 128.55 (C_6H_5), 127.73 (C_6H_5), 123.42 (C_6H_5), 24.07(P$\underline{C}$H$_2\underline{C}$H$_2$P), 23.91 (P$\underline{C}$H$_2$CH$_3$), 18.87 (P$\underline{C}$H$_2$CH$_3$), 9.40 (PCH$_2\underline{C}$H$_3$), 8.68 (PCH$_2\underline{C}$H$_3$). ^{31}P{^{1}H} NMR (202 MHz, C_6D_6, Figure 3.42): δ 54.6 (s). HR-MS (THF, 130V, *m/z*): 628.1851 (Calc. 628.1854).

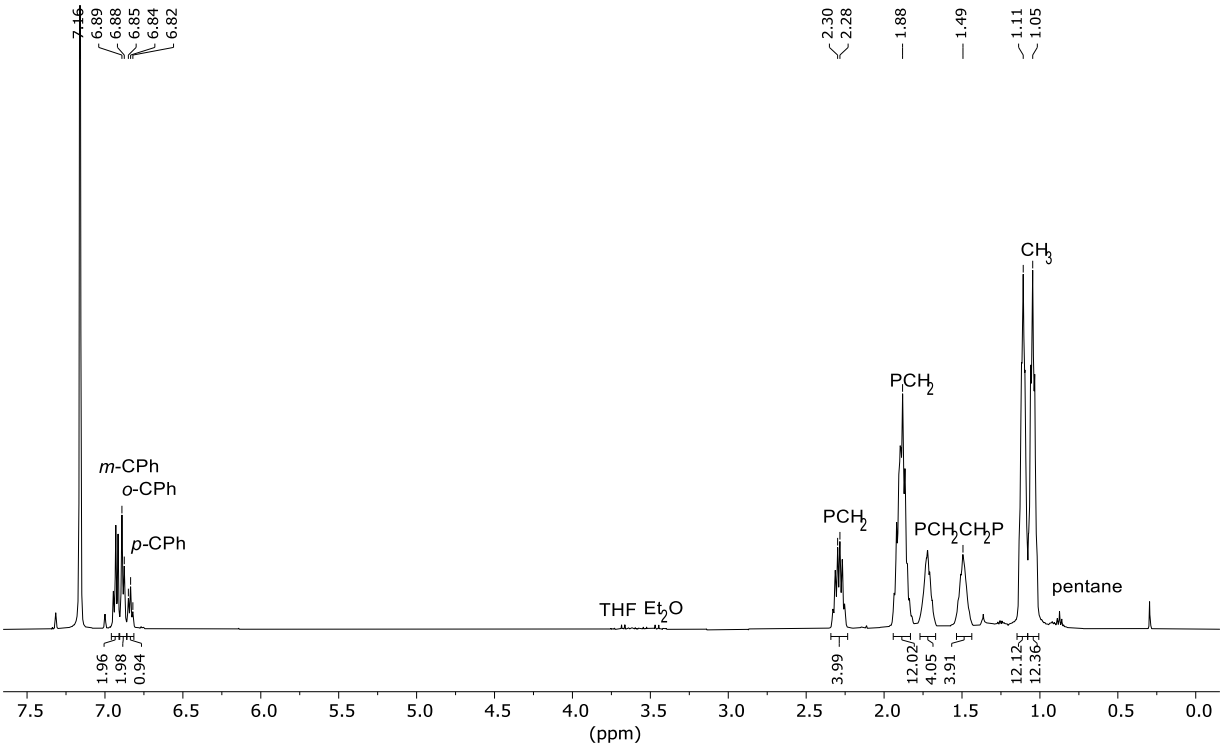

Figure 3.38. ^{1}H NMR spectrum (500 MHz) of **Mo2** in C_6D_6 (7.16 ppm).

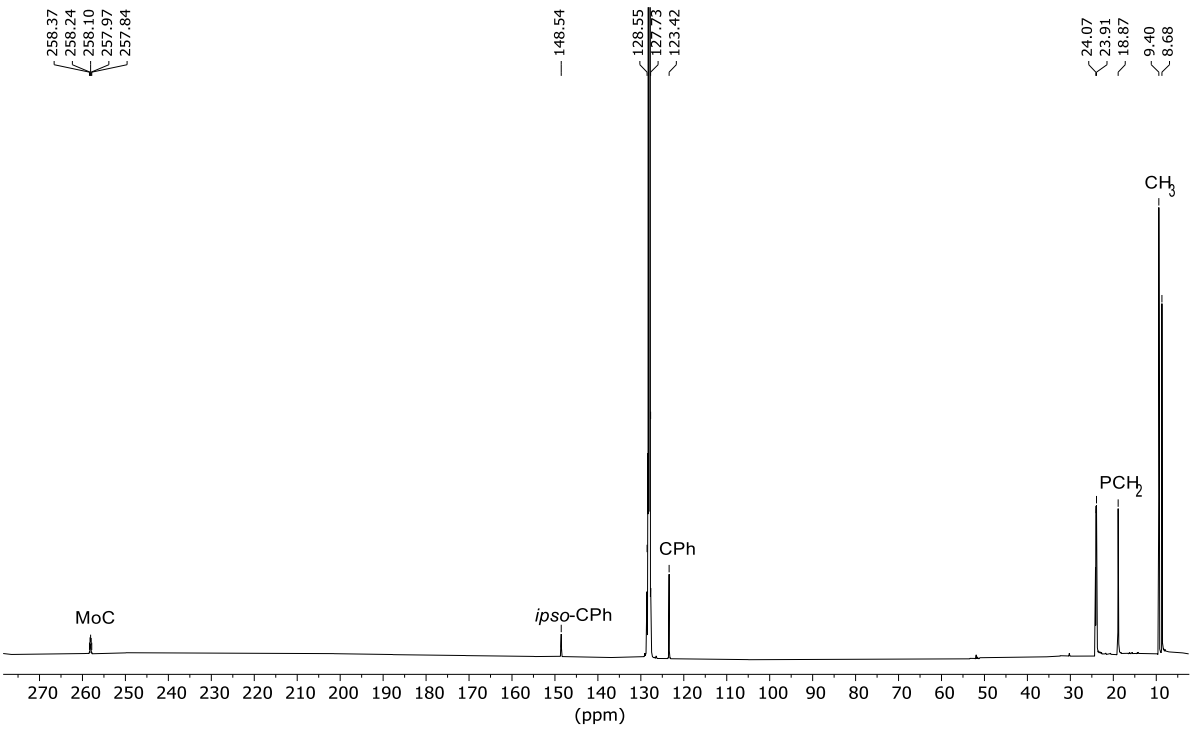

Figure 3.39. ^{13}C{^{1}H} NMR spectrum (126 MHz) of **Mo2** in C_6D_6 (128.06 ppm).

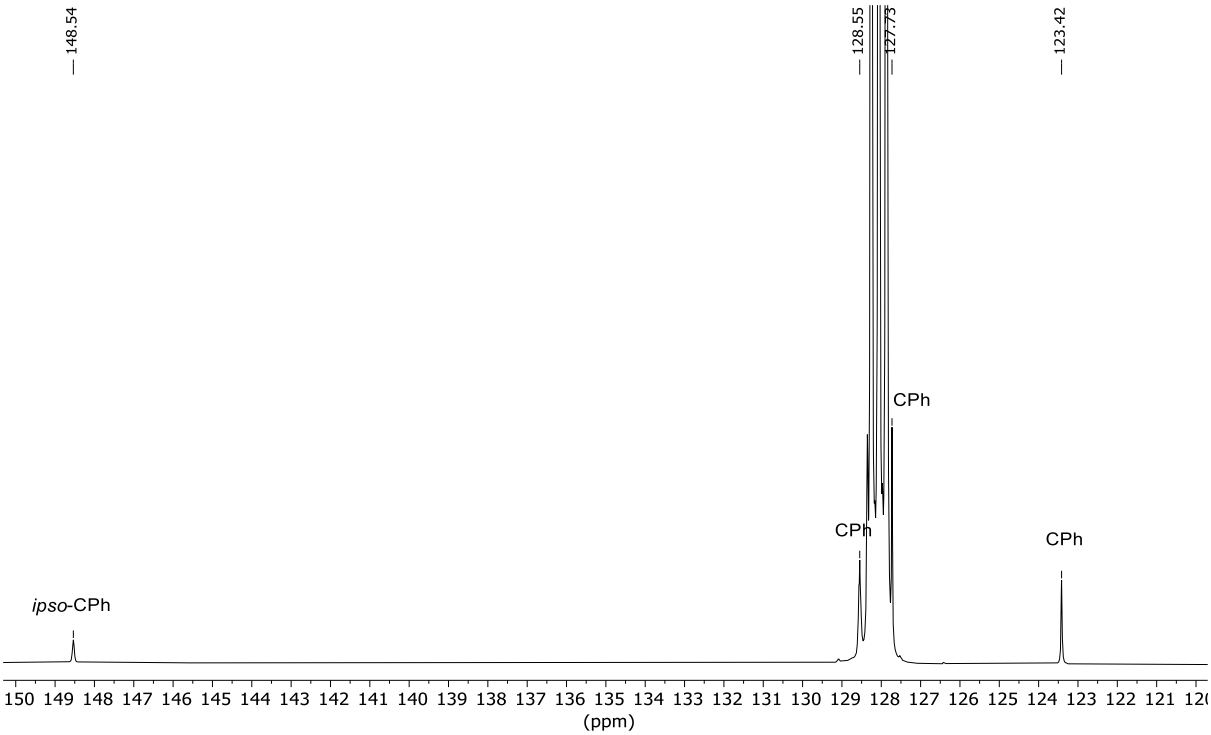

Figure 3.40. $^{13}C\{^{1}H\}$ NMR spectrum (126 MHz) of **Mo2** in C_6D_6 (128.06 ppm) showing aromatic region.

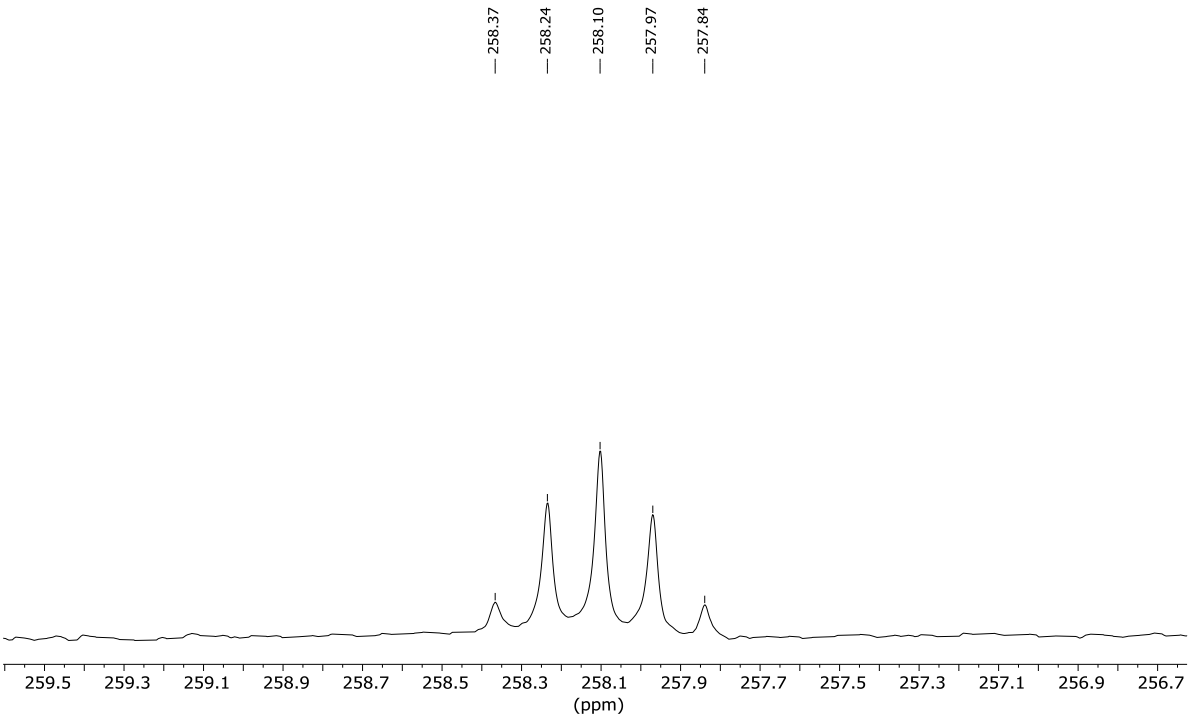

Figure 3.41. $^{13}C\{^{1}H\}$ NMR spectrum (126 MHz) of **Mo2** in C_6D_6 showing the MoC resonance.

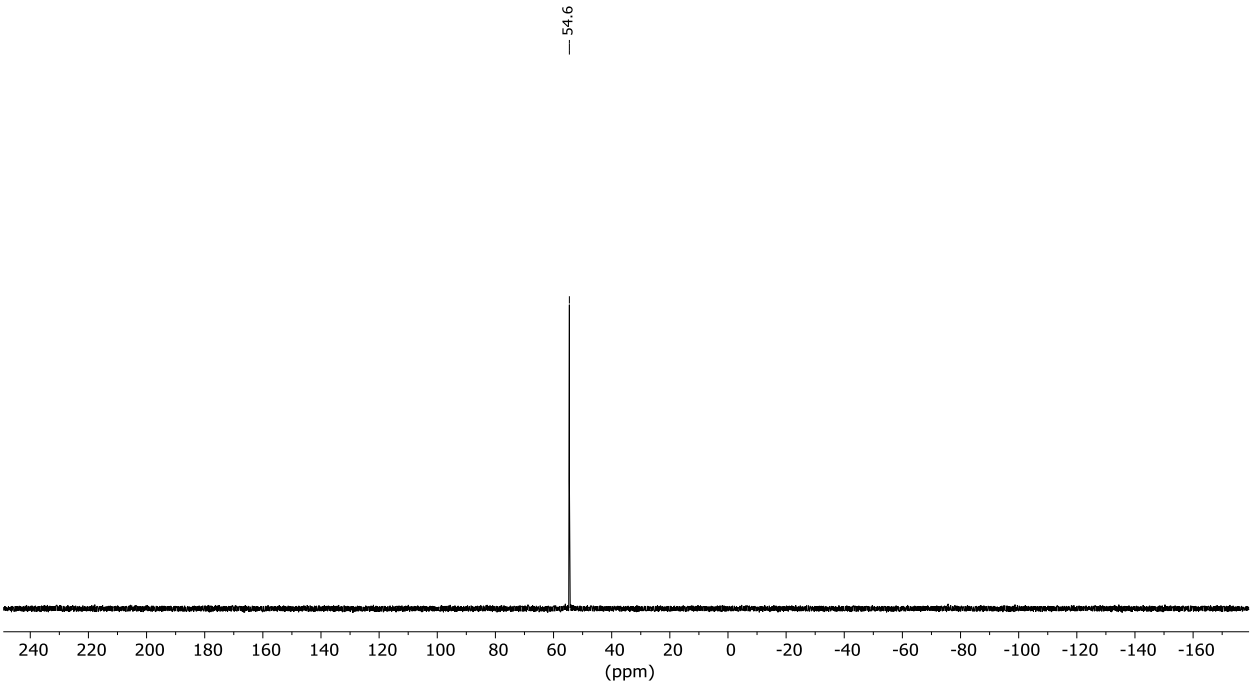

Figure 3.42. $^{31}P\{^{1}H\}$ NMR spectrum (202 MHz) of **Mo2** in C_6D_6.

3.4.6.4. Ta(NPh)(dppe)$_2$Cl (Ta1). To a stirred solution of Ta(NPh)(dme)Cl_3 (0.200 g, 0.428 mmol) in THF (10 mL) at room temperature was added 1,2-bis(diphenylphosphino)ethane (0.358 g, 0.899 mmol). The reaction mixture was stirred for 2 h, during which time the color of the solution gradually changed from yellow to orange with some slow formation of a light-orange precipitate. To this mixture Na/Hg amalgam (0.040 g, 0.4 wt.%, 1.74 mmol Na) was slowly added over 1 min under rapid stirring. Over 16 h, the precipitate dissolved, and the color of the reaction mixture gradually changed from orange to reddish purple with formation of a fine grey precipitate. The reaction mixture was then decanted from the mercury and solids and filtered through a sintered glass frit, which was washed with THF (3 × 10 mL). The filtrate was concentrated to 10 mL under vacuum and acetonitrile (50 mL) was added, which induced precipitation of a reddish-purple powder. The mixture was cooled to –30 ˚C and the solid was

collected by filtration, washed with acetonitrile (3 × 10 mL), and dried under vacuum to give a reddish-purple powder (0.230 g, 45% yield). Crystals suitable for single-crystal X-ray diffraction experiments were grown through slow vapor diffusion of diethyl ether into a CH_2Cl_2 solution of the compound at –30 ˚C. ^{1}H NMR (500 MHz, C_6D_6, Figures 3.43 and 3.44): δ 7.64 (br, 8H, o-PPh_2), 7.46 (br, 8H, o-PPh_2), 6.97 and 6.92 (overlapping m, 24H, m,p-PPh_2), 6.65 (m, 1H, p-NPh), 6.58 (m, 2H, m-NPh), 5.37 (d, 2H, o-NPh), 2.68 (br, 4H, PCH_2CH_2P), 2.44 (br, 4H, PCH_2CH_2P). ^{13}C{^{1}H} NMR (126 MHz, C_6D_6, Figures 3.45 and 3.46): δ 158.55 (C_6H_5), 140.30 (C_6H_5), 138.87 (C_6H_5), 134.44 (PPh_2), 133.90 (PPh_2), 129.11 (PPh_2), 128.56 (PPh_2), 127.53 (C_6H_5), 127.35 (PPh_2), 126.86 (PPh_2), 118.78 (PPh_2), 32.68(m, PCH_2CH_2P). ^{31}P{^{1}H} NMR (202 MHz, C_6D_6, Figure 3.47): δ 53.4 (s). HR-MS (THF, 70V, *m/z*): 1102.2305 (Calc. 1102.2292).

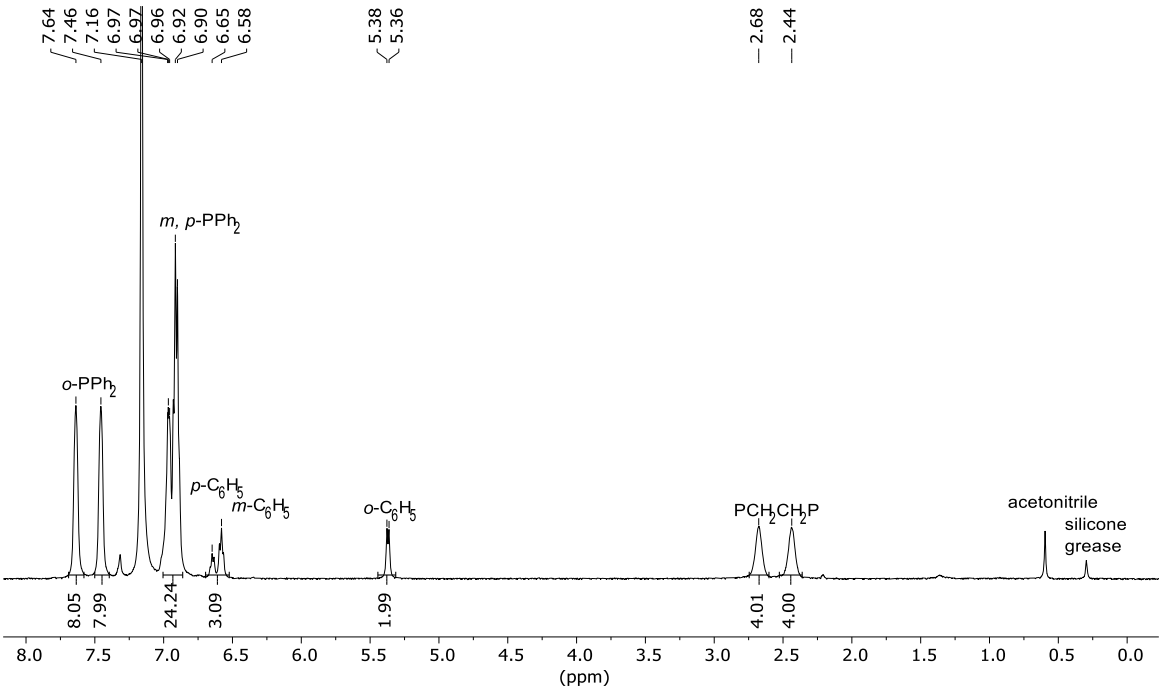

Figure 3.43. ^{1}H NMR spectrum (500 MHz) of **Ta1** in C_6D_6 (7.16 ppm).

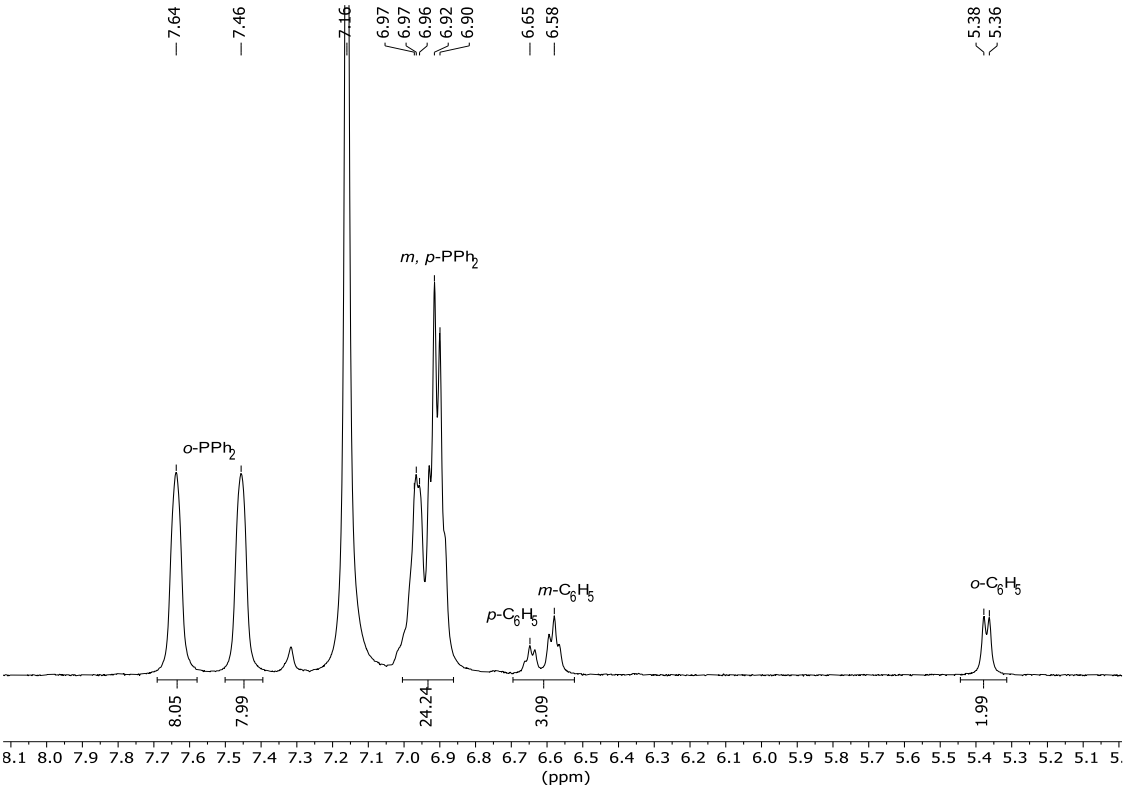

Figure 3.44. ^{1}H NMR spectrum (500 MHz) of **Ta1** in C_6D_6 (7.16 ppm) showing aromatic region.

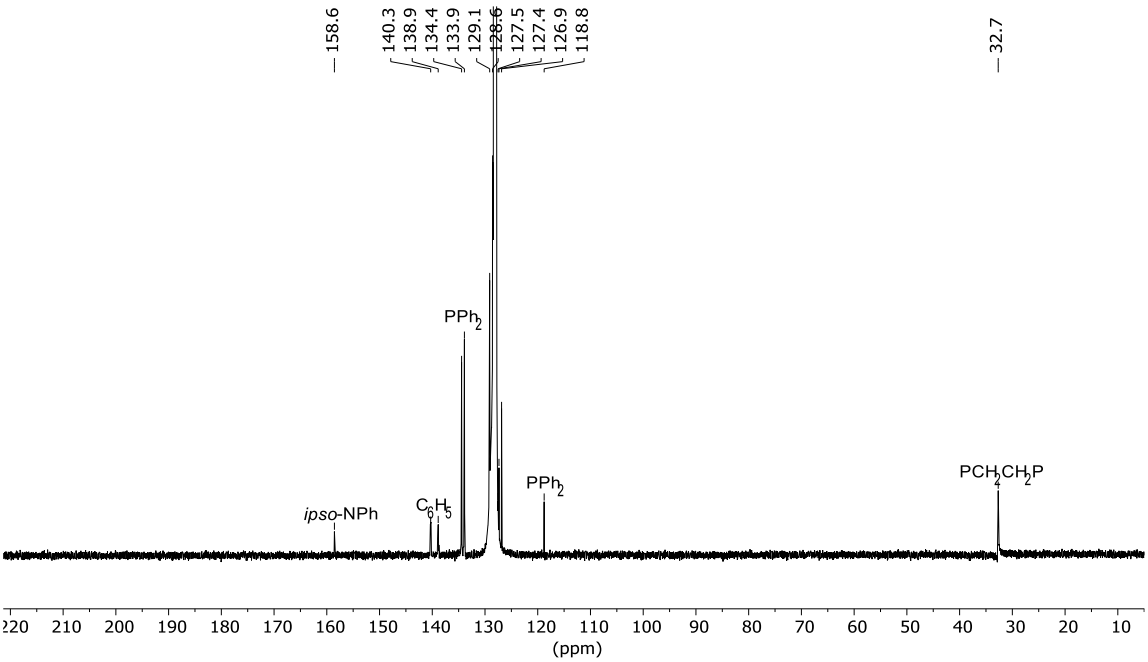

Figure 3.45. $^{13}C\{^{1}H\}$ NMR spectrum (126 MHz) of **Ta1** in C_6D_6 (128.06 ppm).

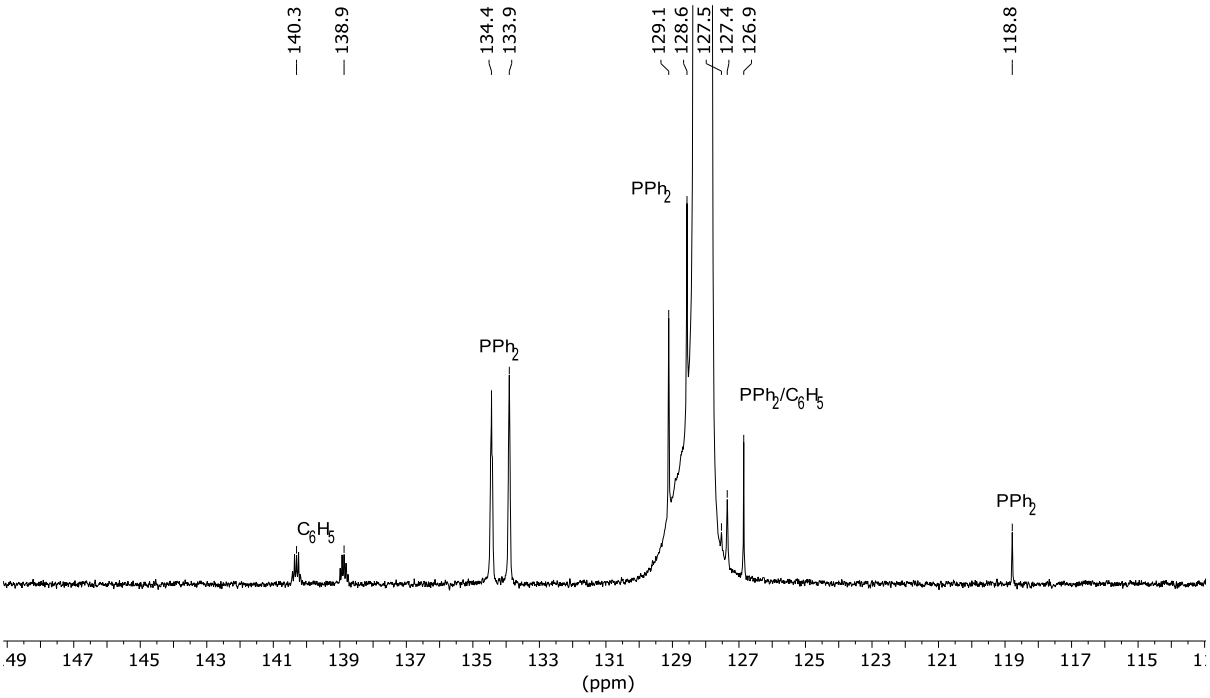

Figure 3.46. $^{13}C\{^{1}H\}$ NMR spectrum (126 MHz) of **Ta1** in C_6D_6 (128.06 ppm) showing aromatic region.

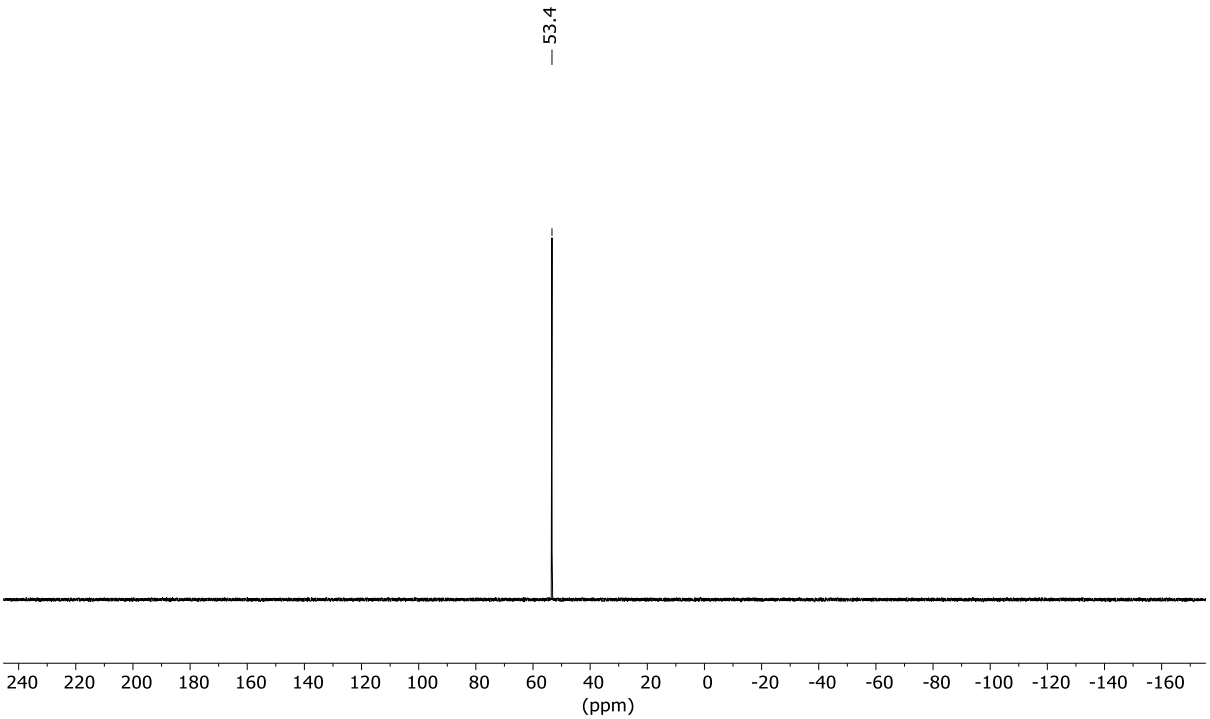

Figure 3.47. $^{31}P\{^{1}H\}$ NMR spectrum (202 MHz) of **Ta1** in C_6D_6.

3.4.6.5. Ta(NPh)(depe)$_2$Cl (Ta2). To a stirred, room temperature solution of Ta(NPh)(dme)Cl$_3$ (0.400 g, 0.856 mmol) in THF (10 mL) was added 1,2-bis(diethylphosphino)ethane (0.371 g, 1.79 mmol). Over the course of 1 hour, a light-yellow precipitate began to form. The reaction mixture was then cooled to –30 ˚C and Na/Hg amalgam (0.050 g, 0.4 wt.%, 2.17 mmol Na) was slowly added under vigorous stirring. The solution rapidly darkened to an emerald green. The reaction mixture was then allowed to warm to room temperature and stirred for 2 h. During this time the solution darkened with concomitant formation of a light grey precipitate. Volatile components were removed in vacuo and the remaining solid was extracted into pentane (10 mL), decanted from the mercury and solids, and filtered through a sintered glass frit. The mercury layer was washed with additional pentane (3 × 10 mL) yielding a dark green filtrate. The filtrate was then concentrated in vacuo to 5 mL and cooled to –30 ˚C overnight to provide large brown/green dichroic needles, which were collected by filtration. ^{1}H and ^{31}P NMR spectra of solutions prepared from the crystals indicated the presence of free depe cocrystallized with the complex, so the complex was dried under high vacuum (<0.001 torr) for 2 days to remove any remaining depe (0.220 g, 35% yield). ^{1}H NMR (500 MHz, C_6D_6, Figure 3.48): δ 7.00 (t, J = 7.7 Hz, 2H, m-Ph), 6.75 (t, J = 7.3 Hz, 1H, p-Ph), 6.50 (d, J = 7.8 Hz, 2H, o-Ph), 2.06 (m, 4H, PC$\underline{H}_2$CH$_3$), 1.94 (m, 8H, PC$\underline{H}_2$CH$_3$), 1.85 (m, 4H, PC$\underline{H}_2$CH$_3$), 1.59 (m, 4H, PC$\underline{H}_2$C$\underline{H}_2$P), 1.38 (m, 4H, PC$\underline{H}_2$C$\underline{H}_2$P), 1.09 (br, 24H, PCH$_2$C$\underline{H}_3$). ^{1}H{^{31}P} NMR (500 MHz, C_6D_6, Figures 3.49 and 3.50): δ 7.00 (t, J = 7.7 Hz, 2H), 6.75 (t, J = 7.3 Hz, 1H), 6.50 (d, 2H, J = 7.8 Hz), 2.07 (dq, J = 15.3, 7.7 Hz, 4H), 1.94 (overlapping dq, J = 15.4, 7.7 Hz, 8H), 1.85 (dq, J = 14.8, 7.6 Hz, 4H), 1.58 (m, 4H), 1.38 (m, 4H), 1.09 (m, J = 15.3, 7.6 Hz, 24H). ^{13}C{^{1}H} NMR (126 MHz, C_6D_6, Figures 3.51 and 3.52): δ 160.74 (ipso-NPh),

128.31 (NPh), 125.77 (NPh), 118.21 (NPh), 27.46 ($P\underline{C}H_2\underline{C}H_2P$), 20.92 ($P\underline{C}H_2CH_3$), 9.97 ($PCH_2\underline{C}H_3$), 8.87 ($PCH_2\underline{C}H_3$). $^{31}P\{^1H\}$ NMR (202 MHz, C_6D_6, Figure 3.53): δ 48.6 (s) HR-MS (THF, 70V, *m/z*): 718.2280 (Calc.718.2292).

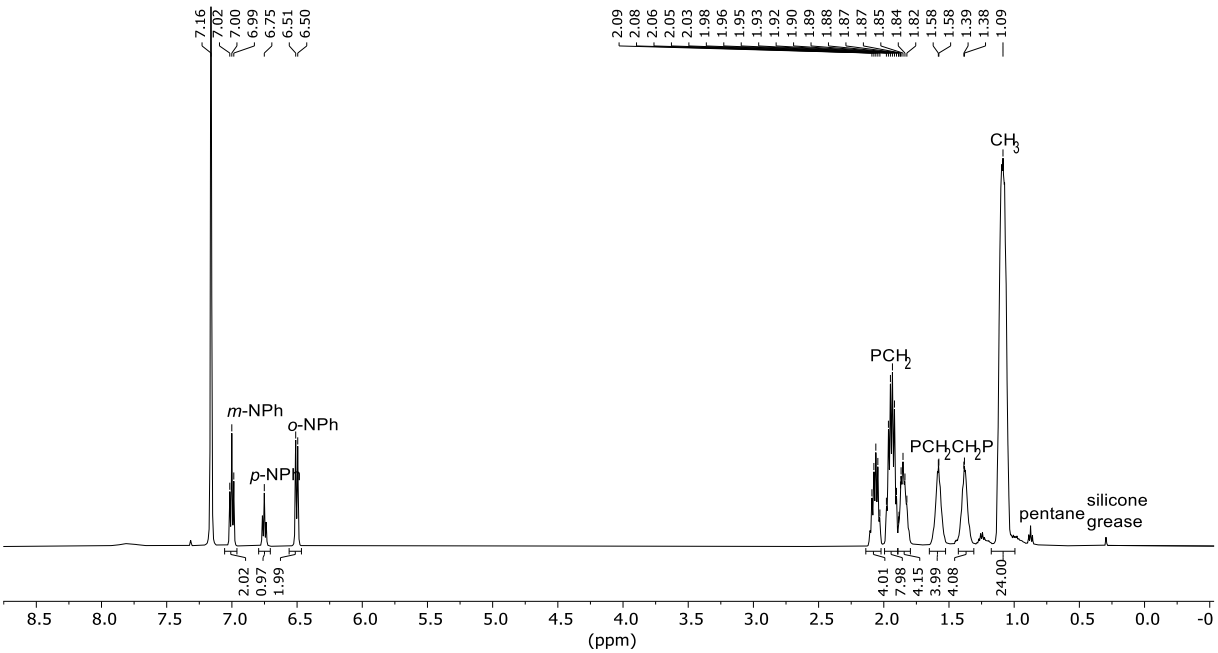

Figure 3.48. ^1H NMR spectrum (500 MHz) of **Ta2** in C_6D_6 (7.16 ppm).

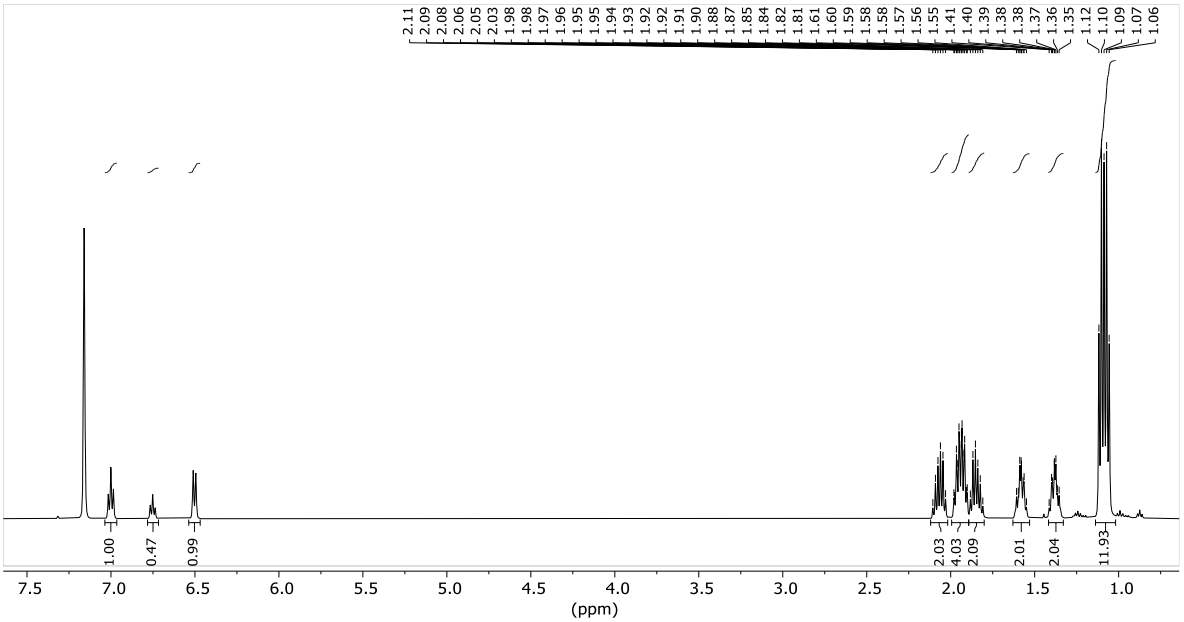

Figure 3.49. $^1H\{^{31}P\}$ NMR spectrum (500 MHz) of **Ta2** in C_6D_6 (7.16 ppm).

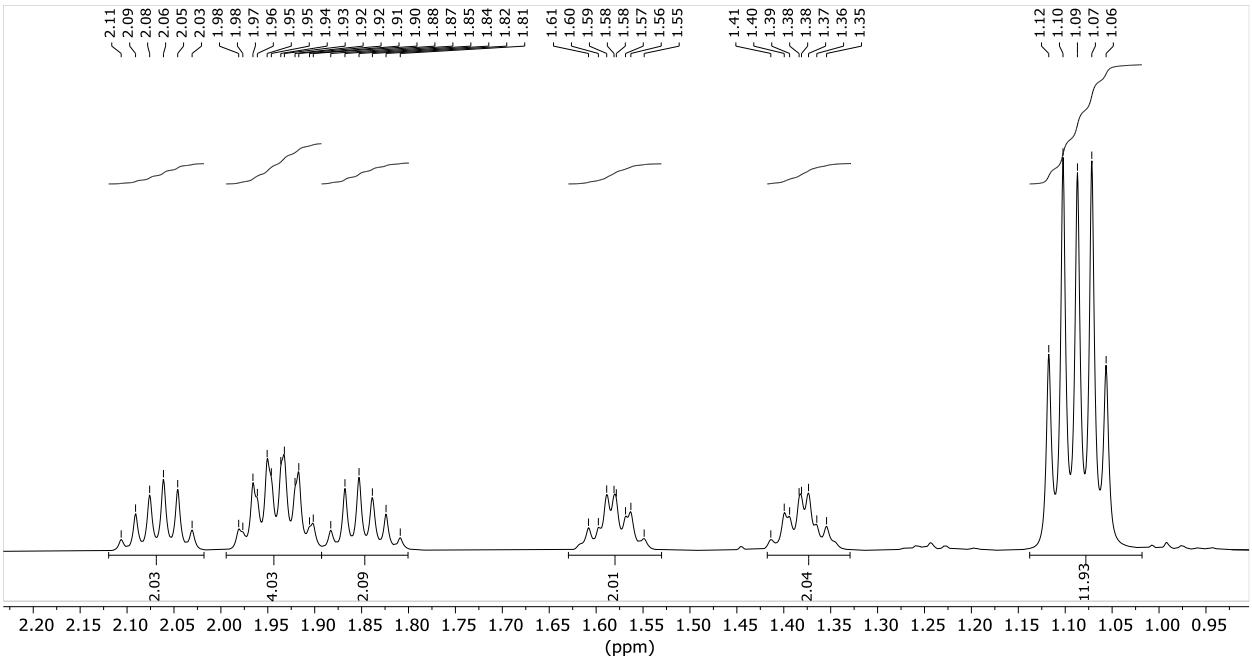

Figure 3.50. $^{1}H\{^{31}P\}$ NMR spectrum (500 MHz) of **Ta2** in C_6D_6 showing aliphatic region.

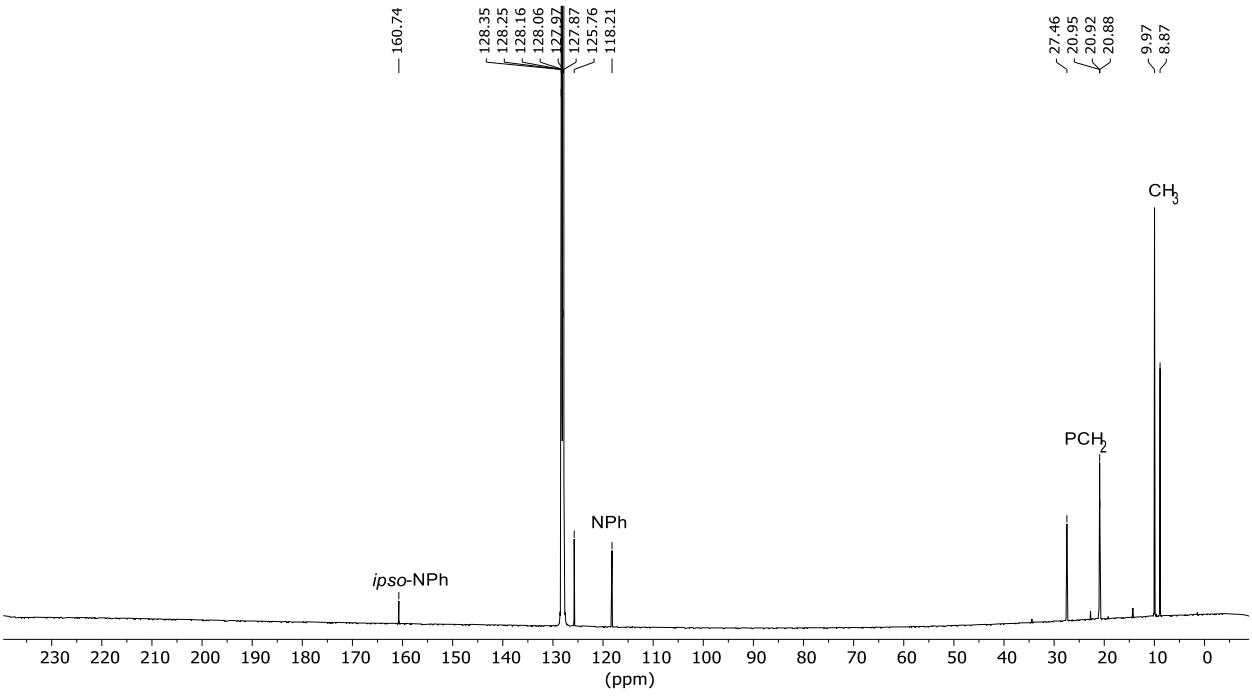

Figure 3.51. $^{13}C\{^{1}H\}$ NMR spectrum (126 MHz) of **Ta2** in C_6D_6 (128.06 ppm).

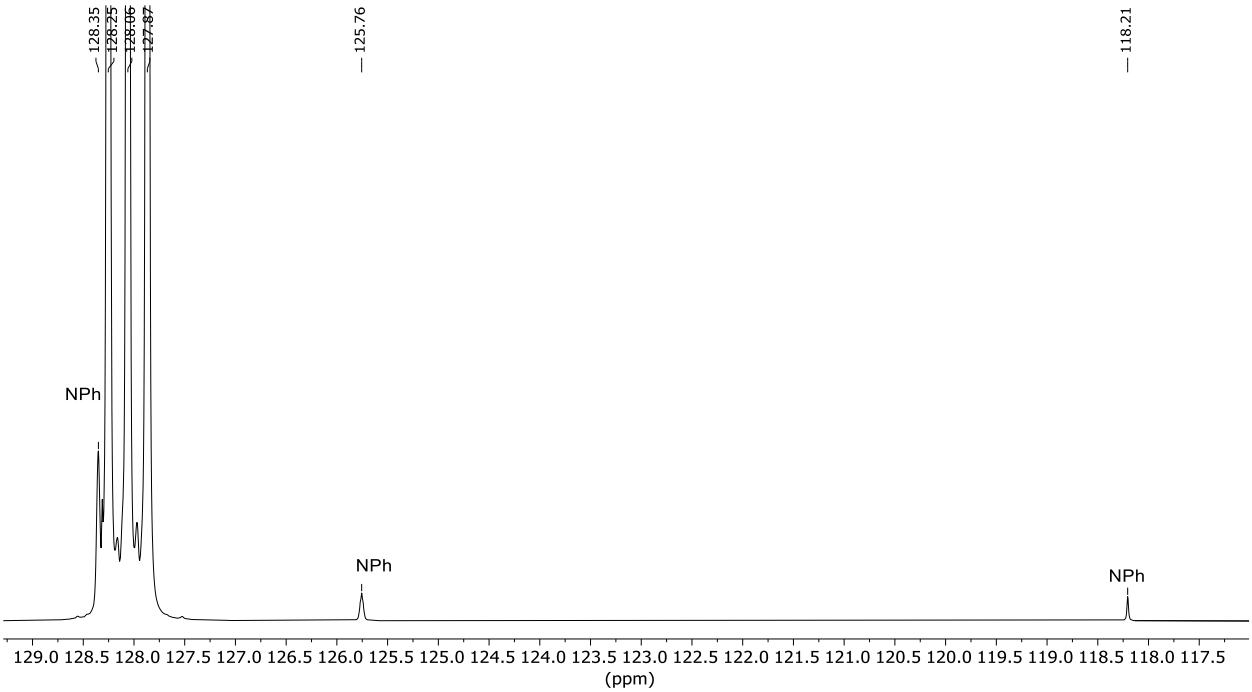

Figure 3.52. $^{13}C\{^{1}H\}$ NMR spectrum (126 MHz) of **Ta2** in C_6D_6 (128.06 ppm) showing aromatic region.

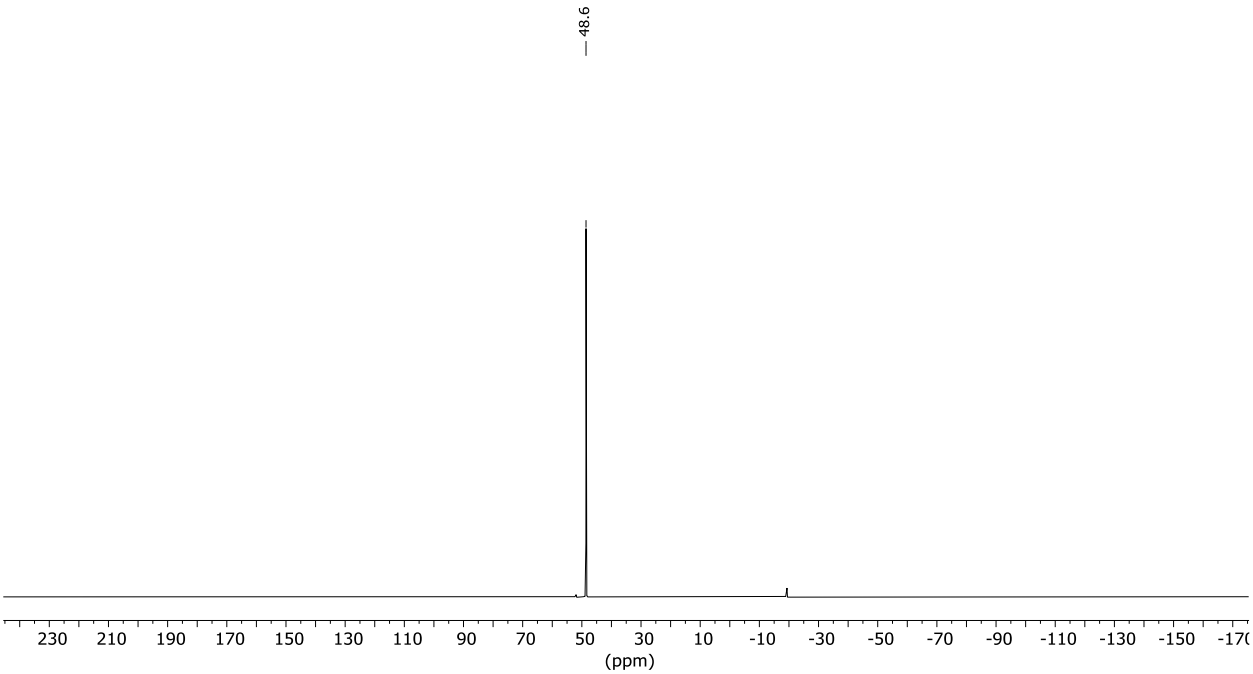

Figure 3.53. $^{31}P\{^{1}H\}$ NMR spectrum (202 MHz) of **Ta2** in C_6D_6. Peak at −15.0 is free depe from decomposition.

3.4.6.6. [Mo(H)(CPh)(depe)$_2$Cl][PF$_6$] (Mo2H). To a stirred solution of Mo(CPh)(depe)$_2$Cl (0.200 g, 0.315 mmol) in THF (10 mL) at room temperature was added a solution of HCl in diethyl ether (0.5 mL, 2M). The color of the reaction mixture rapidly changed from purple to colorless with concomitant formation of a white powder. The suspension was stirred for 2 h and the volatile components were then removed under vacuum. The remaining solid was dissolved in acetonitrile (20 mL) and KPF_6 (0.90 g, 0.488 mmol) was added to the resulting solution, resulting in immediate formation of a white precipitate. The suspension was stirred for 1 h and the volatile components removed under vacuum. The remaining solid was extracted into dichloromethane (30 mL) and filtered through Celite, which was washed with dichloromethane (3 × 5 mL). The filtrate was then concentrated under vacuum to 5 mL, layered with 20 mL of Et_2O, and cooled to –30 ˚C overnight, resulting in formation of an off-white powder. The solid was collected by filtration and washed with toluene (2 × 10 mL) and ether (10 mL) and then dried under vacuum to give an off-white powder (0.148 g, 60% yield). Crystals suitable for single-crystal X-ray diffraction experiments were grown through slow vapor diffusion of diethyl ether into a dichloromethane solution of the compound at –30 ˚C. ^{1}H NMR (400 MHz, CD_2Cl_2, Figure 3.54): δ 7.18 (overlapping m, 3H, m, p-C_6H_5), 6.87 (d, 2H, o- C_6H_5), 2.26 and 2.17 (overlapping m, 24H, PC$\underline{H}_2$), 1.26 (overlapping m, 24H, PCH$_2$C$\underline{H}_3$), −0.05 (q, J_{PH} = 37.3 Hz, Mo−H). ^{13}C{^{31}P}{^{1}H} NMR (126 MHz, CD_2Cl_2, Figures 3.55 and Figure 3.56): δ 274.1 (MoC) 144.3 (C_6H_5), 129.8 (C_6H_5), 129.0 (C_6H_5), 128.9 (C_6H_5), 22.78 (q, PCH$_2$CH$_2$P), 22.04 (P$\underline{C}$H$_2$CH$_3$), 17.58 (P$\underline{C}$H$_2$CH$_3$), 9.19 (PCH$_2\underline{C}$H$_3$), 8.39 (PCH$_2\underline{C}$H$_3$). ^{31}P{^{1}H} NMR (202 MHz, CD_2Cl_2, Figure 3.57): δ 57.67 (br s), −144.62 (sep, J_{PF} = 706 Hz ,PF_6). ^{19}F{^{1}H} NMR (377 MHz, CD_2Cl_2, Figure 3.58): δ −73.0 (d, J_{PF} = 706 Hz, PF_6). HR-MS (THF, 0V, *m/z*): 629.1951 (Calc. 629.1933).

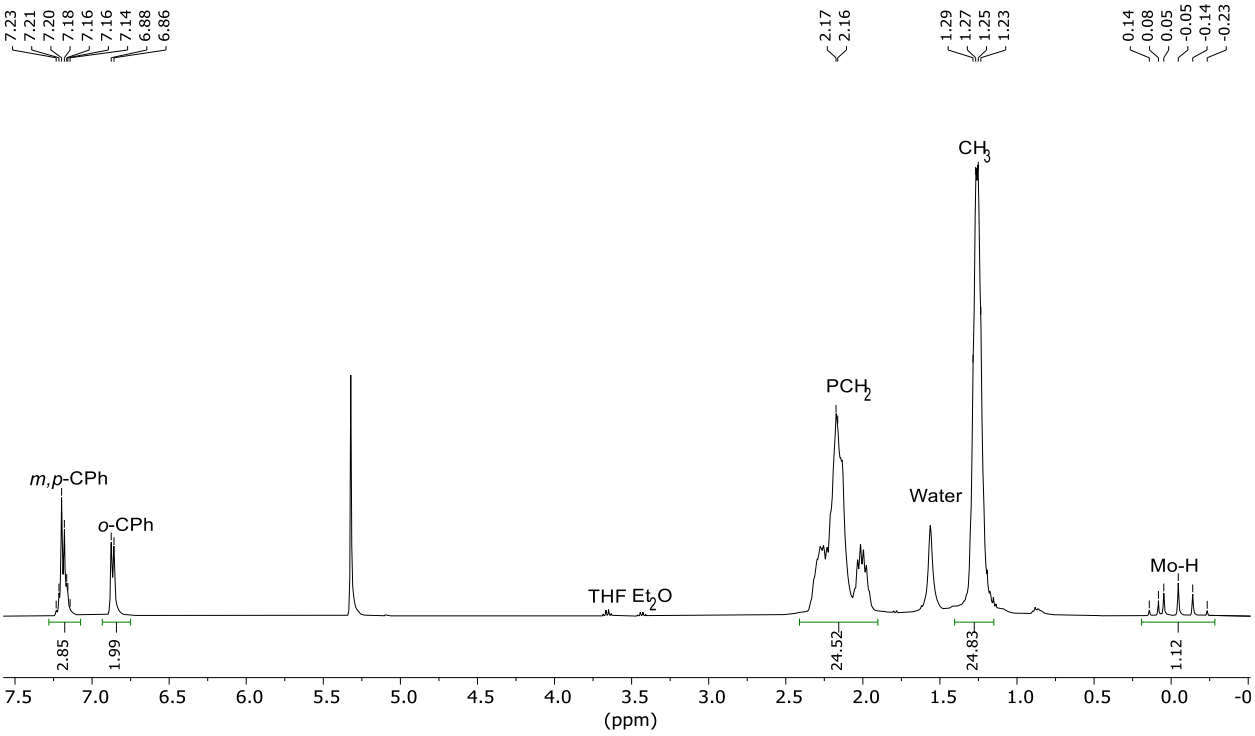

Figure 3.54. ^{1}H NMR spectrum (400 MHz) of **Mo2H** in CD_2Cl_2 (5.32 ppm).

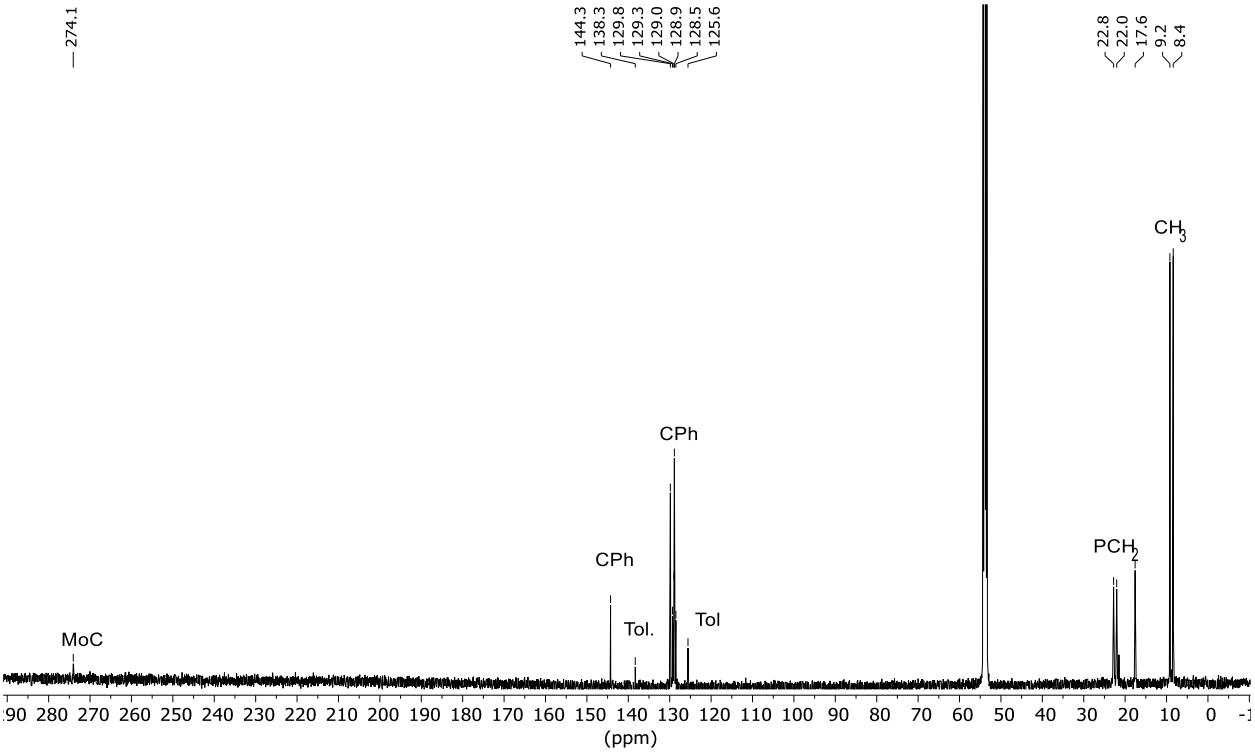

Figure 3.55. $^{13}C\{^{31}P\}\{^{1}H\}$ NMR spectrum (126 MHz) of **Mo2H** in CD_2Cl_2 (53.84 ppm).

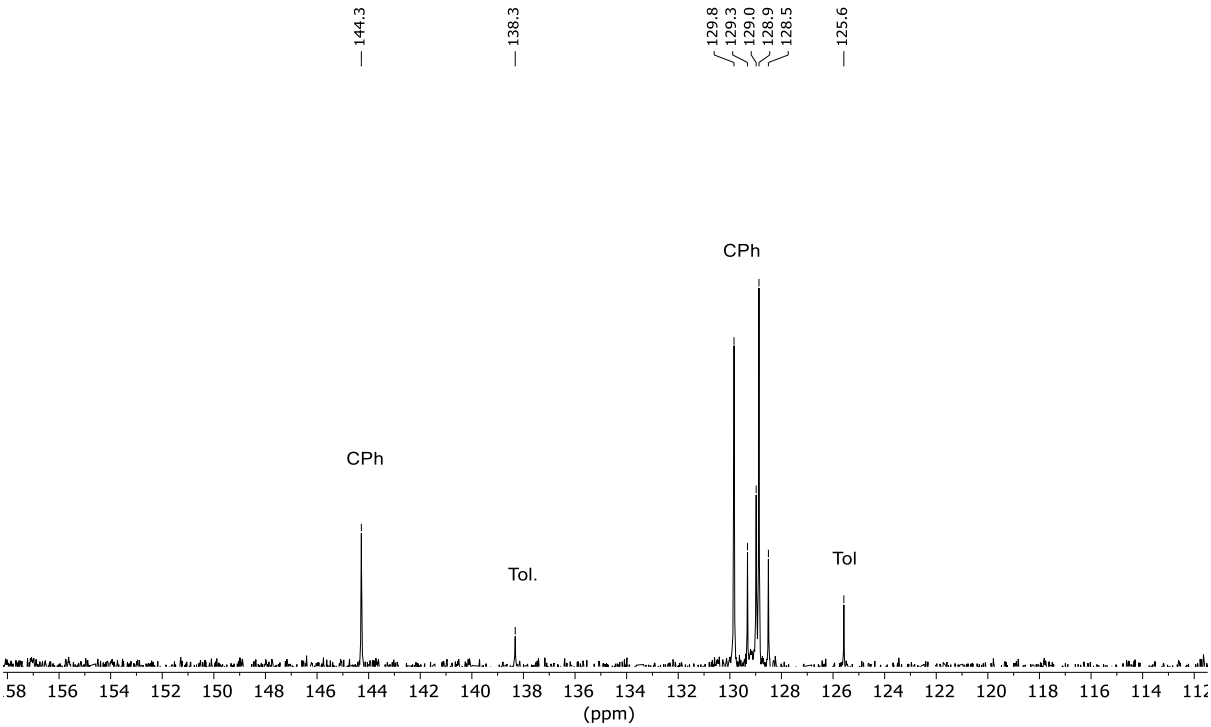

Figure 3.56. $^{13}C\{^{31}P\}\{^{1}H\}$ NMR spectrum (126 MHz) of **Mo2H** in CD_2Cl_2 (53.84 ppm) showing aromatic region.

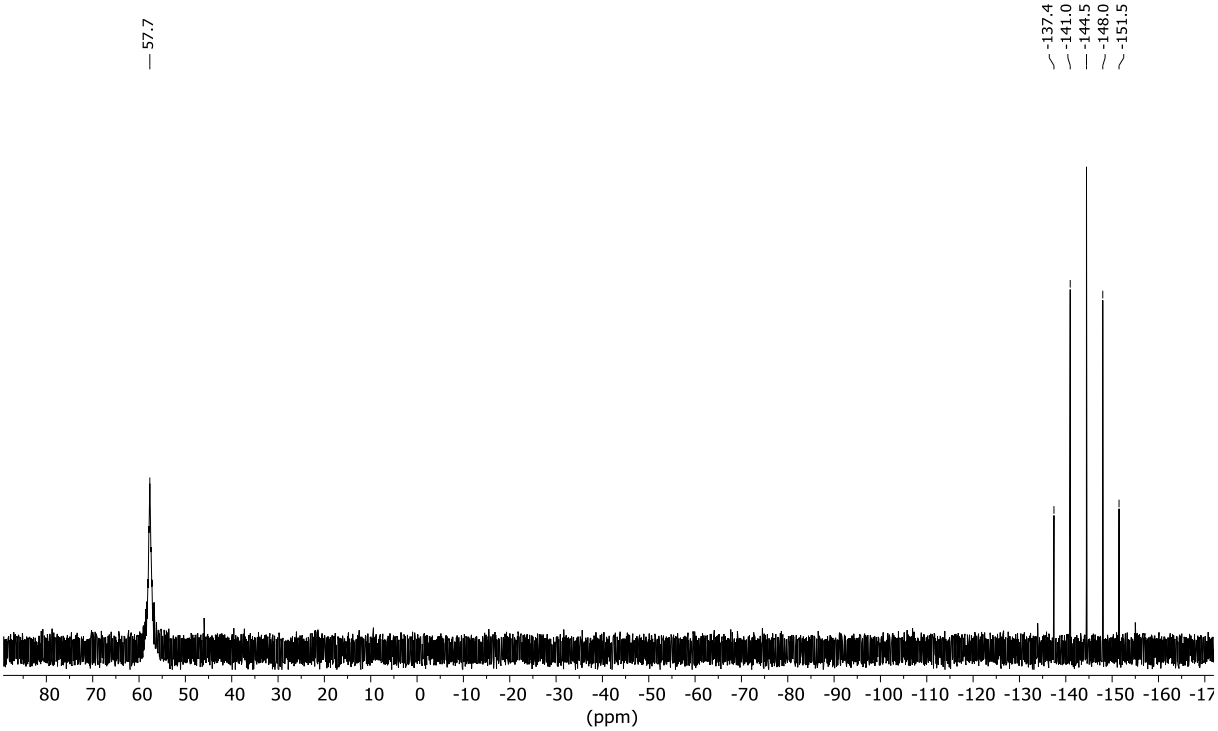

Figure 3.57. $^{31}P\{^{1}H\}$ NMR spectrum (202 MHz) of **Mo2H** in CD_2Cl_2.

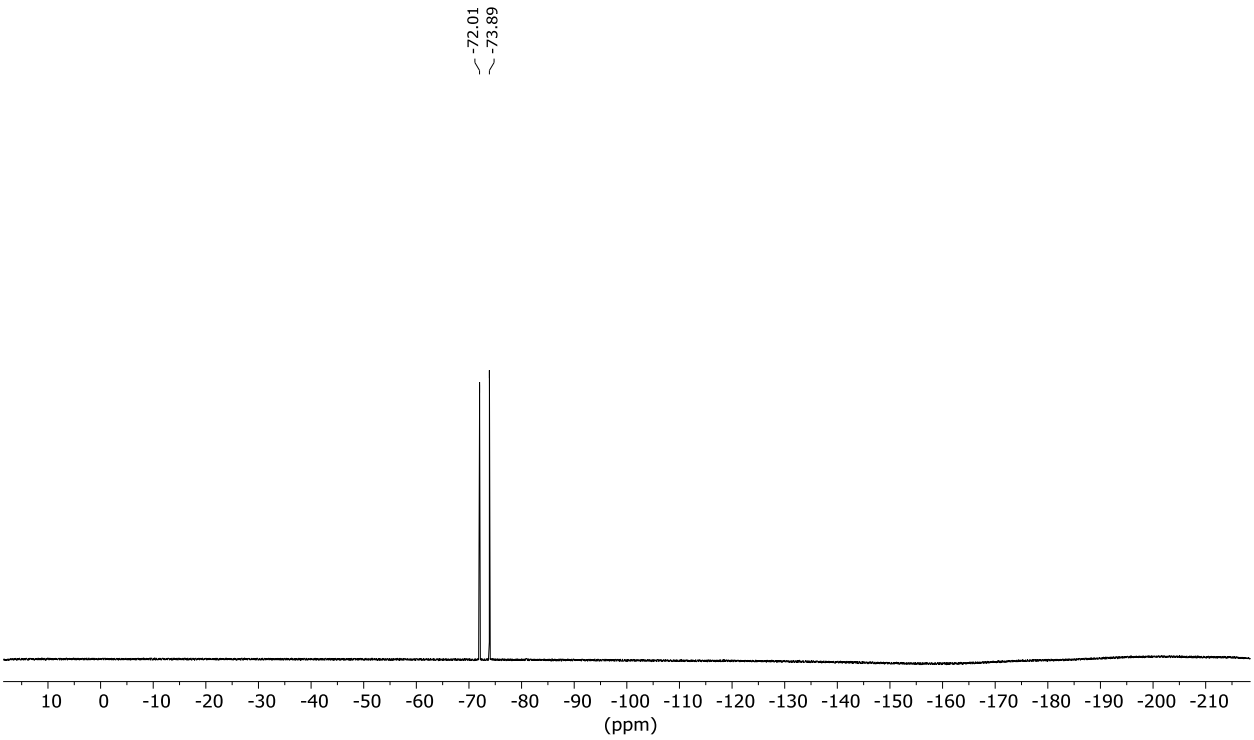

Figure 3.58. $^{19}F\{^{1}H\}$ NMR spectrum (377 MHz) of **Mo2H** in CD_2Cl_2.

3.4.6.7. [Ta(H)(NPh)(dppe)$_2$Cl][BArF$_{20}$] (Ta1H). To a suspension of Ta(NPh)(dppe)$_2$Cl (0.010 g, 0.084 mmol) in C_6D_6 (1 mL) in a J. Young NMR tube at room temperature was added [HBArF$_{20}$][Et$_2$O]$_2$ (0.007 g, 0.0924 mmol, 1.1 eq.). The reaction mixture rapidly turned colorless. The product could not be isolated in pure form and so was characterized by NMR spectroscopy in situ. ^{1}H NMR (500 MHz, C_6D_6, Figures 3.59–3.61): δ 11.32 (tt, J_{HP} = 89.2, 12.5 Hz, 1H, TaH), 7.43 (t, 4H, p-PPh$_2$) , 7.39 (t, 4H, p-PPh$_2$), 7.07 and 7.02 (overlapping m, 16H, PPh$_2$), 6.90 (m, 8H, PPh$_2$) 6.77 (m, 8H, PPh$_2$), 6.66 (t, J = 7.3 Hz, 1H, p-C_6H_5), 6.57 (t, J = 7.7 Hz, 2H, m-C_6H_5), 5.33 (d, J = 7.4 Hz, 2H, o-C_6H_5), 2.61-2.23 (m, 8H, PC$\underline{H}_2$C$\underline{H}_2$P). $^{31}P\{^{1}H\}$ NMR (202 MHz, C_6D_6, Figures 3.62 and 3.63): δ 53.36 (complex m), 27.50 (complex m). $^{19}F\{^{1}H\}$ NMR (471 MHz, C_6D_6, Figure 3.64): δ −131.72 (d, J = 18.0 Hz), −162.26 (t, J = 20.8 Hz), −166.14 (t, J = 19.5 Hz).

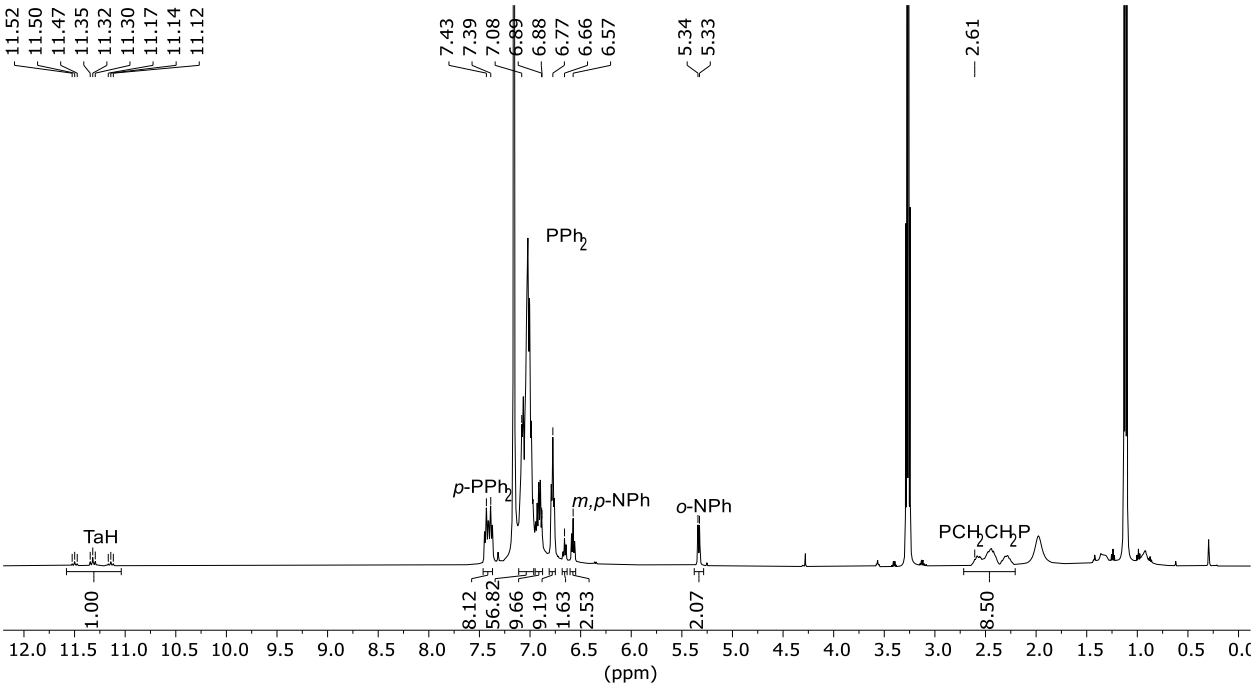

Figure 3.59. ^{1}H NMR spectrum (500 MHz) of **Ta1H** generated *in-situ* in C_6D_6 (7.16 ppm).

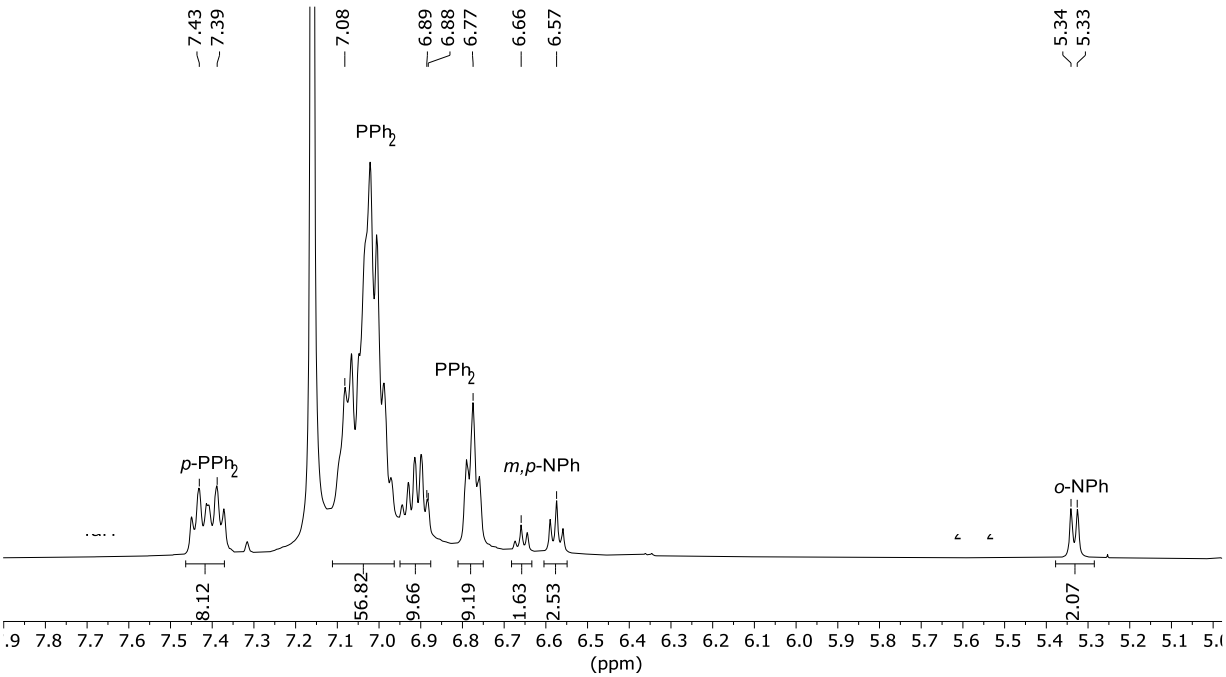

Figure 3.60. ^{1}H NMR spectrum (500 MHz) of **Ta1H** generated *in-situ* in C_6D_6 (7.16 ppm). showing aromatic region.

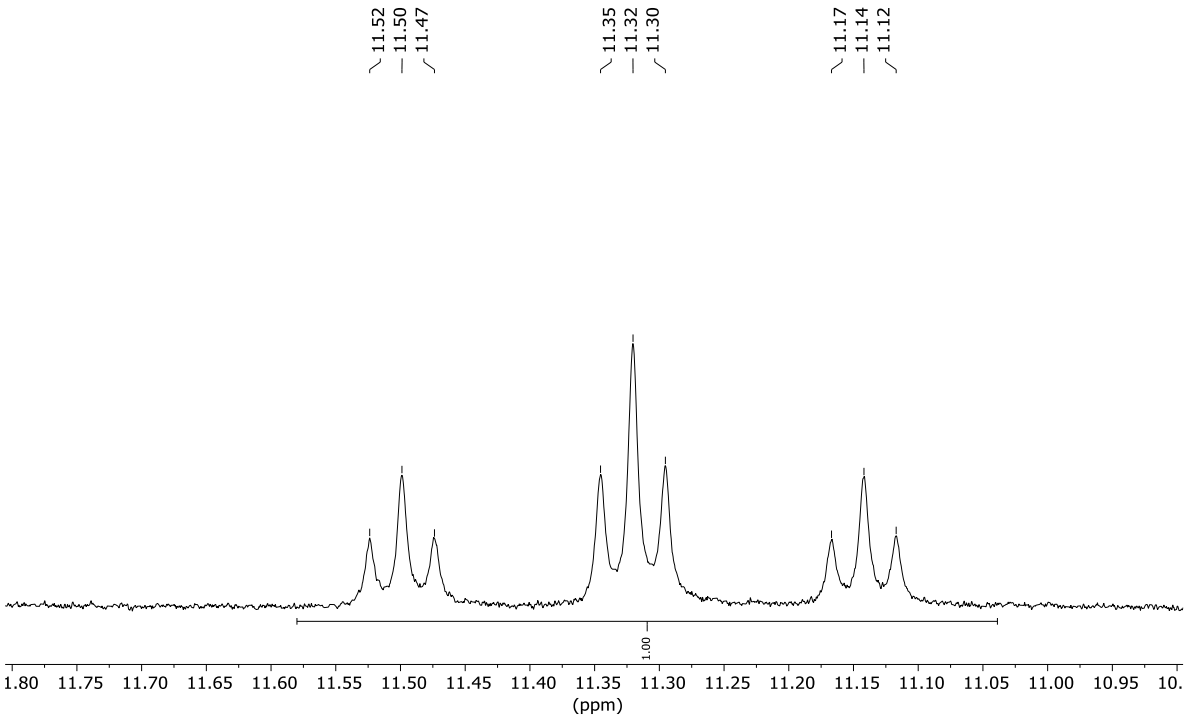

Figure 3.61. ^{1}H NMR spectrum (500 MHz) of **Ta1H** generated *in-situ* in C_6D_6 (7.16 ppm) showing hydride.

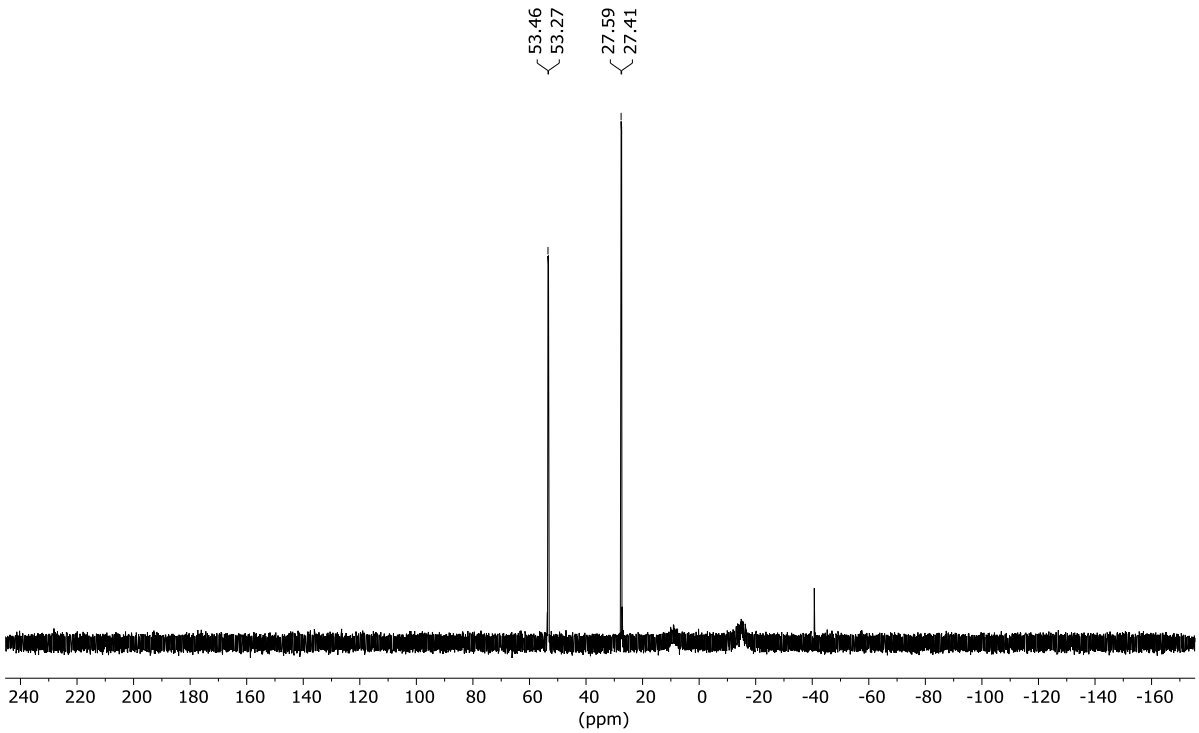

Figure 3.62. ^{31}P{^{1}H} NMR spectrum (202 MHz) of **Ta1H** generated *in-situ* in C_6D_6.

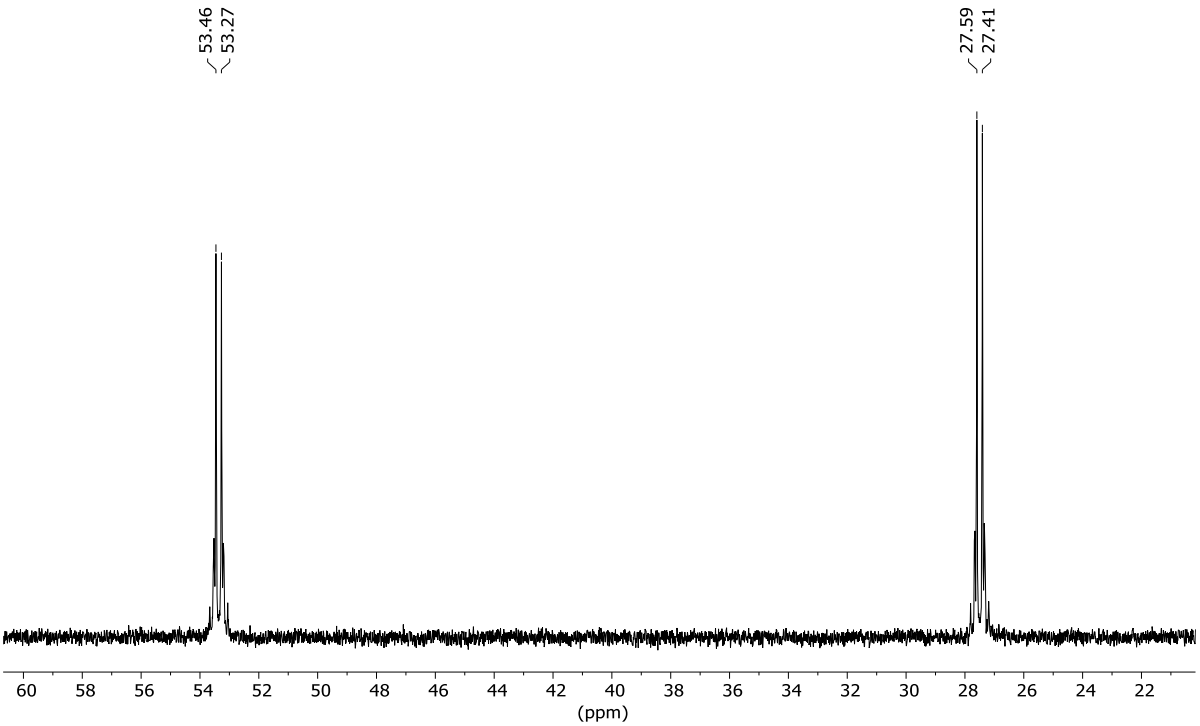

Figure 3.63. $^{31}P\{^{1}H\}$ NMR spectrum (202 MHz) of **Ta1H** generated *in-situ* in C_6D_6 showing coordinated phosphine region.

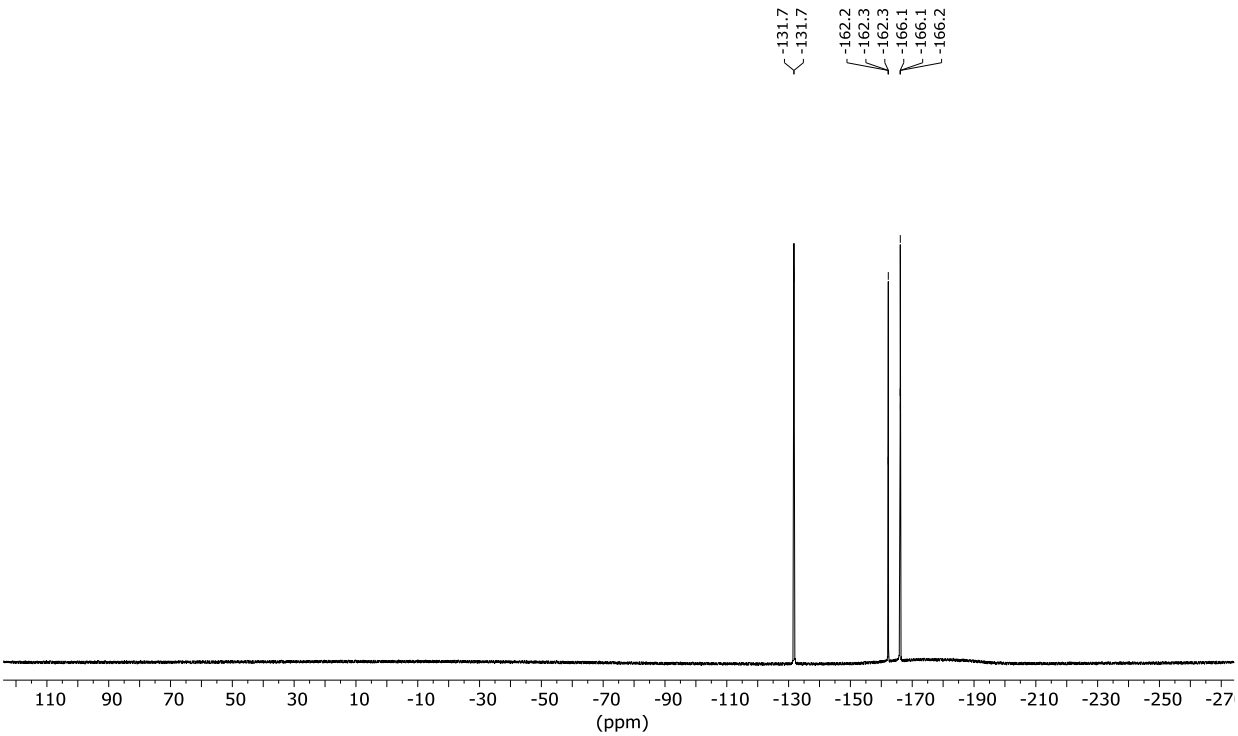

Figure 3.64. $^{19}F\{^{1}H\}$ NMR spectrum (471 MHz) of **Ta1H** generated *in-situ* in C_6D_6.

3.4.7. pKa Measurements on Mo2 and Mo2H.

The pK_a of **Mo2H** was determined using a pK_a bracketing methodology under an inert atmosphere. This was done by preparation of either **Mo2** or **Mo2H** (10 mmol) in 1 mL of THF spiked with 50 μL of C_6D_6 for NMR lock. To this solution, two equivalents of acid (**Mo2**) or base (**Mo2H**) was added and mixed using a pipette. The resulting solution was then transferred to a J. Young NMR tube, sealed, and analyzed using $^{31}P\{^1H\}$ NMR spectroscopy. From successful protonation and deprotonation reactions to the conjugate acid or base, the pK_a was bracketed between [H·Coll][PF_6] and DMAP (Figure 3.65).

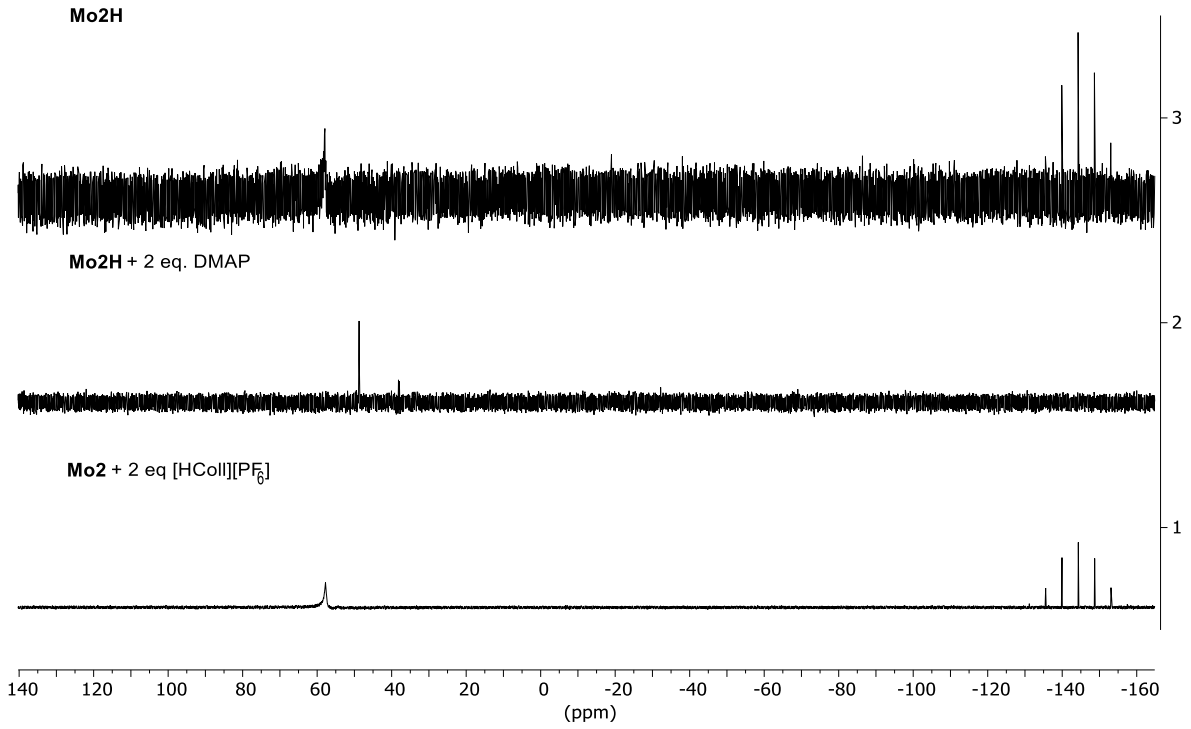

Figure 3.65. $^{31}P\{^1H\}$ NMR spectrum (202 MHz) of pK_a bracketing experiment of **Mo2** and **Mo2H** in THF.

3.5 References.

1. Prier, C. K.; Rankic, D. A.; MacMillan, D. W. C. *Chemical Reviews* **2013**, *113*, 5322-5363.

2. Cambié, D.; Bottecchia, C.; Straathof, N. J. W.; Hessel, V.; Noël, T. *Chemical Reviews* **2016**, *116*, 10276-10341.

3. Romero, N. A.; Nicewicz, D. A. *Chemical Reviews* **2016**, *116*, 10075-10166.

4. Oelgemöller, M. *Chemical Reviews* **2016**, *116*, 9664-9682.

5. McCusker, J. K. *Science* **2019**, *363*, 484-488.

6. Rehm, D.; Weller, A. *Israel Journal of Chemistry* **1970**, *8*, 259-271.

7. Gisbertz, S.; Reischauer, S.; Pieber, B. *Nature Catalysis* **2020**, *3*, 611-620.

8. Yoon, T. P.; Ischay, M. A.; Du, J. *Nature Chemistry* **2010**, *2*, 527-532.

9. Ghosh, I.; Ghosh, T.; Bardagi, J. I.; König, B. *Science* **2014**, *346*, 725-728.

10. Kim, H.; Lee, C. *Angewandte Chemie International Edition* **2012**, *51*, 12303-12306.

11. Nguyen, J. D.; D'Amato, E. M.; Narayanam, J. M. R.; Stephenson, C. R. J. *Nature Chemistry* **2012**, *4*, 854-859.

12. Cahard, E.; Schoenebeck, F.; Garnier, J.; Cutulic, S. P. Y.; Zhou, S.; Murphy, J. A. *Angewandte Chemie International Edition* **2012**, *51*, 3673-3676.

13. Costentin, C.; Robert, M.; Savéant, J.-M. *Journal of the American Chemical Society* **2004**, *126*, 16051-16057.

14. Pause, L.; Robert, M.; Savéant, J.-M. *Journal of the American Chemical Society* **1999**, *121*, 7158-7159.

15. Vibbert, H. B. Group 6 Metal-Oxo and -Alkylidyne Complexes with High Reactivity Derived from π-Antibonding Orbitals. Ph.D., The University of Chicago, United States -- Illinois, 2018.

16. Da Re, R. E.; Hopkins, M. D. *Coordination Chemistry Reviews* **2005**, *249*, 1396-1409.

17. Manna, J.; Gilbert, T. M.; Dallinger, R. F.; Geib, S. J.; Hopkins, M. D. *Journal of the American Chemical Society* **1992**, *114*, 5870-5872.

18. O'Hanlon, D. C.; Cohen, B. W.; Moravec, D. B.; Dallinger, R. F.; Hopkins, M. D. *Journal of the American Chemical Society* **2014**, *136*, 3127-3136.

19. Lovaasen, B. M.; Lockard, J. V.; Cohen, B. W.; Yang, S.; Zhang, X.; Simpson, C. K.; Chen, L. X.; Hopkins, M. D. *Inorganic Chemistry* **2012**, *51*, 5660-5670.

20. Haines, D. E.; O'Hanlon, D. C.; Manna, J.; Jones, M. K.; Shaner, S. E.; Sun, J.; Hopkins, M. D. *Inorganic Chemistry* **2013**, *52*, 9650-9658.

21. Rudshteyn, B.; Vibbert, H. B.; May, R.; Wasserman, E.; Warnke, I.; Hopkins, M. D.; Batista, V. S. *ACS Catalysis* **2017**, *7*, 6134-6143.

22. Pyykko, P. *Chemical Reviews* **1988**, *88*, 563-594.

23. Ikeda, H.; Ito, A.; Sakuda, E.; Kitamura, N.; Takayama, T.; Sekine, T.; Shinohara, A.; Yoshimura, T. *Inorganic Chemistry* **2013**, *52*, 6319-6327.

24. Mohammed, A. K.; Isovitsch, R. A.; Maverick, A. W. *Inorganic Chemistry* **1998**, *37*, 2779-2785.

25. Mann, K. R.; Gray, H. B.; Hammond, G. S. *Journal of the American Chemical Society* **1977**, *99*, 306-307.

26. Colombo, M. G.; Brunold, T. C.; Riedener, T.; Guedel, H. U.; Fortsch, M.; Buergi, H.-B. *Inorganic Chemistry* **1994**, *33*, 545-550.

27. Lai, S.-W.; Cheung, T.-C.; Chan, M. C. W.; Cheung, K.-K.; Peng, S.-M.; Che, C.-M. *Inorganic Chemistry* **2000**, *39*, 255-262.

28. Schoch, T. K.; Main, A. D.; Burton, R. D.; Lucia, L. A.; Robinson, E. A.; Schanze, K. S.; McElwee-White, L. *Inorganic Chemistry* **1996**, *35*, 7769-7775.

29. Barigelletti, F.; Sandrini, D.; Maestri, M.; Balzani, V.; Von Zelewsky, A.; Chassot, L.; Jolliet, P.; Maeder, U. *Inorganic Chemistry* **1988**, *27*, 3644-3647.

30. Fleetham, T.; Ji, Y.; Huang, L.; Fleetham, T. S.; Li, J. *Chemical Science* **2017**, *8*, 7983-7990.

31. Chow, P.-K.; Cheng, G.; Tong, G. S. M.; Ma, C.; Kwok, W.-M.; Ang, W.-H.; Chung, C. Y.-S.; Yang, C.; Wang, F.; Che, C.-M. *Chemical Science* **2016**, *7*, 6083-6098.

32. Büldt, L. A.; Guo, X.; Prescimone, A.; Wenger, O. S. *Angewandte Chemie International Edition* **2016**, *55*, 11247-11250.

33. Herr, P.; Glaser, F.; Büldt, L. A.; Larsen, C. B.; Wenger, O. S. *Journal of the American Chemical Society* **2019**, *141*, 14394-14402.

34. Lang, P. F.; Smith, B. C. *Journal of Chemical Education* **2003**, *80*, 938.

35. Rocklage, S. M.; Schrock, R. R. *Journal of the American Chemical Society* **1982**, *104*, 3077-3081.

36. Rocklage, S. M.; Schrock, R. R. *Journal of the American Chemical Society* **1980**, *102*, 7808-7809.

37. Heinselman, K. S.; Hopkins, M. D. *Journal of the American Chemical Society* **1995**, *117*, 12340-12341.

38. Williams, D. S.; Korolev, A. V. *Inorganic Chemistry* **1998**, *37*, 3809-3819.

39. Tonks, I. A.; Durrell, A. C.; Gray, H. B.; Bercaw, J. E. *Journal of the American Chemical Society* **2012**, *134*, 7301-7304.

40. Heinselman, K. S.; Miskowski, V. M.; Geib, S. J.; Wang, L. C.; Hopkins, M. D. *Inorganic Chemistry* **1997**, *36*, 5530-5538.

41. Morales-Verdejo, C. A.; Newsom, M. I.; Cohen, B. W.; Vibbert, H. B.; Hopkins, M. D. *Chemical Communications* **2013**, *49*, 10566-10568.

42. Churchill, M. R.; Wasserman, H. J.; Turner, H. W.; Schrock, R. R. *Journal of the American Chemical Society* **1982**, *104*, 1710-1716.

43. Wengrovius, J. H.; Schrock, R. R.; Churchill, M. R.; Wasserman, H. J. *Journal of the American Chemical Society* **1982**, *104*, 1739-1740.

44. Holmes, S. J.; Clark, D. N.; Turner, H. W.; Schrock, R. R. *Journal of the American Chemical Society* **1982**, *104*, 6322-6329.

45. Holmes, S. J.; Schrock, R. R. *Journal of the American Chemical Society* **1981**, *103*, 4599-4600.

46. Mayr, A.; Dorries, A. M.; McDermott, G. A.; Van Engen, D. *Organometallics* **1986**, *5*, 1504-1506.

47. Mayr, A.; McDermott, G. A.; Dorries, A. M. *Organometallics* **1985**, *4*, 608-610.

48. Sun, J.; Simpson, C. K.; Hopkins, M. D.; Hock, A. S.; Schrock, R. R. Tungsten Benzylidyne Complexes. In *Inorganic Syntheses: Volume 36*, Inorganic Syntheses, 2014; pp 134-138.

49. Schrock, R. R. *Chemical Reviews* **2002**, *102*, 145-180.

50. Ahmed, K. J.; Chisholm, M. H.; Huffman, J. C. *Organometallics* **1985**, *4*, 1168-1174.

51. Wigley, D. E. Organoimido Complexes of the Transition Metals. In *Progress in Inorganic Chemistry*, Progress in Inorganic Chemistry, 1994; pp 239-482.

52. Sattelberger, A. P.; Wilson, R. B., Jr.; Huffman, J. C. *Journal of the American Chemical Society* **1980**, *102*, 7111-7113.

53. Cotton, F. A.; Falvello, L. R.; Najjar, R. C. *Inorganic Chemistry* **1983**, *22*, 375-377.

54. Chakravarty, A. R.; Cotton, F. A.; Diebold, M. P.; Lewis, D. B.; Roth, W. J. *Journal of the American Chemical Society* **1986**, *108*, 971-976.

55. Cotton, F. A.; Diebold, M. P.; Roth, W. J. *Inorganic Chemistry* **1987**, *26*, 4130-4133.

56. Gianetti, T. L.; Nocton, G.; Minasian, S. G.; Kaltsoyannis, N.; Kilcoyne, A. L. D.; Kozimor, S. A.; Shuh, D. K.; Tyliszczak, T.; Bergman, R. G.; Arnold, J. *Chemical Science* **2015**, *6*, 993-1003.

57. Ballhausen, C. J.; Gray, H. B. *Inorganic Chemistry* **1962**, *1*, 111-122.

58. Da Re, R. E.; Hopkins, M. D. *Inorganic Chemistry* **2002**, *41*, 6973-6985.

59. Rudolph, M.; Autschbach, J. *The Journal of Physical Chemistry A* **2011**, *115*, 14677-14686.

60. Laurent, A. D.; Jacquemin, D. *International Journal of Quantum Chemistry* **2013**, *113*, 2019-2039.

61. Latouche, C.; Skouteris, D.; Palazzetti, F.; Barone, V. *Journal of Chemical Theory and Computation* **2015**, *11*, 3281-3289.

62. Bocarsly, A. B.; Cameron, R. E.; Rubin, H. D.; McDermott, G. A.; Wolff, C. R.; Mayr, A. *Inorganic Chemistry* **1985**, *24*, 3976-3978.

63. Carter, J. D.; Kingsbury, K. B.; Wilde, A.; Schoch, T. K.; Leep, C. J.; Pham, E. K.; McElwee-White, L. *Journal of the American Chemical Society* **1991**, *113*, 2947-2954.

64. Brower, D. C.; Stoll, M.; Templeton, J. L. *Organometallics* **1989**, *8*, 2786-2792.

65. Cavalheiro, C. C. S.; Torraca, K. E.; Schanze, K. S.; McElwee-White, L. *Inorganic Chemistry* **1999**, *38*, 3254-3257.

66. Kingsbury, K. B.; Carter, J. D.; Wilde, A.; Park, H.; McElwee-White, L.; Takusagawa, F. *Journal of the American Chemical Society* **1993**, *115*, 10056-10065.

67. Mayr, A.; Kjelsberg, M. A.; Lee, K. S.; Asaro, M. F.; Hsieh, T. *Organometallics* **1987**, *6*, 2610-2612.

68. Sheridan, J. B.; Pourreau, D. B.; Geoffroy, G. L.; Rheingold, A. L. *Organometallics* **1988**, *7*, 289-294.

69. Garrido, G.; Koort, E.; Ràfols, C.; Bosch, E.; Rodima, T.; Leito, I.; Rosés, M. *The Journal of Organic Chemistry* **2006**, *71*, 9062-9067.

70. Agarwal, R. G.; Coste, S. C.; Groff, B. D.; Heuer, A. M.; Noh, H.; Parada, G. A.; Wise, C. F.; Nichols, E. M.; Warren, J. J.; Mayer, J. M. *Chemical Reviews* **2022**, *122*, 1-49.

71. Rennie, B. E.; Eleftheriades, R. G.; Morris, R. H. *Journal of the American Chemical Society* **2020**, *142*, 17607-17629.

72. Marken, F.; Bond, A. M.; Colton, R. *Inorganic Chemistry* **1995**, *34*, 1705-1710.

73. Jutzi, P.; Müller, C.; Stammler, A.; Stammler, H.-G. *Organometallics* **2000**, *19*, 1442-1444.

74. Pangborn, A. B.; Giardello, M. A.; Grubbs, R. H.; Rosen, R. K.; Timmers, F. J. *Organometallics* **1996**, *15*, 1518-1520.

75. Korolev, A. V.; Rheingold, A. L.; Williams, D. S. *Inorganic Chemistry* **1997**, *36*, 2647-2655.

76. Li, X.; Bai, F.; Liu, C.; Ma, X.; Gu, C.; Dai, B. *Organic Letters* **2021**, *23*, 7445-7449.

77. Fulmer, G. R.; Miller, A. J. M.; Sherden, N. H.; Gottlieb, H. E.; Nudelman, A.; Stoltz, B. M.; Bercaw, J. E.; Goldberg, K. I. *Organometallics* **2010**, *29*, 2176-2179.

78. Neese, F. *WIREs Computational Molecular Science* **2012**, *2*, 73-78.

79. Neese, F. *WIREs Computational Molecular Science* **2018**, *8*, e1327.

80. Ernzerhof, M.; Scuseria, G. E. *The Journal of Chemical Physics* **1999**, *110*, 5029-5036.

81. Adamo, C.; Barone, V. *The Journal of Chemical Physics* **1999**, *110*, 6158-6170.

82. Weigend, F.; Ahlrichs, R. *Physical Chemistry Chemical Physics* **2005**, *7*, 3297-3305.

83. Pantazis, D. A.; Chen, X.-Y.; Landis, C. R.; Neese, F. *Journal of Chemical Theory and Computation* **2008**, *4*, 908-919.

84. van Lenthe, E.; Snijders, J. G.; Baerends, E. J. *The Journal of Chemical Physics* **1996**, *105*, 6505-6516.

85. Izsák, R.; Neese, F. *The Journal of Chemical Physics* **2011**, *135*, 144105.

86. Neese, F.; Wennmohs, F.; Hansen, A.; Becker, U. *Chemical Physics* **2009**, *356*, 98-109.

87. Weigend, F. *Physical Chemistry Chemical Physics* **2006**, *8*, 1057-1065.

88. Eichkorn, K.; Treutler, O.; Öhm, H.; Häser, M.; Ahlrichs, R. *Chemical Physics Letters* **1995**, *240*, 283-290.

89. Hanwell, M. D.; Curtis, D. E.; Lonie, D. C.; Vandermeersch, T.; Zurek, E.; Hutchison, G. R. *Journal of Cheminformatics* **2012**, *4*, 17.

90. Krause, L.; Herbst-Irmer, R.; Sheldrick, G. M.; Stalke, D. *Journal of Applied Crystallography* **2015**, *48*, 3-10.

91. Sheldrick, G. *Acta Crystallographica Section A* **2015**, *71*, 3-8.

92. Dolomanov, O. V.; Bourhis, L. J.; Gildea, R. J.; Howard, J. A. K.; Puschmann, H. *Journal of Applied Crystallography* **2009**, *42*, 339-341.

CHAPTER 4

Computational Prediction of Emissive Triplet States of Tungsten Benzylidyne Chromophores

4.1 Introduction.

Studying and understanding the electronic structures of photoredox chromophores is a key part of further developing and improving their excited-state properties. Experimental data such as redox potentials, electronic absorption spectra, transient-absorption spectra, and luminescence lifetime data are all key tools to help understand excited-state processes. Computational chemistry provides a complementary method to study excited states to gain information not readily available through experiment. A classic example of this is excited-state geometries, which are challenging to study due to their short lifetimes and small geometric changes. Only recently have methods for experimentally measuring excited-state bond changes for transitional metal chromophores been developed, including X-ray transient absorption spectroscopy (XTA).[1] Despite the utility of XTA, it is limited by only probing bonds surrounding the metal center or other heavy elements. Computational study of excited states potentially provides a more accessible and general route for understanding excited-state geometries and relaxation processes. These geometries can then be used to provide photophysical predictions such as emission E_{00}, excited-state branching, and conical intersections.

Our lab has previously shown that d^2 tungsten–benzylidyne complexes exhibit long-lived photoluminescence from the $^3[d_{xy}\rightarrow\pi^*]$ excited state and that this state participates in photoredox reactions.[2-5] To better understand their properties, DFT was employed as a predictive tool.[2, 6-7] These approaches utilized semi-empirical correlations between calculated ground-state properties

and spectroscopic and photophysical measurements, including E_{00}, $E^{0/+}$, λ_{max}, and λ_{em}. In general, the DFT protocol used for prediction showed good correlation with experimental values providing a useful tool for further prediction and development of this class of photoredox chromophores. Unanswered questions that cannot be addressed by such an approach concern how the excited states of these molecules are distorted relative to the ground state and how it relaxes within the triplet manifold. This is important if the photophysics of future chromophores are to be predicted. This study focuses on DFT analysis of a series of related tungsten–benzylidyne phosphine complexes (Figure 4.1), the excited state energies and photophysical properties of which are known from experiment to strongly depend on the phosphine π-acidity and benzylidyne para-substitution. The relative energetics of two low lying triplet states, $^3[d_{xy} \rightarrow \pi^*]$ and $^3[\pi \rightarrow \pi^*]$, were of particular interest, and were studied to determine whether excited-state mixing and crossover of these two states occurs depending on the peripheral substitution of the complex (Figure 4.1).

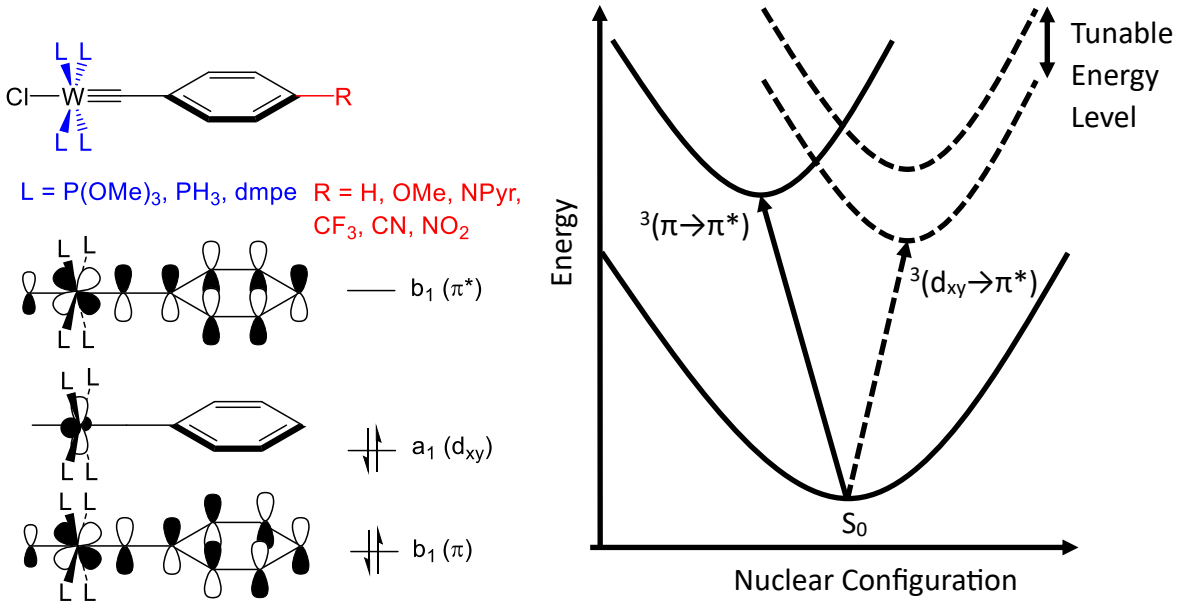

Figure 4.1. Left: Generalized frontier electronic structure of tungsten benzylidynes. Right: Cartoon demonstrating potential excited-state inversion based on peripheral substitution.

The possibility of inversion of the $^3[d_{xy}\rightarrow\pi^*]$ and $^3[\pi\rightarrow\pi^*]$ states was raised by the observation of weak vibronic structure only in the emission spectrum of W(CC_6H_4-4-pyr){$P(OMe)_3$}$_4$Cl, and the fact that its excited-state lifetime is much longer than expected from a simple energy-gap law relationship (Figure 4.2).[2] One possible explanation for this unusual behavior is that emission may be occurring from a different excited state, with the $^3[\pi\rightarrow\pi^*]$ state being a plausible candidate. Very little mention of this excited-state has been made for tungsten benzylidyne chromophores, but studies of isoelectronic rhenium benzylidynes conducted by Che and coworkers have suggested that these complexes emit from the $^3[\pi\rightarrow\pi^*]$ state instead of the typical $^3[d_{xy}\rightarrow\pi^*]$.[8] The $^1[\pi\rightarrow\pi^*]$ transition energies observed in the UV-Vis spectra for these rhenium complexes are comparable to those for tungsten benzylidynes, indicating that the relevant $^3[\pi\rightarrow\pi^*]$ state may be at similar energies for the tungsten compounds. These rhenium complexes luminesce at relatively high energies and possess a strongly stabilized d_{xy} orbital due to both the cationic charge and π-acidic phosphine; this may raise the energy of the $^3[d_{xy}\rightarrow\pi^*]$ state above that of the $^3[\pi\rightarrow\pi^*]$ state. As tungsten d_{xy} orbitals are higher energy than their rhenium analogues, observation of such competition would require both raising the energy of the π orbital manifold and lowering of the d_{xy} orbital to blueshift the $^3[d_{xy}\rightarrow\pi^*]$ state as much as possible, which are maximized for W(CC_6H_4-4-pyr){$P(OMe)_3$}$_4$Cl. As excited-state structures and triplet energies are difficult to determine experimentally, DFT provides an alternative route to study these excited-state features.

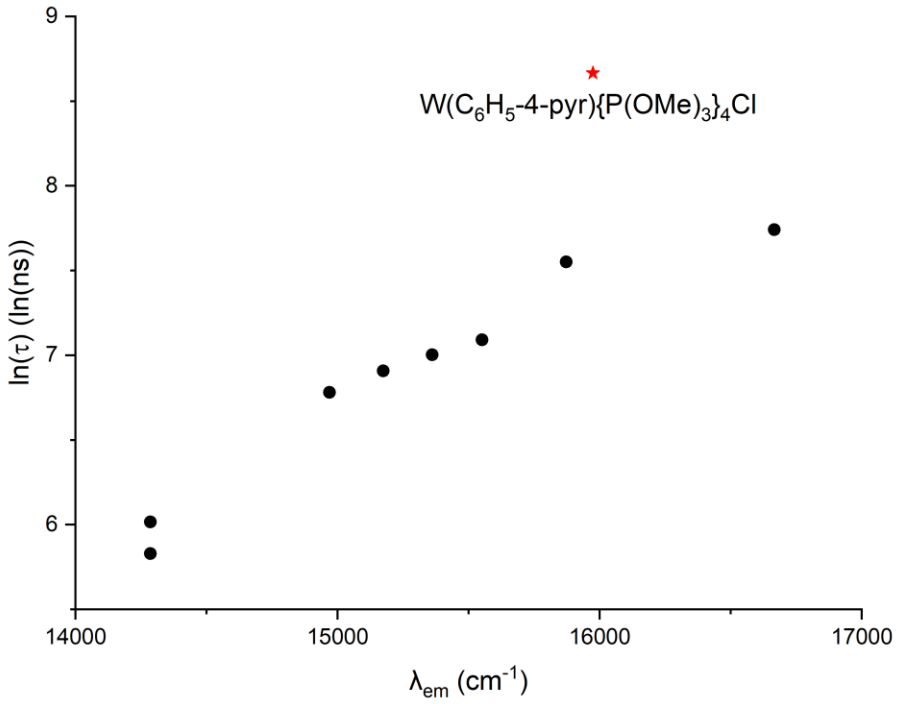

Figure 4.2. Energy-Gap Law plot of structurally related tungsten benzylidyne complexes of form $W(CC_6H_4\text{-}4\text{-}R)(L)_4Cl$.[2]

Ground-state and relaxed excited-state geometry optimizations for a series of complexes were performed to get a better understanding of the relative energies of the $^3[d_{xy}\rightarrow\pi^*]$ and $^3[\pi\rightarrow\pi^*]$ states and how they relax and mix in the excited-state. Two approaches were evaluated to optimize the geometry of the excited triplet states. The first approach utilizes geometries and energies from an unrestricted open-shell DFT (UODFT) calculation, which has previously been used for $W(CPh)(dppe)_2Cl$.[4] The second approach utilizes geometries and energies from time-dependent DFT (TDDFT) calculated triplet states using an excited-state gradient,[9] as implemented in the Orca quantum chemistry package.[10-11] The geometries and energies obtained from these two methods were then used to cross-compare the calculated triplet geometries to evaluate consistency and their applicability to the relaxed triplet state of these chromophores.

4.2 Results and Discussion.

4.2.1 Benchmarking Studies.

Before study of the relevant triplet states, a benchmarking comparison of our group's previous DFT methodology with updated methods and basis sets was done to validate their accuracy. These methods are labeled "Method 1" through "Method 8" and are described in Section 4.4.1. The previous methodology used by our group, termed here "Method 2", employed the B3P86 functional[12] in combination with the LANL2DZ basis set[13-14] and Effective Core Potential (ECP) on tungsten and polarized Dunning-Hay basis sets[15] on all other atoms. This method was selected in those earlier studies based on published benchmarking results for third-row metal complexes[16] and then validated through internal benchmarking studies of experimentally determined tungsten-benzylidyne molecular structures. [16-17] In the present report, an alternative method with lower reported mean deviation from the reference geometry was tested, which was previously not accessible due to computational cost. This method uses the PBE0 functional[18] with the SARC-ZORA-SVP basis set on tungsten[16] and the ZORA-DEF2-SVP basis set on all other atoms in combination with the ZORA Hamiltonian. This is termed "Method 1" and is the preferred new method among those benchmarked (Methods 3–8). To compare the accuracy of these methods for tungsten alkylidyne complexes, crystallographically determined bond parameters about the metal center were compared to their theoretically calculated ones for two complexes with different para-phenyl substituents. Multiple combinations of basis sets, functionals, and additional parameters such as effective core potentials (ECP) and relativistic effects were tested (see Section 4.4.1 and Tables 4.10 and 4.11). Two points of emphasis in the benchmarking study for the newer methods were relativistic correction due to the presence of a third-row metal and larger basis sets for the heavy metal.

Overall, very small differences were found between the optimized geometries and their crystallographically determined geometries. Slight overestimation of the W–Cl and W–P bond lengths are observed across the series. It is possible that elongated W–P bond lengths arise from steric crowding of the metal center which could be accounted for using an additional dispersion correction. Overall, differences are small and within error for DFT and therefore suitable for providing experimentally relevant ground-state geometries.

Given the similarity between the optimized geometries, Method 1 and Method 2 were compared through simulation of electronic absorption spectra using a TDDFT calculation with the Tamm-Dancoff approximation (Table 4.1).[19] Method 1 was found to accurately reproduce experimental $^1[d_{xy}\rightarrow\pi^*]$ transition energies. Method 2 strongly overestimates the $^1[d_{xy}\rightarrow\pi^*]$ transition energy but shows very similar $^1[\pi\rightarrow\pi^*]$ energy across the series. The improved agreement of Method 1 is largely attributed to the difference in functional and the ability of the scalar all electron relativistic basis set to more completely model the electronic structure of the heavy metal center compared to an ECP with a valence electron basis set. Experimental $^3[d_{xy}\rightarrow\pi^*]$ and $^3[\pi\rightarrow\pi^*]$ transition energies are not available for comparison to calculated energies, so it is assumed that the improvement shown by Method 1 to calculate the $^1[d_{xy}\rightarrow\pi^*]$ energy should also improve $^3[d_{xy}\rightarrow\pi^*]$ energies. Furthermore, the PBE0 functional used in Method 1 has historically performed very well for determining excitation energies using TDDFT,[20-22] so utilizing the same functional for both geometry optimization and excited-state energies lends itself well to later excited-state geometry optimizations where accurate prediction of both properties is necessary.

Table 4.1. Comparison of TDDFT and Experimental λ_{max} (nm).

	Electronic Transition	Method 1	Method 2	Expt.[a]
$W(CC_6H_5)(dmpe)_2Cl$	$^1[\pi\rightarrow\pi^*]$	326	329	338
	$^1[d_{xy}\rightarrow\pi^*]$	540	472	535
$W(CC_6H_4\text{-}4\text{-}OMe)(dmpe)_2Cl$	$^1[\pi\rightarrow\pi^*]$	323	328	335
	$^1[d_{xy}\rightarrow\pi^*]$	506	444	503
$W(CC_6H_4\text{-}4\text{-}pyr)(dmpe)_2Cl$	$^1[\pi\rightarrow\pi^*]$	327	345	352
	$^1[d_{xy}\rightarrow\pi^*]$	480	425	485
$W(CC_6H_5)\{P(OMe)_3\}_4Cl$	$^1[\pi\rightarrow\pi^*]$	320	323	328
	$^1[d_{xy}\rightarrow\pi^*]$	426	385	449
$W(CC_6H_4\text{-}4\text{-}pyr)\{P(OMe)_3\}_4Cl$	$^1[\pi\rightarrow\pi^*]$	325	343	350
	$^1[d_{xy}\rightarrow\pi^*]$	394	362	409

[a] Ref 2

4.2.2 Ground-State Electronic Structure Calculations.

The ground-state electronic structures and geometries of ten known and hypothetical tungsten–benzylidyne complexes were studied using Method 1. These complexes in general possess very similar bond parameters about the tungsten center (Table 4.2). Differences in bond lengths vary less than 0.1 Å across the series and fall within expected values for tungsten benzylidynes. Similarly, bond angles about the tungsten center within each subset of phosphines are close to each other confirming that para substitution has little effect on the geometry about the metal center. The major difference in ground-state geometry arises from the equatorial phosphines which vary greatly across the series due to differing steric bulk and their chelating ability. The frontier orbitals for eight of the complexes follow the well-established electronic structure of d^2 tungsten alkylidynes with a π(WCAr) HOMO-1, a non-bonding d_{xy} HOMO, and a π*(WCAr) LUMO (Table 4.3). The two exceptions $W(CC_6H_4\text{-}4\text{-}pyr)\{P(OMe)_3\}_4Cl$ and $W(CC_6H_4\text{-}4\text{-}OMe)\{P(OMe)_3\}_4Cl$, which invert the π(WCAr) and d_{xy} ordering such that

π(WCAr) is the HOMO and d_{xy} is HOMO–1. This is due to the strong π-donation of these particular para substituents, which destabilize the π(WCAr) orbital, and the relatively π-acidic trimethylphosphite ligands, which stabilize d_{xy}. The substituent-controlled destabilization of the π orbitals and stabilization of the d_{xy} orbitals lend credence to the possibility of inversion of the $^3[d_{xy}\rightarrow\pi^*]$ and $^3[\pi\rightarrow\pi^*]$ states.

Table 4.2 Ground state geometries optimized using Method 1.

	W≡C	W–Cl	W–P_{avr}	C(1)–C(2)	C(1)–W–Cl	C(2)–C(1)–W
W(CC_6H_5)(dmpe)$_2$Cl	1.821	2.584	2.456	1.437	179.9	179.9
W(CC_6H_4-4-OMe)(dmpe)$_2$Cl	1.820	2.588	2.454	1.439	179.8	179.6
W(CC_6H_4-4-pyr)(dmpe)$_2$Cl	1.820	2.592	2.451	1.439	179.8	179.6
W(CC_6H_5)(PH_3)$_4$Cl	1.821	2.528	2.442	1.438	179.6	179.4
W(CC_6H_5){P(OMe)$_3$}$_4$Cl	1.817	2.554	2.428	1.437	180	180
W(CC_6H_4-4-OMe){P(OMe)$_3$}$_4$Cl	1.818	2.551	2.427	1.434	179.9	179.9
W(CC_6H_4-4-pyr){P(OMe)$_3$}$_4$Cl	1.820	2.563	2.452	1.432	180	180
W(CC_6H_5-4-CF_3)(dmpe)$_2$Cl	1.822	2.573	2.459	1.434	179.65	178.2
W(CC_6H_5-4-CN)(dmpe)$_2$Cl	1.824	2.567	2.461	1.43	179.8	178.4
W(CC_6H_5-4-NO_2)(dmpe)$_2$Cl	1.825	2.563	2.462	1.428	179.8	178.3

Table 4.3. Ground-State Kohn-Sham Orbitals and TDDFT Transition Energies.

				TDDFT Calculated Transition Energies (cm^{-1})				
Complex	Orbital	Energy (eV)		$^1[\pi\rightarrow\pi^*]$	$^1[d_{xy}\rightarrow\pi^*]$	$^3[\pi\rightarrow\pi^*]$	$^3[d_{xy}\rightarrow\pi^*]$	$^3[d_{xy}\rightarrow\pi^*]$ - $^3[\pi\rightarrow\pi^*]$
$W(CC_6H_5)(dmpe)_2Cl$	L	-0.57	π^*	30693	18526	20532	18105	-2427
	H	-4.26	d_{xy}					
	H-1	-4.98	π					
$W(CC_6H_4\text{-}4\text{-}OMe)(dmpe)_2Cl$	L	-0.32	π^*	30919	19760	20909	19208	-1701
	H	-4.16	d_{xy}					
	H-1	-4.78	π					
$W(CC_6H_4\text{-}4\text{-}pyr)(dmpe)_2Cl$	L	-0.11	π^*	30535	20850	20485	19198	-1287
	H	-4.06	d_{xy}					
	H-1	-4.43	π					
$W(CC_6H_5)(PH_3)_4Cl$	L	-1.03	π^*	31270	20912	21395	19108	-2287
	H	-5.05	d_{xy}					
	H-1	-5.56	π					
$W(CC_6H_5)\{P(OMe)_3\}_4Cl$	L	-0.95	π^*	31272	23456	21733	21642	-91
	H	-5.21	d_{xy}					
	H-1	-5.49	π					
$W(CC_6H_4\text{-}4\text{-}OMe)\{P(OMe)_3\}_4Cl$	L	-0.65	π^*	31484	25458	21841	23689	1848
	H	-5.18	π					
	H-1	-5.21	d_{xy}					
$W(CC_6H_4\text{-}4\text{-}pyr)\{P(OMe)_3\}_4Cl$	L	-0.33	π^*	29529	25355	21027	23580	2553
	H	-4.66	π					
	H-1	-4.84	d_{xy}					
$W(CC_6H_5\text{-}4\text{-}CF_3)(dmpe)_2Cl$	L	-0.95	π^*	29400	16703	19684	17411	-2619
	H	-4.51	d_{xy}					
	H-1	-5.22	π					
$W(CC_6H_5\text{-}4\text{-}CN)(dmpe)_2Cl$	L	-1.45	π^*	27296	13717	17823	15363	-3080
	H	-4.67	d_{xy}					
	H-1	-5.38	π					
$W(CC_6H_5\text{-}4\text{-}NO_2)(dmpe)_2Cl$	L	-2.01	π^*	22044	9226	14833	13226	-3622
	H	-4.73	d_{xy}					
	H-1	-5.47	π					

The excited state energies associated with the ground-state geometries of these complexes were studied using TDDFT. Good agreement was found between the experimental and calculated $^1[d_{xy}\rightarrow\pi^*]$ and $^1[\pi\rightarrow\pi^*]$ transition energies. In agreement with past experimental assignments, the $^1[d_{xy}\rightarrow\pi^*]$ transition energy in general is found to be much lower (by ca. 10000 cm^{-1}) than the $^1[\pi\rightarrow\pi^*]$ transition energy. The relative energies of the $^3[d_{xy}\rightarrow\pi^*]$ and $^3[\pi\rightarrow\pi^*]$ states are less separated for some derivatives. For the parent dmpe complex W(CPh)$(dmpe)_2$Cl, the $^3[d_{xy}\rightarrow\pi^*]$ state is lower in energy than the $^3[\pi\rightarrow\pi^*]$ state by 2427 cm^{-1}. This energy gap decreases with increased para donation from the benzylidyne substituent or increased π-acidity of the equatorial phosphine. Similarly, it increases with increasingly withdrawing benzylidyne para substituents as well. These energy gaps qualitatively parallel the varying gaps between d_{xy} and π(WCAr) orbitals. The effect of the phosphine and benzylidyne substituent can work in concert such that for W$(CC_6H_4$-4-pyr$)\{P(OMe)_3\}_4$Cl and W$(CC_6H_4$-4-OMe$)\{P(OMe)_3\}_4$Cl, the relative energies of the $^3[d_{xy}\rightarrow\pi^*]$ and $^3[\pi\rightarrow\pi^*]$ states are inverted. This supports the possibility of substitution-dependent excited-state inversion, bearing in mind that these energies are from the ground-state minimum and do not necessarily reflect the ordering for the relaxed triplet state.

4.2.3 Triplet State Geometry Optimization.

Calculation of excited-state geometries was studied next. Two different approaches were used (Figure 4.3). The first approach is a simple and accessible UODFT calculation.[23] Instead of modeling the triplet state as an excited-state of the ground state singlet reference, the excited-state triplet is treated as an ordinary unrestricted open-shell ground-state allowing geometry optimization identical to the ground state singlet with only the multiplicity changed. This is a common, computationally accessible method that has shown general use for excited-state predictions.[24] It is important to note that UODFT, by construction, does not confine both electron

spins to the same orbitals, but instead constructs independent α and β orbitals for both spin up and spin down electrons. This breaks the classical description of the triplet state as an excited-state of the ground singlet state reference where an unoccupied orbital is populated from a doubly filled occupied orbital. As a result of breaking the orbital spin pairing, UODFT calculations can suffer from excess spin multiplicity, where the calculated spin multiplicity expectation value is higher than the mathematical spin multiplicity.[25] This excess spin value is called spin contamination, which can have a significant effect in Hartree-Fock calculations and highly correlated and delocalized systems where electrons are easily polarized.

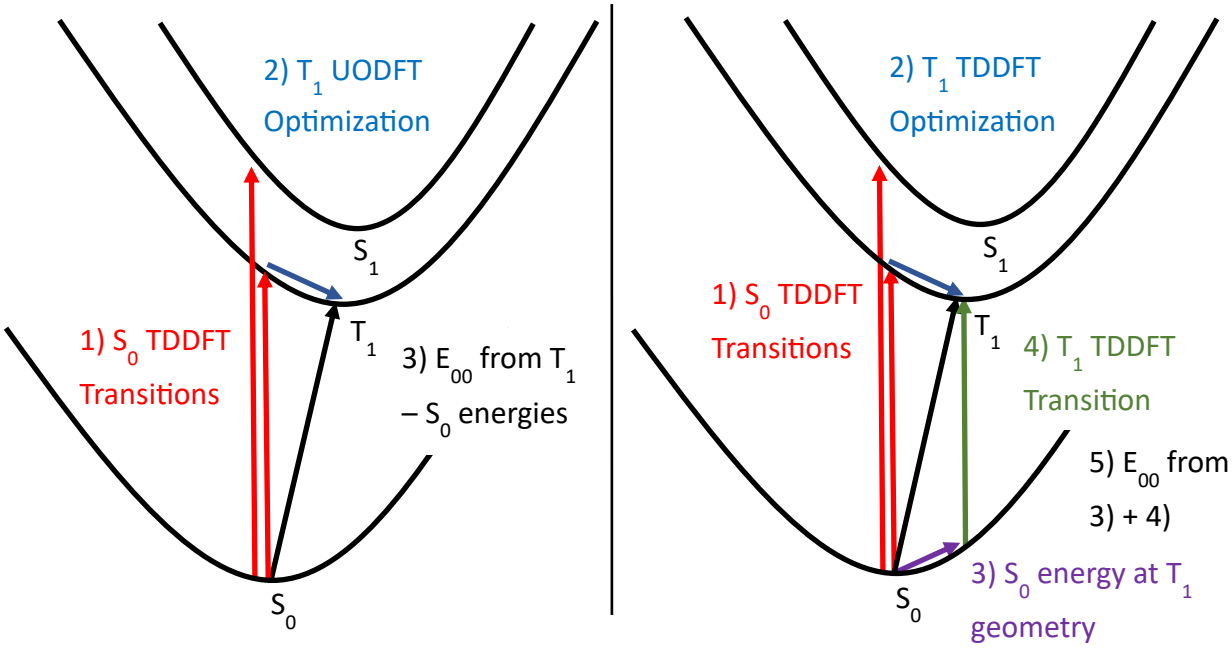

Figure 4.3. Diagrams showing approach for triplet optimization for UODFT (left) and TDDFT (right).

As many hybrid density functionals incorporate some percentage of Hartree-Fock exchange energy, spin contamination can appear in methods beyond Hartree-Fock. Spin-contamination can be remedied by use of restricted open-shell DFT (RODFT) calculations,[26]

which enforces this pairing at greater computational cost. While this method does qualitatively give a more classical excited-state, RODFT calculations typically suffer from their inability to model spin polarization and, as a result, often perform worse than UODFT calculations. Additionally, analytical gradients are unavailable through RODFT calculations in Orca rendering geometry optimizations difficult. The localized triplet states of the tungsten benzylidynes should not suffer from this spin contamination problem. This was tested by comparison of the expectation spin value to its ideal value of 2. The difference between the two is less than 0.05 in all cases confirming that spin contamination is not relevant (Table 4.4).

Table 4.4 Spin Expectation Value for UODFT Optimized Geometries.

	Spin Expectation Value
$W(CC_6H_5)(dmpe)_2Cl$	2.03092
$W(CC_6H_4\text{-}4\text{-}OMe)(dmpe)_2Cl$	2.03045
$W(CC_6H_4\text{-}4\text{-}pyr)(dmpe)_2Cl$	2.02948
$W(CC_6H_5)(PH_3)_4Cl$	2.03379
$W(CC_6H_5)\{P(OMe)_3\}_4Cl$	2.04098
$W(CC_6H_4\text{-}4\text{-}OMe)\{P(OMe)_3\}_4Cl$	2.03777
$W(CC_6H_4\text{-}4\text{-}pyr)\{P(OMe)_3\}_4Cl$	2.02643
$W(CC_6H_5\text{-}4\text{-}CF_3)(dmpe)_2Cl$	2.02803
$W(CC_6H_5\text{-}4\text{-}CN)(dmpe)_2Cl$	2.03054
$W(CC_6H_5\text{-}4\text{-}NO_2)(dmpe)_2Cl$	2.03165

The second approach was through TDDFT optimization of the excited state geometry. Here, since analytical gradients can be calculated using Orca at the DFT level, the triplet state geometry can be optimized from a TDDFT calculation without any restrictions. Computationally, this approach is much more expensive due to the construction of excited-state gradients and, in this case, is further complicated by the presence of a triplet instability during optimization.

Triplet instabilities are known issues with TDDFT calculations and arise from the inclusion of exact exchange in hybrid functionals.[27] The instability leads to underestimation of certain triplet state energies and, during the TDDFT optimizations, results in convergence failure due to the emergence of an imaginary excitation energy during geometry optimization arising from the formulation of the eigenvalue equation within the TDDFT framework. To avoid this, the Tamm-Dancoff approximation was used, which prevents the emergence of imaginary eigenvalues and has been shown to improve general triplet excitation energies.[28]

To verify the choice of functional for optimization of the T_1 state by TDDFT, various hybrid functionals including two range-separated methods (ωB97X and CAM-B3LYP) were benchmarked to compare the calculated E_{00} of the final T_1 optimized state estimated from the difference in single point energies to their experimentally determined value for two complexes (Table 4.12). Only PBE0 and the two range-separated functionals give experimentally reasonable predictions for both complexes, but both range-separated functionals predict the T_1 state for $W(CC_6H_5)(dmpe)_2Cl$ as a $^3[\pi\rightarrow\pi^*]$ state instead of experimentally confirmed $^3[d_{xy}\rightarrow\pi^*]$. This is attributed to dramatic overestimation of the $^3[d_{xy}\rightarrow\pi^*]$ energy, which is inferred from their similar overestimation of the $^1[d_{xy}\rightarrow\pi^*]$ energy. It is interesting to note that the set of functionals utilizing the three-parameter Becke hybrid exchange correlation functional without range separation (B3LYP, B3PW91, B3P86, and B97) all underestimate E_{00} by a decent margin. Only with the inclusion of range-separation for the CAM-B3LYP and ωB97X functionals do the energies become reasonable for both complexes. We propose that this difference arises from the Hartree-Fock exchange energy included in the overall exchange-correlation energy. Both range-separated functionals have variable Hartree-Fock Exchange energy that increases in contribution with greater separation to improve long-range exchange interaction energies.[29] This naturally

increases the amount of net Hartree-Fock exchange energy contribution within the system. For comparison, ωB97X possesses 15.7706% Hartree-Fock energy which increases up to 100%[30] while CAM-B3LYP possesses 19% Hartree-Fock energy that increases up to 65%.[29] The PBE0 functional does not possess this variable contribution but instead contains fixed 25% Hartree-Fock exchange energy[31] compared to 20% for B3LYP.[31] Hartree-Fock exchange energy is known to have a significant impact on transition metal covalency and energies[32] and therefore should have a large impact on the ($d_{xy}\rightarrow\pi^*$) transition energies since they have significant d-d parentage.[33-34] This helps to explain why PBE0 performs better for describing excited-states.

4.2.4 UODFT Excited-State Geometries.

The changes in bond distances and angles in the T_1 excited state calculated using the UODFT method are shown in Table 4.5. The data focus on distortions about the tungsten center and alkylidyne as these contribute the most to the orbitals associated with the $^3[d_{xy}\rightarrow\pi^*]$ and $^3[\pi\rightarrow\pi^*]$ excited states. For all compounds, there is a clear increase in W≡C bond length, a quinoidal distortion, and a contraction of the C(1)–C(2) bond. This is consistent with population of the phenyl-conjugated π*(WCAr) LUMO in both possible T_1 excited states, which reduces the formal W–C bond order from 3 to 2.5. Elongation of the W≡C bond correlates with increased para-donation on the benzylidyne, as for OMe and Pyr, and increased π-acidity of the phosphine. On the other hand, reduced para-donation from electron-withdrawing groups lead to smaller bond W≡C bond length changes. Marginal changes are found for both W–P_{avr} bond lengths and W–Cl bond lengths, consistent with their minimal character contributing to the frontier orbitals.

Table 4.5. Comparison of S_0 and T_1 Geometries for UODFT Method.[a]

		W≡C	W–Cl	W–P_{avr}	C(1)–C(2)	C(1)–W–Cl	C(2)–C(1)–W	δ_r
W(CC_6H_5)($dmpe)_2$Cl	S_0	1.821	2.584	2.456	1.437	179.9	179.9	0.007
	T_1	1.871	2.594	2.495	1.391	178.6	179.6	0.023
	T_1-S_0	**0.05**	0.01	0.0395	**-0.046**	-1.3	-0.3	**0.016**
W(CC_6H_4-4-OMe)($dmpe)_2$Cl	S_0	1.82	2.588	2.454	1.439	179.8	179.6	0.012
	T_1	1.892	2.568	2.484	1.389	171.3	178.1	0.026
	T_1-S_0	**0.072**	-0.02	0.02975	**-0.05**	-8.5	-1.5	**0.014**
W(CC_6H_4-4-pyr)($dmpe)_2$Cl	S_0	1.82	2.592	2.451	1.439	179.8	179.6	0.013
	T_1	1.927	2.541	2.464	1.375	172.5	176.3	0.029
	T_1-S_0	**0.107**	-0.051	0.013	**-0.064**	-7.3	-3.3	**0.016**
W(CC_6H_5)($PH_3)_4$Cl	S_0	1.821	2.528	2.442	1.438	179.6	179.4	0.006
	T_1	1.929	2.491	2.449	1.377	169.4	176.5	0.048
	T_1-S_0	**0.108**	-0.037	0.00725	**-0.061**	-10.2	-2.9	**0.042**
W(CC_6H_5){$P(OMe)_3$}$_4$Cl	S_0	1.817	2.554	2.428	1.437	180	180	0.007
	T_1	1.955	2.492	2.424	1.367	179.9	180	0.025
	T_1-S_0	**0.138**	-0.062	-0.0045	**-0.07**	-0.1	0	**0.018**
W(CC_6H_4-4-OMe){$P(OMe)_3$}$_4$Cl	S_0	1.818	2.551	2.427	1.434	179.9	179.9	0.012
	T_1	1.954	2.494	2.426	1.361	179.7	179.6	0.033
	T_1-S_0	**0.136**	-0.057	-0.001	**-0.073**	-0.2	-0.3	**0.021**
W(CC_6H_4-4-pyr){$P(OMe)_3$}$_4$Cl	S_0	1.82	2.563	2.452	1.432	180	180	0.014
	T_1	1.943	2.509	2.426	1.357	179.9	179.9	0.035
	T_1-S_0	**0.123**	-0.054	-0.026	**-0.075**	-0.1	-0.1	**0.021**
W(CC_6H_5-4-CF_3)($dmpe)_2$Cl	S_0	1.822	2.573	2.459	1.434	179.65	178.2	0.021
	T_1	1.878	2.564	2.491	1.387	175.6	179.6	0.054
	T_1-S_0	**0.056**	-0.009	0.032	**-0.047**	-4.05	1.4	**0.033**
W(CC_6H_5-4-CN)($dmpe)_2$Cl	S_0	1.824	2.567	2.461	1.43	179.8	178.4	0.026
	T_1	1.866	2.57	2.497	1.389	177.3	179	0.061
	T_1-S_0	**0.042**	0.003	0.036	**-0.041**	-2.5	0.6	**0.035**
W(CC_6H_5-4-NO_2)($dmpe)_2$Cl	S_0	1.825	2.563	2.462	1.428	179.8	178.3	0.022
	T_1	1.852	2.573	2.503	1.395	178.8	178.5	0.053
	T_1-S_0	**0.027**	0.01	0.041	**-0.033**	-1	0.2	**0.031**

[a] Changes highlighted in bold denote significant bond changes observed for all calculated complexes

Inspection of the calculated spin density for the UODFT optimized T_1 states provides further insight on assignment of the state and trends in the optimized triplet geometries (Table 4.6). Large W spin density is calculated in all systems, consistent with the large metal character in the frontier occupied orbitals, while relatively little spin density is found on both the Cl and the equatorial phosphines. The phosphine spin density remains remarkably invariant across the series despite their varying π-acidity. This confirms that the triplet state is largely metal and benzylidyne centered and is consistent with the minimal change in W–P_{avr} bond lengths in the excited-state. As the para-donor strength of the benzylidyne substituent is increased, the spin density on the tungsten center is gradually reduced with a concomitant increase in spin density on the benzylidyne. Similar spin density migration to the benzylidyne occurs with both π-acidic phosphine ligands. On the other hand, para-withdrawing groups have very little influence on tungsten or benzylidyne spin density, which remain close to that of the parent dmpe complex.

Table 4.6. Calculated Löwdin Spin Densities from UODFT Method.

	W	CC_6H_5-4-R	Cl	PR_n
$W(CC_6H_5)(dmpe)_2Cl$	1.279	0.557	0.011	0.153
$W(CC_6H_4$-4-OMe$)(dmpe)_2Cl$	1.125	0.673	0.031	0.171
$W(CC_6H_4$-4-pyr$)(dmpe)_2Cl$	0.948	0.884	0.043	0.125
$W(CC_6H_5)(PH_3)_4Cl$	0.912	0.821	0.073	0.195
$W(CC_6H_5)\{P(OMe)_3\}_4Cl$	0.755	1.012	0.087	0.145
$W(CC_6H_5$-4-OMe$)\{P(OMe)_3\}_4Cl$	0.771	1.023	0.086	0.120
$W(CC_6H_4$-4-pyr$)\{P(OMe)_3\}_4Cl$	0.760	1.042	0.075	0.122
$W(CC_6H_5$-4-$CF_3)(dmpe)_2Cl$	1.230	0.601	0.021	0.149
$W(CC_6H_5$-4-CN$)(dmpe)_2Cl$	1.265	0.595	0.015	0.125
$W(CC_6H_5$-4-$NO_2)(dmpe)_2Cl$	1.261	0.595	0.011	0.133

Rendering of the spin density isosurfaces provides further insight into the nature of the T_1 state. For the parent $W(CPh)(dmpe)_2Cl$ complex, the tungsten center shows clear tungsten d_{xy}

and π* character allowing unambiguous assignment of the lowest triplet state as $^3[d_{xy}\rightarrow\pi^*]$ (Figure 4.4). With increasing donation of the para substituent, the tungsten gradually adopts more dπ character as evidenced by formation of an equatorial nodal plane and the π asymmetry about the tungsten center. This is proposed to be due to inversion of the order of the $^3[d_{xy}\rightarrow\pi^*]$ and $^3[\pi\rightarrow\pi^*]$ states (Figures 4.9-13). As the benzylidyne is substituted with more donating para substituents, the energy of the π* orbital is gradually raised relative to the d_{xy} while, similarly, increasing the π-acidity of the phosphines stabilizes the d_{xy} orbital relative to π*. Both lead to an overall increase of the $d_{xy}\rightarrow\pi^*$ energy gap and shift to higher energy of the $^3[d_{xy}\rightarrow\pi^*]$ state. On the other hand, the $^3[\pi\rightarrow\pi^*]$ energy remains largely invariant as donating or withdrawing substituents will act on both orbitals relatively equally resulting in only marginal changes upon substitution. Only with the strongly para-withdrawing substituents such as NO_2 and CN, which strongly polarize the benzylidyne, do the predicted $^3[\pi\rightarrow\pi^*]$ energies significantly decrease.

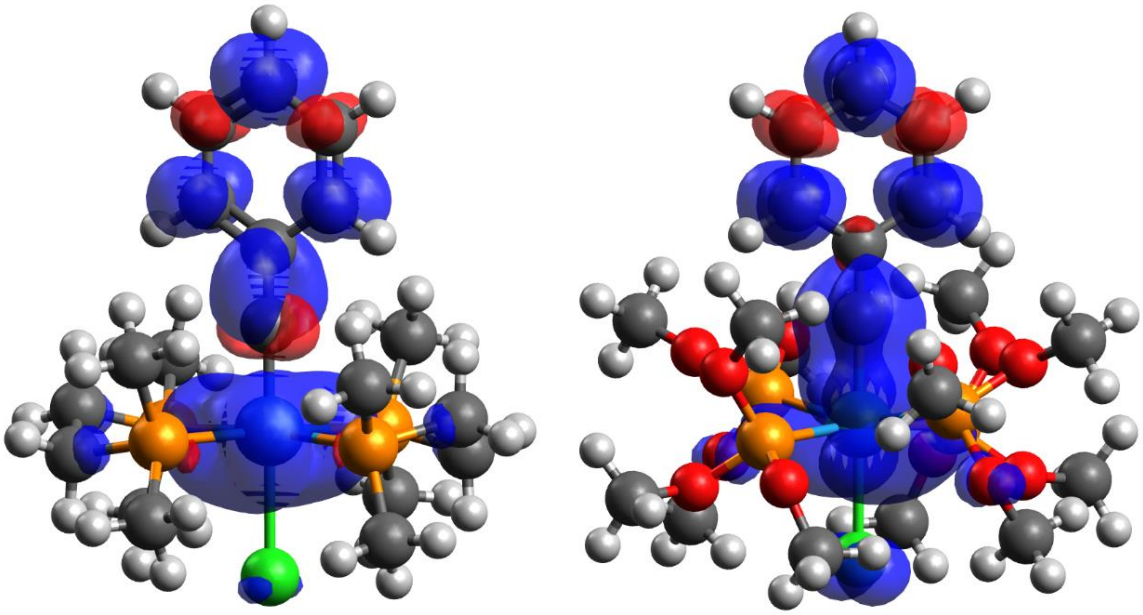

Figure 4.4. Spin density isosurfaces for the T_1 states of $W(CC_6H_5)(dmpe)_2Cl$ (left) and $W(CC_6H_5)\{P(OMe)_3\}_4Cl$ (right) rendered at an isovalue of 0.002.

The state-crossing is consistent with the observation that the parent $W(CPh)(dmpe)_2Cl$ complex and derivatives with CF_3, CN, and NO_2 substituted benzylidynes display similar calculated geometries and spin densities, as these all preserve the lowest energy $^3[d_{xy}\rightarrow\pi^*]$ state. As the T_1 state becomes $^3[\pi\rightarrow\pi^*]$ the corresponding depopulated tungsten orbital is π(WCAr). This induces a greater change in W≡C bond length since the formal bond order is decreasing from three to two. Similar trends were found from the ground-state TDDFT calculations where the T_1 state changes from $^3[d_{xy}\rightarrow\pi^*]$ to $^3[\pi\rightarrow\pi^*]$ for the phosphite complexes. Those calculated TDDFT energies do not exactly reproduce the trend found here because they are not relaxed triplet geometries. By optimization and allowing the triplet state to relax, the two relevant triplet states are allowed to mix and relax yielding the observed mixed geometries. This allows a gradual increase of the $^3[\pi\rightarrow\pi^*]$ contribution to the optimized triplet state up to the point where the energetic ordering inverts and the $^3[\pi\rightarrow\pi^*]$ is now the lowest triplet state.

A second, more subtle geometric change in the T_1 state is a calculated rotation of the benzylidyne phenyl group about the WC axis, such that the phenyl plane is nearly parallel to a pair of trans phosphorus nuclei. This is attributed to mixing of the phosphine π-accepting orbital with the π* LUMO, which helps to delocalize the spin and stabilize the singly occupied π* orbital. Due to the slight saddling of the WP_4 plane, one pair of trans phosphorus nuclei will mix slightly better with the π* orbital and induces rotation of the phenyl ring to be orthogonal to this pair to maximize overlap. To further elaborate this rotation, the relaxed geometries of $W(CC_6H_5)(PH_3)_4Cl$ and $W(CC_6H_5)(dmpe)_2Cl$ were studied upon rotation of the phenyl about the WC axis in the ground state (Figures 4.5 and 4.6). For both complexes, phenyl rotation proceeds with a very small barrier. For $W(CC_6H_5)(PH_3)_4Cl$, steric effects are minimal, and the energy profile should be governed solely by the electronic interaction of the phosphine with the

benzylidyne unit. As expected, the rotation barrier in the gas phase is < 0.2 kcal/mol, consistent with the cylindrical symmetry of the π interaction and the small mixing with the phosphine due to their mutually orthogonal coordination (Figure 4.5). A much larger barrier of ca. 2 kcal/mol for rotation is found for $W(CC_6H_5)(dmpe)_2Cl$ due to the steric pressure introduced by the phosphine methyl groups (Figure 4.6). The two stable conformers place the phenyl bisecting the phosphine ethyl backbone and in the cleft between the two phosphines matching experimentally determined crystallographic structures for tungsten benzylidyne complexes.[4, 6] This suggests that rotation of the phosphine in the T_1 excited-state must overcome steric repulsion and is due to electronic stabilization of the triplet state by delocalization onto the phosphine.

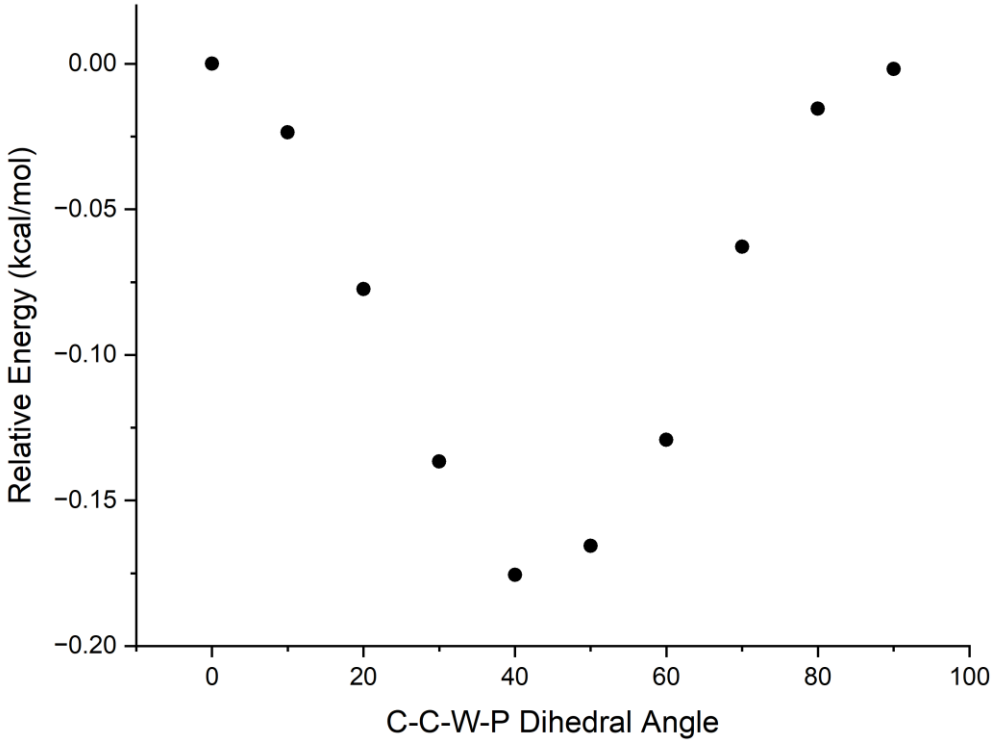

Figure 4.5. Relative energies of benzylidyne phenyl rotation about the WC axis for $W(CC_6H_5)(PH_3)_4Cl$ in the ground state.

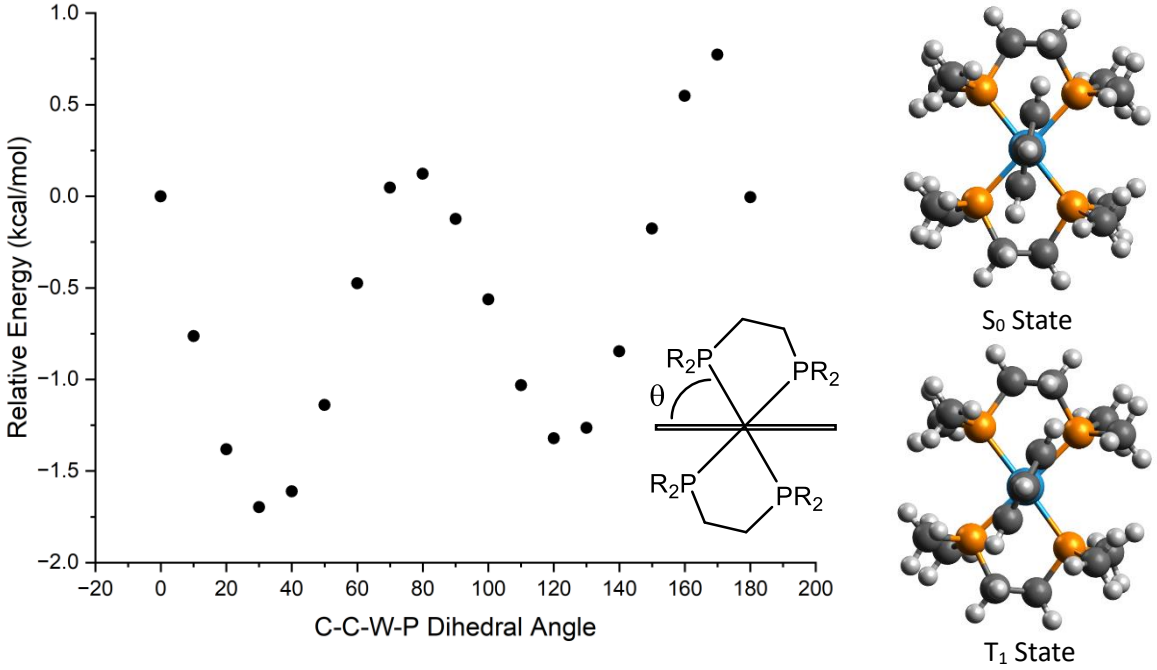

Figure 4.6. Left: Relative ground-state energies of benzylidyne phenyl rotation about the WC axis for $W(CC_6H_5)(dmpe)_2Cl$. Right: comparison of the S_0 and T_1 geometries of $W(CC_6H_5)(dmpe)_2Cl$.

To test how much this rotation perturbs other excited-state energies, a relaxed T_1 geometry scan for phenyl rotation about the WC axis for $W(CC_6H_5)(PH_3)_4Cl$ was performed with a subsequent TDDFT calculation to obtain the corresponding excited-state surfaces (Figure 4.7). It is found that the $^3[\pi\rightarrow\pi^*]$ T_1 state is stabilized by 0.02 eV when the phenyl is coplanar with a set of trans phosphines, while it is maximized when the phenyl bisects the angle formed by two cis phosphines. Similar geometric stabilization is found for the $^3[d_{xy}\rightarrow\pi^*]$ and $^1[\pi\rightarrow\pi^*]$ states by 0.08 eV and 0.07 eV respectively. This confirms the hypothesis that rotation is electronically driven by delocalization onto the phosphine. The magnitude of electronic stabilization is still smaller than the ground-state rotational barrier found for $W(CC_6H_5)(dmpe)_2Cl$ indicating that steric bulk will still be the dominant factor in the rotation of the benzylidyne phenyl group in the excited-state.

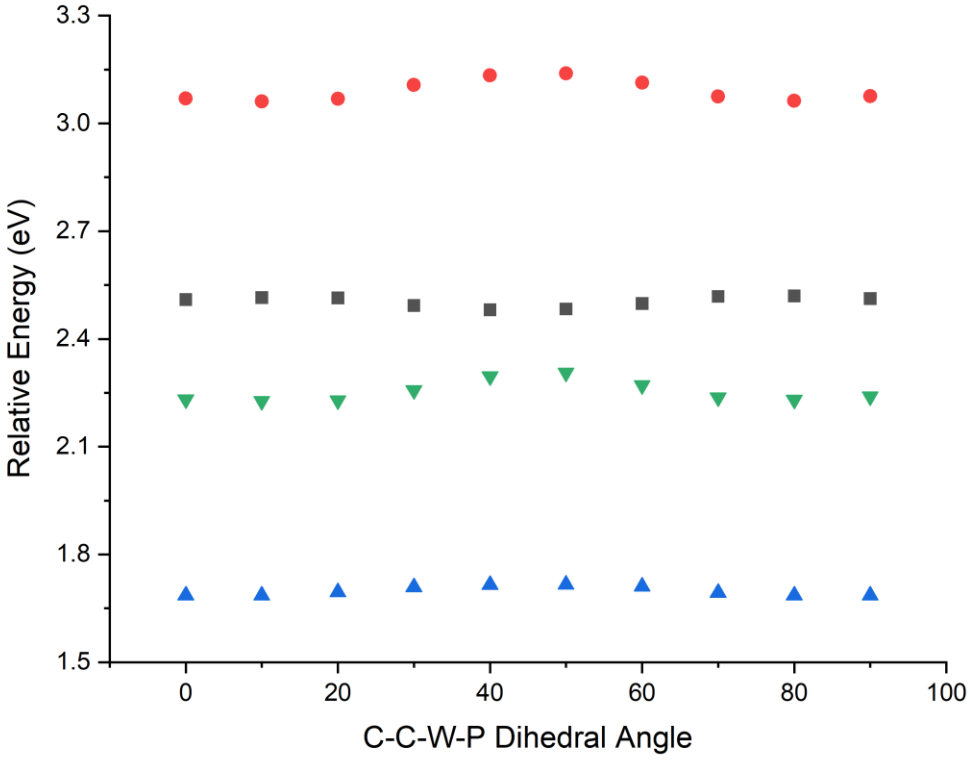

Figure 4.7. Relative excited-state energies upon phenyl rotation about the WC axis for $W(CC_6H_5)(PH_3)_4Cl$. Blue: $^3[\pi\rightarrow\pi^*]$, Green: $^3[d_{xy}\rightarrow\pi^*]$, Black: $^1[d_{xy}\rightarrow\pi^*]$, Red: $^1[\pi\rightarrow\pi^*]$.

4.2.5 TDDFT Excited-State Geometries.

Similar to the results of the UODFT calculations, TDDFT calculations of T_1 excited state geometries show elongation of the W≡C bond length and a quinoidal distortion in the excited-state (Table 4.13). The magnitude of W≡C bond elongation in the T_1 state again correlates with increasing para π-donation and increased phosphine π-acidity. Rotation of the benzylidyne plane parallel to a set of trans phosphorus nuclei is also observed, as was found for the UODFT geometries. This is attributed to the same stabilization of the π* LUMO by mixing with the phosphine π-accepting orbitals. Inspection of the transition difference densities provides further insight into the origin of the structural changes in the TDDFT optimized T_1 state (Figure 4.8). For the parent $W(CC_6H_5)(dmpe)_2Cl$ complex, the excited-state is predominantly $^3(d_{xy}\rightarrow\pi)$.

Progressing towards more electron donating phenyl substituents and π-acidic phosphines, the excited state gains more $^3[\pi\rightarrow\pi^*]$ character (Figures 4.14-18). This change from $^3[d_{xy}\rightarrow\pi^*]$ to $^3[\pi\rightarrow\pi^*]$ character explains both the change in bond parameters observed for the TDDFT optimized T_1 state and their relative trend. For $W(CC_6H_4\text{-}4\text{-}pyr)\{P(OMe)_3\}_4Cl$, most of the depleted transition density on the tungsten atom is strongly polarized towards the alkylidyne with almost no density lying below the WP_4 plane. This results in nearly the entire transition density lying on the benzylidyne ligand. This same trend towards $^3[d_{xy}\rightarrow\pi^*]$ and $^3[\pi\rightarrow\pi^*]$ excited-state inversion was found by the UODFT method as well providing additional evidence that such inversion is occurring.

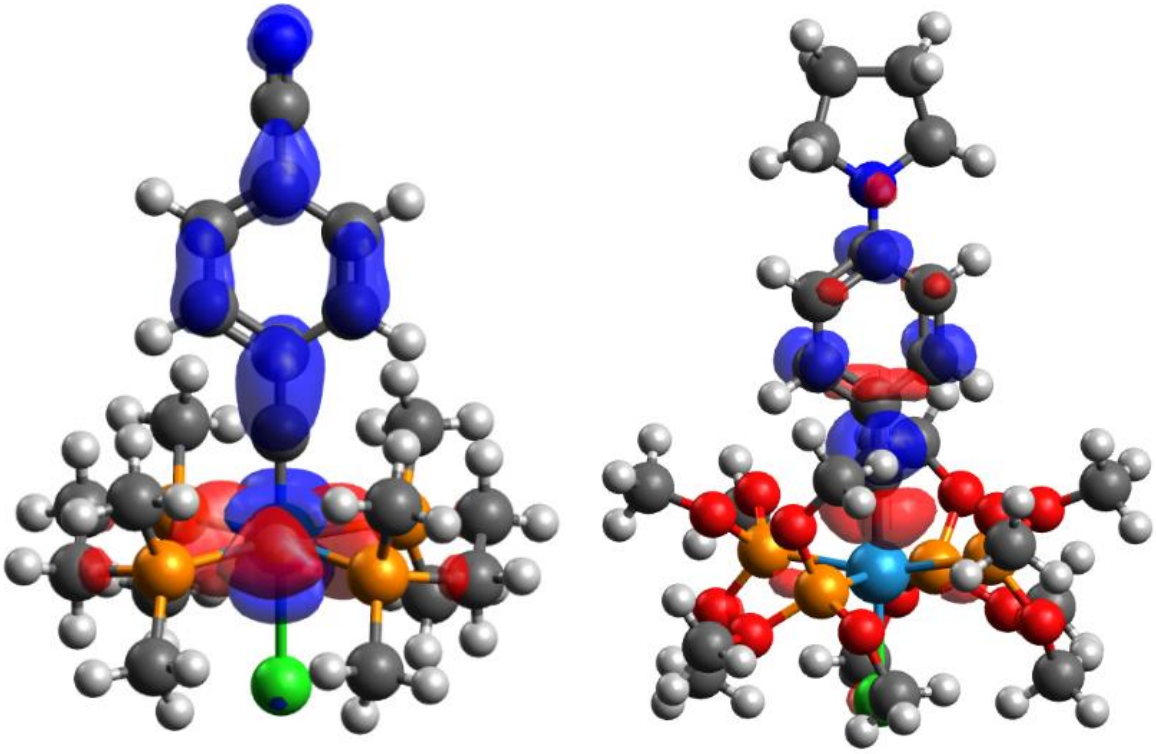

Figure 4.8. Transition density isosurfaces of $W(CC_6H_5\text{-}4\text{-}CN)(dmpe)_2Cl$ (left) and $W(CC_6H_4\text{-}4\text{-}pyr)\{P(OMe)_3\}_4Cl$ (right) rendered at an isovalue of 0.002.

The T_1 optimized geometries obtained from these two methods were next compared to each other (Table 4.14). There are many areas of similarity but a few striking differences. Both methods accurately reproduce experimentally determined E_{00} values for all measured compounds (Table 4.7). This highlights the strength of these methods to give useful predictions for excited-state energies and provides a set of complementary tools to computationally screen photocatalysts and their photoredox capabilities. Both methods also predict nearly identical excited-state geometries for the phosphite complexes and the dmpe complexes with electron-withdrawing para substituents. These sets of complexes exhibit $^3[\pi\rightarrow\pi^*]$ or $^3[d_{xy}\rightarrow\pi^*]$ character as judged by the rendered spin density and transition density from both UODFT and TDDFT calculations respectively. The phosphite complexes are particularly notable because the agreement lends credence to the prediction of excited-state inversion to the $^3[\pi\rightarrow\pi^*]$ state for these complexes. Experimentally, some limitation of E_{00} is found for $W(CC_6H_5)\{P(OMe)_3\}_4Cl$ and $W(CC_6H_4\text{-}4\text{-}pyr)(P(OMe)_3)_4Cl$ which exhibit E_{00} of 2.24 eV and 2.27 eV respectively despite their differing $^1[d_{xy}\rightarrow\pi^*]$ energies. This suggests that the added photochemical driving force within the benzylidyne framework may be limited by the energy of the $^3[\pi\rightarrow\pi^*]$ T_1 state, which is largely invariant upon para-substitution.

Table 4.7. Comparison of Experimental and Calculated E_{00} Energies.

	UODFT E_{00} (eV)	TDDFT E_{00} (eV)	expt. E_{00} (eV)[a]
$W(CC_6H_5)(dmpe)_2Cl$	1.93	1.92	1.98
$W(CC_6H_4\text{-}4\text{-}OMe)(dmpe)_2Cl$	2.08	2.15	2.11
$W(CC_6H_4\text{-}4\text{-}pyr)(dmpe)_2Cl$	2.15	2.15	2.25
$W(CC_6H_5)\{P(OMe)_3\}_4Cl$	2.24	2.25	2.24
$W(CC_6H_5\text{-}4\text{-}OMe)\{P(OMe)_3\}_4Cl$	2.28	2.27	2.38
$W(CC_6H_4\text{-}4\text{-}pyr)\{P(OMe)_3\}_4Cl$	2.29	2.28	2.27

[a] Ref 2

In contrast to these areas of agreement, particularly poor agreement is found between the UODFT and TDDFT for the dmpe and PH_3 complexes (Table 4.8). This is exemplified by the large differences in the C(1)–W–Cl bond angle and smaller differences in the W≡C, W–Cl and W–P_{avr} bond lengths showing no discernable trend. Given the symmetry of both the $^3[d_{xy}\rightarrow\pi^*]$ and $^3[\pi\rightarrow\pi^*]$ states, distortion of the C(1)–W–Cl bond angle is unexpected. Such nontotally symmetric bond distortions might be expected if a first or second-order Jahn-Teller effect were active. The absence of degeneracies in the frontier orbitals rules out first order Jahn-Teller effects. A second-order Jahn-Teller effect could be present since the $^3[d_{xy}\rightarrow\pi^*]$ and $^3[\pi\rightarrow\pi^*]$ states have different symmetry but there is not a plausible orbital argument why the C–W–Cl bending coordinate would result in stabilization of the T_1 state. Further, as excited-state geometries are being examined across a series of complexes with varying $^3[d_{xy}\rightarrow\pi^*]$ and $^3[\pi\rightarrow\pi^*]$ energies, the second-order Jahn-Teller effect should present itself as a rational trend related to the energy difference between the two states. Instead, distinctly opposite trends in the C(1)–W–Cl bond angles are found for the UODFT and TDDFT methods. For the UODFT method, the largest C(1)–W–Cl distortions are observed for $W(CC_6H_5)(PH_3)_4Cl$ while for TDDFT it is for $W(CC_6H_5)(dmpe)_2Cl$. This discounts the possibility of a second-order Jahn-Teller effect and points to a general failure of these methods for predicting the T_1 geometries of these particular compounds. Deviation in the C(1)–W–Cl is notable as it modifies the strength of the trans effect felt by other ligands from the alkylidyne leading to mismatches in the W≡C, W–Cl, and W–P_{avr} bond lengths.

Table 4.8. Comparison of UODFT and TDDFT T_1 Geometries for Select Complexes.[a]

		W≡C	W–Cl	W–P_{avr}	C(1)–W–Cl	C(2)–C(1)–W
W(CC_6H_5)($dmpe)_2$Cl	UO T_1	1.871	2.594	2.495	178.6	179.6
	TD T_1	1.892	2.546	2.471	167.1	178.3
	ΔT_1	**0.021**	**-0.048**	**-0.024**	**-11.5**	**-1.3**
W(CC_6H_4-4-OMe)($dmpe)_2$Cl	UO T_1	1.892	2.568	2.484	171.3	178.1
	TD T_1	1.936	2.515	2.455	173.6	178.1
	ΔT_1	**0.044**	**-0.053**	**-0.029**	**2.3**	0
W(CC_6H_4-4-pyr)($dmpe)_2$Cl	UO T_1	1.927	2.541	2.464	172.5	176.3
	TD T_1	1.943	2.518	2.449	179.9	180
	ΔT_1	**0.016**	**-0.023**	**-0.015**	**7.4**	**3.7**
W(CC_6H_5)($PH_3)_4$Cl	UO T_1	1.929	2.491	2.449	169.4	176.5
	TD T_1	1.957	2.465	2.445	179.6	179.8
	ΔT_1	**0.028**	**-0.026**	-0.004	**10.2**	**3.3**

[a] Changes highlighted in bold indicate significant difference between two calculated geometries.

4.2.6 Limitations of the Methods.

The failure of both these methods to produce identical geometries for the T_1 for W(CC_6H_5)($dmpe)_2$Cl, W(CC_6H_4-4-OMe)($dmpe)_2$Cl, W(CC_6H_4-4-pyr)($dmpe)_2$Cl, and W(CC_6H_5)($PH_3)_4$Cl is inherent to the way they describe the electronic structure of the triplet state. Both UODFT and TDDFT are single reference methods and are incapable of properly describing the electronic structure of the excited-state when two states of inherently different character are close in energy.[35-40] This problem has been extensively documented in the quantum chemistry literature with no current method suitable for this type of problem even for simple systems like Group 6 hexacarbonyl complexes.[35]

From ground-state geometry TDDFT calculations, the $^3[d_{xy}\rightarrow\pi^*]$ and $^3[\pi\rightarrow\pi^*]$ states are predicted to be close in energy. This would suggest that the relaxed triplet state should be influenced by both the $^3[d_{xy}\rightarrow\pi^*]$ and $^3[\pi\rightarrow\pi^*]$ states as manifested by mixing of the optimized

triplet density isosurfaces. By construction, the UODFT and TDDFT methods will calculate the triplet state slightly differently, and therefore will mix the two states in a different manner. This gives different T_1 geometries for both methods since neither method can properly treat the state mixing in a true multiconfigurational manner. The difference between the C(1)–W–Cl distortions predicted by the two methods is a result of this. For the W(CC_6H_5){$P(OMe)_3$}$_4$Cl, W(CC_6H_4-4-OMe){$P(OMe)_3$}$_4$Cl, and W(CC_6H_4-4-pyr){$P(OMe)_3$}$_4$Cl $^3[\pi\rightarrow\pi^*]$ complexes and the W(CC_6H_5-4-CF_3)$(dmpe)_2$Cl, W(CC_6H_5-4-CN)$(dmpe)_2$Cl, and W(CC_6H_5-4-NO_2)$(dmpe)_2$Cl $^3[d_{xy}\rightarrow\pi^*]$ complexes, the C(1)–W–Cl bond angle is linear. This same bond angle would therefore be expected to be linear for mixed states as well since there should be no added stabilizing effect by distorting along this bond angle. Instead, the distortion likely serves to spatially mix these two states because the computational method is otherwise incapable of doing so. This nonphysical distortion brings into question whether the excited-state geometries for the cases where these states intersect are true excited-state geometries and not just a computational artifact. The good agreement between experimental and predicted E_{00} for these complexes suggest that useful information can still be obtained from these calculations and lie close to the energetic minimum on the excited-state surface, but the geometry and electronic structure of these states would require further examination.

A better way to calculate properties of compounds with close-lying $^3[d_{xy}\rightarrow\pi^*]$ and $^3[\pi\rightarrow\pi^*]$ states would be to use a multiconfiguration method that can treat the excited-state in a more complete manner with regards to its configuration space. Unfortunately, these methods are much too expensive for the experimentally relevant complexes and would require much too large active-spaces to properly model these systems. Additionally, attempted ground-state geometry optimizations from these methods were not experimentally accurate, precluding their use for

optimizing excited-state geometries even for truncated complexes. Given this limitation, to investigate the multiconfigurational nature of the T_1 state, a CASSCF calculation with a (12e, 11o) active space on the $W(CC_6H_5)(PH_3)_4Cl$ complex, which displays the largest C(1)–W–Cl distortion, was performed. Since CASSCF is strongly basis set dependent, the basis set size on all atoms was increased to their respective TZVPP and QZVPP sizes for the metal center and all other atoms respectively ensuring full basis set convergence. From this calculation, the T_1 state possesses 51.3% ($\pi\rightarrow\pi^*$) character and 22.9% ($d_{xy}\rightarrow\pi^*$) with smaller contribution from other higher lying configurations. This confirms the strongly multiconfigurational nature of the excited-state and importance of state mixing of the $^3[d_{xy}\rightarrow\pi^*]$ and $^3[\pi\rightarrow\pi^*]$ states.

4.3 Conclusions.

A set of UODFT and TDDFT methods have been investigated to model the excited-state properties of tungsten benzylidyne chromophores. In general, excited-state structures all show geometric changes consistent with population of the π^* orbital which is exemplified by elongation of the W≡C bond length. Evidence of inversion of the T_1 excited-state from $^3[d_{xy}\rightarrow\pi^*]$ to $^3[\pi\rightarrow\pi^*]$ is found and is driven by use of more π-acidic phosphines and strongly para-donating substituents on the benzylidyne. The inversion is geometrically evidenced by a further increase in the W≡C bond length, quinoidal distortion of the phenyl group, and increased spin density on the benzylidyne. Through excited-state geometry optimization, these methods are able to provide good estimation of the excited-state E_{00} across both triplet state characters allowing computational screening for photoredox applications. Unfortunately, these methods do not always produce consistent triplet state geometries. For complexes where the $^3[d_{xy}\rightarrow\pi^*]$ and $^3[\pi\rightarrow\pi^*]$ energies are close, the two methods diverge in optimized geometry. This highlights the importance of analyzing multiconfigurational character when complicated excited-state

dynamics are present. Finally, low temperature and transient absorption studies are proposed pertaining particularly to the trimethyl phosphite complexes in which one can elaborate the proposed $^3[\pi\rightarrow\pi^*]$ excited-state.

4.4 Experimental Section.

4.4.1 Density Functional Theory (DFT) Calculations.

All DFT calculations were performed using ORCA software package version 4.2[10-11] except for those with Method 2 and Method 5, which were performed with Gaussian 16 RevC.01. All calculations were performed using the Method 1 unless otherwise noted. Kohn-Sham orbitals were visualized using Avogadro 1.2.0.[41] UODFT T_1 geometries were optimized using Method 1 with the multiplicity set to 3. TDDFT T_1 geometries were optimized using Method 1 with TDA=True, TRIPLETS=True, NROOTS=5, IROOT=1, and IROOTMULT= TRIPLET. Ground state TDDFT transitions were calculated using Method 1 with TDA=True, NROOTS=10, and TRIPLETS=True. CASSCF calculations were calculated using the SARC-ZORA-TZVPP[16] basis set on tungsten, ZORA-DEF2-QZVPP on all other atoms with the ZORA Hamiltonian.[42-43] RIJK with the DEF2/JK auxiliary basis set was used to accelerate the calculations. A (12e, 11o) active space with 8 triplet and 4 singlet roots was used to calculate the CASSCF active space with convergence tolerance set to 1e-7 and TRAFOSTEP RI to accelerate the calculation.

Method 1. Geometry optimizations were carried out using the PBE0 hybrid functional[18] with the SARC-ZORA-SVP[16] basis set was used for W and the ZORA-DEF2-SVP basis set on all other atoms in combination with the modified ZORA Hamiltonian.[42-43] No symmetry constraints were applied. The RIJCOSX algorithm was used to accelerate the calculation with or

GRID6 and GRIDX6 integration grids for all atoms and custom Grid IntAcc for W set to 10 and NOFINALGRID for final single point energies. The KDIIS and SOSCF algorithms were used to accelerate SCF convergence. The lack of imaginary frequencies confirmed that the calculated geometries were local minima on the calculated potential energy surface.

Method 2. Geometry optimizations were carried out in Gaussian16[44] using the B3P86 hybrid functional[12] with the LANL2DZ basis set [13-14] and ECP[14] used for W and polarized Dunning-Hay basis sets[15] on all other atoms. No symmetry constraints were applied during optimization and the integration grid was set to ultrafine.

Method 3. Calculations were performed identically to Method 1 with the SARC-SORA-TZVP basis set on W and ZORA-DEF2-TZVP on all other atoms.

Method 4. Calculations were performed identically to Method 1 with the SARC-SORA-TZVPP basis set on W and ZORA-DEF2-TZVPP on all other atoms.

Method 5. Calculations were performed in Gaussian16 using the PBE0 functional with the DEF2-SVP[45] basis set and ECP on tungsten and the 6-311G*[46] basis set on all other atoms. The integration grid was set to ultrafine on all atoms and no symmetry constraints were applied.

Method 6. Calculations were performed in Gaussian16 using the PBE0 functional with the DEF2-SVP basis set and the SDD ECP[47] on tungsten with the DEF2-SVP basis set on all other atoms. The integration grid was set to ultrafine on all atoms and no symmetry constraints were applied.

Method 7. Calculations were performed identically to Method 1 with the functional set to B3P86.

Method 8. Calculations were performed identically to Method 1 with the functional set to B3PW91.[14]

Table 4.9. Experimental Photophysical Data for Select Tungsten–Benzylidyne Complexes.[a]

	$^1[\pi\rightarrow\pi^*]$ (cm^{-1})	$^1[d_{xy}\rightarrow\pi^*]$ (cm^{-1})	$^3(d_{xy}\leftarrow\pi^*)$ (cm^{-1})	FWHM (cm^{-1})	E_{00} (eV)	τ (μs)
W(CPh)(dmpe)$_2$Cl	29586	18692	14285	2974	1.98	0.41
W(CC$_6$H$_4$-4-OCH$_3$)(dmpe)$_2$Cl	29851	19881	14970	3081	2.11	0.88
W(CC$_6$H$_4$-4-pyr)(dmpe)$_2$Cl	28409	20619	15873	3380	2.25	1.9
W(CPh){P(OMe)$_3$}$_4$Cl	30488	22272	15552	4115	2.27	1.2
W(CC$_6$H$_4$-4-OCH$_3$){P(OMe)$_3$}$_4$Cl	30675	23364	16666	4399	2.38	2.3
W(CC$_6$H$_4$-4-pyr){P(OMe)$_3$}$_4$Cl	28571	24450	15974	3705	2.24	5.8

[a] Ref 2

Table 4.10. Geometry Benchmarking Study of Various DFT Methods for $W(CC_6H_5)(dmpe)_2Cl$.

	Bond Lengths (Å) and Angles (˚)								
Nuclei	Crystal Structure[a]	Meth. 1	Meth. 2	Meth. 3	Meth. 4	Meth. 5	Meth. 6	Meth. 7	Meth. 8
W≡C	1.829(2)	1.821	1.817	1.821	1.811	1.820	1.824	1.814	1.814
W–Cl	2.5834(5)	2.584	2.612	2.594	2.574	2.621	2.612	2.550	2.550
W–P(1)	2.4332(6)	2.456	2.465	2.459	2.446	2.488	2.486	2.439	2.437
W–P(2)	2.4445(6)	2.455	2.454	2.444	2.449	2.473	2.485	2.437	2.439
W–P(3)	2.4432(6)	2.456	2.45	2.449	2.445	2.488	2.486	2.439	2.439
W–P(4)	2.4272(6)	2.455	2.46	2.445	2.449	2.473	2.485	2.439	2.437
$W–P_{avr}$	2.4370[6]	2.456	2.457	2.449	2.447	2.481	2.486	2.4385	2.438
C(1)–C(2)	1.433(3)	1.437	1.439	1.433	1.432	1.434	1.44	1.433	1.433
C(1)–W–Cl	178.38(6)	179.94	179.86	179.67	179.9	179.8	179.98	179.6	179.6
C(2)–C(1)–W	176.76(16)	179.9	177.94	178.61	179.9	178.07	179.96	179.5	179.5
$cis(P–W–P)_{min,avr}$	80.758[19]	80.68	80.85	80.279	80.40	80.34	80.51	89.80	89.80
$cis(P–W–P)_{max,avr}$	98.75[19]	98.72	98.32	99.216	99.125	98.88	98.87	90.0	90.0
$C(1)–W–P_{min}$	89.04(6)	93.22	92.22	91.92	92.54	92.2	93.03	92.01	92.3
$C(1)–W–P_{max}$	98.03(6)	95.21	98.07	95.65	95.19	96.39	95.78	92.82	92.74
$C(1)–W–P_{avr}$	93.60[6]	94.225	94.84	93.78	93.87	94.29	94.41	92.44	92.52

[a] Ref 6

Table 4.11. Geometry Benchmarking Study of Various DFT Methods for W(CC_6H_4-4-pyr)$(dmpe)_2Cl$.

	Bond Lengths (Å) and Angles (˚)								
Nuclei	Crystal Structure[a]	Meth. 1	Meth. 2	Meth. 3	Meth. 4	Meth. 5	Meth. 6	Meth. 7	Meth. 8
W≡C	1.8197(18)	1.82	1.818	1.81	1.811	1.821	1.800	1.814	1.917
W–Cl	2.5832(4)	2.592	2.621	2.603	2.581	2.633	2.619	2.55	2.504
W–P(1)	2.4295(5)	2.451	2.461	2.441	2.444	2.469	2.482	2.439	2.445
W–P(2)	2.4367(5)	2.450	2.458	2.455	2.441	2.484	2.482	2.437	2.458
W–P(3)	2.4320(5)	2.452	2.449	2.441	2.444	2.484	2.482	2.439	2.423
W–P(4)	2.4286(5)	2.452	2.444	2.454	2.442	2.469	2.482	2.439	2.457
W–P_{avr}	2.4319[5]	2.451	2.453	2.448	2.443	2.477	2.482	2.439	2.446
C(1)–C(2)	1.442(2)	1.439	1.44	1.434	1.433	1.437	1.441	1.433	1.374
C(1)–W–Cl	179.74(6)	179.79	179.53	179.7	179.9	179.8	179.92	179.6	164.9
C(2)–C(1)–W	179.49(14)	179.6	177.66	178.7	179.8	178.1	179.82	179.5	177.9
cis(P–W–P)$_{min,avr}$	81.129[16]	80.81	81.06	80.43	80.54	80.50	94.20	89.80	85.41
cis(P–W–P)$_{max,avr}$	99.203[16]	98.66	98.15	99.13	99.05	98.89	97.18	90.00	96.10
C(1)–W–P_{min}	90.40(5)	92.85	92.02	91.67	92.38	92.03	80.64	92.01	79.10
C(1)–W–P_{max}	95.63(5)	94.97	97.43	95.38	94.9	96.28	98.83	92.82	104.60
C(1)–W–P_{avr}	92.97[5]	93.97	94.74	93.54	93.63	94.13	89.71	92.44	88.86

[a] Ref 6

Table 4.12. Comparison of Calculated T_1 State Assignments and E_{00} Energies by TDDFT for Various Functionals.[a]

	$W(CC_6H_5)(dmpe)_2Cl$		$W(CC_6H_4\text{-}4\text{-}pyr)(dmpe)_2Cl$	
Functional[a]	E_{00} (eV)	T_1 character	E_{00} (eV)	T_1 character
PBE0	1.92	$^3[d\text{-}\pi^*]$	2.15	$^3[\pi\text{-}\pi^*]$
B3LYP	1.46	$^3[d\text{-}\pi^*]$	1.84	$^3[\pi\text{-}\pi^*]$
B3PW91	1.53	$^3[d\text{-}\pi^*]$	1.85	$^3[\pi\text{-}\pi^*]$
B3P86	1.53	$^3[d\text{-}\pi^*]$	1.82	$^3[\pi\text{-}\pi^*]$
B97	1.49	$^3[d\text{-}\pi^*]$	1.85	$^3[\pi\text{-}\pi^*]$
CAM-B3LYP	1.93	$^3[\pi\text{-}\pi^*]$	1.91	$^3[\pi\text{-}\pi^*]$
ωB97X	1.99	$^3[\pi\text{-}\pi^*]$	2.10	$^3[\pi\text{-}\pi^*]$
Expt.	1.98	N/A	2.14	N/A

[a] All other parameters identical to Method 1 except for functional

Table 4.13. Comparison of S_0 and T_1 Geometries Using the TDDFT Method.[a]

		W≡C	W–Cl	W–P_{avr}	C(1)–C(2)	C(1)–W–Cl	C(2)–C(1)–W	δ_r
W(CC_6H_5)($dmpe)_2$Cl	S_0	1.821	2.584	2.456	1.437	179.9	179.9	0.007
	T_1	1.892	2.546	2.471	1.39	167.1	178.3	0.022
	T_1-S_0	**0.071**	-0.038	0.016	**-0.047**	-12.8	-1.6	**0.015**
W(CC_6H_4-4-OMe)($dmpe)_2$Cl	S_0	1.82	2.588	2.454	1.439	179.8	179.6	0.012
	T_1	1.936	2.515	2.455	1.377	173.6	178.1	0.031
	T_1-S_0	**0.116**	-0.073	0.001	**-0.062**	-6.2	-1.5	**0.019**
W(CC_6H_4-4-pyr)($dmpe)_2$Cl	S_0	1.82	2.592	2.451	1.439	179.8	179.6	0.013
	T_1	1.943	2.518	2.449	1.370	179.9	180	0.038
	T_1-S_0	**0.123**	-0.074	-0.002	**-0.069**	0.1	0.4	**0.025**
W(CC_6H_5)($PH_3)_4$Cl	S_0	1.821	2.528	2.442	1.438	179.6	179.4	0.006
	T_1	1.954	2.457	2.435	1.373	179.6	179.9	0.027
	T_1-S_0	**0.133**	-0.071	-0.007	**-0.065**	0	0.5	**0.021**
W(CC_6H_5)($P(OMe)_3)_4$Cl	S_0	1.817	2.554	2.428	1.437	180	180	0.007
	T_1	1.947	2.494	2.424	1.371	179.9	180	0.025
	T_1-S_0	**0.13**	-0.06	-0.004	**-0.066**	-0.1	0	**0.018**
W(CC_6H_4-4-OMe)($P(OMe)_3)_4$Cl	S_0	1.818	2.551	2.427	1.434	179.9	179.9	0.012
	T_1	1.946	2.498	2.425	1.368	179.8	179.8	0.032
	T_1-S_0	**0.128**	-0.053	-0.002	**-0.066**	-0.1	-0.1	**0.020**
W(CC_6H_4-4-pyr)($P(OMe)_3)_4$Cl	S_0	1.82	2.563	2.424	1.432	180	180	0.014
	T_1	1.937	2.506	2.425	1.365	179.9	179.9	0.033
	T_1-S_0	**0.117**	-0.057	0.001	**-0.067**	-0.1	-0.1	**0.019**
W(CC_6H_5-4-CF_3)($dmpe)_2$Cl	S_0	1.822	2.573	2.459	1.434	179.65	178.2	0.021
	T_1	1.868	2.572	2.486	1.392	176.4	179.3	0.05
	T_1-S_0	**0.046**	-0.001	0.027	**-0.042**	-3.25	1.1	**0.029**
W(CC_6H_5-4-CN)($dmpe)_2$Cl	S_0	1.824	2.567	2.461	1.43	179.8	178.4	0.026
	T_1	1.853	2.582	2.492	1.359	178.6	179.1	0.058
	T_1-S_0	**0.029**	0.015	0.031	**-0.071**	-1.2	0.7	**0.032**
W(CC_6H_5-4-NO_2)($dmpe)_2$Cl	S_0	1.825	2.563	2.462	1.428	179.8	178.3	0.022
	T_1	1.831	2.588	2.496	1.41	179.7	178.6	0.044
	T_1-S_0	**0.006**	0.025	0.034	**-0.018**	-0.1	0.3	**0.022**

[a] Changes highlighted in bold denote significant bond changes observed for all calculated complexes

Table 4.14. Comparison of T_1 Geometries Obtained Using TDDFT and UODFT Methods.[a]

		W≡C	W–Cl	W–P_{avr}	C(1)–W–Cl	C(2)–C(1)–W	UO E_{00} (eV)	TD E_{00} (eV)	expt. E_{00} (eV)
W(CC_6H_5)($dmpe)_2$Cl	UO T_1	1.871	2.594	2.495	178.6	179.6	1.93	1.92	1.98
	TD T_1	1.892	2.546	2.471	167.1	178.3			
	ΔT_1	**0.021**	**-0.048**	**-0.024**	**-11.5**	**-1.3**			
W(CC_6H_4-4-OMe)($dmpe)_2$Cl	UO T_1	1.892	2.568	2.484	171.3	178.1	2.08	2.15	2.11
	TD T_1	1.936	2.515	2.455	173.6	178.1			
	ΔT_1	**0.044**	**-0.053**	**-0.029**	**2.3**	0			
W(CC_6H_4-4-pyr)($dmpe)_2$Cl	UO T_1	1.927	2.541	2.464	172.5	176.3	2.15	2.15	2.25
	TD T_1	1.943	2.518	2.449	179.9	180			
	ΔT_1	**0.016**	**-0.023**	**-0.015**	**7.4**	**3.7**			
W(CC_6H_5)($PH_3)_4$Cl	UO T_1	1.929	2.491	2.449	169.4	176.5	2.12	1.95	N/A
	TD T_1	1.957	2.465	2.445	179.6	179.8			
	ΔT_1	**0.028**	**-0.026**	**-0.004**	**10.2**	**3.3**			
W(CC_6H_5)($P(OMe)_3)_4$Cl	UO T_1	1.955	2.492	2.424	179.9	180	2.24	2.25	2.24
	TD T_1	1.947	2.494	2.424	179.9	180			
	ΔT_1	-0.008	0.002	0.000	0	0			
W(CC_6H_4-4-OMe)($P(OMe)_3)_4$Cl	UO T_1	1.954	2.494	2.426	179.7	179.6	2.28	2.27	2.38
	TD T_1	1.946	2.498	2.425	179.8	179.8			
	ΔT_1	-0.008	0.004	-0.001	0.1	0.2			
W(CC_6H_4-4-pyr)($P(OMe)_3)_4$Cl	UO T_1	1.943	2.509	2.426	179.9	179.9	2.29	2.28	2.27
	TD T_1	1.937	2.506	2.425	179.9	179.9			
	ΔT_1	-0.006	-0.003	-0.001	0	0			
W(CC_6H_5-4-CF_3)($dmpe)_2$Cl	UO T_1	1.878	2.564	2.491	175.6	179.6	1.92	1.92	N/A
	TD T_1	1.868	2.572	2.486	176.4	179.3			
	ΔT_1	-0.01	0.008	-0.005	0.8	-0.3			
W(CC_6H_5-4-CN)($dmpe)_2$Cl	UO T_1	1.866	2.57	2.497	177.3	179	1.72	1.72	N/A
	TD T_1	1.853	2.582	2.492	178.6	179.1			
	ΔT_1	-0.013	0.012	-0.005	1.3	0.1			
W(CC_6H_5-4-NO_2)($dmpe)_2$Cl	UO T_1	1.852	2.573	2.503	178.8	178.5	1.51	1.46	N/A
	TD T_1	1.831	2.588	2.496	179.7	178.6			
	ΔT_1	-0.021	0.015	-0.007	0.9	0.1			

[a] Changes highlighted in bold indicate significant difference between two calculated geometries.

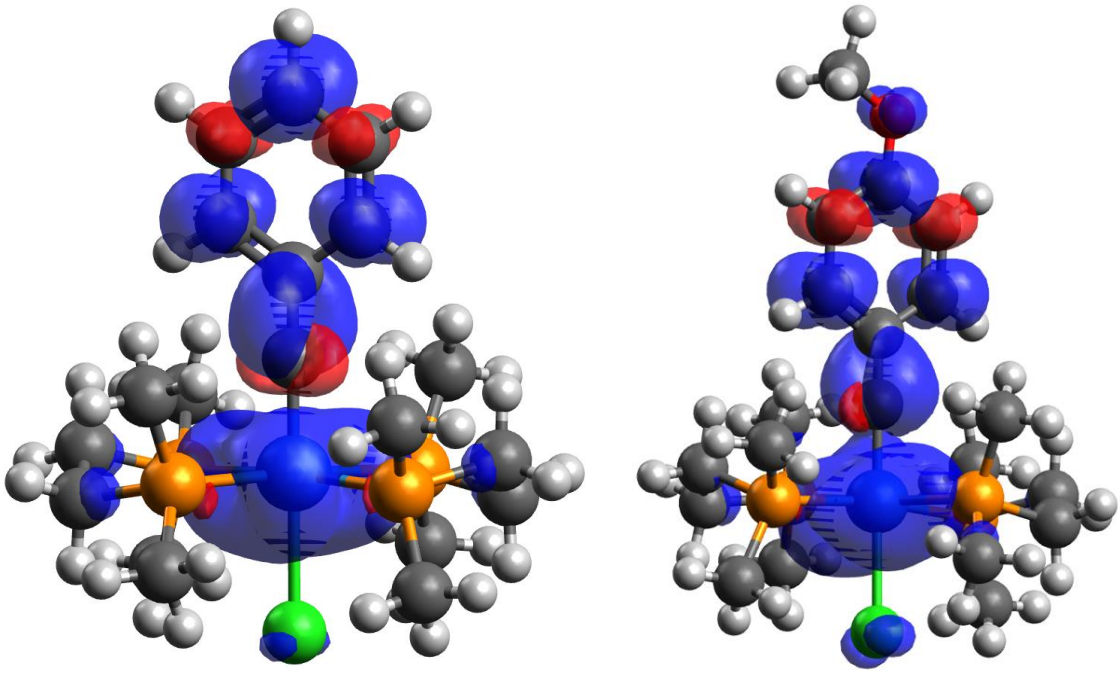

Figure 4.9. UODFT T_1 optimized spin density isosurfaces of $W(CC_6H_5)(dmpe)_2Cl$ (left) and $W(CC_6H_5\text{-}4\text{-}OMe)(dmpe)_2Cl$ (right) rendered at an isovalue of 0.002.

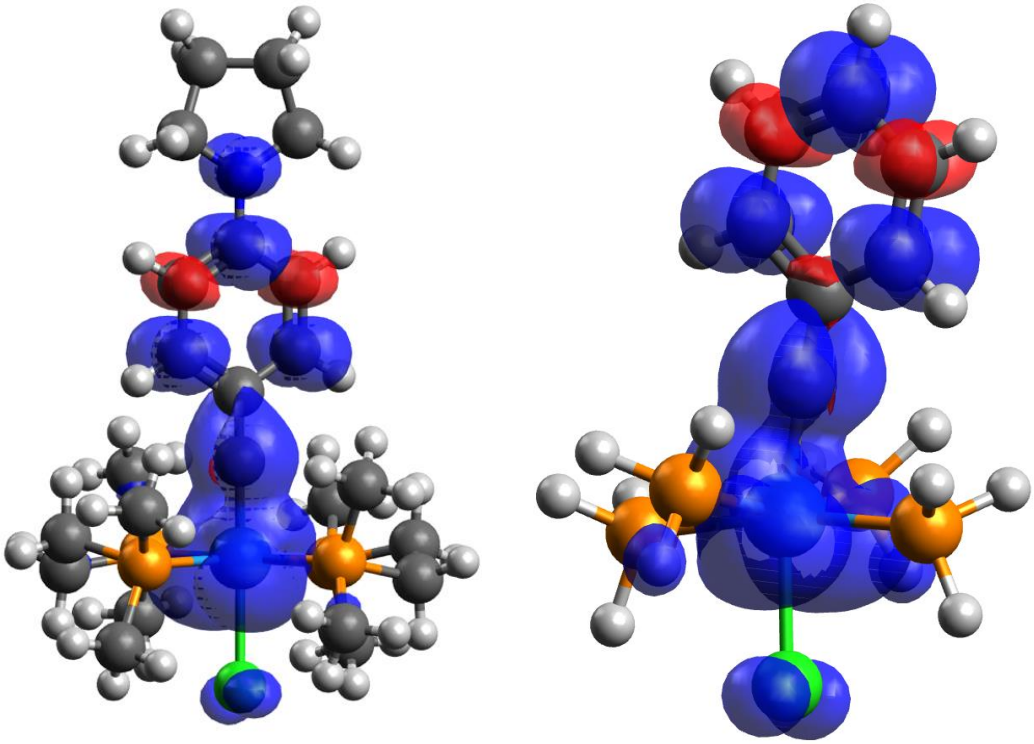

Figure 4.10. UODFT T_1 optimized spin density isosurfaces of $W(CC_6H_5\text{-}4\text{-}pyr)(dmpe)_2Cl$ (left) and $W(CC_6H_5)(PH_3)_4Cl$ (right) rendered at an isovalue of 0.002.

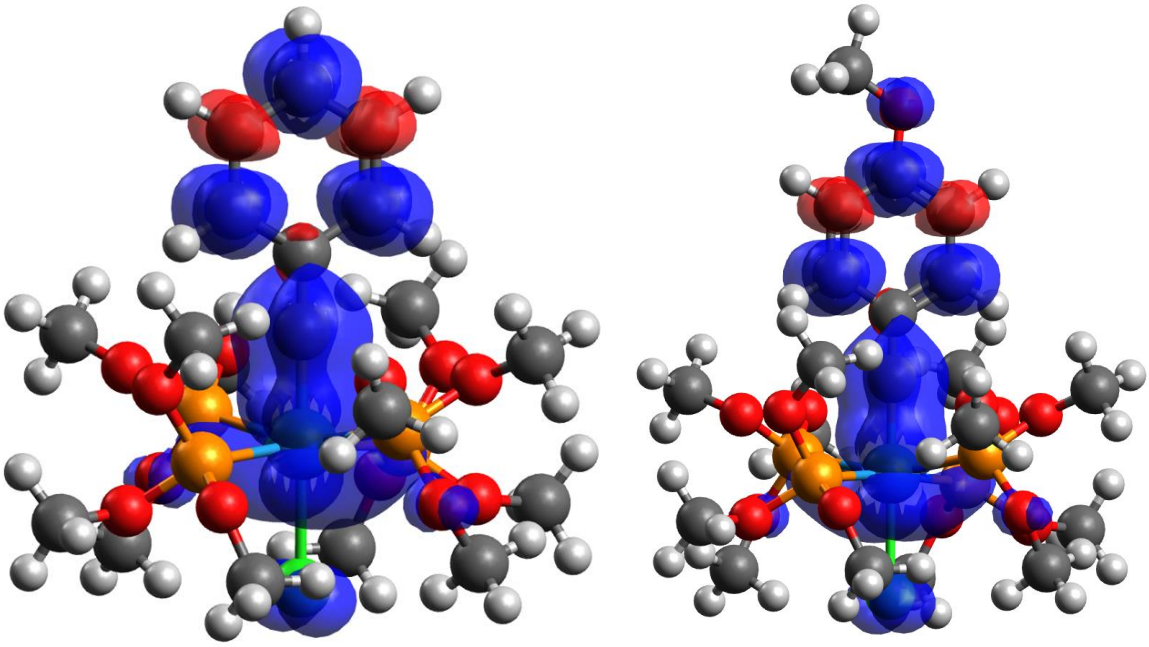

Figure 4.11. UODFT T_1 optimized spin density isosurfaces of $W(CC_6H_5)\{P(OMe)_3\}_4Cl$ (left) and $W(CC_6H_5\text{-}4\text{-}OMe)\{P(OMe)_3\}_4Cl$ (right) rendered at an isovalue of 0.002.

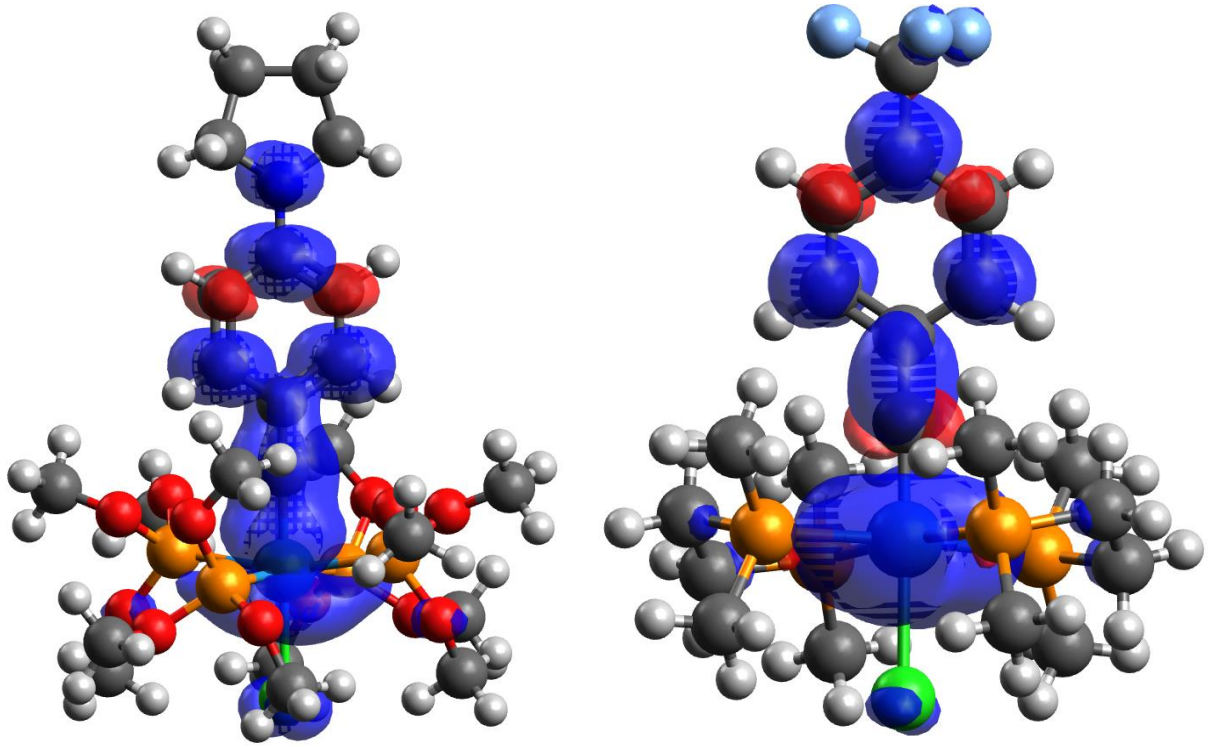

Figure 4.12. UODFT T_1 optimized spin density isosurfaces of $W(CC_6H_5\text{-}4\text{-}pyr)\{P(OMe)_3\}_4Cl$ (left) and $W(CC_6H_5\text{-}4\text{-}CF_3)\{P(OMe)_3\}_4Cl$ (right) rendered at an isovalue of 0.002.

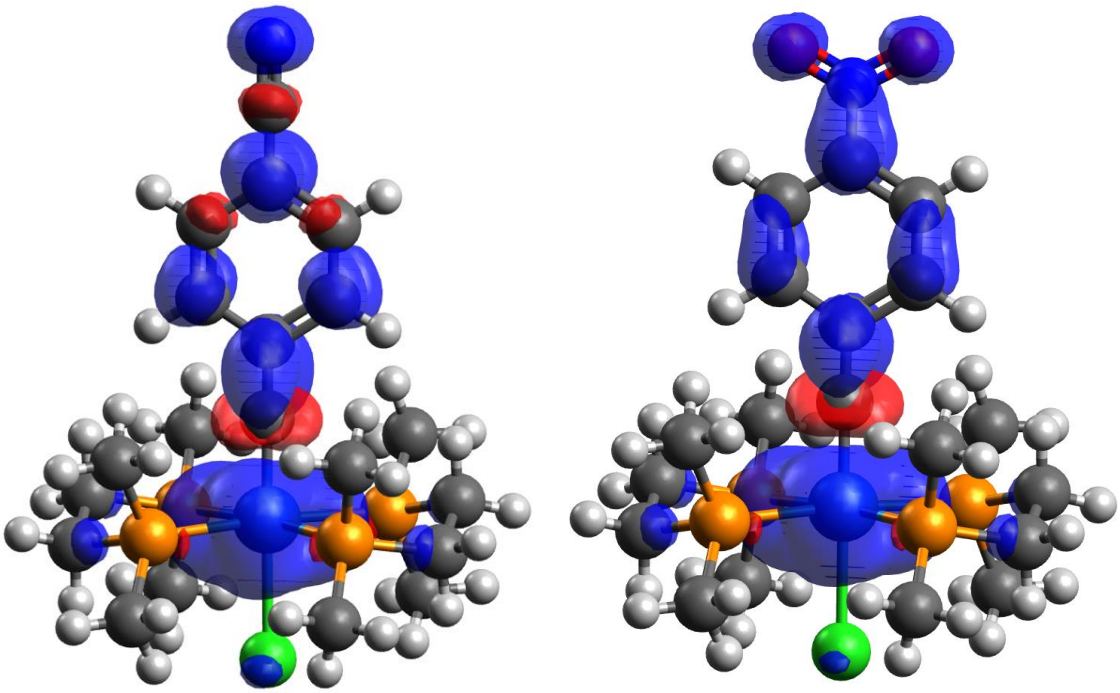

Figure 4.13. UODFT T_1 optimized spin density isosurfaces of W(CC_6H_5-4-CN)(dmpe)$_2$Cl (left) and W(CC_6H_5-4-NO_2)(dmpe)$_2$Cl (right) rendered at an isovalue of 0.002.

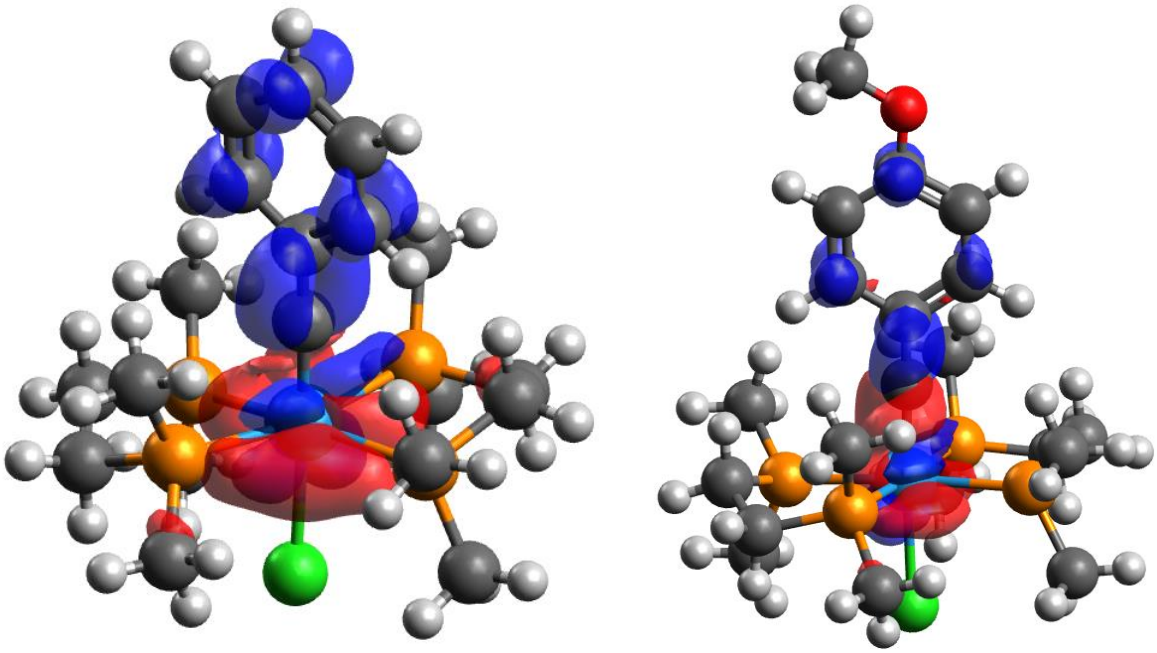

Figure 4.14. TDDFT T_1 optimized transition density isosurfaces of W(CC_6H_5)(dmpe)$_2$Cl (left) and W(CC_6H_5-4-OMe)(dmpe)$_2$Cl (right) rendered at an isovalue of 0.002.

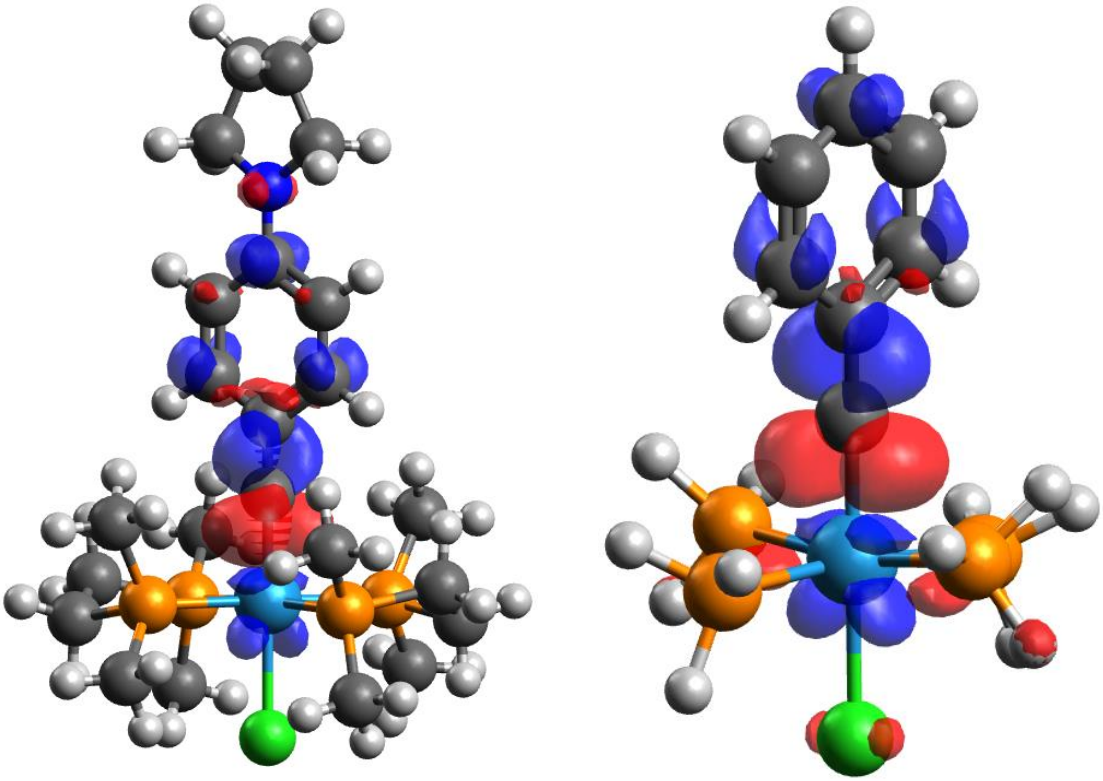

Figure 4.15. TDDFT T_1 optimized transition density isosurfaces of $W(CC_6H_5\text{-}4\text{-}pyr)(dmpe)_2Cl$ (left) and $W(CC_6H_5)(PH_3)_4Cl$ (right) rendered at an isovalue of 0.002.

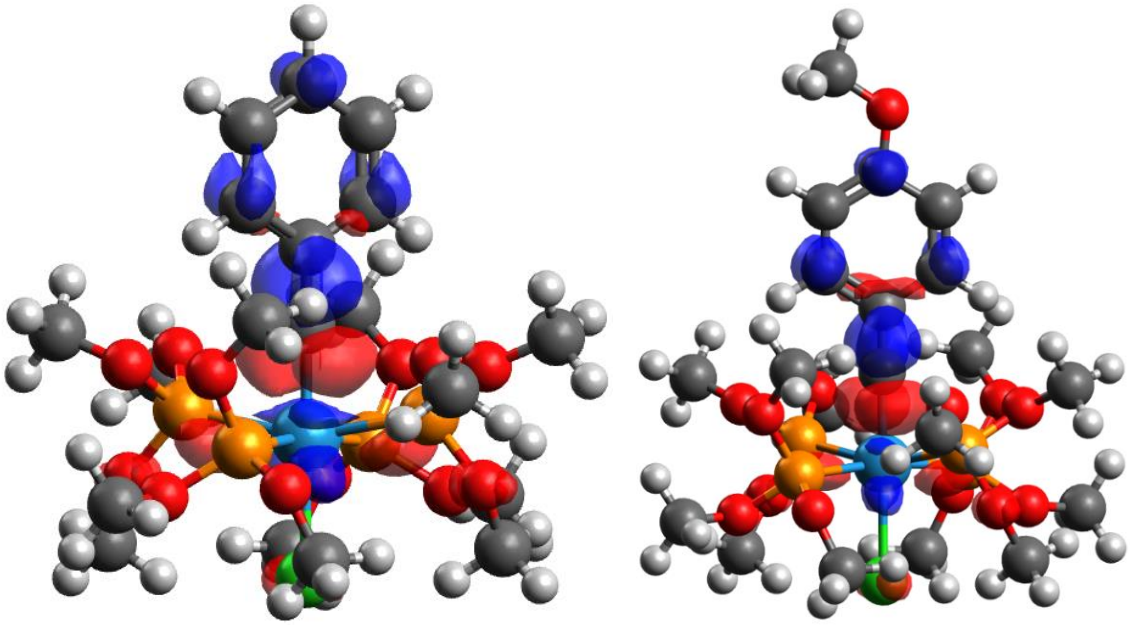

Figure 4.16. TDDFT T_1 optimized transition density isosurfaces of $W(CC_6H_5)\{P(OMe)_3\}_4Cl$ (left) and $W(CC_6H_5\text{-}4\text{-}OMe)\{P(OMe)_3\}_4Cl$ (right) rendered at an isovalue of 0.002.

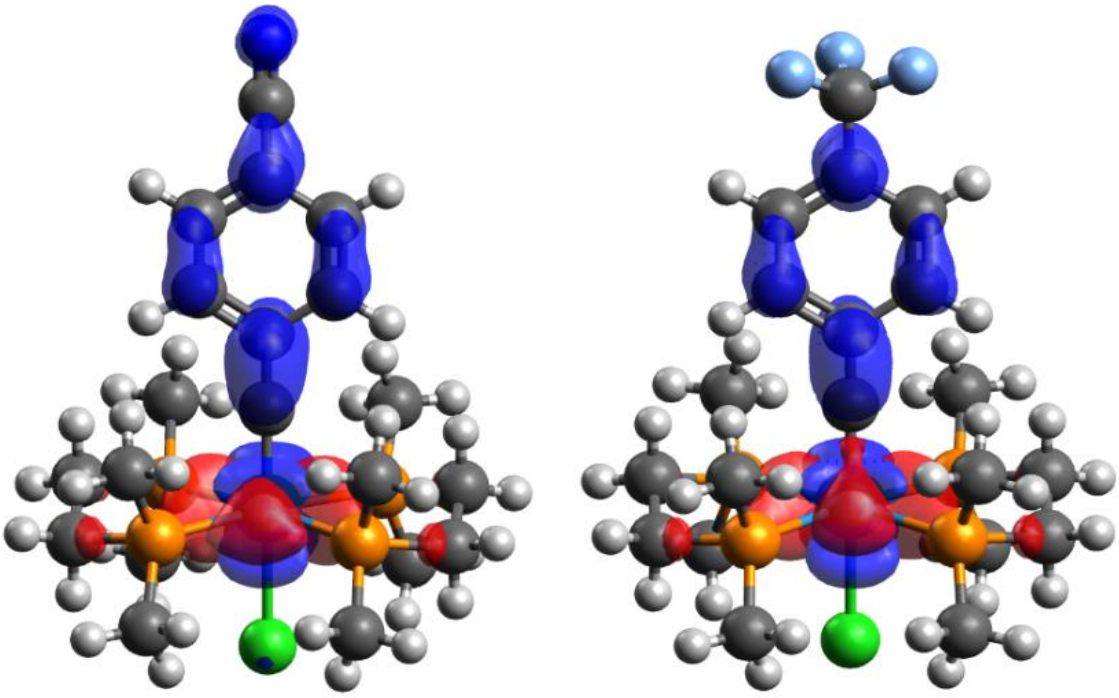

Figure 4.17. TDDFT T_1 optimized transition density isosurfaces of W(CC_6H_5-4-pyr){$P(OMe)_3$}$_4$Cl (left) and W(CC_6H_5-4-CF_3){$P(OMe)_3$}$_4$Cl (right) rendered at an isovalue of 0.002.

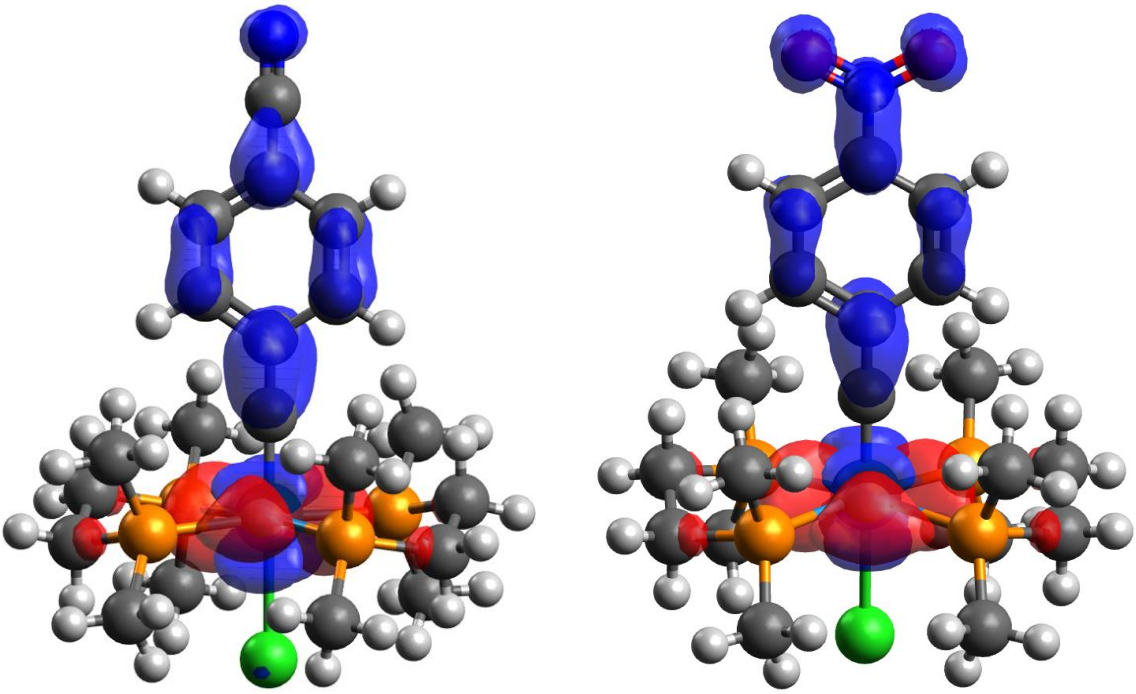

Figure 4.18. TDDFT T_1 optimized transition density isosurfaces of W(CC_6H_5-4-CN)$(dmpe)_2$Cl (left) and W(CC_6H_5-4-NO_2)$(dmpe)_2$Cl (right) rendered at an isovalue of 0.002.

4.5 References.

1. Chen, L. X. X-Ray Transient Absorption Spectroscopy. In *X-Ray Absorption and X-Ray Emission Spectroscopy*, 2016; pp 213-249.

2. Vibbert, H. B. Group 6 Metal-Oxo and -Alkylidyne Complexes with High Reactivity Derived from π-Antibonding Orbitals. Ph.D., The University of Chicago, United States -- Illinois, 2018.

3. Manna, J.; Gilbert, T. M.; Dallinger, R. F.; Geib, S. J.; Hopkins, M. D. *Journal of the American Chemical Society* **1992**, *114*, 5870-5872.

4. Lovaasen, B. M.; Lockard, J. V.; Cohen, B. W.; Yang, S.; Zhang, X.; Simpson, C. K.; Chen, L. X.; Hopkins, M. D. *Inorganic Chemistry* **2012**, *51*, 5660-5670.

5. O'Hanlon, D. C.; Cohen, B. W.; Moravec, D. B.; Dallinger, R. F.; Hopkins, M. D. *Journal of the American Chemical Society* **2014**, *136*, 3127-3136.

6. Rudshteyn, B.; Vibbert, H. B.; May, R.; Wasserman, E.; Warnke, I.; Hopkins, M. D.; Batista, V. S. *ACS Catalysis* **2017**, *7*, 6134-6143.

7. Haines, D. E.; O'Hanlon, D. C.; Manna, J.; Jones, M. K.; Shaner, S. E.; Sun, J.; Hopkins, M. D. *Inorganic Chemistry* **2013**, *52*, 9650-9658.

8. Xue, W.-M.; Wang, Y.; Chan, M. C.-W.; Su, Z.-M.; Cheung, K.-K.; Che, C.-M. *Organometallics* **1998**, *17*, 1946-1955.

9. Furche, F.; Ahlrichs, R. *The Journal of Chemical Physics* **2002**, *117*, 7433-7447.

10. Neese, F. *WIREs Computational Molecular Science* **2012**, *2*, 73-78.

11. Neese, F. *WIREs Computational Molecular Science* **2018**, *8*, e1327.

12. Perdew, J. P. *Physical Review B* **1986**, *33*, 8822-8824.

13. Chiodo, S.; Russo, N.; Sicilia, E. *The Journal of Chemical Physics* **2006**, *125*, 104107.

14. Hay, P. J.; Wadt, W. R. *The Journal of Chemical Physics* **1985**, *82*, 299-310.

15. Dunning, T. H., Jr. *The Journal of Chemical Physics* **2003**, *53*, 2823-2833.

16. Pantazis, D. A.; Chen, X.-Y.; Landis, C. R.; Neese, F. *Journal of Chemical Theory and Computation* **2008**, *4*, 908-919.

17. Bühl, M.; Reimann, C.; Pantazis, D. A.; Bredow, T.; Neese, F. *Journal of Chemical Theory and Computation* **2008**, *4*, 1449-1459.

18. Ernzerhof, M.; Scuseria, G. E. *The Journal of Chemical Physics* **1999**, *110*, 5029-5036.

19. Hirata, S.; Head-Gordon, M. *Chemical Physics Letters* **1999**, *314*, 291-299.

20. Latouche, C.; Skouteris, D.; Palazzetti, F.; Barone, V. *Journal of Chemical Theory and Computation* **2015**, *11*, 3281-3289.

21. Laurent, A. D.; Jacquemin, D. *International Journal of Quantum Chemistry* **2013**, *113*, 2019-2039.

22. Jacquemin, D.; Wathelet, V.; Perpète, E. A.; Adamo, C. *Journal of Chemical Theory and Computation* **2009**, *5*, 2420-2435.

23. Pople, J. A.; Nesbet, R. K. *The Journal of Chemical Physics* **1954**, *22*, 571-572.

24. Ziegler, T.; Rauk, A.; Baerends, E. J. *Theoretica chimica acta* **1977**, *43*, 261-271.

25. Menon, A. S.; Radom, L. *The Journal of Physical Chemistry A* **2008**, *112*, 13225-13230.

26. Filatov, M.; Shaik, S. *Chemical Physics Letters* **1999**, *304*, 429-437.

27. Peach, M. J. G.; Williamson, M. J.; Tozer, D. J. *Journal of Chemical Theory and Computation* **2011**, *7*, 3578-3585.

28. Peach, M. J. G.; Tozer, D. J. *The Journal of Physical Chemistry A* **2012**, *116*, 9783-9789.

29. Iikura, H.; Tsuneda, T.; Yanai, T.; Hirao, K. *The Journal of Chemical Physics* **2001**, *115*, 3540-3544.

30. Chai, J.-D.; Head-Gordon, M. *The Journal of Chemical Physics* **2008**, *128*, 084106.

31. Adamo, C.; Barone, V. *The Journal of Chemical Physics* **1999**, *110*, 6158-6170.

32. Szilagyi, R. K.; Metz, M.; Solomon, E. I. *The Journal of Physical Chemistry A* **2002**, *106*, 2994-3007.

33. Dierksen, M.; Grimme, S. *The Journal of Physical Chemistry A* **2004**, *108*, 10225-10237.

34. Záliš, S.; Ben Amor, N.; Daniel, C. *Inorganic Chemistry* **2004**, *43*, 7978-7985.

35. Rosa, A.; Baerends, E. J.; van Gisbergen, S. J. A.; van Lenthe, E.; Groeneveld, J. A.; Snijders, J. G. *Journal of the American Chemical Society* **1999**, *121*, 10356-10365.

36. Dreuw, A.; Head-Gordon, M. *Chemical Reviews* **2005**, *105*, 4009-4037.

37. Neese, F. *Coordination Chemistry Reviews* **2009**, *253*, 526-563.

38. González, L.; Escudero, D.; Serrano-Andrés, L. *ChemPhysChem* **2012**, *13*, 28-51.

39. Daniel, C. *Coordination Chemistry Reviews* **2015**, *282-283*, 19-32.

40. Zobel, J. P.; González, L. *JACS Au* **2021**, *1*, 1116-1140.

41. Hanwell, M. D.; Curtis, D. E.; Lonie, D. C.; Vandermeersch, T.; Zurek, E.; Hutchison, G. R. *Journal of Cheminformatics* **2012**, *4*, 17.

42. Heully, J. L.; Lindgren, I.; Lindroth, E.; Mrtensson-Pendrill, A. M. *Physical Review A* **1986**, *33*, 4426-4429.

43. van Lenthe, E.; Snijders, J. G.; Baerends, E. J. *The Journal of Chemical Physics* **1996**, *105*, 6505-6516.

44. *Gaussian 16 Rev. C.01*; Wallingford, CT, 2016.

45. Weigend, F.; Ahlrichs, R. *Physical Chemistry Chemical Physics* **2005**, *7*, 3297-3305.

46. Krishnan, R.; Binkley, J. S.; Seeger, R.; Pople, J. A. *The Journal of Chemical Physics* **2008**, *72*, 650-654.

47. Dolg, M.; Wedig, U.; Stoll, H.; Preuss, H. *The Journal of Chemical Physics* **1987**, *86*, 866-872.

CHAPTER 5

Bright Ligand-Centered Fluorescence of Copper Carbene Complexes

5.1 Introduction.

Photoredox catalysis (PRC) has established itself as a useful tool to access new chemical reactivity in small molecules.[1] From the Rehm-Weller Approximation,[2] one can rationalize that designing a strong visible light photoreductant necessitates a reducing ground state. This design principle has been widely used to synthesize a variety of highly reducing chromophores capable of engaging in PRC.[3-9] Highly reducing chromophores are important for engaging electron rich alkyl and aryl halides. For a simple molecule such as iodobenzene, the ground-state reduction potential determined by electrochemistry is −2.6 V vs. $Fc^{0/+}$.[10] This is inaccessible by classical chromophores such as porphyrins, $Ru(bpy)_3^{2+}$, and even *fac*-$Ir(ppy)_3$.[1] Substitution of the benzene ring with donating substituents or using lighter and cheaper halide derivatives lowers this potential and makes reductive activation of these substrates even more challenging. Because of this, identifying design principles for chromophores capable of achieving strongly negative excited-state oxidation potentials should greatly enable the use of PRC with these substrates.

From an electrostatic perspective, adding negative charge to a chromophore will make it more reducing by raising the energies of its occupied orbitals. Harnessing the decreased potential of the anion could allow access to even more reducing excited states if the basic electronic structure of the chromophore remains intact. This has been shown for a series of organic chromophores formed by deprotonation, reduction, and hydride transfer.[6-9, 11-14] While this succeeds in generating extremely reducing chromophores with excited-state oxidation potentials exceeding −3.00 V vs. $Fc^{0/+}$ in some cases, their generality for PRC use can be limited by poorly

characterized excited states and short excited-state lifetimes. Anionic chromophores formed by deprotonation are particularly interesting since only catalytic base is necessary to form the photocatalyst and can also be later incorporated into the photocatalytic cycle. The pK_a of the anion can also be tuned by peripheral substitution to suit the desired reaction. Previous studies using deprotonated chromophores have used phenol and phenol-derived chromophores, which benefit from stabilization of the anionic charge on the oxygen.[12-13] These catalysts are formed through *in situ* deprotonation with excess base to form the anion, which can then initiate the desired photocatalytic reaction. We hypothesized that stabilization of anionic chromophores by coordination to a suitable metal center could retain high excited-state potentials while conferring additional stability towards the chromophore. For this to be effective, the metal should be a spectator to the excited-state and possess a large gap between reduction and oxidation potentials (Figure 5.1).

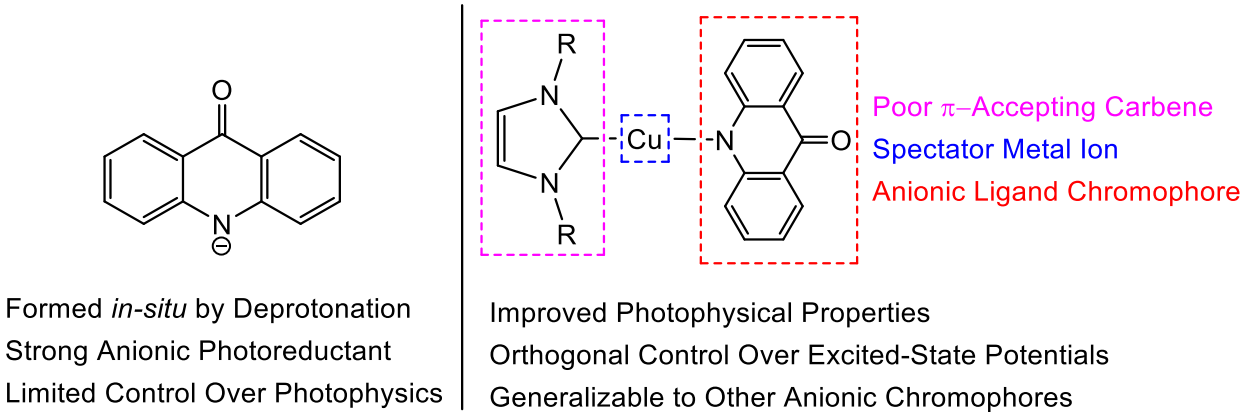

Figure 5.1. General design for stabilization of anionic acridone chromophores.

Linear carbene-metal-amide (CMA) are a recently developed class of chromophores that have gained interest for their strong and tunable emission properties.[15-22] These complexes consist of a strongly σ-donating carbene with sterically bulky sidearms, a Group 11 metal, and an

aryl amide. Conventional CMA chromophores emit through an LLCT pathway. Here, due to symmetry allowed $3dz^2-4s$ orbital mixing, the highest lying metal d-orbital is buried. As a result, the metal mostly serves as an electronic bridge between the two ligands allowing the excited-state to be largely dictated by carbene and amide fragments. Choice of π-acidic carbenes and π-donating amides lead to a low-lying LLCT state that, due to orthogonal HOMO and LUMO orbitals on the amide and carbene fragment, respectively, contracts the S_1-T_1 energy gap, enabling these complexes to undergo thermally-activated delayed fluorescence through rapid forward and reverse intersystem crossing. This enables high emission quantum yields up to approaching unity[15] and relatively short excited-state lifetimes despite poor spin-orbit coupling from the organic fragments. Alternatively, recent studies on CMA complexes using a carbazole (Cz) amide and imidazolidene carbene Cu(IPr)(Cz) and Cu(IMes)(Cz) have shown slightly different photophysics.[18] Here, the imidazolidene carbene is an extremely poor π-acceptor, destabilizing LLCT emission and instead leading to emission from purely ligand-centered excited-states. In solution, emission is observed from a ^{1}Cz state while solid-state measurements show emission from both ^{1}Cz and ^{3}Cz states with moderate quantum yields, indicating poor electronic coupling to the copper carbene fragment. Notably, this is the only example of pure intraligand-centered emission from a linear CMA complex and suggests the possibility of accessing general ligand-centered excited states within this framework.

Acridone is a simple organic chromophore, whose excited-state properties have been well studied.[23-27] Acridone possesses a fluorescent S_1 state arising from a nitrogen-centered π_{HOMO} to carbonyl-centered π^*_{LUMO} transition. This $^1(\pi,\pi^*)$ S_1 state displays ultrafast El-Sayed allowed intersystem crossing to a nearby triplet $^3(n,\pi^*)$ T_2 state arising from an in-plane oxygen lone pair from the carbonyl with an excited-state equilibrium establishing within 10 ps.[23, 25] This rapid

forward and reverse intersystem crossing equilibrium has been studied in other diaryl ketones such as xanthone and thioxanthone and has shown promise for use in OLED devices and for photocatalysis.[13, 28-29] Given its interesting photophysical properties, we hypothesized that the acridone anion would be a suitable chromophore for linear copper CMA complex displaying ligand-centered emission and may be useful as a photocatalyst due to its potentially high excited-state oxidation potential and nanosecond excited-state lifetime. The orbitally separated HOMO and LUMO orbitals suggest coordination-dependent electronic and optical properties, which along with the stability and wide electrochemical gap of the linear CMA motif, should allow external and rational control of the acridone optical and electrochemical properties through steric protection and orbital mixing with the (IPr)Cu fragment without modifying its skeleton. In this chapter, we characterize how the electronic and optical properties of 2,7-dimethylacridone (H**L**) are strongly perturbed upon deprotonation in the form of a cryptate salt and subsequent coordination and stabilization to form a linear CMA complex and highlight how these methods can be used to control relevant properties for photoredox applications (Figure 5.1).

5.2 Results and Discussion.

5.2.1 Synthesis and Characterization.

The compound **KCryptL** ([K(2.2.2-crypt)]**L**) was synthesized via the reaction between 2,7-dimethylacridone (H**L**) and one equivalent of K[N(SiMe$_3$)$_2$] in THF at room temperature, followed by addition of [2.2.2]-cryptand (Scheme 5.1). Immediately upon the addition of K[N(SiMe$_3$)$_2$], the presence of **L**$^-$ was evidenced by the color change of the reaction mixture from light yellow to orange-yellow and concomitant appearance of bright green fluorescence under ambient light. Isolation of the crude product and recrystallization from a 1:1 mixture of

toluene and diethyl ether provided yellow microcrystalline product in 74% yield. **KCryptL** is soluble in THF, acetonitrile, and 1,3-difluorobenzene and sparingly soluble in benzene and toluene. The identity of **KCryptL** was established by ^{1}H- and ^{13}C-NMR spectroscopy, high-resolution mass spectrometry, and a single-crystal X-ray diffraction study. Omitting the addition of 2.2.2-cryptand from the above synthetic procedure provides the salt K**L**, which is also luminescent and soluble in THF, acetonitrile, and 1,3-difluorobenzene. **KCryptL** was the focus of physical measurements in this study to reduce possible effects from ion pairing.

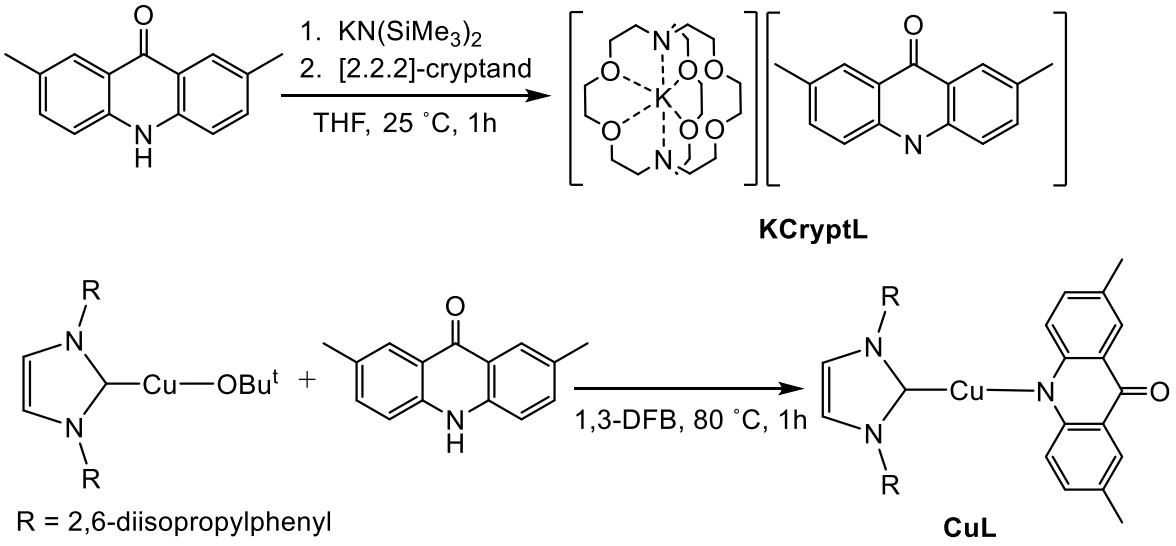

Scheme 5.1. Synthetic route for synthesis of **KCryptL** and **CuL**.

The compound **CuL** ((IPr)Cu(**L**)) was synthesized from the reaction between (IPr)Cu(OBu^{t})[30] (1.5 equiv.) and H**L** (1 equiv.) in 1,3-difluorobenzene at 80 ˚C (Scheme 5.1). Upon addition of H**L** to a solution of (IPr)Cu(OBu^{t}), the colorless solution quickly turned bright yellow with sky blue luminescence observed at the solvent meniscus under ambient light. Cooling the reaction mixture to –30 ˚C provides yellow needles of **CuL** in 60% yield. The identity and composition of **CuL** were established by ^{1}H- and ^{13}C-NMR spectroscopy, high-resolution mass spectrometry, and single-crystal X-ray diffraction. The compound is soluble in

acetonitrile, 1,3-difluorobenzene, and THF and sparingly solubility in toluene, benzene, and 1-methylnaphthalene. The complex was found to be air and moisture sensitive. This was unexpected, since other copper imidazolyl carbene amide complexes have been reported to be air and moisture stable.[18]

The choice of (IPr)Cu(OBu^t) as a starting material for **CuL** warrants comment in view of the fact that many (NHC)Cu(amido) (NHC = *N*-heterocyclic carbene) complexes have been prepared in high yield via one-pot reactions between (NHC)CuCl, the corresponding amine, and a base.[15-21] Application of these methods to the synthesis of **CuL** and several related (NHC)M(Acr) (Acr$^-$ = *N*-deprotonated acridone, ($C_{13}H_8NO^-$) complexes (IPr)Cu(Acr), (IPr)Au(Acr), (IPr*)Cu**L**, and (IPent)Cu(Acr; IPr* = 1,3-bis(2,6-bis(diphenylmethyl)-4-methylphenyl)imidazo-2-ylidene and IPent = 1,3-bis(2,6-bis(1-ethylpropyl)phenyl)imidazol-2-ylidene) generally provided the desired product in impure form, with acridone (or H**L**) being the principal contaminant (see Section 5.4.6.3). Separation of acridone from the product was difficult owing to their similar solubilities; even after multiple purification steps, the product was found to contain approximately 0.5% acridone by ^{1}H NMR spectroscopy. This could potentially arise from either decomposition upon dissolution of the crystals, cocrystallization of free acridone with the product, or formation of a solid solution within the crystal, among other possibilities. The minimal difference in distribution of electron density and low concentration of free acridone in grown single crystals prevented being able to conclusively assign any one of these crystallographic possibilities. The solutions from which these single crystals were grown were identified to have free acridone by ^{1}H NMR, so the as-grown single crystals cannot be confirmed as only containing the desired product. Through multiple synthetic attempts and recrystallization of the crude product, various sources of decomposition were found including contact with

filtration media, trace water, and oxygen. Attempts to recrystallize from dichloromethane also displayed large increases in free acridone in addition to formation of the Cu(IPr)(Cl) precursor. The insolubility of the final product also posed a challenge owing to inherited insolubility of the acridone ligand. This led to sparing but detectable solubility in most solvents, limiting our ability to cleanly recrystallize the desired product.

To avoid these solubility issues and synthesize an isolable pure compound, syntheses of other derivatives were attempted to identify a stable product suitable for further study. Changing the metal center from copper to gold was hypothesized to increase metal-ligand bond strength and reduce steric clash of the acridone with the carbene. These synthetic attempts were met with similar solubility and decomposition challenges as with the copper system. To solve some of the solubility issues of the acridone ligand, ligands bearing longer alkyl groups such as 2,7-di-*tert*-butylacridone or the IPent carbene were prepared to aid in purification of the product. In both cases, the resulting increase in solubility of the final product facilitated workup but did not prevent decomposition or aid in separation of free ligand from the product. In addition, close inspection of prepared 2,7-di-*tert*-butylacridone by the literature route was not completely pure by ^{1}H NMR due to contamination by the monoalkylated product. These products were unable to be separated by chromatography or recrystallization, leading to additional side products during the synthesis of the final metallated complex. Given the benefits in solubility by alkylation of acridone, the commercially available 2,7-dimethylacridone was used to avoid the previous purity issue from the *tert*-butyl derivative. To determine if bimolecular reactivity was a major source of decomposition, the sterically bulky IPr* was tested as choice of carbene. Even in this case, after filtration, an increase in free acridone was observed. The increased bulk and insolubility of the carbene due to the additional phenyl groups dramatically reduced the solubility of the product

rendering the final product relatively insoluble. This essentially reversed the improvement in separation from alkylating the acridone and hindered purification of this complex.

Replacing (IPr)CuCl with (IPr)Cu(OBu^t) as starting material solved these problems due to the increased solubility of (IPr)Cu(OBu^t). The pre-installed OBu^t ligand acts an internal base to deprotonate acridone while avoiding formation of any alkali-metal salts. This removes subsequent dissolution and filtration steps and avoids one source decomposition. This copper synthon is very soluble in variety solvents, whereas the desired product is fairly insoluble due to the acridone ligand. Therefore, use of an excess of this synthon should completely consume any free amine while the desired product should cleanly precipitate out solution. Ultimately, it was found that use of 1.5 equivalents of the copper synthon to one equivalent of acridone while heating to 80 ˚C to ensure complete reaction was enough to fully drive the reaction to completion and ensure complete consumption of the free amine. Crystallization of the product directly from the reaction mixture by cooling to −30 ˚C forms **CuL** as yellow needles, which could then be collected by filtration and dried to afford the analytically pure product suitable for further photophysical study and analysis. While this method was not tested for complexes other than **CuL**, it should be suitable for the clean synthesis of those complexes as well.

5.2.2 Molecular Structures.

The molecular structures of **KCryptL** and **CuL** were investigated through single-crystal X-ray diffraction experiments and DFT calculations. For **KCryptL**, the crystal structure exhibits discrete [K(2.2.2-cryptand)]$^+$ and **L**$^-$ ions (Figures 5.2, 5.30, and 5.31). The bond distances and angles within the anion are broadly similar to those determined from a crystal structure of *N*-ethylacridone (EtAcr, Table 5.1); the principal differences are for metrical parameters that

include the nitrogen atom, consistent with loss of H^+ and associated gain of negative charge. Strikingly, the $\mathbf{L}^-$ ion is nonplanar, with the oxygen and nitrogen atoms lying 0.395 Å and 0.155 Å above the mean plane, respectively, and the methyl group carbon atoms 0.151 Å and 0.246 Å below the plane. Examination of the inter-ion contacts that are shorter than the sum of van der Waals radii does not point to a specific interaction that accounts for this distortion, so its origin is ascribed to nonspecific packing forces. Consistent with this distortion being a consequence of the solid-state structure, the calculated gas-phase structures of $\mathbf{L}^-$ and K**L** are planar and possess bond distances and angles within $\mathbf{L}^-$ that are in reasonable agreement with those found in the crystal structure (Table 5.1 and Table 5.2).

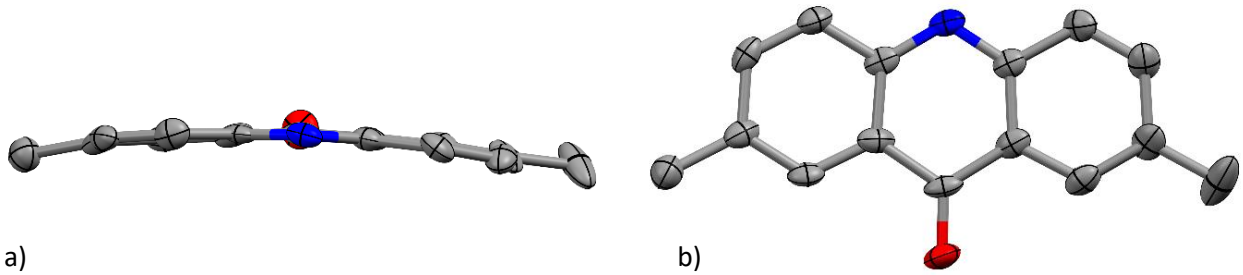

Figure 5.2. Thermal-ellipsoid representations (50% probability ellipsoids) of **KCryptL** viewed (a) side-on and (b) face-on, determined by single-crystal X-ray diffraction. Hydrogen atoms, interstitial solvent, and cation are omitted for clarity.

Table 5.1. Select Bond Lengths (Å) and Angles (˚) from X-ray Crystallography.

	CuL	**KCryptL**	EtAcr[a]	Cu(IPr) (Acr)	Au(IPr) (Acr)	Cu(IPr*) (**L**)
$C-N_{Acr,\ avg}$	1.373(3)	1.346(7)	1.390(2)	1.377(11)	1.374(4)	1.369(2)
C−O	1.244(3)	1.251(6)	1.2400(17)	1.244(10)	1.249(4)	1.247(2)
$C-N_{Acr}-C$	117.48(17)	116.3(4)	120.60(12)	117.3(7)	118.5(3)	117.84(14)
C−C(O)−C	115.21(18)	114.0(4)	115.46(12)	115.6(8)	116.2(3)	114.94(15)
$M-C_{NHC}$	1.866(2)			1.867(7)	2.038(2)	1.8592(16)
$M-N_{Acr}$	1.8774(17)			1.868(6)	1.972(3)	1.8752(14)
$N_{Acr}-M-C_{NHC}$	177.01(8)			177.3(3)	177.34(11)	178.30(7)

[a] Ref 31

Table 5.2. Selected Bond Lengths (Å) and Angles (˚) from DFT Optimized Structures.

	CuL	**KCryptL**	H**L**	Au(IPr)(Acr)	**L**$^{-}$	K**L**
C−$N_{Acr,\ avg}$	1.368	1.342	1.369	1.371	1.344	1.357
C−O	1.229	1.253	1.222	1.227	1.241	1.230
C−N_{Acr}−C	117.97	116.49	123.06	118.77	116.25	117.23
C−C(O)−C	114.26	114.07	115.25	114.4	113.56	114.17
M−C_{NHC}	1.895			1.988		
M−N_{Acr}	1.893			2.047		
N_{Acr}−M−C_{NHC}	177.3			177.15		

The molecular structure of **CuL** (Figure 5.3) provided by a single-crystal X-ray diffraction study exhibits the expected linear geometry at the Cu center (∠(N_{Acr}–Cu–C_{NHC}) = 177.01(8)˚) and nearly coplanar **L** and imidazole units(∠(N–C_{NHC}–N_{Acr}–C)$_{avg}$ = 2.7[2]˚). Unlike for **KCryptL**, the **L** ligand of **CuL** is planar. The Cu–N_{Acr} and Cu–C_{NHC} bond lengths (1.8774(17) Å and 1.866(2) Å, respectively; Table 5.1) are within the ranges found for other CMA complexes (*d*(Cu–C_{NHC}) = 1.86–1.90 Å; *d*(Cu–N_{Acr}) = 1.85–1.87 Å),[16-20, 32] and the C–O bond length, and those within the heterocycle, are close to those for EtAcr (Table 5.1) except for the C–$N_{Acr,\ avg}$ bond length and C–N_{Acr}–C bond angle, which are perturbed by coordination to copper.[16-21, 31-32] The observed bond distances and angles are in good agreement with those provided by a DFT calculation (Table 5.1 and Table 5.2) The coplanar orientation of **L** and imidazole units differs from that reported for the related carbazole complex (IPr)Cu(Cz), for which the corresponding units are oriented perpendicular to each other (torsion angle 89.9˚).[18] DFT calculations on **CuL** that attempted to assess the relative energies of the planar and hypothetical perpendicular rotamers did not identify a local minimum for the perpendicular structure and always converged to the planar structure. This indicates that the perpendicular orientation is highly disfavored for **CuL** and its physical properties are associated with the planar structure.

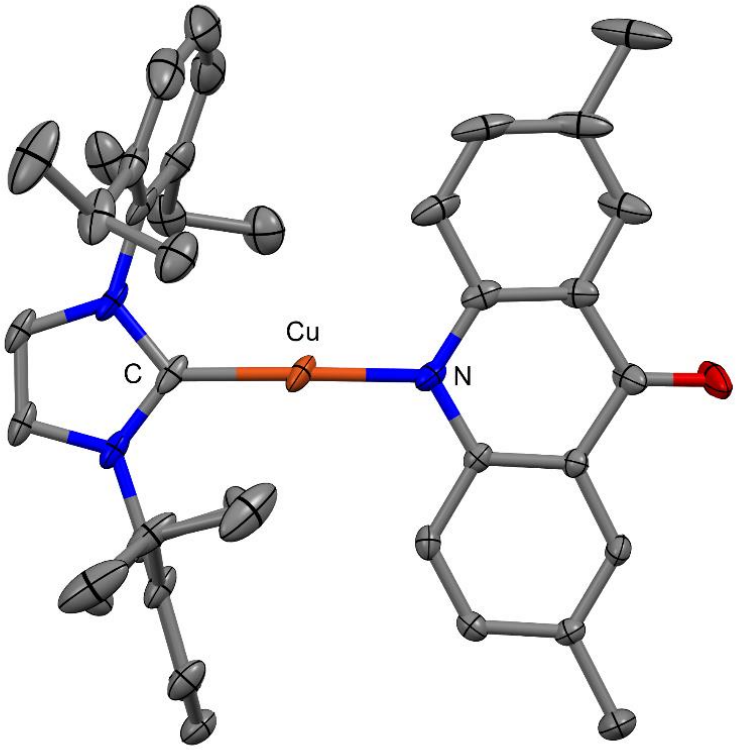

Figure 5.3. Thermal-ellipsoid representations (50% probability ellipsoids) of **CuL** determined by single-crystal X-ray diffraction. Hydrogen atoms and interstitial Et_2O omitted for clarity.

X-ray crystal structures of the related complexes Cu(IPr)(Acr), Au(IPr)(Acr), and Cu(IPr*)(**L**), obtained from crystals separated from impure product mixtures containing acridone, as noted above, also display linear 2-coordinate geometries at the metal center (Table 5.1). Unlike **CuL**, the closely related derivatives Cu(IPr)(Acr) (Figures 5.4 and 5.5) and Au(IPr)(Acr) (Figures 5.6 and 5.7), which lack the methyl groups on **L**, display intermolecular O···H hydrogen bonding between the carbonyl and imidazole (Cu: $CO_L{\cdots}C_3N_2H_2$ = 3.047 Å; Au: $CO_L{\cdots}C_3N_2H_2$ = 2.995 Å), producing 1D chain structures. Despite different steric bulk about the carbene and choice of metal center, the relevant acridone bond parameters are essentially identical to each other. Even the crystal structure of Cu(IPr*)(**L**) (Figure 5.8), with an extremely

bulky carbene ligand, shows essentially identical bond lengths to the other copper derivatives with the steric bulk projecting away from the acridone and imidazole plane. The crystallographically determined C–O bond length for all reported metallated acridone derivatives are within 3σ error compared to EtAcr at 1.2400(17) Å (Table 5.1).[31] These bond lengths are close despite the presence of hydrogen-bonding chains in two of the crystals which could elongate the C–O bond length. This suggests that these hydrogen-bonds are relatively weak and so only minimally affect the carbonyl bond. The $C–N_{Acr,\ avg}$ bond lengths are likewise within 3σ error of one another, but are statistically shorter than that measured for EtAcr at 1.390(2) Å.[31] These deviations are small enough that they are likely not significant to the overall electronic structure of the molecule.

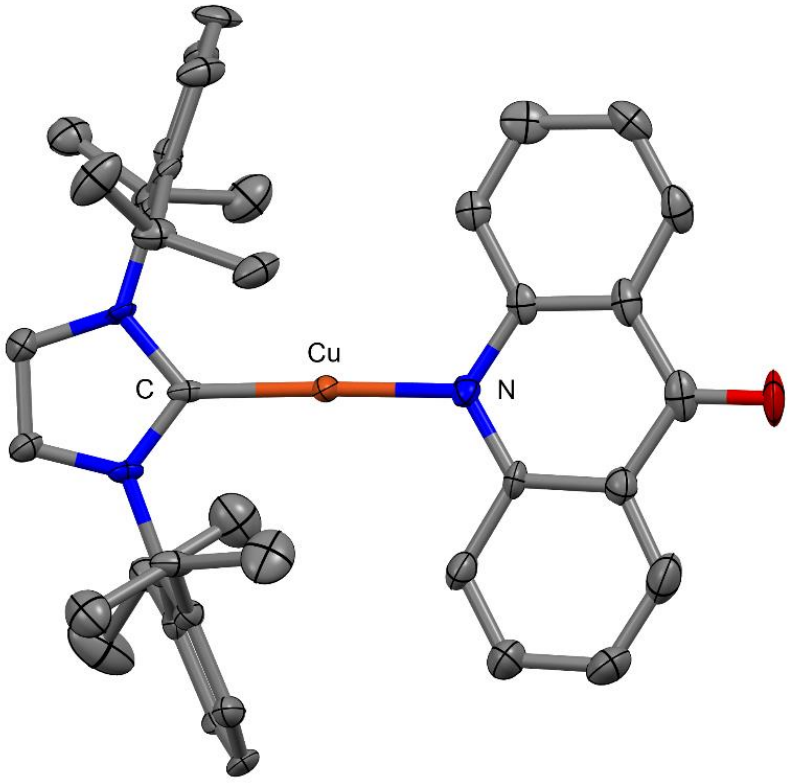

Figure 5.4. Thermal-ellipsoid representation of Cu(IPr)(Acr) (50% probability ellipsoids). Interstitial THF is omitted for clarity.

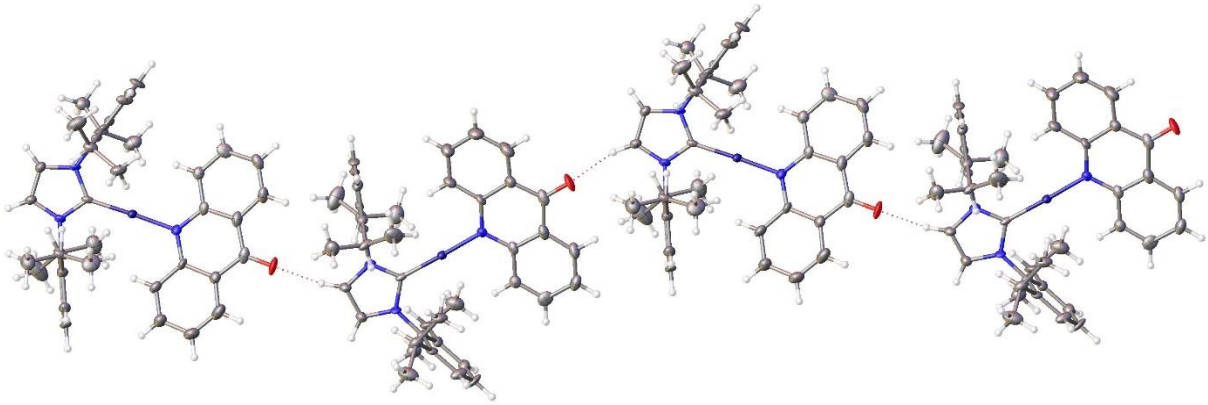

Figure 5.5. Thermal-ellipsoid representation of Cu(IPr)(Acr) showing hydrogen bonding chain (50% probability ellipsoids). Interstitial THF is omitted for clarity.

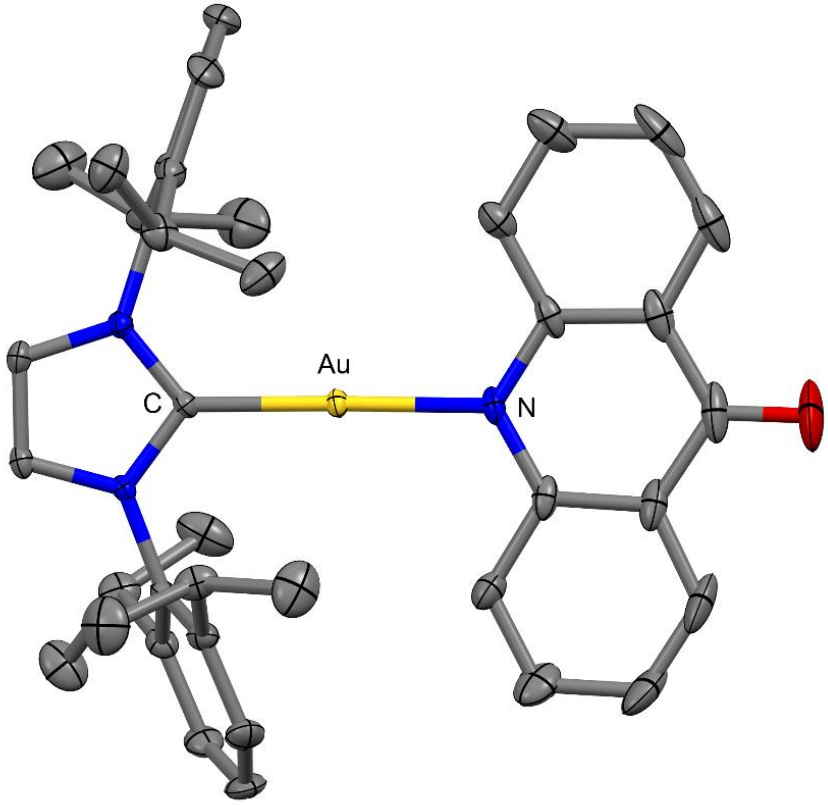

Figure 5.6. Thermal-ellipsoid representation of Au(IPr)(Acr) (50% probability ellipsoids). Interstitial acetone is omitted for clarity.

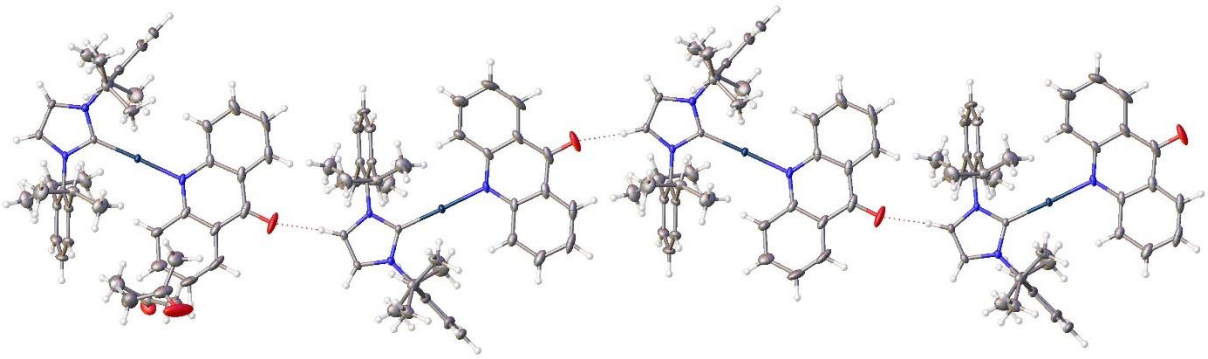

Figure 5.7. Thermal-ellipsoid representation of Au(IPr)(Acr) (50% probability ellipsoids) showing intermolecular hydrogen-bonding between imidazole CH and acridone CO groups.

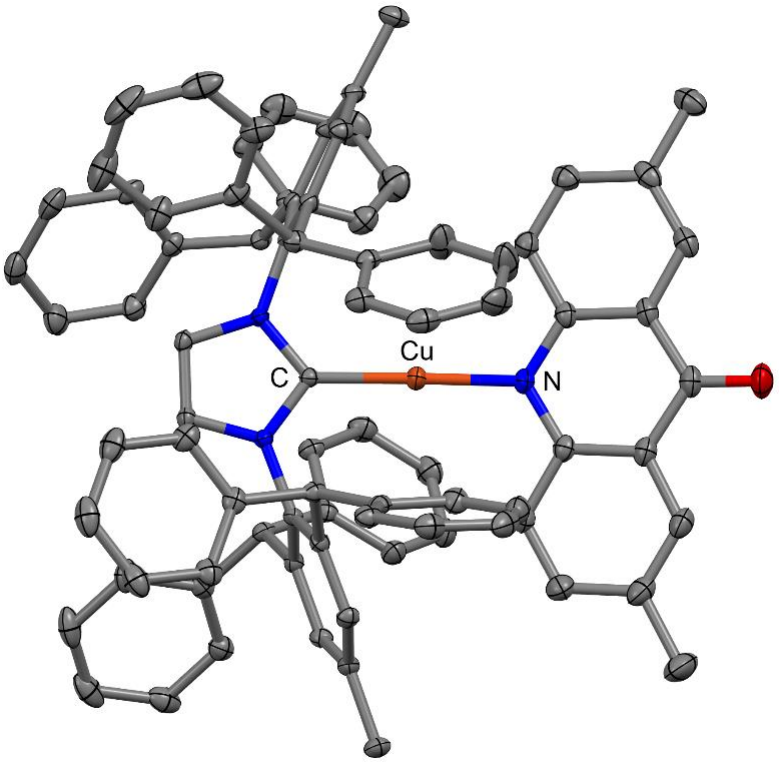

Figure 5.8. Thermal-ellipsoid representation of Cu(IPr*)(**L**) (50% probability ellipsoids). Interstitial acetonitrile is omitted for clarity.

The frontier orbitals of H**L**, K**L**, and **CuL** were elucidated through DFT calculations to provide a framework for interpreting their electronic spectra and photophysical properties

(Figure 5.9). For all complexes, the HOMO is an acridone π orbital (π_{HOMO}). For **CuL**, the HOMO also carries minor contribution from the copper d_{xz} orbital. The HOMO–1 for all complexes is the acridone carbonyl oxygen lone pair (n) orthogonal to the π system. The LUMO for H**L** and K**L** is a π* orbital with significant carbonyl character, whereas for **CuL** this orbital is predicted to lie at LUMO+4, ca. 0.4 eV above the LUMO, with the latter being an NHC π* orbital. Copper d orbitals are not expected to significantly contribute to low-lying electronic transitions, with the highest-lying occupied orbital with copper character found at HOMO−5 and displaying predominant Cu $3dz^2$ character with symmetry allowed 4s orbital character due to the linear ligand field as expected for a CMA complex.

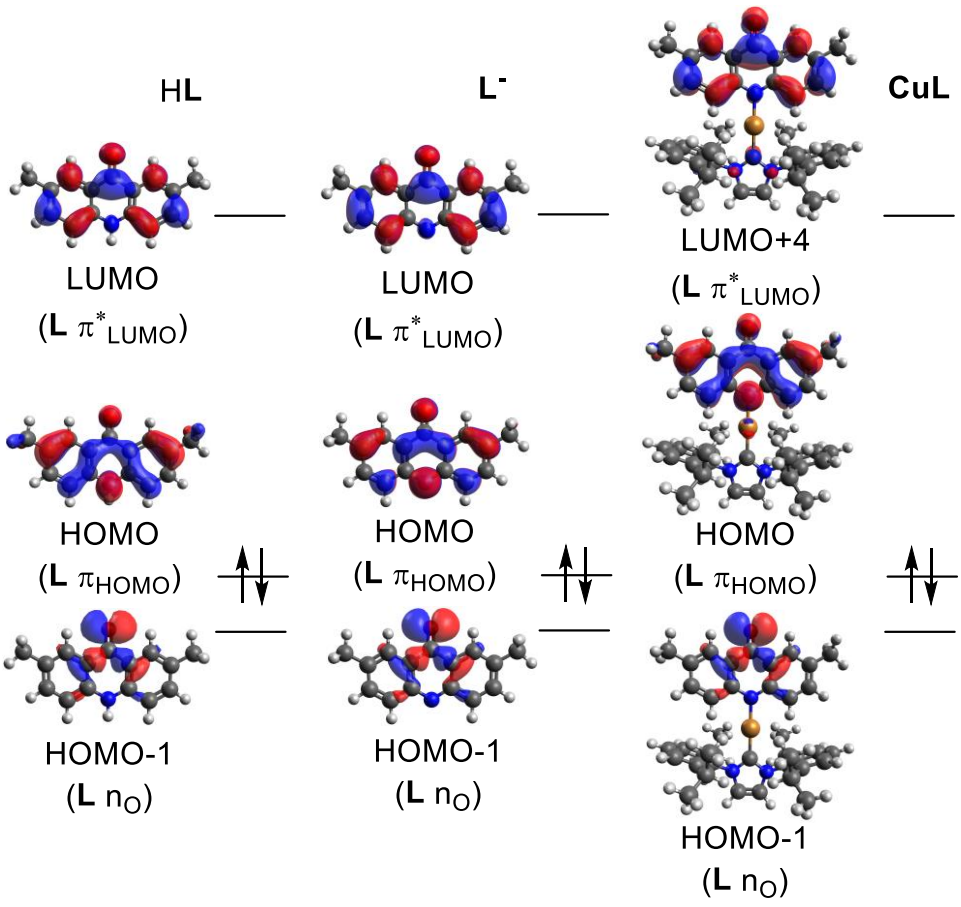

Figure 5.9. Kohn-Sham orbitals and their respective orbital fragment parentage for H**L**, **L**$^{-}$, and **CuL**. For clarity, only frontier orbitals relevant to acridone are shown.

These frontier acridone centered orbitals undergo a pronounced shift to higher energies upon deprotonation of the nitrogen to form the final complexes (Table 5.3). The overall acridone orbital energies are remarkably similar between the K**L** and **CuL** with energy differences less than 0.2 eV. These energies are much higher than that of H**L** with the acridone π_{HOMO} increasing by roughly 1.3 eV, the oxygen lone pair HOMO−1 by 1.1 eV, and the acridone π* LUMO/LUMO+4 by roughly 1 eV. The larger increase in the HOMO energy is consistent with increased negative charge built up on the nitrogen due to deprotonation. The HOMO and HOMO−1 are found for K**L** at −4.516 eV and −5.784 eV respectively. While the charge is compensated by the potassium or copper cations, these are clearly insufficient Lewis acids to stabilize the increased negative charge. Both deprotonated complexes also display contracted HOMO-LUMO gaps and increased HOMO-HOMO-1 energy gaps. This would suggest an overall redshift of HOMO-LUMO transition upon deprotonation while the increased HOMO-HOMO-1 energy gap would indicate the relative destabilization of the T_2 ^{3}(n,π*) state relative to the S_1 ^{3}(n,π*) state which could be relevant for the luminescence of these complexes.

Table 5.3. Select Kohn-Sham Orbital Energies from DFT Optimized Structures.

Orbital energy (eV)	**CuL**	**KCryptL**	H**L**	**L**$^-$	**KL**
L π_{LUMO}	-0.666	-0.591	-1.644	2.357	-0.719
NHC π_{LUMO}	-1.053				
L π_{HOMO}	-4.593	-4.323	-5.868	-1.281	-4.516
L n	-5.842	-5.942	-6.904	-2.756	-5.784

5.2.3 Electrochemical Characterization.

To gauge the strength of **KCryptL** and **CuL** as reductants, cyclic voltammetry of each complex was performed. The cyclic voltammograms of both complexes are fully irreversible

precluding Randles-Sevcik analyses. For oxidation, **KCryptL** displays one oxidation peak at E_{pa} = –0.50 V vs. $Fc^{0/+}$ (Figure 5.10 and Table 5.4) assigned to formation of the charge-neutral aminyl radical while **CuL** displays two oxidation peaks at E_{pa} = 0.35 V vs. $Fc^{0/+}$ and E_{pa} = 0.55 V vs. $Fc^{0/+}$ assigned to acridone and copper oxidation respectively (Figure 5.11 and Table 5.4). The first oxidation for both complexes can be assigned from the DFT calculated HOMO orbitals (Figure 5.9) and comparison to other CMA complexes. As **KCryptL** does not display a second oxidation event, the second oxidation for **CuL** is assigned as copper-centered.

Table 5.4. Electrochemical Peak Potentials (vs $FeCp_2^{0/+}$) Observed by Cyclic Voltammetry.[a]

	E_{pc1} (V)	E_{pc2} (V)	E_{pa1} (V)	E_{pa2} (V)
KCryptL	-2.79		-0.50	
CuL	-2.90	-3.29	0.35	0.55
N-Phenyl-2,7-di-*tert*-butylacridone[b]	-2.83	-3.45	0.96	

[a] THF solution containing 0.1M $[N^nBu_4][PF_6]$, ν = 100 mVs^{-1}. [b] Ref 24

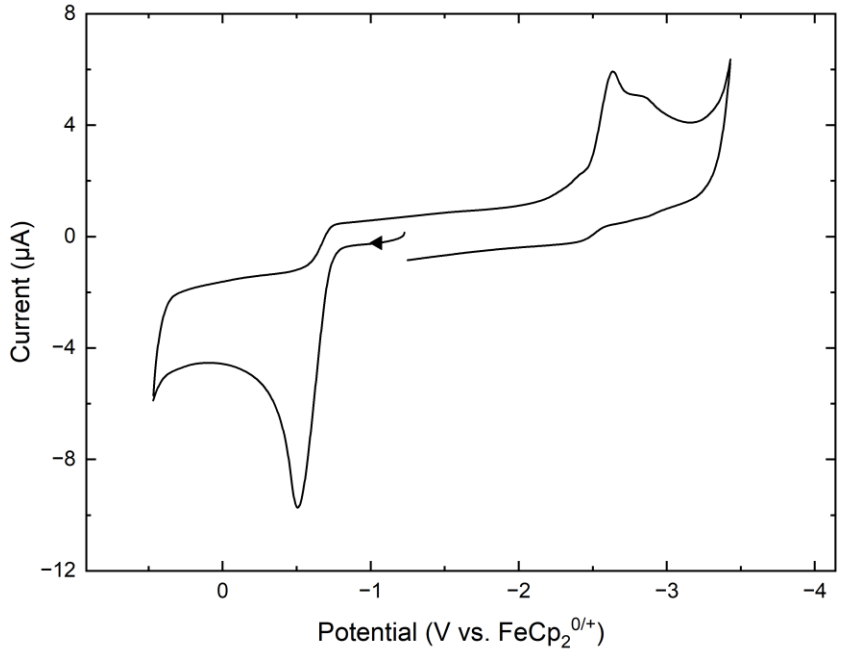

Figure 5.10. First scan of the cyclic voltammogram of **KCryptL** (0.001 M) in THF containing 0.1M $[N^nBu_4][PF_6]$ (ν = 100 mVs^{-1}).

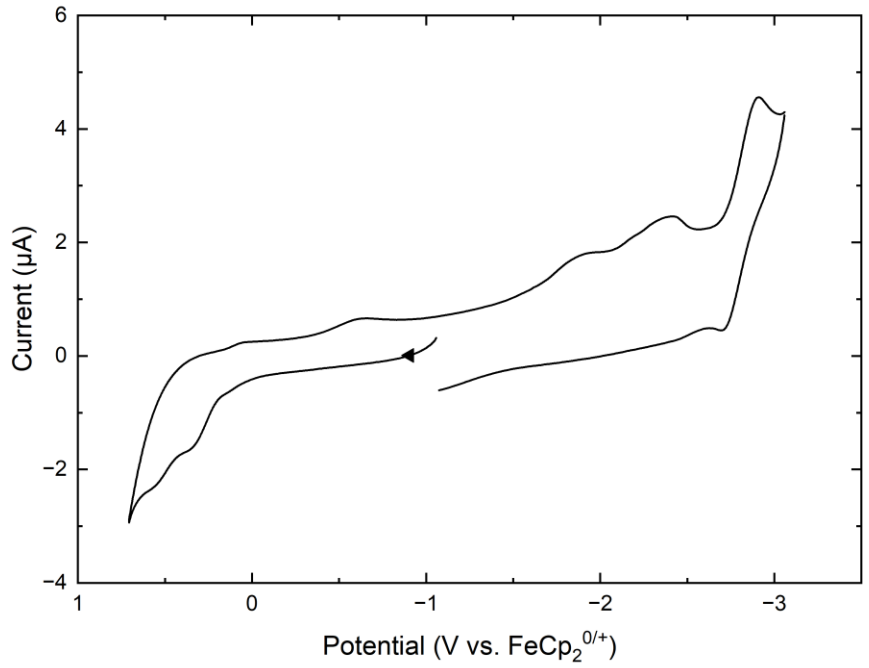

Figure 5.11. First scan of the cyclic voltammogram of **CuL** (0.001 M) in THF containing 0.1M $[N^nBu_4][PF_6]$ (ν = 100 mVs^{-1}).

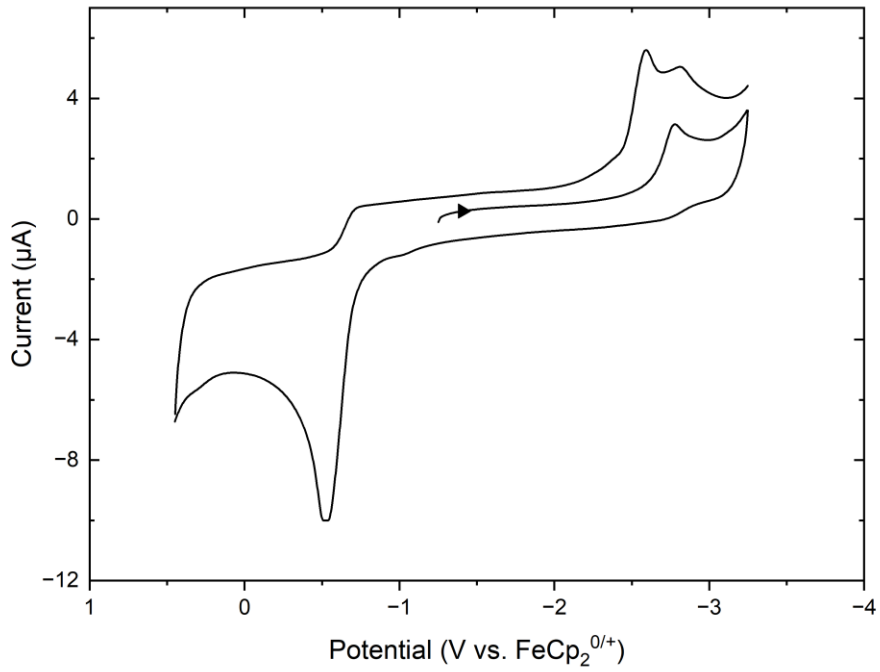

Figure 5.12. First scan of the cyclic voltammogram of **KCryptL** (0.001 M) in THF containing 0.1M $[N^nBu_4][PF_6]$ (ν = 100 mVs^{-1}).

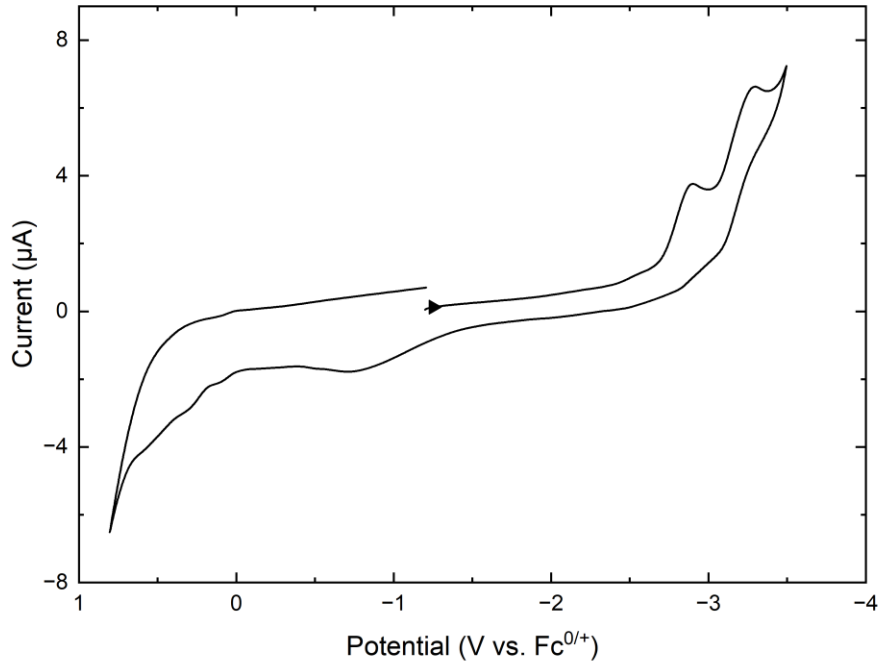

Figure 5.13. First scan of the cyclic voltammogram of **CuL** (0.001 M) in THF containing 0.1M $[N^nBu_4][PF_6]$ (ν = 100 mVs^{-1}).

For reduction, **KCryptL** displays one reduction peak at E_{pc} = –2.79 V vs. $Fc^{0/+}$ to generate the putative radical ketyl dianion, while **CuL** shows two peaks at E_{pc} = –2.90 V vs. $Fc^{0/+}$ and E_{pc} = –3.29 V vs. $Fc^{0/+}$ both assigned to reduction of the acridone ligand (Figures 5.12 and 5.13). The reduction for **KCryptL** can be assigned from the DFT-calculated LUMO orbitals (Figure 5.9) as well as similarity to that of a reported of the *in situ* generated acridone anion with reduction at –2.84 V vs. $Fc^{0/+}$ and oxidation at –0.16 V vs. $Fc^{0/+}$.[13] Differences in potential can be attributed to change in solvent from THF to DMSO and introduction of two methyl groups for H**L**. For **CuL**, assignments can be made by comparison to a related *N*-phenyl-2,7-di-*tert*-butylacridone[24] which displays quasi-reversible reductions at E_{pc} = –2.83 V vs. $Fc^{0/+}$ and E_{pc} = –3.45 V vs. $Fc^{0/+}$. The slight cathodic shift found for **CuL** is attributed to stabilization of the generated anion by the carbene. This differs from our analysis by DFT, which predicts an NHC-

centered LUMO that lies 0.387 eV below the acridone-centered LUMO+4. To validate our assignment, electrochemistry of a reported Au(IPr)(bim) (bim = 5H-benzo[4,5]imidazo[1,2] imidazole) complex shows no reduction features within the solvent window out to –3.0 V vs. $Fc^{0/+}$, indicating that IPr reduction should not be accessible at the first peak potential.[21]

Two things stand out from the electrochemical peak potentials. The first is the negative oxidation potential found for **KCryptL** which is 0.85 V more negative than **CuL** (Table 5.4). This is consistent with the significant destabilization of the HOMO by deprotonation to the $\mathbf{L}^-$ ion. Compared to the *N*-phenylacridone, this difference is 1.46 V, highlighting the huge gain in reducing power by deprotonation and partial stabilization by the copper carbene in **CuL**. By contrast, the reduction potential is essentially unperturbed spanning only 0.11 V with the charge neutral **CuL** being the most negative at E_{pc} = –2.90 V vs. $Fc^{0/+}$. This suggests decoupling of the HOMO and LUMO energy levels by substitution at the nitrogen and suggests that transition-metal coordination may be useful as a general tool to control ground-state oxidation potentials of these anions.

The voltammograms of both complexes are complicated by decomposition products that appear after either initial oxidation or reduction. For **KCryptL**, after an initial anodic sweep, a second irreversible feature appears at E_{pc} = –2.60 V vs. $Fc^{0/+}$ with no new cathodic features (Figure 5.12). This feature is persistent across multiple sweeps and indicates formation of a new species arising from oxidative decomposition of **KCryptL**. Similarly, the irreversible nature of **CuL** redox peaks, gives rise to new anodic and cathodic features after an initial sweep. Assignment of these decomposition products were not possible as they continue to speciate in solution upon further redox cycling. Halting the voltammetry sweep before the second oxidation or reduction event still led to fully irreversible redox waves and speciation of the analyte.

5.2.4 Electronic Absorption Spectroscopy.

The electronic-absorption spectra of **KCryptL** and **CuL** were studied to probe the nature of the lowest-lying excited states and investigate the extent to which **L**-centered states are perturbed by coordination to copper. The spectra of the two compounds in THF solution (Figure 5.14) are qualitatively similar to each other, each consisting of two prominent, vibronically structured bands in the $\lambda > 300$ nm region. The lowest energy band (**KCryptL** (THF): $\lambda(0,0)$ = 467 nm, ε_{max} = 6500 $M^{-1}cm^{-1}$; **CuL** (THF): $\lambda(0,0)$ = 440 nm, ε_{max} = 13300 $M^{-1}cm^{-1}$) is assigned to the orbital transition between the **L**-centered π_{HOMO} to π_{LUMO}, by analogy to the assignments for the lowest-energy band of acridone ($\lambda(0,0)$ = 398 nm, ε_{max} = 8870 $M^{-1}cm^{-1}$),[33] H**L** ($\lambda(0,0)$ = 398 nm), and as suggested by the assignments for frontier orbitals provided by the DFT calculation (Figure 5.9). Unlike **CuL**, this transition for **KCryptL** is weakly solvatochromic with small differences in λ_{abs} observed ranging from 458 nm in acetonitrile to 467 nm in THF (Table 5.5, Figures 5.15 and 5.16). This trend does not follow solvent polarity and may be due to charge pairing effects of the anion. The higher-energy prominent band (**KCryptL**: λ = 360 nm, ε_{max} = 13400 $M^{-1}cm^{-1}$; **CuL**: λ = 335 nm, ε_{max} = 18500 $M^{-1}cm^{-1}$; THF) is assigned to another acridone-centered transition since this transition is also observed in **KCryptL**. The corresponding band for free acridone is hypothesized to lie at much higher energy (λ = 255 nm).[33]

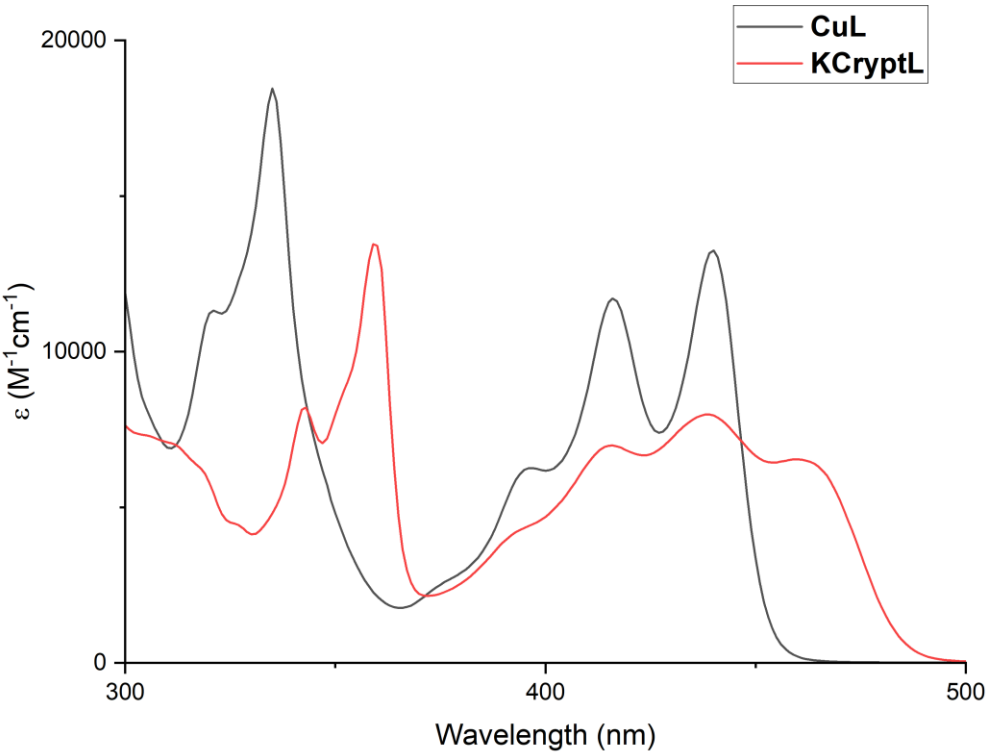

Figure 5.14. Electronic absorption spectrum of **CuL** and **KCryptL** in THF.

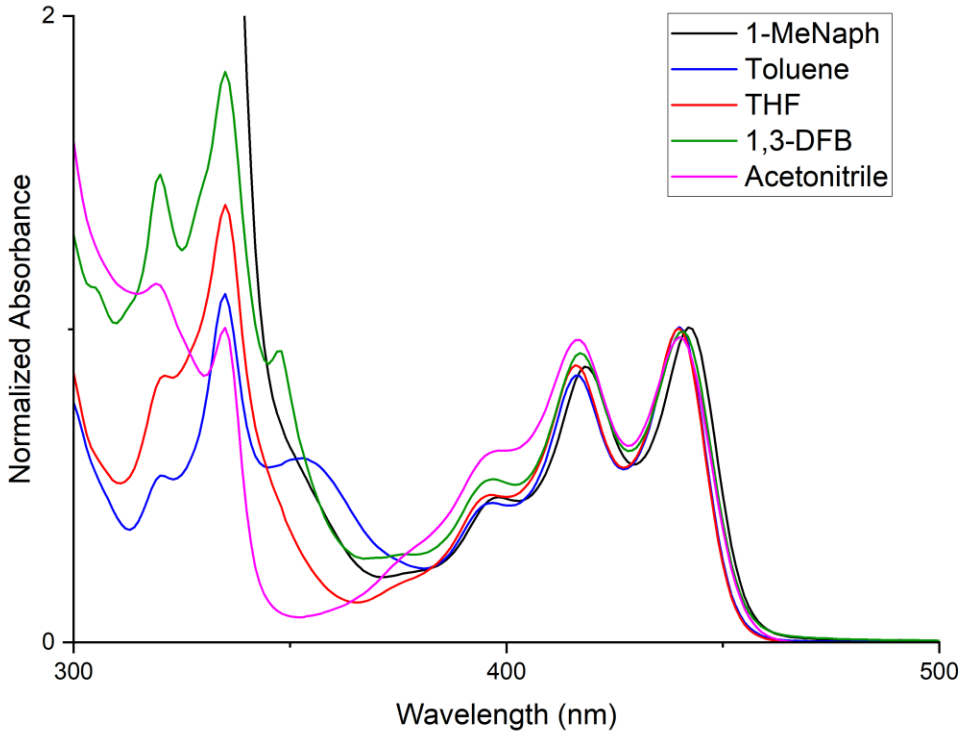

Figure 5.15. Electronic absorption spectra of **CuL** in various solvents.

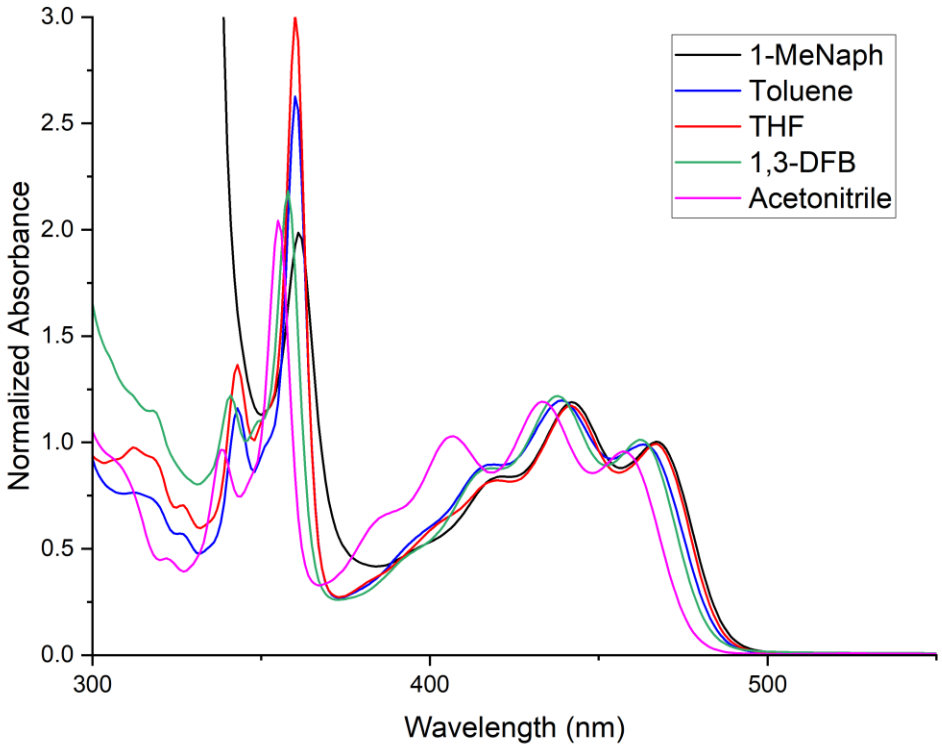

Figure 5.16. Electronic absorption spectra of **KCryptL** collected in various solvents.

The vibronic structure exhibited by the lowest-energy band is compound dependent. Whereas the bands for **CuL** and H**L**, have similar vibronic profiles with maximum intensity at the 0-0 band (Figure 5.17), the band for **KCryptL** exhibits broader vibronic features and maximizes at the 0–1 vibronic transition. The vibronic frequency (measured between the 0–0 and 0–1 features) is also substantially smaller for **KCryptL** (1262 cm^{-1} in THF) than for **CuL** (1311 cm^{-1}) and H**L** (1302 cm^{-1}). Integration of the intensity under the entire first vibronically structured band gives similar values for both **KCryptL** and **CuL**. As both transitions are expected to display similar oscillator strength due to originating from the same transition, this suggests that the excited-state distortion for **KCryptL** is larger than that for **CuL** and H**L**.

Table 5.5. Photophysical Data for **CuL**, **KCryptL,** and H**L.**

	KCryptL					**CuL**					H**L**
Solvent	1-MN	Tol.	1,3-DFB	THF	MeCN	1-MN	Tol.	1,3-DFB	THF	MeCN	THF
$\lambda_{abs}(0,0)$ (nm)	467	465	462	467	458	442	440	441	440	440	402
$\lambda_{abs}(0,1)$ (nm)	442	440	437	441	433	418	416	417	416	416	382
$\lambda_{abs}(0,2)$ (nm)	418	416	416	418	406	397	395	396	394	395	363
$\lambda_{abs}(0,3)$ (nm)	397	395	394	396	385	376	374	374	376	376	346
$\bar{\nu}_{abs}$ (cm^{-1})	1211	1222	1238	1262	1261	1299	1311	1305	1311	1311	1302
$\lambda_{em}(0,0)$ (nm)	484	480	480	483	475	450	448	450	448	449	410
$\lambda_{em}(0,1)$ (nm)	516	511	511	515	506	478	475	478	475	478	432
$\lambda_{em}(0,2)$ (nm)	553	552	548	553	541	512	509	510	508	510	463
$\lambda_{em}(0,3)$ (nm)	601	600	591	599	588	549	544	549	546	549	499
$\bar{\nu}_{em}$ (cm^{-1})	1281	1264	1264	1286	1290	1302	1269	1301	1302	1351	1242
Stokes Shift (cm^{-1})	752	672	812	709	781	402	406	454	406	456	485

1-MN = 1-methylnaphthalene, 1,3-DFB = 1,3-difluorobenzene, THF = tetrahydrofuran

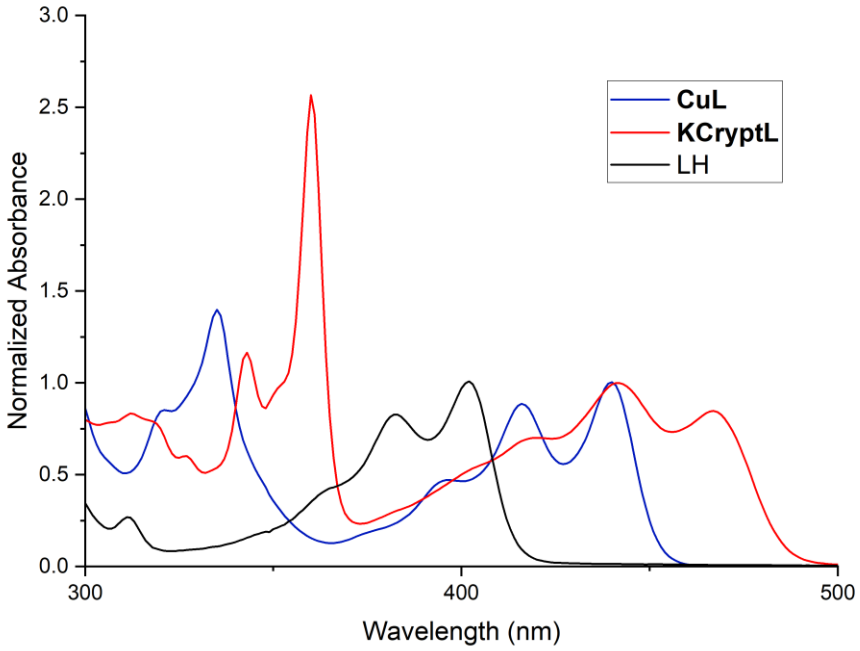

Figure 5.17. Electronic absorption spectra of **CuL**, **KCryptL**, and H**L** in THF.

Both **CuL** and **KCryptL** display markedly lower-energy **L**-centered π_{HOMO} to π_{LUMO} transitions compared to H**L** (Figure 5.24). This is attributed to buildup of negative charge at the nitrogen by deprotonation leading to an increase in the HOMO energy of the molecule. By electrochemistry, the HOMO energy is strongly destabilized going from H**L** to **CuL** to **KCryptL** while the LUMO remains relatively unperturbed. This raising of the HOMO energy while maintaining similar LUMO energies contracts the overall HOMO-LUMO energy gap and leads to the observed decrease in the π_{HOMO} to π_{LUMO} transition energy for **CuL** and **KCryptL**. Coordination to copper provides greater stabilization of the anionic charge on acridone in **CuL** and consequently lowers the HOMO energy and the corresponding π_{HOMO} to π_{LUMO} transition energy to an intermediate value.

In addition to the two low energy bands of **KCryptL** and **CuL**, the spectrum of **CuL** shows a third, broad band centered at λ = 354 nm in toluene (Figure 5.15). This feature is

solvatochromic, blue shifting as the solvent is changed from toluene to 1,3-DFB to THF to acetonitrile, at which point it is obscured by the higher intensity band at λ = 335 nm. This band is assigned to the **L** $\pi_{HOMO} \rightarrow$ IPr π_{LUMO} LLCT transition due to its high intensity ($\varepsilon_{max} \approx 5000$ $M^{-1}cm^{-1}$) comparable to other CMA complex LLCT transitions and its strong solvatochromic behavior. The energy of this transition is much higher compared to the LLCT transitions observed for emissive (NHC)Cu(Cz) complexes containing a π-acidic carbene such as a cyclic alkyl amino carbene(CAAC) or a monoamido-aminocarbene (MAC), which lie between 400 nm to 550 nm,[16, 21, 32] consistent with the stronger π-acidity of CAAC and MAC carbenes than IPr.

The electronic absorption spectrum of **KCryptL** can be compared with that reported for samples containing deprotonated acridone in which the chromophore is produced *in situ* through reaction of acridone with excess base.[13] The spectrum reported for a sample containing acridone and 20 equivalents of tetramethylguanidine in DMSO[13] exhibits bands at ~460 nm and ~360 nm matching observed bands for **KCryptL**, but also contains features attributable to free acridone, as evidenced by the strong absorption of the 0-0 band of free acridone at ~390 nm, indicating that a sizable portion of acridone remains protonated. Electronic spectra have not been reported for photocatalytically relevant reaction mixtures containing deprotonated acridone and excess Cs_2CO_3, so these conditions were replicated in order to acquire the spectra. The UV-vis spectrum of a mixture of H**L** and excess Cs_2CO_3 in DMSO under nitrogen is essentially identical to that of isolated **KCryptL** (Figure 5.18); no bands due to H**L** are observed. Bubbling air through this solution for 1 min leads to minimal changes in the UV-Vis spectrum (Figure 5.19), indicating that $\mathbf{L}^-$ can be stabilized in air by the presence of excess Cs_2CO_3. Removal of Cs_2CO_3 from the sample by filtration resulted in a decrease in the intensity of the $\mathbf{L}^-$ band at 462 nm and appearance and growth of the band of free acridone at 404 nm within one minute of filtration.

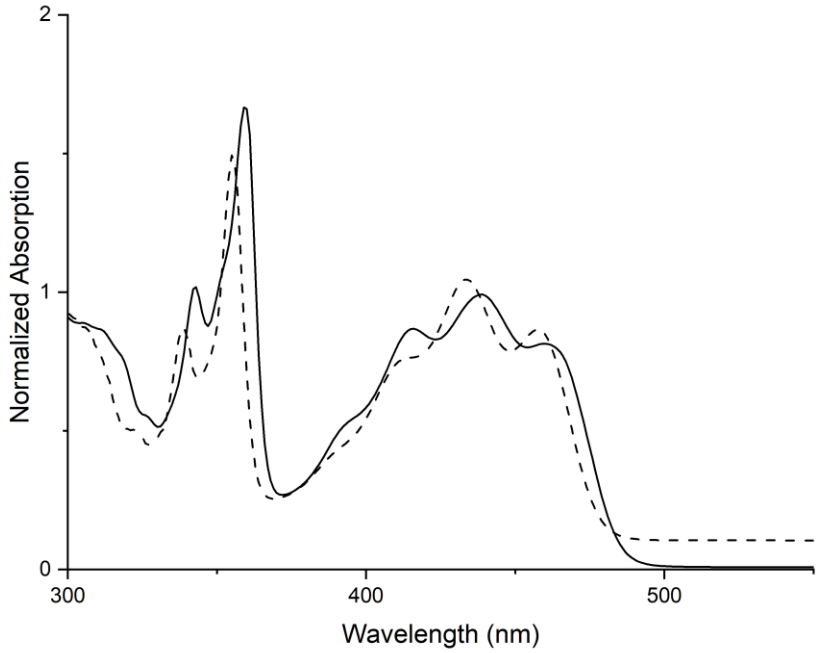

Figure 5.18. Electronic absorption spectra of *in-situ* generated $\mathbf{L}^-$ in DMSO with Cs_2CO_3 (dashed) and **KCryptL** in THF (solid).

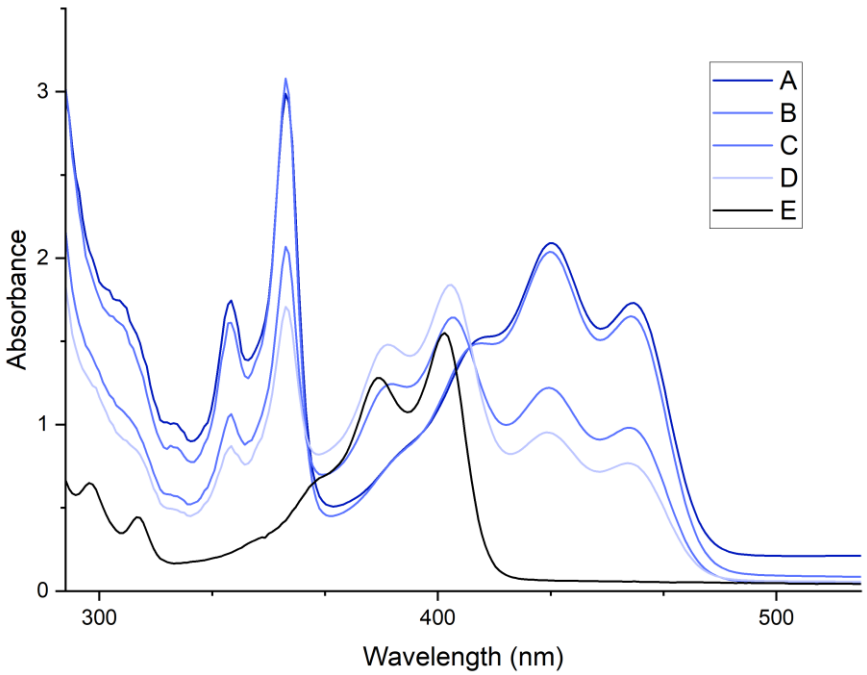

Figure 5.19. Electronic-absorption spectra H**L** in DMSO after A) addition of 30 eq. of Cs_2CO_3 B) 60 s bubbling ambient air, C) filtration of solid Cs_2CO_3 and D) additional 60 s bubbling ambient air. E) H**L**.

5.2.5 Photoluminescence and Photophysics.

Both **KCryptL** and **CuL** exhibit bright visible photoluminescence under ambient light. The emission spectra of **KCryptL** ($\lambda_{em}(0,0)$ = 467 nm) and **CuL** ($\lambda_{em}(0,0)$ = 448 nm) in THF (Figure 5.20) display clear vibronic progression assigned as fluorescence from the **L**-centered S_1 state on the basis of the overlap of the absorption and emission 0-0 bands (Figures 5.21-23). Very small Stokes shifts are found for **CuL** with a shift of only 406 cm^{-1} in THF, which is close to that found for H**L** at 485 cm^{-1}. The Stokes shift for **KCryptL** in THF is slightly larger at 709 cm^{-1}. The vibronic profiles of the three bands resemble each other, with the emission bands of **CuL** and H**L** being approximate mirror images of their lowest energy absorption bands. In contrast, the emission band for **KCryptL** is not a mirror image of its lowest-energy absorption band. The frequency observed for the emission progression for **KCryptL** (1286 cm^{-1}) is distinctly higher than found for the absorption band (1262 cm^{-1}), whereas the progression frequencies for **CuL** and H**L** are the same (within experimental error) in their respective spectra (**CuL**: emission 1302 cm^{-1}, absorption 1311 cm^{-1}; H**L**: emission 1295 cm^{-1} absorption 1302 cm^{-1}; Table 5.5). Moreover, the intensity progression for **KCryptL** follows that found for H**L** and **CuL** suggesting that their S_1 geometry is similar. This change in vibronic spacing and intensity progression from ground to excited state in addition to the larger Stokes shift points to **KCryptL** undergoing a larger excited-state structural distortion than H**L** or **CuL** as indicated in the absorption spectra as well. This parallels the observation from the ground-state structures that deprotonation results in distortions near the nitrogen atom.

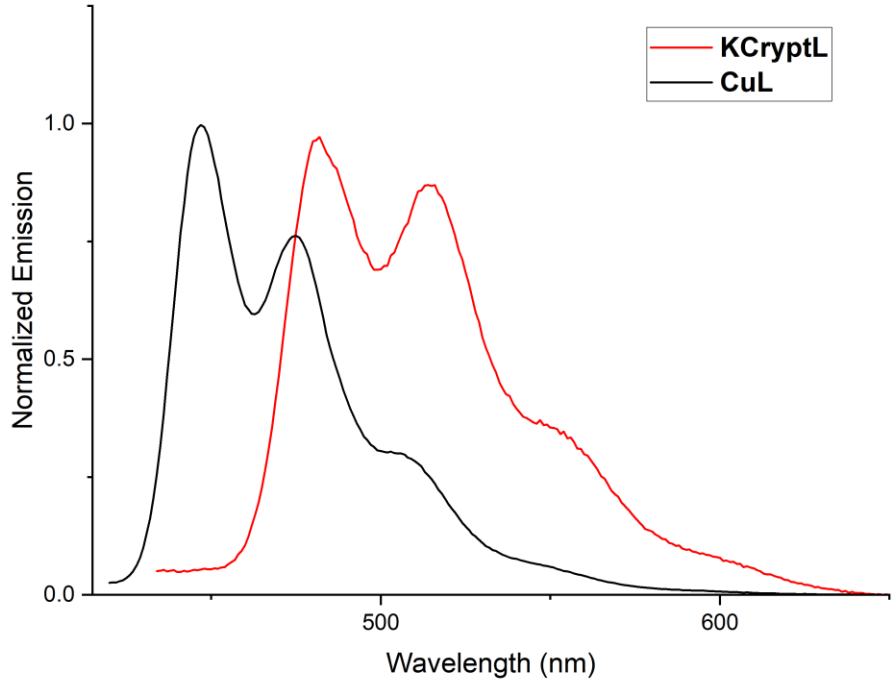

Figure 5.20. Normalized emission spectra of **KCryptL** and **CuL** in THF collected under N_2.

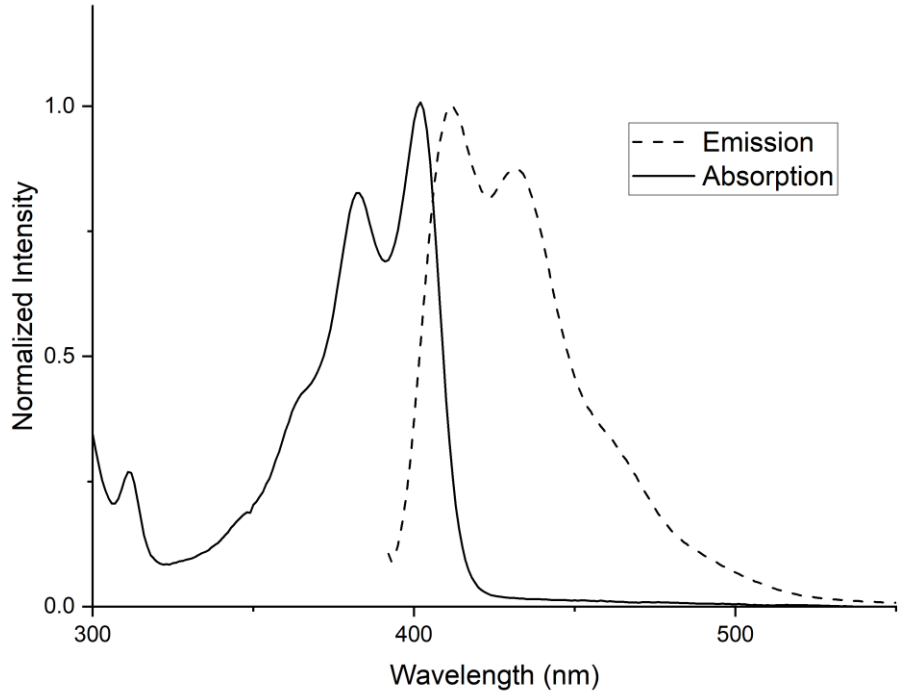

Figure 5.21. Electronic-absorption and emission spectra of H**L** in THF.

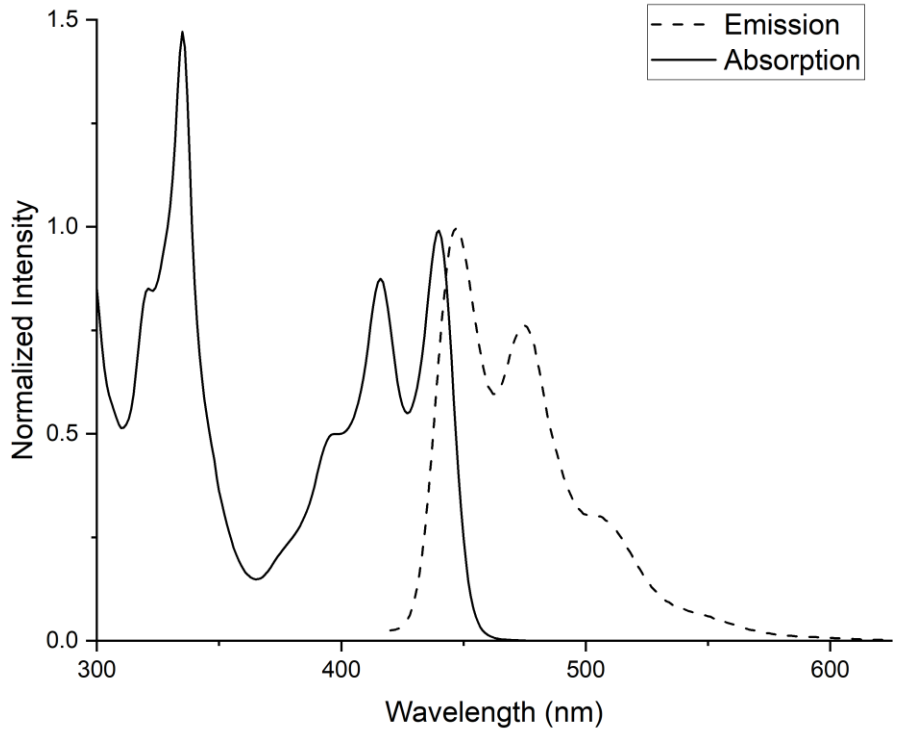

Figure 5.22. Normalized electronic-absorption and emission spectra of **CuL** in THF.

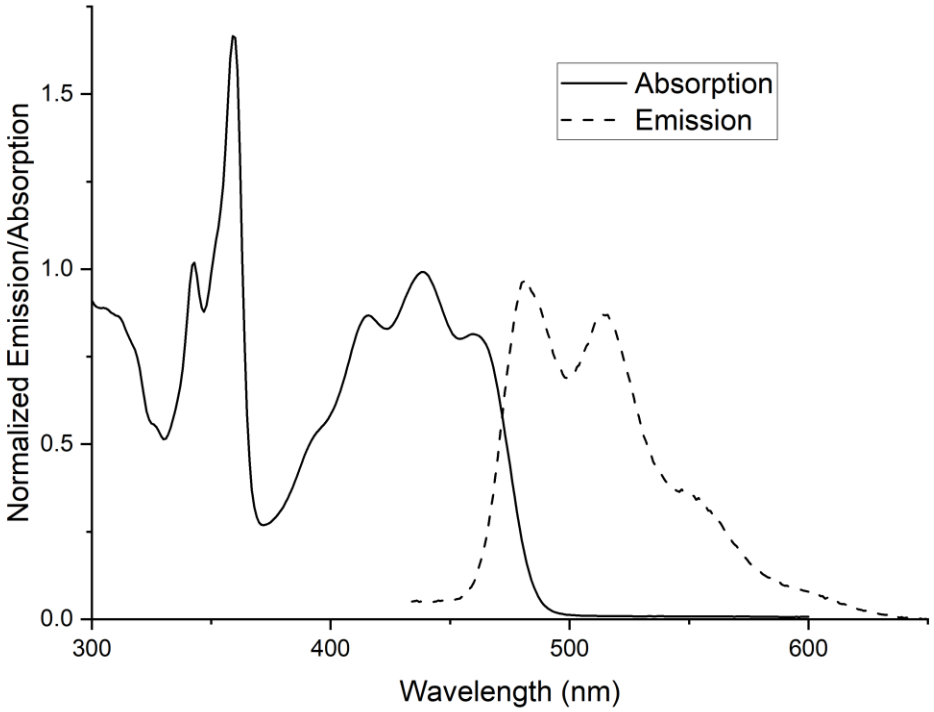

Figure 5.23. Normalized electronic-absorption and emission spectra of **KCryptL** in THF.

The photoluminescence lifetimes for **KCryptL** and **CuL** are on the *ca.*10 ns time scale, consistent with fluorescence from the acridone-localized S_1 $^1(\pi,\pi^*)$ state conforming to single-exponential decay (Figures 5.32-40). Luminescence decay following excitation provides fluorescence lifetimes (in THF) of 27.2 ns for **KCryptL** and 13.7 ns for CuL (Table 5.5). The excited-state lifetime found for **KCryptL** is close to that of the previously reported *in-situ* generated deprotonated acridone in DMSO (18.47 ns).[13] Consistent with the visibly bright luminescence for these compounds, the fluorescence quantum yields approach unity in THF (Φ **KCryptL** = 0.97, Φ **CuL** = 0.95). From this, radiative and nonradiative decay rates can be calculated in various solvents. In THF, **KCryptL** displays a fast radiative rate of $k_r = 3.6 \times 10^7\ s^{-1}$ and $k_{nr} = 1.1 \times 10^6\ s^{-1}$ while **CuL** displays even faster radiative rates with $k_r = 6.3 \times 10^7\ s^{-1}$ and $k_{nr} = 3.3 \times 10^6\ s^{-1}$ in the same solvent. The difference in radiative rates between **KCryptL** and **CuL** in THF can be attributed to a Strickler-Berg-like relationship between the larger extinction coefficient of the 0−0 bands for **CuL** (ε_{max} = 13300 $M^{-1}cm^{-1}$) and **KCryptL** (ε_{max} = 6500 $M^{-1}cm^{-1}$).

Photophysical data were measured in various solvents to gain further insight into the emission for these complexes. **CuL** shows effectively no solvatochromism with $\lambda_{em}(0,0)$ differing by only 2 nm from 448 nm in toluene to 450 nm in 1,3-difluorobenzene (Figure 5.24). The emission maximum for **KCryptL**, on the other hand, is weakly solvatochromic ranging from to $\lambda_{em}(0,0)$ = 484 nm in 1-methylnaphthalene to $\lambda_{em}(0,0)$ = 475 nm in acetonitrile (Table 5.5 and Figure 5.25)). Similarly small shifts were found for the absorption spectra with **KCryptL**. The measured lifetimes for these complexes are strongly solvent dependent, with the longer lifetimes found for more polar solvents (Table 5.6). This could be due to stabilization of

the charge-transfer-like nature of the acridone intraligand S_1 $^1(\pi,\pi^*)$ excited-state. For both complexes, the longest lifetimes were measured in acetonitrile with τ = 28.0 ns for **KCryptL** and τ = 15.8 ns for **CuL**. Longer lifetimes for **KCryptL** may also be due to greater structural relaxation in the excited-state compared to **CuL** as inferred by differences the Franck-Condon vibronic progression and Stokes shift. The shortest lifetimes were measured in 1-methylnaphthalene with τ = 15.0 ns for **KCryptL** and τ = 7.2 ns for **CuL**. These fluorescence lifetimes are slightly longer than those previously found for the parent acridone in acetonitrile (τ = 5.5 ns).[25]

Table 5.6 Additional Photophysical Data for **CuL**, **KCryptL**.

	KCryptL					**CuL**				
	1-MN	Tol.	1,3-DFB	THF	MeCN	1-MN	Tol.	1,3-DFB	THF	MeCN
τ (ns)	15.0	20.6	20.2	27.2	28.0	7.2	11.8	13.7	15.2	15.8
ϕ	0.55	0.74	0.26	0.97	0.96	0.54	>0.99	0.94	0.95	0.95
k_r (10^7 s^{-1})	3.7	3.6	1.3	3.6	3.4	7.5	8.4	6.9	6.3	6.0
k_{nr} (10^7 s^{-1})	3.0	1.3	3.7	0.11	0.14	6.4	<0.085	0.44	0.33	0.32

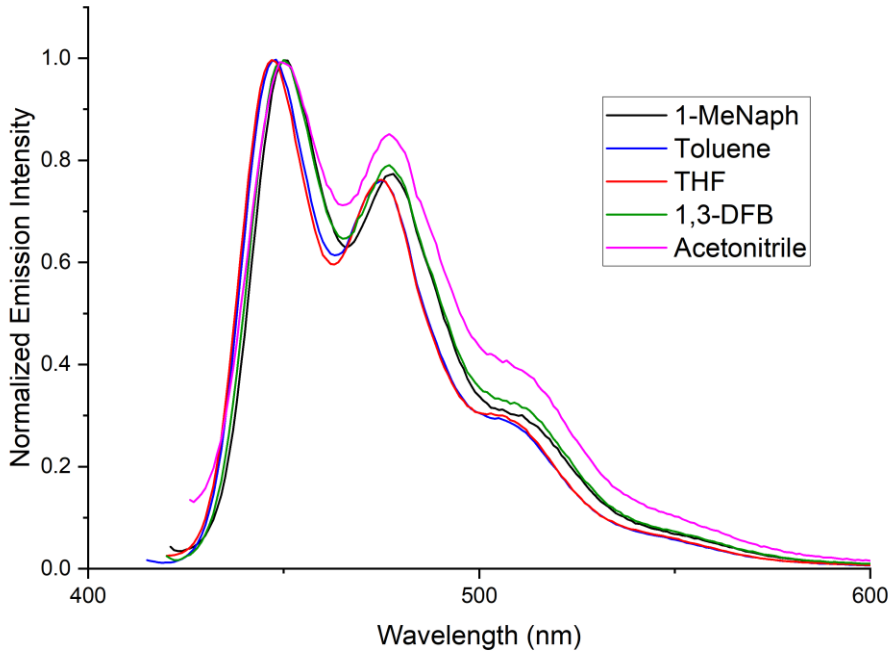

Figure 5.24. Emission spectra of **CuL** in various solvents. Spectrum in acetonitrile cut off due to H**L** emission from decomposition.

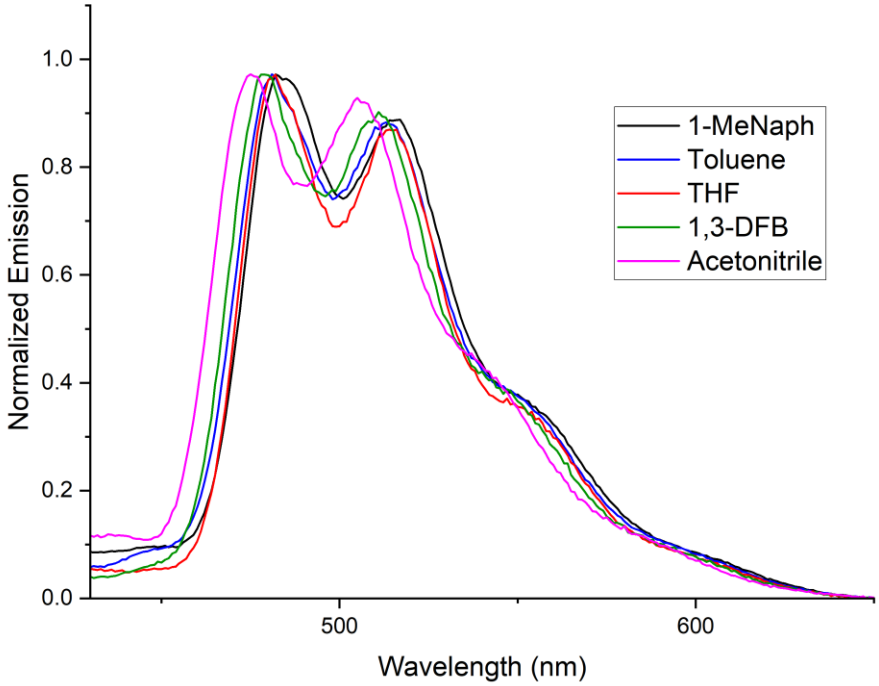

Figure 5.25. Emission spectra of **KCryptL** in various solvents.

The quantum yields for these complexes are also solvent dependent. While **KCryptL** displays highly variable quantum yield with no discernable trend, quantum yields for **CuL** are >90% in all solvents except for 1-methylnaphthalene (Table 5.6). For both complexes, comparison of the solvent dependent radiative and nonradiative rates show a small decrease in the radiative rates going towards more polar solvents with 1,3-difluorobenzene standing out as an outlier for **KCryptL** ($k_r = 1.3 \times 10^7$). Nonradiative decay rates for **KCryptL** are relatively large in toluene and 1,3-difluorobenzene while corresponding rates for **CuL** remain small. Due to the similarity of their excited-states, this indicates interaction of the **KCryptL** excited-state with other pathways detrimental for emission and photoredox applications. Paired with the difference in solvatochromic behavior and vibronic progression, these data highlight the influence of stabilization of the acridone anion by coordination to a copper carbene center and steric protection by the carbene ligand to reduced excited-state reactivity pathways and maintain photophysical properties closer to that of the parent protonated chromophore.

Acridone is known to display solvent-dependent quantum yield based off the relative energies of the S_1 and T_2 states which dictate relative population of the ultrafast equilibrium established upon photoexcitation.[25] We wished to determine whether this equilibrium was being established for **CuL** and **KCryptL**. Due to the ultrafast nature of this equilibrium, it is not possible to observe the establishment of this equilibrium using nanosecond TCSPC. Instead, various studies have used 1-methylnaphthalene as a triplet-triplet energy transfer (TTET) quencher for aromatic ketones such as benzophenone, xanthone, and acridone due to its low triplet energy of 2.58 eV[35] with energy transfer occurring within picoseconds.[25, 29, 36] The $^1(n,\pi^*)$ transition is formally dipole forbidden and therefore cannot be resolved by conventional

absorption studies. Since this transition is not expected to be significantly perturbed by deprotonation as judged by the DFT calculated energy gaps (**CuL** ΔE = 5.176 eV, **KCryptL** ΔE = 5.351 eV, H**L** ΔE = 5.260 eV), 1-methylnaphthalene should still be a competent quencher if an excited triplet state is being accessed. With the acridone T_2 state measured to be 3.11 eV in acetonitrile,[25] complete quenching of emission for **KCryptL** and **CuL** should occur in neat 1-methylnaphthalene due to rapid TTET to the solvent bath. Instead, both **KCryptL** and **CuL** still show fluorescence in this solvent with a slight increase in nonradiative decay rate to $k_{nr} = 3.0 \times 10^7\ s^{-1}$ and $k_{nr} = 6.4 \times 10^7\ s^{-1}$ respectively, bringing into question whether this energy transfer could be occurring. Similarly high nonradiative decay rates were found in toluene and 1,3-difluorobenzene for **KCryptL** making analysis difficult for this complex. For **CuL**, the nonradiative decay rate increases by an order of magnitude in 1-methylnaphthalene compared to toluene with similar radiative decay rates suggesting a chemical difference between these two solvents despite their similar solvating properties. The predicted excited-state oxidation potential of **CuL** is $E^{*/+}$ = -2.30 V vs. $Fc^{0/+}$ which is well below the reduction potential of naphthalene.[37] Similarly, the predicted excited-state reduction potential for **CuL** is $E^{*/-}$ = -0.25 V vs. $Fc^{0/+}$ which is much too low to oxidize an aromatic molecule ruling out excited-state electron transfer as a possible quenching mechanism. All observed TCSPC decay traces are cleanly fit by a monoexponential function down to the background, precluding emission by delayed fluorescence or other emissive pathways. This suggests that the ultrafast acridone-centered S_1-T_2 equilibrium is not being accessed for these complexes. Further elucidation of any branching excited-state kinetics is beyond the scope of the spectroscopic methods used here and would likely require in-depth ultrafast transient-absorption to explain.

The emission of **CuL** can be compared to the closely related Cu(IPr)(Cz) and Cu(IMes)(Cz) complexes.[18] These complexes display fluorescence from a local excited ^{1}Cz state in solution that broadens and redshifts at higher concentration due to aggregation effects and display dual emission from the ^{1}Cz and ^{3}Cz state in the solid state. No fluorescence quantum yields were given for these complexes in solution, but solid-state measurements of Cu(IPr)(Cz) give 7.9% phosphorescence and 24.6% fluorescence quantum yields with fluorescence lifetimes (τ = 16, 24 ns) and phosphorescence lifetimes (τ = 55 ms) consistent with an organic emitter. Delayed fluorescence was not observed indicating intersystem crossing that is competitive with fluorescence and slow reverse intersystem crossing to repopulate the S_1 state. This is not observed for **CuL** where emission has similar fluorescence lifetimes with very high fluorescence yields but no evidence of any other emitting state or aggregation effects. The absorption for the coordinated carbazole also does not shift upon coordination to the copper carbene or in the LiCz alkali salt.[38] The observed optical shift observed in acridone can therefore be attributed to the presence of the carbonyl group which functions as the acceptor orbital for the lowest energy optical transition. As found by electrochemistry, this LUMO energy level is essentially unchanged upon deprotonation and coordination giving rise to the shift in the lowest energy transition observed by UV-Vis and emission spectra.

These results present **CuL** as a unique transition-metal chromophore that emits pure ligand-centered fluorescence with high quantum yields in fluid solution with coordination sensitive luminescence. These emission quantum yields are comparable to some the best performing CMA complexes including the Cu(CAAC)(L) and Cu(MAC)(L) complexes, which emit which display broad structureless emission at similar wavelengths from LLCT excited-state through a combination of prompt and delayed fluorescence with variable quantum yields up to

>99%.[15-21] These properties suggest that Cu(IPr)(X) may be useful as a general scaffold for stabilizing anionic chromophores while maintaining strongly reducing excited-state oxidation potentials, which can be estimated for **CuL** to be $E^{*/+} = -2.30$ V vs. $Fc^{0/+}$. While deprotonation to form anionic chromophores can serve to both anodically shift excited-state potentials and bathochromically shift their absorption maximum as found for **KCryptL** ($E^{*/+} = -3.06$ V vs. $Fc^{0/+}$), these molecules can suffer from larger excited-state distortions and various excited-state decomposition pathways resulting in lower-than-expected lifetimes and quantum yields. These can be mitigated by coordination to the bulky copper carbene stabilizing the excited-state and improving the photophysical properties of the chromophore to behave more like the parent chromophore. The combination of high quantum yield and rapid fluorescence could be of use in potential OLED applications if challenges associated with stability and redox speciation can be overcome.

5.2.6 Attempted Excited-State DFT Analysis.

To supplement the experimental photophysical data, further computational methods were utilized to give further insight on the excited-state behavior of these molecules. Various methods were utilized to try to reproduce the absorption spectra of both complexes. Simple TDDFT methods using a variety of functionals including range-separated hybrids, double-hybrids, and meta-hybrids all dramatically overestimated the energy for the lowest-lying acridone S_1 state for **CuL**. Attempts using higher levels of theory to account for deficiencies in the TDDFT framework including CASSCF-NEVPT2, and even DLPNO-STEOM-CCSD on truncated models of these complexes still resulted in dramatic overestimation well beyond conventional errors for these methods.[39-40] This prevented further analysis of the relative energies of the low lying excited-states in these complexes and specific comparison of the relative energies of the

acridone S_1 and T_2 states. These methods were also not able to reproduce the spectra of simple unsubstituted acridone. It is not clear why these methods fail. Analyses based off of Kohn-Sham orbital energies estimate that the S_1 (**CuL** ΔE = 3.927 eV, **KCryptL** ΔE = 3.732 eV, H**L** ΔE = 4.224 eV) state is bathochromically shifted by a greater degree than the T_2 state (**CuL** ΔE = 5.176 eV, **KCryptL** ΔE = 5.351 eV, H**L** ΔE = 5.260 eV), but since actual excited-state energies go well beyond a simple orbital energy level analysis, the presence of the S_1-T_2 equilibrium or the exact energy difference between the two excited states cannot be ascertained.

5.3. Conclusions.

We have demonstrated the electrochemical and optical properties of the acridone anion as an isolated salt and as a ligand in a series of CMA complexes. These complexes display very similar geometries for the acridone ligand despite their difference in overall charge and coordination. DFT calculations comparing these complexes show the significant destabilization of the frontier orbital energies upon deprotonation with electrochemical studies confirming that deprotonation significantly destabilizes the HOMO while the LUMO is relatively unperturbed. Similar features are found in the optical absorption and emission spectra, where the S_1 transition is acridone centered and sensitive to deprotonation and coordination to the copper center. Here, **KCryptL** displays the most redshifted absorption and emission maximum followed by **CuL** and H**L**. Lifetimes and quantum yields for the emission show high fluorescence yields with fast radiative rates indicative of acridone-centered emission. Quantum yields and radiative rates are improved upon coordination to copper in **CuL** up to >99% and 8.4 x 10^7 s^{-1} respectively while **KCryptL** shows highly varying quantum yields and radiative rates highlighting the improved photophysical properties upon coordination. Additionally, estimates of $E^{*/+}$ between **CuL**, **KCryptL**, and H**L**, show control of the excited-state oxidation potential established by

coordination suggesting linear copper carbene complexes as a general scaffold for stabilizing highly reducing photoreductants.

5.4 Experimental Section

5.4.1 General Procedures.

All manipulations were performed under a nitrogen atmosphere using standard Schlenk and glovebox techniques, unless otherwise noted. Solvents used for synthesis and electrochemistry were HPLC grade and purified by passing them under nitrogen pressure through an anaerobic, stainless steel system consisting of either two 4.5 in × 24 in (1 gal) columns of activated A2 alumina (CH_3CN, Et_2O, CH_2Cl_2, THF) or one column of activated A2 alumina and one column of activated BASF R3-11 catalyst (toluene, pentane)[41] and stored over activated 4Å molecular sieves. 1,3-Difluorobenzene was dried on a solvent purification system over activated alumina and stored over 4Å molecular sieves under nitrogen. Solvents used for NMR spectroscopy were degassed by freeze-pump-thaw cycles and stored under nitrogen over 4Å molecular sieves. (IPr)Cu(OBu^t) was prepared according to a standard procedure.[30] Ferrocene was recrystallized from absolute ethanol and then sublimed under vacuum. 1-Methylnaphthalene was dried over activated 4Å molecular sieves overnight before being degassed and purified by vacuum distillation and stored under nitrogen over 4Å molecular sieves. All other reagents were procured from commercial sources and used as received. ^{1}H- and ^{13}C{^{1}H}- NMR spectra were collected using a 500 MHz Bruker Avance II+ spectrometer equipped with a ^{1}H{^{19}F, ^{13}C} QNP probe or a 400 MHz Bruker DRX spectrometer equipped with a BBO probe. Chemical shifts were referenced against known solvent resonances.[42] High resolution mass spectra were collected using a Agilent 6224 TOF installed with ESI/APCI in positive ion mode.

5.4.2 Electrochemistry.

Cyclic voltammetry experiments were conducted at room temperature under a nitrogen atmosphere in a glovebox with a Bioanalytical Systems 100 B/W Electrochemical Workstation. A three-electrode configuration was utilized with a Pt-disk working electrode (area approx. 0.2 cm^2), a Pt-disk counter electrode, and a Ag-wire quasi-reference electrode. Ferrocene was added at the conclusion of each experiment as an internal redox-potential reference. Measurements were performed on THF solutions containing roughly 0.001 M analyte and 0.1 M $[NBu^n_4][PF_6]$ as supporting electrolyte.

5.4.3 Electronic Spectroscopic and Photophysical Measurements.

Solution samples for electronic-absorption and fluorescence spectroscopy were prepared in a nitrogen-filled glovebox in sealable, air-tight cuvettes with path lengths of 1 mm and 1 cm, respectively, unless described otherwise. Electronic-absorption spectra were collected using a Cary 300 UV-visible spectrophotometer. Emission spectra were recorded with a wavelength-calibrated Photon Technology International (PTI) Quantmaster fluorimeter equipped with a Peltier-cooled R928 photomultiplier tube (PMT). The emission monochromator was wavelength-calibrated using the emission lines of an Ar lamp with wavelength accuracy < 0.5 nm over the entire detection range. The excitation monochromator was wavelength-calibrated using the calibrated emission monochromator. Emission spectra were collected and individually corrected for instrument response. Relative emission quantum yields were measured using optically dilute samples (absorbance < 0.1 at excitation wavelength and any region that overlapped with the emission spectrum) against an absorbance-matched sample of perylene in cyclohexane (ϕ_{em} = 0.94).[43] Emission lifetimes were measured on a ChronosBH fluorimeter (ISS, Inc.) using time-

correlated single photon counting (TCSPC) methods. The fluorimeter contained Becker-Hickl SPC-130 detection electronics and an HPM-100-40 Hybrid PMT detector. Excitation was provided by a 405 nm picosecond pulsed laser source (Hamamatsu PLP-10). Emission wavelengths for detection were selected with a 550 nm bandpass filter with 40 nm band width. The instrument response function (IRF) was measured to be approximately 0.1 ns by detection of light scattered by a 1% solution of Ludox LS colloidal silica in deionized water. Luminescence decay lifetimes were fit via a using Origin software. Analysis of residual plots indicate all samples exhibit single exponential decay.

5.4.4 Density Functional Theory Calculations.

Calculations were performed using ORCA software package version 4.2[44-45] using the Def2-TZVP basis set for all atoms.[46] Calculations were carried out using the PBE0 hybrid functional,[47] which has been shown to provide accurate geometries for transition metal complexes.[48] No symmetry constraints were applied. The RIJCOSX algorithm[49-50] with DEF2/J[51-52] was used to accelerate the calculation, with GRID4 and GRIDX4 integration grids for all atoms and NOFINALGRID for final SCF energies. The absence of imaginary frequencies confirmed that the calculated geometries were local minima on the calculated potential energy surface. Kohn-Sham orbitals were visualized using Avogadro 1.2.0.[53]

5.4.5 Single-Crystal X-Ray Diffraction Measurements.

Diffraction data were measured at 100 K on a Bruker D8 VENTURE diffractometer equipped with a microfocus Mo-target X-ray tube (λ = 0.71073 Å) and PHOTON 100 CMOS detector. Data were collected using ω scans to survey a sphere of reciprocal space. Data reduction and integration were performed with the Bruker APEX3 software package (Bruker

AXS, version 2017.3-0, 2018). Data were scaled and corrected for absorption effects using the multi-scan procedure as implemented in SADABS (Bruker AXS, version 2014/5).[54] The structure was solved by SHELXT (Version 2018/2)[55] and refined by a full-matrix least-squares procedure using OLEX2[56] (XL refinement program version 2018/3).[55] All atoms were refined with anisotropic thermal parameters. Hydrogen atoms were included in idealized positions for structure factor calculations**.**

5.4.6 Synthesis and Characterization of Compounds

5.4.6.1 Synthesis of [KCrypt-222][Me$_2$Acr] (KCryptL). To a stirred, yellow suspension of 2,7-dimethylacridone (HAcrMe$_2$, H**L**; 0.100 g, 0.447 mmol) in THF (10 mL) at room temperature was added K[N(SiMe$_3$)$_2$] (0.088 g, 0.447 mmol), resulting in immediate dissolution of the solid to produce an orange-yellow solution with bright green fluorescence at the solvent meniscus. After 30 min, cryptand-222 (0.168 g, 0.447 mmol) was added and the reaction mixture was stirred for 1 h. The reaction mixture was filtered through a Celite pad on a fritted glass filter to remove a trace amount of unreacted H**L** and the volatile components were removed from the filtrate under vacuum, leaving a bright yellow powder. The powder was suspended in 4 mL toluene to remove any remaining K[N(SiMe$_3$)$_2$] and cryptand-222; 10 mL of diethyl ether was then added, and the mixture was cooled to –30 ˚C overnight to induce precipitation of the product. The powder was collected by filtration and washed with diethyl ether (3 × 5 mL) and dried under vacuum (0.211 g, 74% yield). Bright-yellow crystals of **KCryptL** suitable for single-crystal X-ray diffraction experiments were grown by slow vapor diffusion of pentane into a THF solution of the compound at –30 ˚C. The complex is air and moisture sensitive. ^{1}H NMR (400 MHz, CD_3CN; Figure 5.26): δ 8.04 (s, 2H, **L** 1-H), 7.44 (d, *J* = 8.6 Hz, 2H, **L** 4-H), 7.21 (dd, *J* = 8.6 and 2.3 Hz, 2H, **L** 3-H), 3.54 (s, 12H, crypt OCH$_2$CH$_2$O),

3.50 (m, 12H, crypt NC$\underline{H}_2$), 2.50 (m, 12H, crypt NCH$_2$C$\underline{H}_2$), 2.40 (s, 6H, **L** C$\underline{H}_3$). ^{13}C NMR (101 MHz, CD_3CN; Figure 5.27): δ 175.7 (**L** $\underline{C}$O), 150.3 (**L** $\underline{C}$CO), 131.9 (**L**), 127.2 (**L**), 126.5 (**L**), 125.4 (**L**), 122.9 (**L**), 71.2 (crypt O$\underline{C}H_2\underline{C}H_2$O), 68.4 (crypt NCH$_2\underline{C}H_2$), 54.7 (crypt N$\underline{C}H_2$), 21.4 (**L** $\underline{C}H_3$). HR-MS (THF, 70 V, *m*/*z*): 637.3172 (Calc. 637.3129).

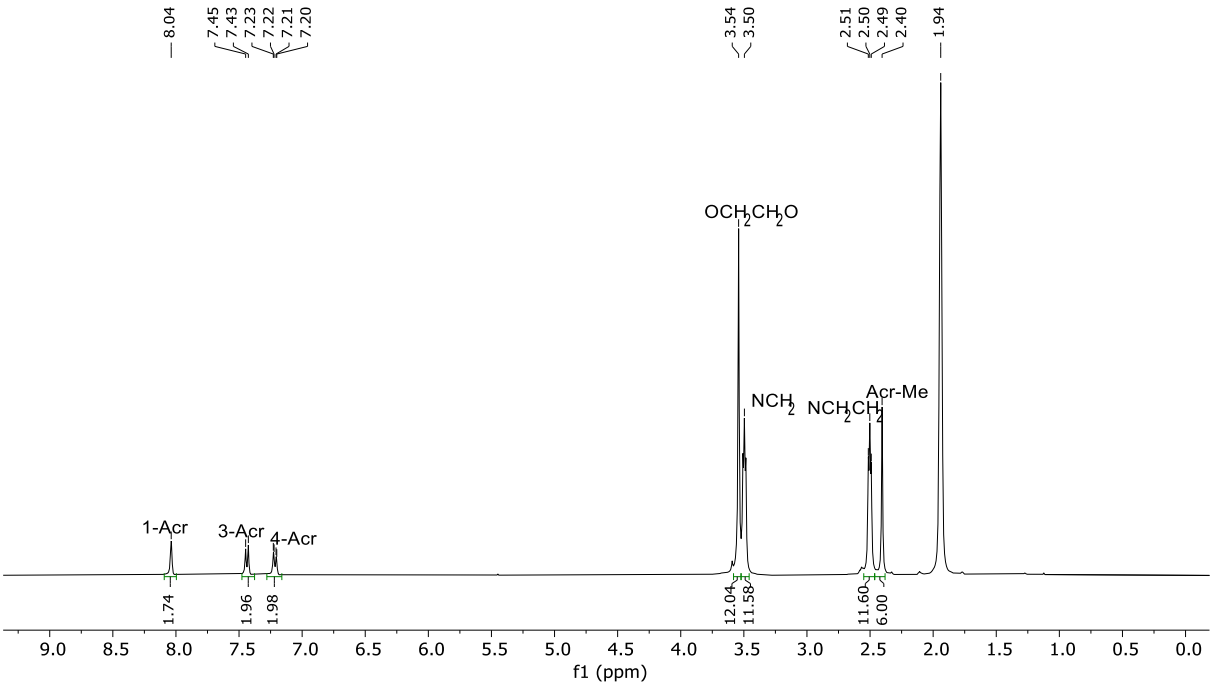

Figure 5.26. ^{1}H NMR spectrum (400 MHz) of **KCryptL** in CD_3CN (δ 1.94).

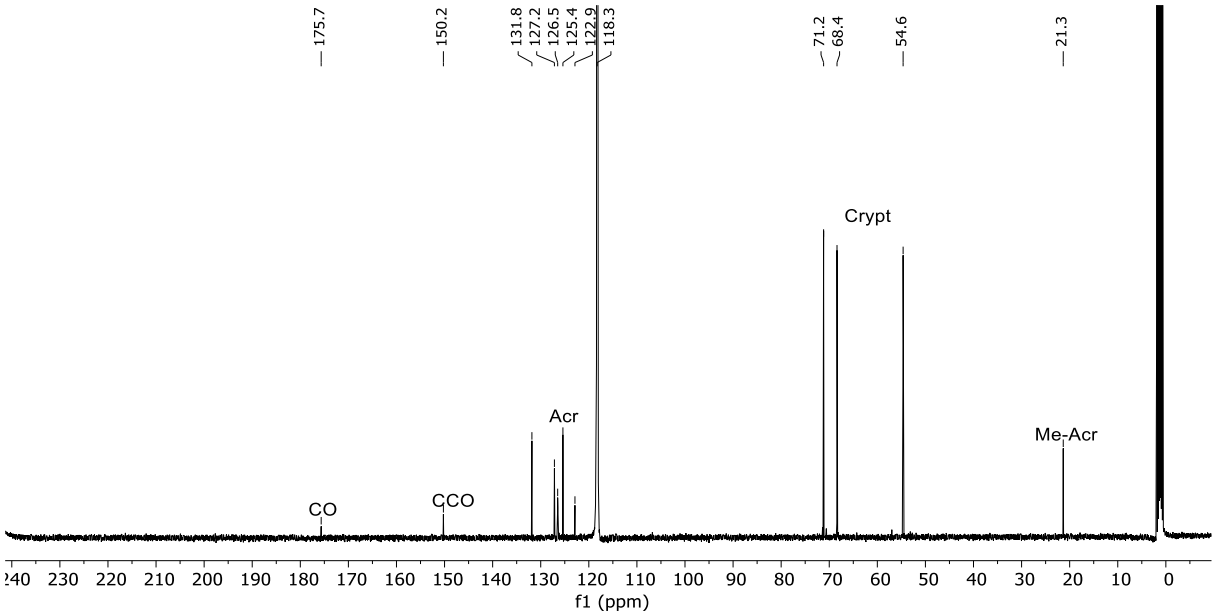

Figure 5.27. $^{13}C\{^{1}H\}$ NMR spectrum (101 MHz) of **KCryptL** in CD_3CN (δ 1.3, 118.3).

5.4.6.2 Synthesis of (IPr)CuL (CuL). To a stirred, colorless solution of (IPr)Cu(OBu^t) (0.352 g, 0.671 mmol, 1.5 equiv) in 1,3-difluorobenzene (8 mL) at room temperature was added solid 2,7-dimethylacridone (HAcrMe$_2$, H**L**, 0.100 g, 0.447 mmol), producing a suspension of yellow H**L** and resulting in an immediate color change of the solution to bright yellow. Bright, sky-blue fluorescence was observed concomitantly at the solvent meniscus. The reaction mixture was stirred for 2 h, after which some suspended yellow solid was still present. The solution was then heated to 80 ˚C with stirring for 1 h, resulting in complete dissolution of the precipitate. The reaction mixture was then cooled to –30 ˚C overnight, which induced crystallization of the product as bright yellow needles. The crystals were collected by filtration, washed with diethyl ether (3 × 5 mL), and dried under vacuum (0.181 g, 60% yield). Crystals of **CuL**•Et$_2$O with suitable for single-crystal X-ray diffraction experiments were grown by slow diffusion of diethyl ether vapor into a THF solution of the compound at –30 ˚C. The complex is air and moisture

sensitive, as evidenced by the appearance of signals due to H**L** in ^{1}H-NMR spectra of samples not handled under inert atmosphere. ^{1}H NMR (500 MHz, CD_3CN; Figure 5.28): δ 7.89 (d, *J* = 2.1 Hz, 2H, **L** 1-H), 7.77 (t, *J* = 7.8 Hz, 2H, IPr *p*-Ph), 7.64 (s, 2H, IPr Im-H), 7.54 (d, *J* = 7.8 Hz, 4H, IPr *m*-Ph), 6.83 (dd, *J* = 8.6, 2.3 Hz, 2H, **L** 3-H), 6.15 (d, *J* = 8.5 Hz, 2H, **L** 4-H), 2.69 (sep, *J* = 6.9 Hz, 4H, IPr $CH_3C\underline{H}CH_3$), 2.32 (s, 6H, **L** $C\underline{H}_3$), 1.28 (d, *J* = 6.9 Hz, 12H, IPr $C\underline{H}_3CHC\underline{H}_3$), 1.19 (d, *J* = 6.9 Hz, 12H, IPr $C\underline{H}_3CHC\underline{H}_3$). ^{13}C{^{1}H} NMR (126 MHz, C_6D_6; Figure 5.29) δ 180.5 (IPr N$\underline{C}$N), 176.9 (**L** $\underline{C}$O), 149.5 (**L** $\underline{C}$CO), 147.4 (IPr Im), 135.7, 133.5, 131.9, 128.7, 125.7, 125.4, 125.0, 124.3, 122.8, 29.7 (IPr $CH_3\underline{C}HCH_3$), 24.9 (IPr $\underline{C}H_3CH\underline{C}H_3$), 24.1 (IPr $\underline{C}H_3CH\underline{C}H_3$), 20.9 (**L** $\underline{C}H_3$). HR-MS (THF, 0 V, *m*/*z*): 675.3250 (Calc. 675.3233).

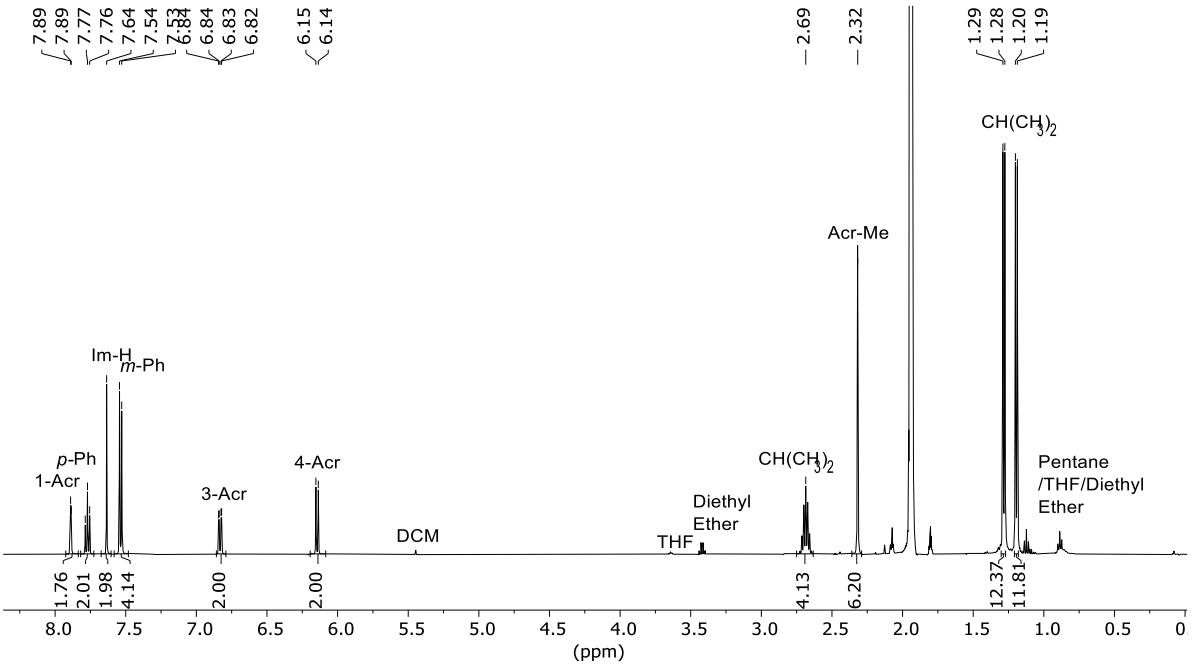

Figure 5.28. ^{1}H NMR spectrum (500 MHz) of **CuL** in CD_3CN (δ 1.94).

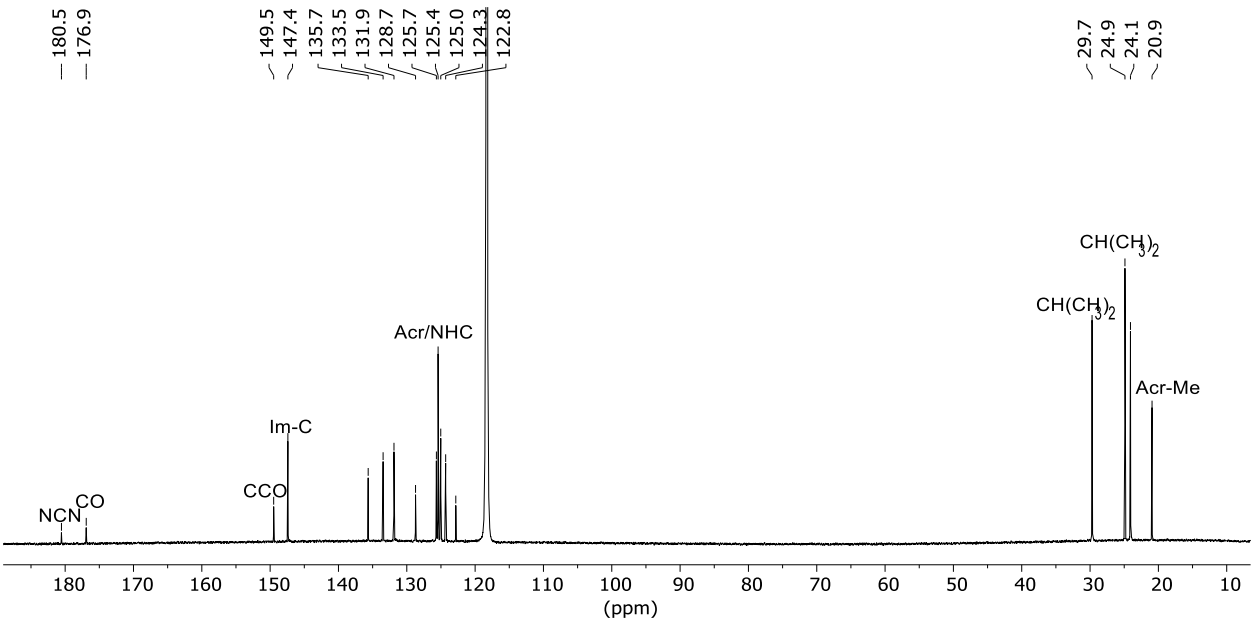

Figure 5.29. $^{13}C\{^{1}H\}$ NMR spectrum (126 MHz) of **CuL** in C_6D_6 (δ 128.1).

5.4.6.3 Generalized Attempted Synthesis of other (NHC)M(acr) Derivatives. To a stirred colorless solution of (NHC)M(Cl) (1 equiv) in THF (20 ml) was added acridone (1 equiv) producing a suspension of yellow acridone. This was followed by addition of $K[N(SiMe_3)_2]$ (1.05 equiv) upon which the color of the solution slowly changed from colorless to bright yellow with bright blue fluorescence observed at the solvent meniscus. The reaction mixture was stirred for 2 h, during which the acridone dissolved and some of the (NHC)M(Acr) precipitated as a yellow solid. After this, the solution was filtered through a sintered glass frit to remove KCl and washed with additional solvent (acetone, acetonitrile, THF, or 1,3-DFB) until the washings ran clear. The volatile components were removed from the filtrate under vacuum, leaving a yellow powder which was then suspended in solvent (acetone, acetonitrile, THF, or 1,3-DFB; 5 to 10 mL) and stirred to redissolve the powder. The solution was then either cooled to –30 ˚C overnight or layered with Et_2O (20 mL) and cooled to –30 ˚C overnight, which induced crystallization of the product. The crystals were collected by filtration, washed with diethyl ether,

and dried under vacuum to give the final products which were determined to be impure by ^{1}H NMR spectroscopy. Crystals suitable for single-crystal X-ray diffraction experiments were grown by either slow diffusion of diethyl ether vapor into a solution of the product at –30 ˚C, or by slow cooling of a concentrated solution of the impure product from room temperature to –30 ˚C.

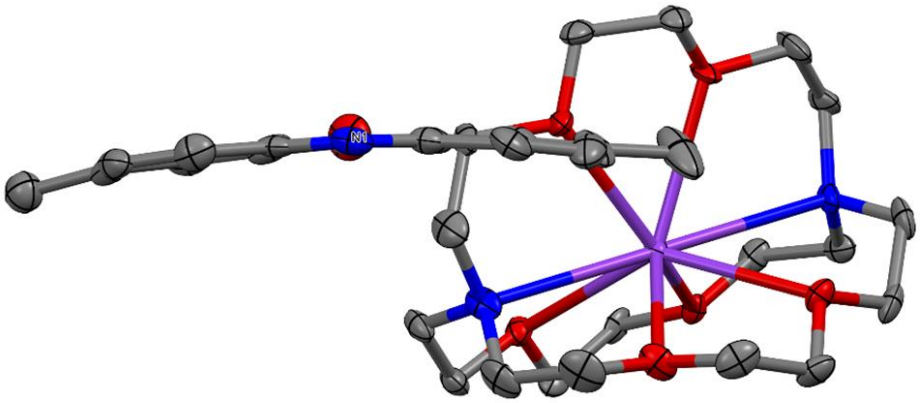

Figure 5.30. Thermal-ellipsoid representation of **KCryptL** (50% probability ellipsoids) showing curvature of the $\mathbf{L}^{-}$ ion.

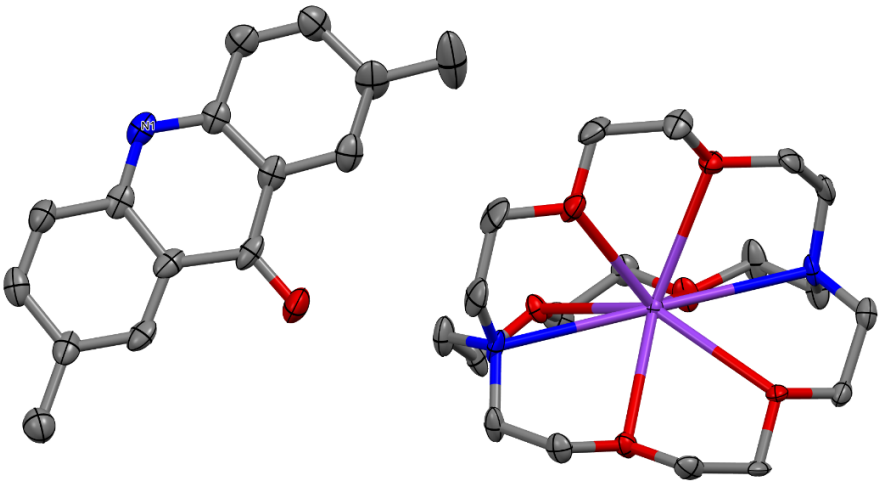

Figure 5.31. Thermal-ellipsoid representation of **KCryptL** (50% probability ellipsoids) showing acridone face.

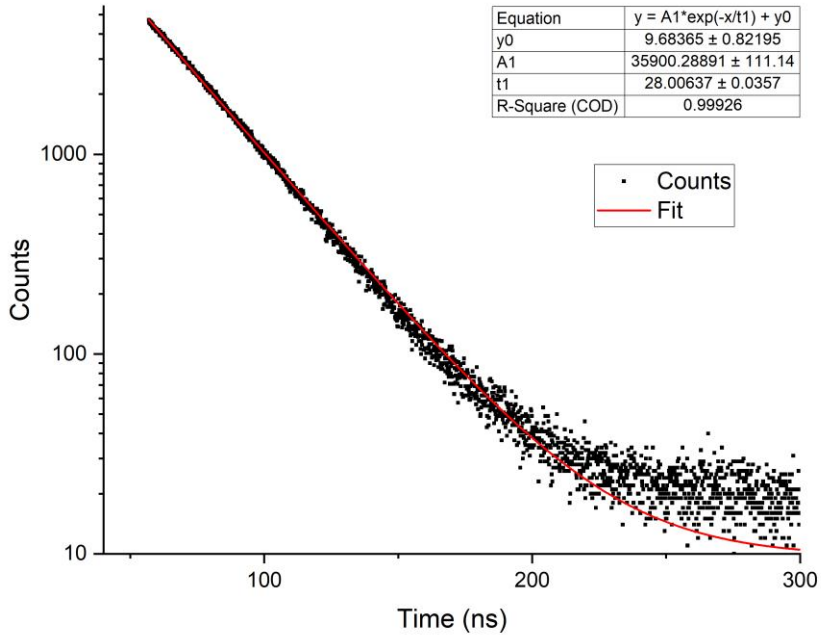

Figure 5.32. TCSPC trace of **KCryptL** in MeCN collected using 405 nm excitation and 550 nm bandpass filter with 40 nm band width.

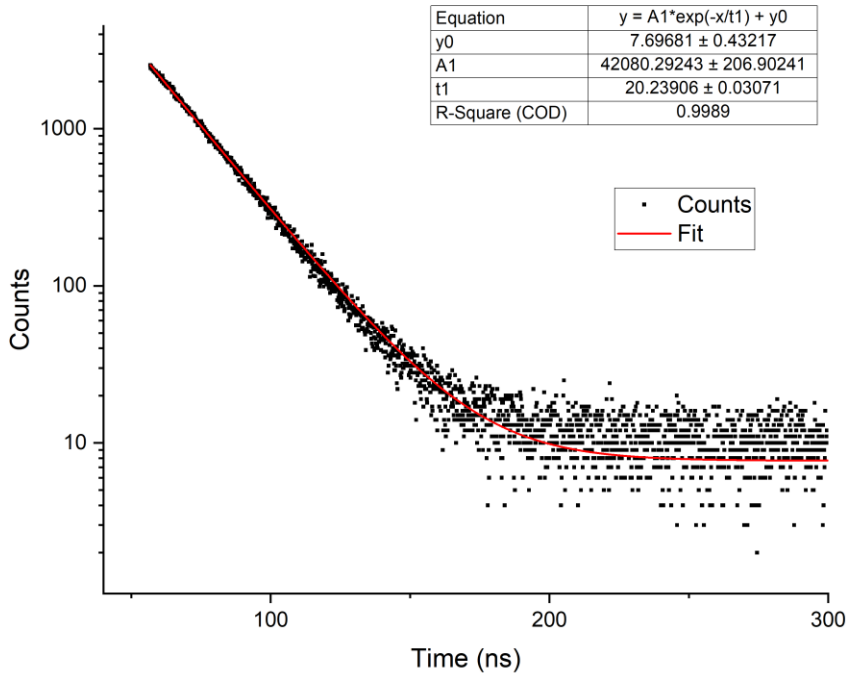

Figure 5.33. TCSPC trace of **KCryptL** in 1,3-DFB collected using 405 nm excitation and 550 nm bandpass filter with 40 nm band width.

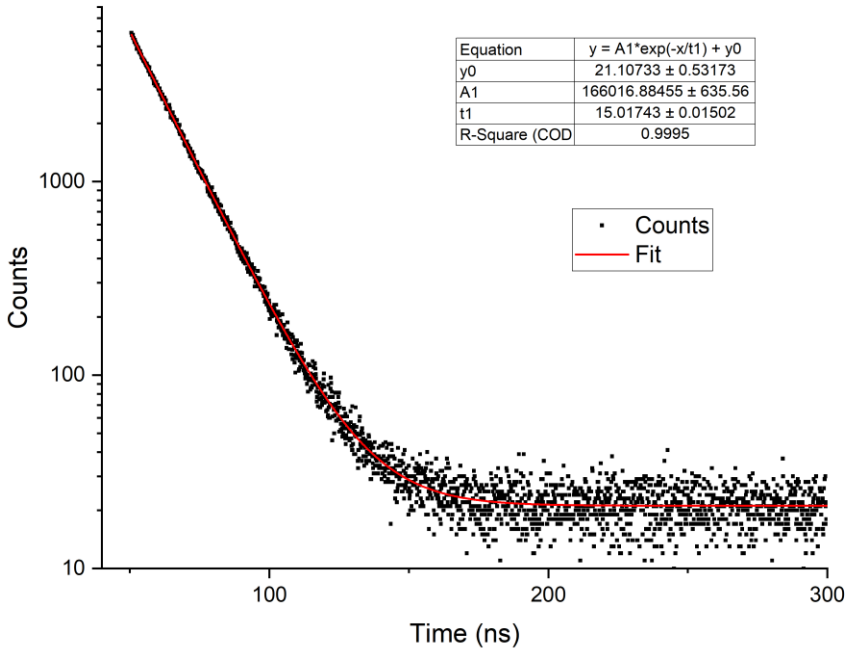

Figure 5.34. TCSPC trace of **KCryptL** in 1-methylnaphthalene collected using 405 nm excitation and 550 nm bandpass filter with 40 nm band width.

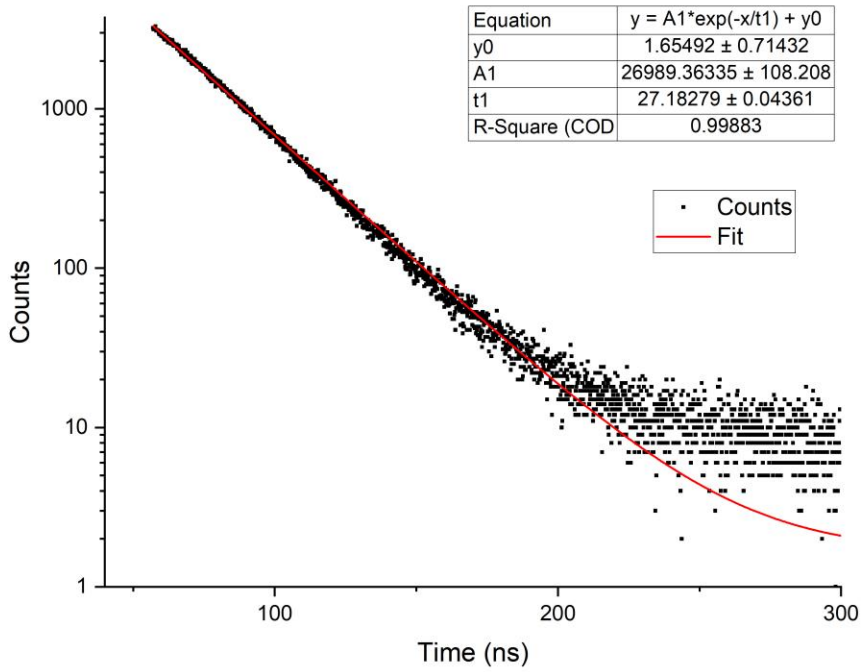

Figure 5.35. TCSPC trace of **KCryptL** in THF collected using 405 nm excitation and 550 nm bandpass filter with 40 nm band width.

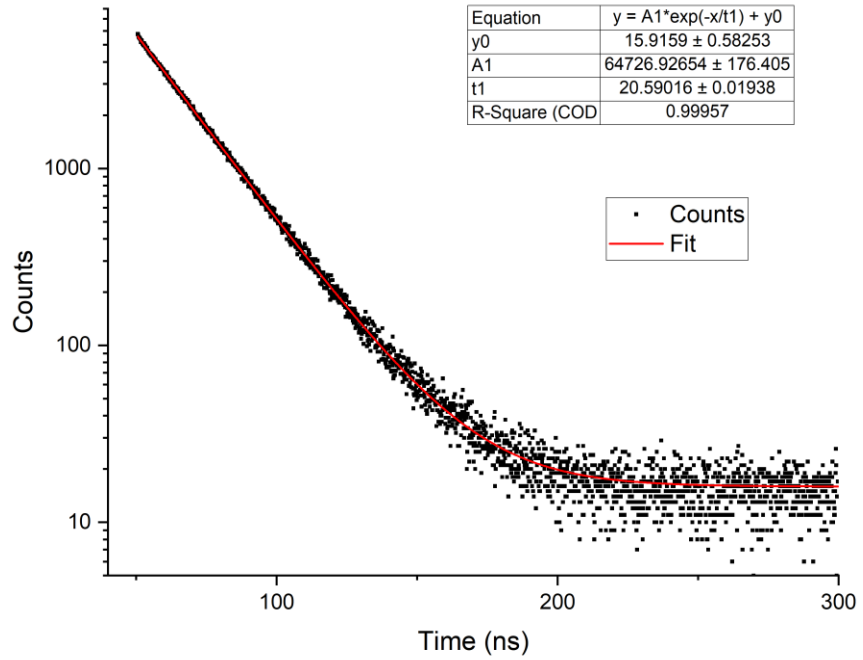

Figure 5.36. TCSPC trace of **KCryptL** in toluene collected using 405 nm excitation and 550 nm bandpass filter with 40 nm band width.

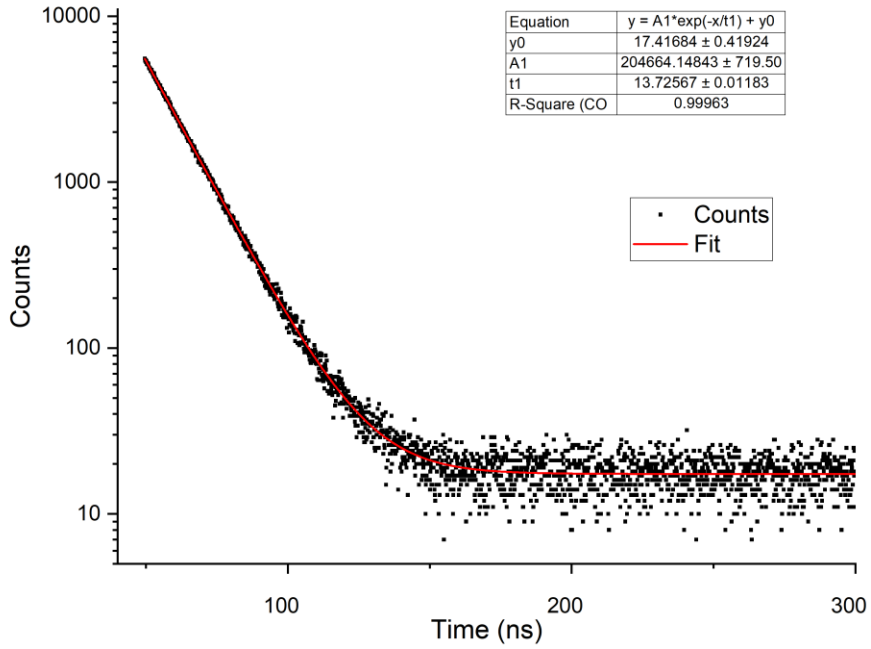

Figure 5.37. TCSPC trace of **CuL** in 1,3-DFB collected using 405 nm excitation and 550 nm bandpass filter with 40 nm band width.

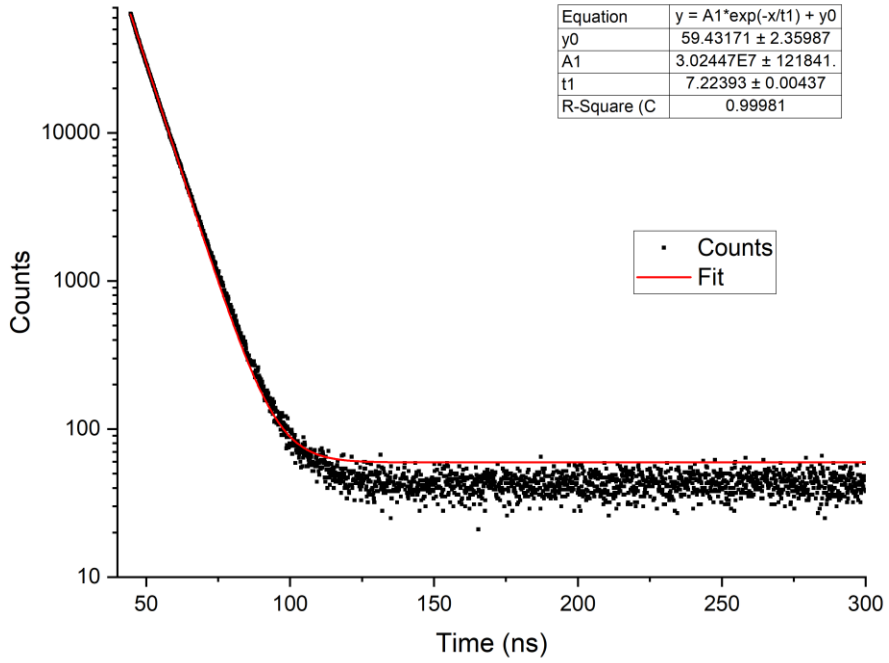

Figure 5.38. TCSPC trace of **CuL** in 1-methylnaphthalene collected using 405 nm excitation and 550 nm bandpass filter with 40 nm band width.

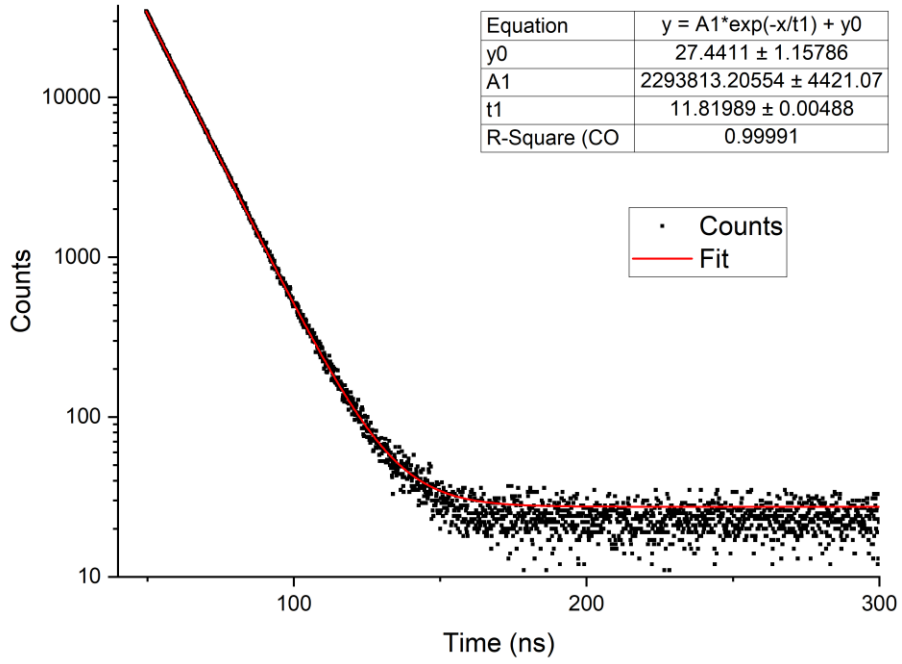

Figure 5.39. TCSPC trace of **CuL** in toluene collected using 405 nm excitation and 550 nm bandpass filter with 40 nm band width.

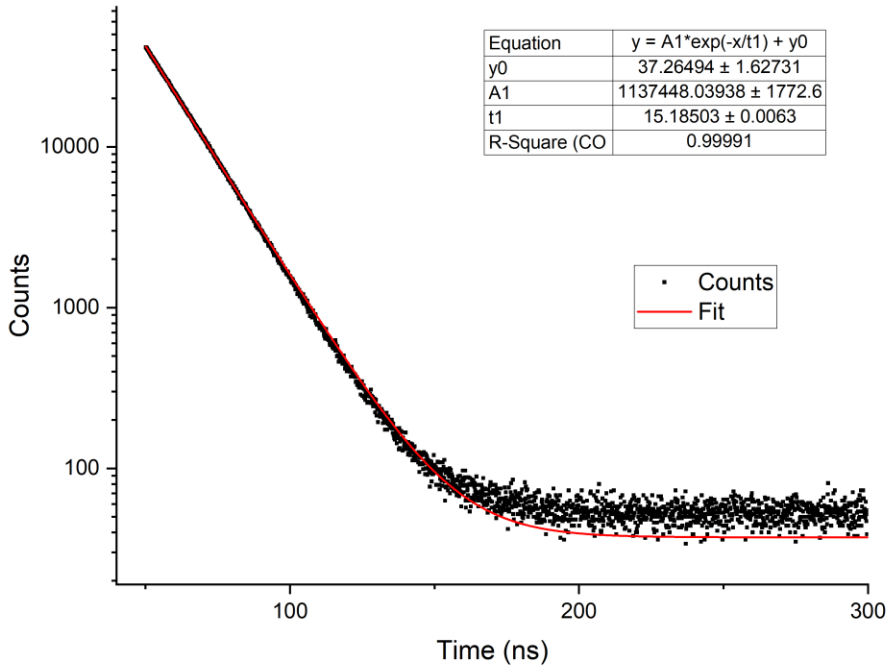

Figure 5.40. TCSPC trace of **CuL** in THF collected using 405 nm excitation and 550 nm bandpass filter with 40 nm band width.

5.5 References.

1. Prier, C. K.; Rankic, D. A.; MacMillan, D. W. C. *Chemical Reviews* **2013**, *113*, 5322-5363.

2. Rehm, D.; Weller, A. *Israel Journal of Chemistry* **1970**, *8*, 259-271.

3. MacKenzie, I. A.; Wang, L.; Onuska, N. P. R.; Williams, O. F.; Begam, K.; Moran, A. M.; Dunietz, B. D.; Nicewicz, D. A. *Nature* **2020**, *580*, 76-80.

4. Uoyama, H.; Goushi, K.; Shizu, K.; Nomura, H.; Adachi, C. *Nature* **2012**, *492*, 234-238.

5. Kim, H.; Kim, H.; Lambert, T. H.; Lin, S. *Journal of the American Chemical Society* **2020**, *142*, 2087-2092.

6. Rieth, A. J.; Gonzalez, M. I.; Kudisch, B.; Nava, M.; Nocera, D. G. *Journal of the American Chemical Society* **2021**, *143*, 14352-14359.

7. Ghosh, I.; Ghosh, T.; Bardagi, J. I.; König, B. *Science* **2014**, *346*, 725-728.

8. Cole, J. P.; Chen, D.-F.; Kudisch, M.; Pearson, R. M.; Lim, C.-H.; Miyake, G. M. *Journal of the American Chemical Society* **2020**, *142*, 13573-13581.

9. Cowper, N. G. W.; Chernowsky, C. P.; Williams, O. P.; Wickens, Z. K. *Journal of the American Chemical Society* **2020**, *142*, 2093-2099.

10. Pause, L.; Robert, M.; Savéant, J.-M. *Journal of the American Chemical Society* **1999**, *121*, 7158-7159.

11. Schmalzbauer, M.; Marcon, M.; König, B. *Angewandte Chemie International Edition* **2021**, *60*, 6270-6292.

12. Liang, K.; Liu, Q.; Shen, L.; Li, X.; Wei, D.; Zheng, L.; Xia, C. *Chemical Science* **2020**, *11*, 6996-7002.

13. Schmalzbauer, M.; Ghosh, I.; König, B. *Faraday Discussions* **2019**, *215*, 364-378.

14. Baek, Y.; Reinhold, A.; Tian, L.; Jeffrey, P. D.; Scholes, G. D.; Knowles, R. R. *Journal of the American Chemical Society* **2023**, *145*, 12499-12508.

15. Hamze, R.; Peltier, J. L.; Sylvinson, D.; Jung, M.; Cardenas, J.; Haiges, R.; Soleilhavoup, M.; Jazzar, R.; Djurovich, P. I.; Bertrand, G.; et al. *Science* **2019**, *363*, 601-606.

16. Shi, S.; Jung, M. C.; Coburn, C.; Tadle, A.; Sylvinson M. R, D.; Djurovich, P. I.; Forrest, S. R.; Thompson, M. E. *Journal of the American Chemical Society* **2019**, *141*, 3576-3588.

17. Gernert, M.; Balles-Wolf, L.; Kerner, F.; Müller, U.; Schmiedel, A.; Holzapfel, M.; Marian, C. M.; Pflaum, J.; Lambert, C.; Steffen, A. *Journal of the American Chemical Society* **2020**, *142*, 8897-8909.

18. Li, J.; Wang, L.; Zhao, Z.; Li, X.; Yu, X.; Huo, P.; Jin, Q.; Liu, Z.; Bian, Z.; Huang, C. *Angewandte Chemie International Edition* **2020**, *59*, 8210-8217.

19. Romanov, A. S.; Jones, S. T. E.; Gu, Q.; Conaghan, P. J.; Drummond, B. H.; Feng, J.; Chotard, F.; Buizza, L.; Foley, M.; Linnolahti, M.; et al. *Chemical Science* **2020**, *11*, 435-446.

20. Tzouras, N. V.; Martynova, E. A.; Ma, X.; Scattolin, T.; Hupp, B.; Busen, H.; Saab, M.; Zhang, Z.; Falivene, L.; Pisanò, G.; et al. *Chemistry – A European Journal* **2021**, *27*, 11904-11911.

21. Muniz, C. N.; Schaab, J.; Razgoniaev, A.; Djurovich, P. I.; Thompson, M. E. *Journal of the American Chemical Society* **2022**, *144*, 17916-17928.

22. Muniz, C. N.; Archer, C. A.; Applebaum, J. S.; Alagaratnam, A.; Schaab, J.; Djurovich, P. I.; Thompson, M. E. *Journal of the American Chemical Society* **2023**, *145*, 13846-13857.

23. Rai-Constapel, V.; Marian, C. M. *RSC Advances* **2016**, *6*, 18530-18537.

24. Liu, R.; Gao, H.; Zhou, L.; Ji, Y.; Zhang, G. *ChemistrySelect* **2019**, *4*, 7797-7804.

25. Lv, M.; Wang, X.; Pan, H.; Chen, J. *The Journal of Physical Chemistry B* **2021**, *125*, 13291-13297.

26. Thom, K. A.; Wieser, F.; Diestelhorst, K.; Reiffers, A.; Czekelius, C.; Kleinschmidt, M.; Bracker, M.; Marian, C. M.; Gilch, P. *The Journal of Physical Chemistry Letters* **2021**, *12*, 5703-5709.

27. Mei, Y.; Liu, D.; Li, J.; Wang, J. *Journal of Materials Chemistry C* **2022**, *10*, 16524-16535.

28. Rai-Constapel, V.; Salzmann, S.; Marian, C. M. *The Journal of Physical Chemistry A* **2011**, *115*, 8589-8596.

29. Satzger, H.; Schmidt, B.; Root, C.; Zinth, W.; Fierz, B.; Krieger, F.; Kiefhaber, T.; Gilch, P. *The Journal of Physical Chemistry A* **2004**, *108*, 10072-10079.

30. Mankad, N. P.; Laitar, D. S.; Sadighi, J. P. *Organometallics* **2004**, *23*, 3369-3371.

31. Takeda, T.; Akutagawa, T. *Chemistry – A European Journal* **2016**, *22*, 7763-7770.

32. Hamze, R.; Peltier, J. L.; Sylvinson, D.; Jung, M.; Cardenas, J.; Haiges, R.; Soleilhavoup, M.; Jazzar, R.; Djurovich, P. I.; Bertrand, G.; et al. *Science* **2019**, *363*, 601-606.

33. Beak, P.; Fry, F. S., Jr.; Lee, J.; Steele, F. *Journal of the American Chemical Society* **1976**, *98*, 171-179.

34. Cintã, P., S.,; Morari, C. *Spectrochimica Acta Part A: Molecular and Biomolecular Spectroscopy* **2004**, *60*, 337-342.

35. McClure, D. S. *The Journal of Chemical Physics* **1949**, *17*, 905-913.

36. Högemann, C.; Vauthey, E. *The Journal of Physical Chemistry A* **1998**, *102*, 10051-10059.

37. Connelly, N. G.; Geiger, W. E. *Chemical Reviews* **1996**, *96*, 877-910.

38. Ahn, J. M.; Ratani, T. S.; Hannoun, K. I.; Fu, G. C.; Peters, J. C. *Journal of the American Chemical Society* **2017**, *139*, 12716-12723.

39. Berraud-Pache, R.; Neese, F.; Bistoni, G.; Izsák, R. *Journal of Chemical Theory and Computation* **2020**, *16*, 564-575.

40. Sarkar, R.; Loos, P.-F.; Boggio-Pasqua, M.; Jacquemin, D. *Journal of Chemical Theory and Computation* **2022**, *18*, 2418-2436.

41. Pangborn, A. B.; Giardello, M. A.; Grubbs, R. H.; Rosen, R. K.; Timmers, F. J. *Organometallics* **1996**, *15*, 1518-1520.

42. Fulmer, G. R.; Miller, A. J. M.; Sherden, N. H.; Gottlieb, H. E.; Nudelman, A.; Stoltz, B. M.; Bercaw, J. E.; Goldberg, K. I. *Organometallics* **2010**, *29*, 2176-2179.

43. Berlman, I. B. In *Handbook of Fluorescence Spectra of Aromatic Molecules (Second Edition)*, Berlman, I. B. Ed.; Academic Press, 1971.

44. Neese, F. *WIREs Computational Molecular Science* **2012**, *2*, 73-78.

45. Neese, F. *WIREs Computational Molecular Science* **2018**, *8*, e1327.

46. Weigend, F.; Ahlrichs, R. *Physical Chemistry Chemical Physics* **2005**, *7*, 3297-3305.

47. Ernzerhof, M.; Scuseria, G. E. *The Journal of Chemical Physics* **1999**, *110*, 5029-5036.

48. Bühl, M.; Reimann, C.; Pantazis, D. A.; Bredow, T.; Neese, F. *Journal of Chemical Theory and Computation* **2008**, *4*, 1449-1459.

49. Neese, F.; Wennmohs, F.; Hansen, A.; Becker, U. *Chemical Physics* **2009**, *356*, 98-109.

50. Izsák, R.; Neese, F. *The Journal of Chemical Physics* **2011**, *135*, 144105.

51. Weigend, F. *Physical Chemistry Chemical Physics* **2006**, *8*, 1057-1065.

52. Eichkorn, K.; Treutler, O.; Öhm, H.; Häser, M.; Ahlrichs, R. *Chemical Physics Letters* **1995**, *240*, 283-290.

53. Hanwell, M. D.; Curtis, D. E.; Lonie, D. C.; Vandermeersch, T.; Zurek, E.; Hutchison, G. R. *Journal of Cheminformatics* **2012**, *4*, 17.

54. Krause, L.; Herbst-Irmer, R.; Sheldrick, G. M.; Stalke, D. *Journal of Applied Crystallography* **2015**, *48*, 3-10.

55. Sheldrick, G. *Acta Crystallographica Section A* **2015**, *71*, 3-8.

56. Dolomanov, O. V.; Bourhis, L. J.; Gildea, R. J.; Howard, J. A. K.; Puschmann, H. *Journal of Applied Crystallography* **2009**, *42*, 339-341.